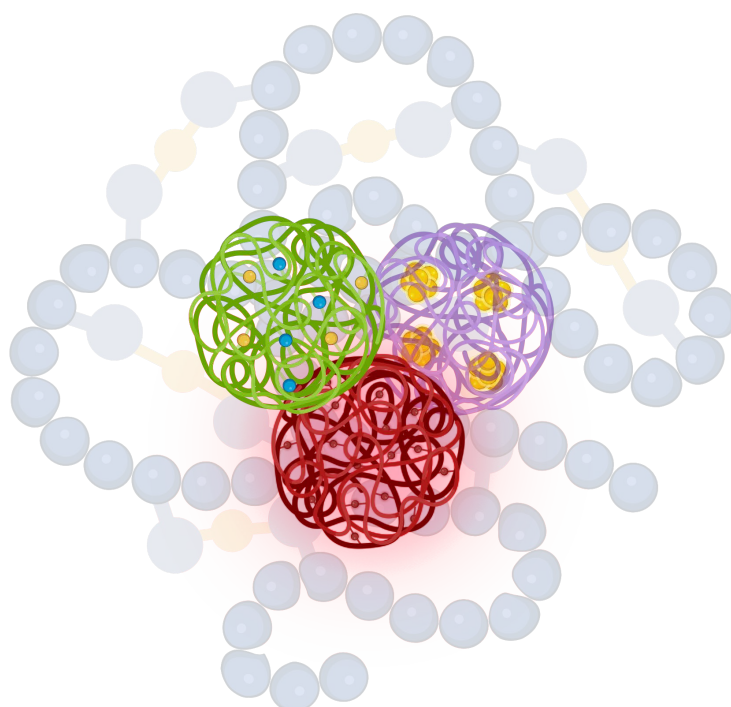


# Synthesis of Single-Chain Nanoparticles for Catalysis and Sensing



Author: Jokin Pinacho Olaciregui

Supervisors: Prof. José A. Pomposo and Prof. Daniel Taton

Donostia – San Sebastián, 2024



# CONTENTS

<b>ABSTRACT .....</b>	<b>7</b>
<b>RESUMEN.....</b>	<b>11</b>
<b>RÉSUMÉ .....</b>	<b>16</b>
<b>1. INTRODUCTION.....</b>	<b>21</b>
1.1. NANOSCIENCE AND SOFT MATTER.....	23
1.2. SINGLE-CHAIN NANOPARTICLES .....	25
1.2.1. <i>Design and synthesis of SCNPs</i> .....	26
1.2.1.1. Precursor synthesis.....	27
1.2.1.2. Precursor functionalization.....	29
1.2.1.3. Intrachain Folding/Collapse.....	30
1.2.1.4. Morphology of Single-Chain Nanoparticles (SCNPs) in Solution.....	36
1.3. APPLICATIONS OF SCNPs .....	38
1.3.1. <i>Catalysis</i> .....	39
1.3.2. <i>Sensing</i> .....	46
1.3.3. <i>Nanomedicine</i> .....	48
1.3.4. <i>Other applications</i> .....	51
1.5. REFERENCES.....	52
<b>2. OUTLINE AND OBJECTIVES OF THE THESIS.....</b>	<b>61</b>
<b>3. LANTHANIDE-BASED SINGLE-CHAIN NANOPARTICLES AS “VISUAL” PASS/FAIL SENSORS OF MAXIMUM PERMISSIBLE CONCENTRATION OF CU<sup>2+</sup> IONS IN DRINKING WATER .....</b>	<b>65</b>
3.1 MOTIVATION .....	67
3.2 INTRODUCTION.....	67
3.3. MATERIALS, TECHNIQUES AND METHODS .....	69
3.3.1. <i>Materials</i> .....	69
3.3.2. <i>Techniques</i> .....	70
3.3.3. <i>Methods</i> .....	71
3.4. RESULTS AND DISCUSSION .....	72
2.4.1. <i>Eu-SCNPs as m.p.c.(Cu<sup>2+</sup>) “visual” pass/fail sensors</i> .....	72
3.4.2. <i>Tb-SCNPs as m.p.c.(Cu<sup>2+</sup>) “visual” pass/fail sensors</i> .....	84
3.4.3. <i>Dy-SCNPs as m.p.c.(Cu<sup>2+</sup>) “visual” pass/fail sensors</i> .....	93
3.5. CONCLUSIONS .....	100
3.6. REFERENCES.....	101

<b>4. GOLD NANOCCLUSERS SYNTHESIZED WITHIN SINGLE-CHAIN NANOPARTICLES AS CATALYTIC NANOREACTORS IN WATER</b> .....	<b>105</b>
4.1. MOTIVATION.....	107
4.2. INTRODUCTION.....	107
4.3. MATERIALS AND METHODS.....	109
4.3.1. <i>Materials</i> .....	109
4.3.2. <i>Techniques</i> .....	109
4.4. PROCEDURES.....	110
4.4.1. <i>Procedure for the Synthesis of Poly(OEGMA-co-AEMA)</i> .....	110
4.4.2. <i>Procedure for the Synthesis of Gold Nanoclusters (Au-NCs) within Poly(OEGMA-co-AEMA) Single-Chain Nanoparticles (SCNPs)</i> .....	111
4.4.3. <i>Procedure for the Reduction of 4-Nitrophenol Catalyzed by AuNCs/SCNPs</i> .....	111
4.4.4. <i>Procedure for the Reduction of Nitrobenzene Catalyzed by AuNCs/SCNPs</i> .....	112
4.4.5. <i>Procedure for the Reduction of 3-(4-Nitrophenyl)-1,3-oxazolidin-2-one Catalyzed by Au-NCs/SCNPs</i> .....	112
4.5. RESULTS AND DISCUSSION.....	113
4.5.1. <i>Synthesis of Gold Nanoclusters within Single-Chain Nanoparticles (Au-NCs/SCNPs)</i> .....	113
4.5.2. <i>Gold Nanoclusters within Single-Chain Nanoparticles (AuNCs/SCNPs) as Catalytic Nanoreactors</i> .....	118
4.5.2.1. <i>Reduction of 4-Nitrophenol to 4-Aminophenol Catalyzed by Au-NCs/SCNPs</i> .....	118
4.5.2.2. <i>Reduction of Nitrobenzene to Aniline Catalyzed by Au-NCs/SCNPs</i> .....	125
4.5.2.3. <i>Reduction of 3-(4-Nitrophenyl)-1,3-oxazolidin-2-one to 3-(4-Aminophenyl)-1,3-oxazolidin-2-one Catalyzed by Au-NCs/SCNPs</i> .....	132
4.6. CONCLUSIONS.....	138
4.7. REFERENCES.....	140
<b>5. CONSECUTIVE ONE-POT ALKYNE SEMIHYDROGENATION/ ALKENE DIOXYGENATION REACTIONS BY PT(II)/CU(II) SINGLE-CHAIN NANOPARTICLES IN GREEN SOLVENT</b> .....	<b>143</b>
5.1. MOTIVATION.....	145
5.2. INTRODUCTION.....	145
5.3. MATERIALS AND METHODS.....	147
5.3.1. <i>Materials</i> .....	147
5.3.2. <i>Techniques</i> .....	148
5.4. PROCEDURES.....	149
5.4.1. <i>Synthesis of P0</i> .....	149
5.4.2. <i>Synthesis of P1</i> .....	149
5.4.3. <i>Synthesis of P1-SCNPs (as a control)</i> .....	150
5.4.4. <i>Synthesis of Pt(II)-SCNPs</i> .....	150

5.4.5. Synthesis of Pt(II)/Cu(II)-SCNPs.....	150
5.4.6. Synthesis of Cu(II)-SCNPs (as a control).....	151
5.4.7. General procedure for the consecutive one-pot alkyne semihydrogenation/alkene dioxxygenation reactions catalysed by .....	151
Pt(II)/Cu(II)-SCNPs in NBP at r.t. ....	151
5.5. RESULTS AND DISCUSSION .....	152
5.6. CONCLUSIONS .....	169
5.7. REFERENCES.....	170
<b>6. CONCLUSIONS .....</b>	<b>173</b>
<b>7. PUBLICATIONS.....</b>	<b>177</b>
<b>8. EXPERIMENTAL TECHNIQUES.....</b>	<b>181</b>
SIZE EXCLUSION CHROMATOGRAPHY (SEC).....	183
DYNAMIC LIGHT SCATTERING (DLS) .....	186
NUCLEAR MAGNETIC RESONANCE (NMR).....	187
FOURIER TRANSFORM INFRARED SPECTROSCOPY (FTIR).....	188
ULTRAVIOLET-VISIBLE SPECTROSCOPY (UV-Vis).....	189
FLUORESCENCE SPECTROSCOPY .....	190
ELEMENTAL ANALYSIS (EA).....	191
INDUCTIVELY COUPLED PLASMA MASS SPECTROMETRY (ICP-MS) .....	192
UV IRRADIATION .....	192
TRANSMISSION ELECTRON MICROSCOPY (TEM) .....	193
REFERENCES.....	194
<b>AGRADECIMIENTOS/ACKNOWLEDGMENTS.....</b>	<b>197</b>



## Abstract

This thesis dives into the world of Single-Chain Nanoparticles (SCNPs), from design to synthesis, by combining different metallic elements designed for applications in sensing and catalysis. Single-Chain Polymer Nanoparticles (SCNPs) are nanoscale particles formed by the folding and intramolecular cross-linking of single polymer chains. They exhibit unique properties such as high surface area, tuneable size, and the ability to encapsulate various substances, making them promising for applications in nanomedicine, catalysis, and material science. **Chapter 1** of this Thesis serves as an introduction to the topic of SCNPs, detailing their formation, properties, and potential applications. This chapter aims to provide a comprehensive overview of the state of the art in SCNP research, allowing the progress made in this Thesis to be understood in the context of existing knowledge and technological advancements at the outset.

Against this background, this work tries to further tailor the capabilities of SCNPs over and above the conventional functionalities with the help of a review that attempted to explore the most unique chemical and physical properties displayed by some metals, such as lanthanides (Eu, Tb and Dy), gold, platinum, and copper. Indeed, integration of metals within the SCNP architecture enhances their catalytic performance not only through their electronic and surface properties but also considers specific features of these metals' interaction with light and molecules to enhance their sensing properties. For example, gold's outstanding electron transfer characteristics or platinum's resistance to a myriad of conditions, have been used as a catalyst toward a variety of chemical transformations with a unique preciseness and ruggedness. On the other hand, the luminescence lanthanides are employed in the preparation of SCNPs for use as highly sensitive and selective sensors for environmental analytes. In the conjunction of knowledge comprising chemistry, material science, and nanotechnology, this is an interdisciplinary approach giving a comprehensive study over the synthesis of metal incorporated SCNPs. This thesis brings a series of well-designed experiments that not only contribute to the basic knowledge of SCNP assembly and strategies for metal integration but also open the door to new possibilities in applications in catalysis and

sensing technologies, highlighting the potential of SCNPs as a versatile and powerful tool in nanotechnological and materials scientific applications.

The present study in **Chapter 2** is aimed at synthesis and characterization of a new class of water-soluble lanthanide-containing SCNPs that have potential for visual sensing of  $\text{Cu}^{2+}$  ions for up to their maximum permissible concentration (m.p.c.) in drinking water. This novel sensing mechanism explores the characteristic properties of lanthanides and the structural benefits of SCNPs to design an easy, sensitive, and selective tool for monitoring copper ions, an important environmental and health concern. Even if copper is an important micro-element, it has the potential to turn into a toxic element at high concentrations, posing alarming situations both for the environment and human health. In this work, we developed europium (Eu), terbium (Tb), and dysprosium (Dy) integrated SCNPs that exhibit distinct fluorescence color changes under ultraviolet light upon reacting with  $\text{Cu}^{2+}$  ions, facilitating a straightforward "visual" pass/fail test.

The approach of this process lies in the development of an amphiphilic random copolymer decorated with beta-ketoester functional groups, able to complex lanthanide ions, so as to obtain water-soluble lanthanide-containing SCNPs. This method does intrachain complexation of  $\beta$ -ketoester/lanthanide, which is significance for the formation and function of these nanoparticles. The characterization of SCNPs has been made by different approaches: size-exclusion chromatography (SEC), dynamic light scattering (DLS), inductively coupled plasma mass spectrometry (ICP-MS), and fluorescence spectroscopy. SCNPs have been successfully formed and are able to sensitize copper ions ( $\text{Cu}^{2+}$ ).

The results seem to clearly indicate that all three Eu-, Tb- and Dy-based SCNPs can be very useful for a direct, visual detection of an excess  $\text{Cu}^{2+}$  concentration in water by the naked eye, due to the respective red-to-transparent, green-to-transparent and yellowto-transparent color changes under UV light. In summary, this work provides an important advance in environmental monitoring technology with the presentation of lanthanide-based SCNPs as effective, easy-to-use sensors for an important task: providing safe

drinking water. This approach will not only give help towards public health and environmental protection but opens the avenue for new development in terms of similar sensors for other contaminants.

**Chapter 3** was based on developing a novel idea comprising the synthesis of gold nanoclusters (Au-NCs) within single-chain nanoparticles (SCNPs) and to apply the former as a nanoreactor in aqueous catalysis. The efficiency and selectivity of metalloenzymes in cellular environments have provoked interest in the present study, which needs to be mimicked by natural catalysts using simplified metalloenzyme-mimetic nano-objects. As opposed to most metal-containing SCNPs reported so far, wherein the metal ions are complexed, in this work, the objective was the encapsulation of metal nanoclusters, more precisely Au-NCs with sizes smaller than 5 nm, within the SCNPs, in order to exploit their emergent catalytic properties.

For the synthesis of Au-NCs/SCNPs, an amphiphilic random copolymer of poly (OEGMAco-AEMA) was used to self-assemble in water and form SCNPs, reducing agent Au(III) ions to Au(0). The beta-ketoester groups located in the AEMA units along the copolymer chain acted as very effective reductants and stabilizing agents for the Au-NCs. On the other hand, characterizations with TEM, DLS, and UV-Vis spectroscopy did establish a good conformation of formed and stable Au-NCs/SCNPs.

The study revealed new utilities of these nanostructures as catalytic nanoreactors for the reduction of 4-nitrophenol, nitrobenzene, and 3-(4-nitrophenyl)-1,3-oxazolidinone by borohydride ( $\text{BH}_4^-$ ) in water at r.t. These reactions well represent benchmarks for the assessment of the catalytic activity of the synthesized Au-NCs/SCNPs in water and, therefore, open up an entirely new scope for potential applications regarding use in catalysis, biomedicine, energy, and electronics.

These results, therefore, open new avenues for the synthesis and incorporation of metal nanoclusters within SCNPs for advanced catalysis in aqueous media. The fact that polymer and metal nanocluster-based systems actually manage to emulate

metalloenzyme activity has thus opened up promises in developing efficient, stable, and selective catalytic systems within a wide field of applications.

**Chapter 4** introduces a novel approach to catalysis with heterobimetallic Pt(II)/Cu(II) single-chain polymer nanoparticles (SCNPs) introducing strategically placed  $\alpha$ -diazo- $\beta$ -ketoester and naked  $\beta$ -ketoester functional groups within the SCNPs structure. It involves photoactivated carbene generation with 365 nm wavelength light and Pt(II) ions, selecting dichloro(1,5-cyclooctadiene)Pt(II) for its affinity with the generated carbene moieties. Subsequently, Cu(II) is introduced through reactions with Cu(II) acetate, resulting in a polymeric structure of Cu(II)-( $\beta$ -ketoester)<sub>2</sub> complexes. This dual metal incorporation is essential for folding the polymeric precursor into the final nanoscopic structure, as evidenced by infrared spectroscopy, size exclusion chromatography, and dynamic light scattering, indicating the formation of well-defined Pt(II)/Cu(II)-SCNPs.

The novelty of this investigation lies in developing and applying these novel SCNPs as heterobimetallic soft nanocatalysts for consecutive one-pot alkyne semi-hydrogenation and alkene dioxygenation reactions. This process demonstrates high efficiency and specificity of the nanocatalyst in catalysis within a single reaction environment, significantly conducted in N-butylpyrrolidone, a green solvent alternative to dimethylformamide (DMF), aligning the project with green chemistry principles by minimizing toxic solvent use and enhancing chemical process sustainability.

This comprehensive work contributes to catalytic science and the exploration of a new class of heterobimetallic nanocatalysts, representing a multifaceted approach at the materials science, chemistry, and environmental sustainability interface. It bears relevance for organic synthesis and materials development, aiming at complex chemical transformations. Furthermore, it has implications for environmentally friendly industrial processes, promoting the adoption of green solvents in chemical manufacturing. The successful implementation of Pt(II)/Cu(II)-SCNPs in catalysis marks a significant advancement towards designing efficient, environmentally friendly catalytic systems, potentially revolutionizing research and application in nanotechnology and green chemistry.

## Resumen

Esta tesis se adentra en el mundo de las nanopartículas de cadena única (SCNPs), desde su diseño hasta su síntesis, combinando diferentes elementos metálicos diseñados para aplicaciones en detección y catálisis. Las nanopartículas de cadena única (SCNPs) son partículas a escala nanométrica formadas por el plegamiento y entrecruzamiento intramolecular de cadenas de polímeros individuales. Exhiben propiedades únicas, como una alta superficie específica, tamaño ajustable y la capacidad de encapsular diversas sustancias, lo que las hace prometedoras para aplicaciones en nanomedicina, catálisis y ciencia de materiales. El **Capítulo 1** de esta tesis sirve como introducción al tema de las SCNPs, detallando su formación, propiedades y aplicaciones potenciales. Este capítulo tiene como objetivo proporcionar una visión completa del estado del arte en la investigación sobre SCNPs, permitiendo entender el progreso realizado en esta tesis en el contexto del conocimiento existente y los avances tecnológicos.

En este contexto, este trabajo intenta ajustar aún más las capacidades de las SCNPs más allá de las funcionalidades convencionales, mediante una revisión que explora las propiedades químicas y físicas más únicas exhibidas por algunos metales, como los lantánidos (Eu, Tb y Dy), el oro, el platino y el cobre. De hecho, la integración de metales dentro de la arquitectura de las SCNPs mejora su rendimiento catalítico no solo a través de sus propiedades electrónicas y de superficie, sino que también considera características específicas de la interacción de estos metales con la luz y las moléculas para mejorar sus propiedades de detección. Por ejemplo, las características excepcionales de transferencia de electrones del oro o la resistencia del platino a una miríada de condiciones se han utilizado como catalizadores para una variedad de transformaciones químicas con una precisión y robustez únicas. Por otro lado, los lantánidos luminiscentes se emplean en la preparación de SCNPs para su uso como sensores altamente sensibles y selectivos para analitos ambientales. En la conjunción del conocimiento que abarca la química, la ciencia de materiales y la nanotecnología, este es un enfoque interdisciplinario que ofrece un estudio integral sobre la síntesis de SCNPs incorporados con metales. Esta tesis presenta una serie de experimentos bien diseñados que no solo contribuyen al conocimiento básico del ensamblaje de SCNPs y

estrategias para la integración de metales, sino que también abren la puerta a nuevas posibilidades en aplicaciones en tecnologías de catálisis y detección, destacando el potencial de las SCNPs como una herramienta versátil y poderosa en aplicaciones nanotecnológicas y científicas de materiales.

El estudio presente en el **Capítulo 2** está dirigido a la síntesis y caracterización de una nueva clase de SCNPs que contienen lantánidos solubles en agua y que tienen potencial para la detección visual de iones  $\text{Cu}^{2+}$  hasta su concentración máxima permitida (m.p.c.) en agua potable. Este novedoso mecanismo de detección explora las propiedades características de los lantánidos y los beneficios estructurales de las SCNPs para diseñar una herramienta fácil, sensible y selectiva para monitorear iones de cobre, una importante preocupación ambiental y de salud. Aunque el cobre es un microelemento importante, tiene el potencial de convertirse en un elemento tóxico en altas concentraciones, planteando situaciones alarmantes tanto para el medio ambiente como para la salud humana. En este trabajo, desarrollamos SCNPs integrados con europio (Eu), terbio (Tb) y disprosio (Dy) que exhiben cambios de color fluorescente distintivos bajo luz ultravioleta al reaccionar con iones  $\text{Cu}^{2+}$ , facilitando una prueba "visual" sencilla de aprobación o rechazo.

El enfoque de este proceso radica en el desarrollo de un copolímero aleatorio anfifílico decorado con grupos funcionales beta-cetoéster, capaces de complejar iones de lantánidos, para obtener SCNPs que contienen lantánidos solubles en agua. Este método realiza una complejación intramolecular de  $\beta$ -cetoéster/lantánido, lo cual es significativo para la formación y función de estas nanopartículas. La caracterización de las SCNPs se ha realizado mediante diferentes enfoques: cromatografía de exclusión por tamaño (SEC), dispersión de luz dinámica (DLS), espectrometría de masas con plasma acoplado inductivamente (ICP-MS) y espectroscopía de fluorescencia. Las SCNPs se han formado con éxito y son capaces de detectar iones de cobre ( $\text{Cu}^{2+}$ ).

Los resultados parecen indicar claramente que todas las SCNPs basadas en Eu, Tb y Dy pueden ser muy útiles para la detección visual directa del exceso de concentración de  $\text{Cu}^{2+}$  en agua a simple vista, debido a los respectivos cambios de color de rojo a

transparente, verde a transparente y amarillo a transparente bajo luz UV. En resumen, este trabajo proporciona un avance importante en la tecnología de monitoreo ambiental con la presentación de SCNPs basadas en lantánidos como sensores efectivos y fáciles de usar para una tarea importante: proporcionar agua potable segura. Este enfoque no solo ayudará en la protección de la salud pública y el medio ambiente, sino que también abre el camino para el desarrollo de sensores similares para otros contaminantes.

El **Capítulo 3** se basó en el desarrollo de una idea novedosa que comprende la síntesis de nanoclústeres de oro (Au-NCs) dentro de nanopartículas de cadena única (SCNPs) y en aplicar estos últimos como nanoreactores en catálisis acuosa. La eficiencia y selectividad de las metaloenzimas en ambientes celulares han provocado interés en el presente estudio, que necesita ser imitado por catalizadores naturales utilizando nanoobjetos simplificados miméticos de metaloenzimas. A diferencia de la mayoría de las SCNPs que contienen metales reportadas hasta ahora, en las que los iones metálicos están complejados, en este trabajo, el objetivo fue la encapsulación de nanoclústeres metálicos, más precisamente Au-NCs con tamaños menores a 5 nm, dentro de las SCNPs, para explotar sus propiedades catalíticas emergentes.

Para la síntesis de Au-NCs/SCNPs, se utilizó un copolímero aleatorio anfifílico de poli (OEGMA-co-AEMA) para autoensamblarse en agua y formar SCNPs, reduciendo los iones de Au(III) a Au(0). Los grupos beta-cetoéster ubicados en las unidades de AEMA a lo largo de la cadena de copolímero actuaron como reductores y agentes estabilizadores muy efectivos para los Au-NCs. Por otro lado, las caracterizaciones con TEM, DLS y espectroscopía UV-Vis establecieron una buena conformación de Au-NCs/SCNPs formados y estables.

El estudio reveló nuevas utilidades de estas nanoestructuras como nanoreactores catalíticos para la reducción de 4-nitrofenol, nitrobenceno y 3-(4-nitrofenil)-1,3-oxazolidin-2-ona por borohidruro ( $\text{BH}_4^-$ ) en agua a temperatura ambiente. Estas reacciones representan puntos de referencia para la evaluación de la actividad catalítica de los Au-NCs/SCNPs sintetizados en agua y, por lo tanto, abren un alcance

completamente nuevo para aplicaciones potenciales en catálisis, biomedicina, energía y electrónica.

Estos resultados, por lo tanto, abren nuevas avenidas para la síntesis e incorporación de nanoclústeres metálicos dentro de SCNPs para catálisis avanzada en medios acuosos. El hecho de que los sistemas basados en polímeros y nanoclústeres metálicos logren emular la actividad de las metaloenzimas ha abierto promesas en el desarrollo de sistemas catalíticos eficientes, estables y selectivos dentro de un amplio campo de aplicaciones.

El **Capítulo 4** introduce un enfoque novedoso para la catálisis con nanopartículas de polímero de cadena única heterobimetálicas Pt(II)/Cu(II), introduciendo estratégicamente grupos funcionales  $\alpha$ -dialdo- $\beta$ -cetoéster y  $\beta$ -cetoéster desnudos dentro de la estructura de las SCNPs. Implica la generación de carbeno fotoactivado con luz de longitud de onda de 365 nm y iones de Pt(II), seleccionando Pt(II) dicloro(1,5-ciclooctadieno) por su afinidad con los moieties de carbeno generados. Posteriormente, se introduce Cu(II) a través de reacciones con acetato de Cu(II), resultando en una estructura polimérica de complejos Cu(II)-( $\beta$ -cetoéster)<sub>2</sub>. Esta incorporación dual de metales es esencial para el plegamiento del precursor polimérico en la estructura nanoscópica final, como lo evidencia la espectroscopía infrarroja, la cromatografía de exclusión por tamaño y la dispersión de luz dinámica, indicando la formación de SCNPs bien definidas de Pt(II)/Cu(II).

La novedad de esta investigación radica en desarrollar y aplicar estas nuevas SCNPs como nanocatalizadores blandos heterobimetálicos para reacciones consecutivas de semi-hidrogenación de alquinos y dioxygenación de alquenos en un solo paso. Este proceso demuestra una alta eficiencia y especificidad del nanocatalizador en catálisis dentro de un único entorno de reacción, realizado significativamente en N-butilpirrolidona, una alternativa de solvente verde al dimetilformamida (DMF), alineando el proyecto con los principios de la química verde al minimizar el uso de solventes tóxicos y mejorar la sostenibilidad del proceso químico.

Esta Tesis doctoral contribuye a la ciencia catalítica y a la exploración de una nueva clase de nanocatalizadores heterobimetálicos, representando un enfoque multifacético en la interfaz de la ciencia de materiales, la química y la sostenibilidad ambiental. Es relevante para la síntesis orgánica y el desarrollo de materiales, apuntando a transformaciones químicas complejas. Además, tiene implicaciones para procesos industriales ambientalmente amigables, promoviendo la adopción de solventes verdes en la fabricación química. La implementación exitosa de SCNPs Pt(II)/Cu(II) en catálisis marca un avance significativo hacia el diseño de sistemas catalíticos eficientes y respetuosos con el medio ambiente, potencialmente revolucionando la investigación y aplicación en nanotecnología y química verde.

## Résumé

Cette thèse explore le monde des nanoparticules à chaîne unique (SCNPs), de leur conception à leur synthèse, en combinant différents éléments métalliques destinés à des applications dans la détection et la catalyse. Les nanoparticules polymères à chaîne unique (SCNPs) sont des particules à l'échelle nanométrique formées par le repliement et la réticulation intramoléculaire de chaînes polymères uniques. Elles présentent des propriétés uniques telles qu'une grande surface, une taille modulable et la capacité d'encapsuler diverses substances, ce qui les rend prometteuses pour des applications en nanomédecine, catalyse et science des matériaux. Le **chapitre 1** de cette thèse sert d'introduction au sujet des SCNPs, détaillant leur formation, leurs propriétés et leurs applications potentielles. Ce chapitre vise à fournir un aperçu complet de l'état de l'art dans la recherche sur les SCNPs, permettant de comprendre les progrès réalisés dans cette thèse dans le contexte des connaissances existantes et des avancées technologiques.

Dans ce contexte, ce travail tente de développer davantage les capacités des SCNPs au-delà des fonctionnalités conventionnelles en s'appuyant sur une revue qui a tenté d'explorer les propriétés chimiques et physiques les plus uniques affichées par certains métaux, tels que les lanthanides (Eu, Tb et Dy), l'or, le platine et le cuivre. En effet, l'intégration des métaux dans l'architecture des SCNPs améliore leurs performances catalytiques non seulement grâce à leurs propriétés électroniques et de surface, mais prend également en compte les caractéristiques spécifiques de l'interaction de ces métaux avec la lumière et les molécules pour améliorer leurs propriétés de détection. Par exemple, les caractéristiques exceptionnelles de transfert d'électrons de l'or ou la résistance du platine à une myriade de conditions ont été utilisées comme catalyseur pour diverses transformations chimiques avec une précision et une robustesse uniques. D'autre part, les lanthanides luminescents sont utilisés dans la préparation des SCNPs pour servir de capteurs hautement sensibles et sélectifs pour les analytes environnementaux. En combinant des connaissances en chimie, science des matériaux et nanotechnologie, il s'agit d'une approche interdisciplinaire offrant une étude

complète sur la synthèse des SCNPs incorporant des métaux. Cette thèse présente une série d'expériences bien conçues qui non seulement contribuent aux connaissances de base sur l'assemblage des SCNPs et les stratégies d'intégration des métaux, mais ouvrent également la voie à de nouvelles possibilités d'applications dans les technologies de catalyse et de détection, mettant en lumière le potentiel des SCNPs comme outil polyvalent et puissant dans les applications nanotechnologiques et scientifiques des matériaux.

L'étude présentée dans le **chapitre 2** vise la synthèse et la caractérisation d'une nouvelle classe de SCNPs contenant des lanthanides solubles dans l'eau, ayant le potentiel de détecter visuellement les ions  $\text{Cu}^{2+}$  jusqu'à leur concentration maximale admissible (m.p.c.) dans l'eau potable. Ce nouveau mécanisme de détection explore les propriétés caractéristiques des lanthanides et les avantages structurels des SCNPs pour concevoir un outil facile, sensible et sélectif pour la surveillance des ions cuivre, une préoccupation importante pour l'environnement et la santé. Bien que le cuivre soit un micro-élément important, il peut devenir un élément toxique à des concentrations élevées, posant des situations alarmantes tant pour l'environnement que pour la santé humaine. Dans ce travail, nous avons développé des SCNPs intégrant de l'euporium (Eu), du terbium (Tb) et du dysprosium (Dy) qui présentent des changements de couleur distincts sous lumière ultraviolette lors de la réaction avec les ions  $\text{Cu}^{2+}$ , facilitant un test visuel simple "pass/fail".

L'approche de ce processus réside dans le développement d'un copolymère aléatoire amphiphile décoré de groupes fonctionnels bêta-cétoester, capable de complexer les ions lanthanides, afin d'obtenir des SCNPs contenant des lanthanides solubles dans l'eau. Cette méthode réalise une complexation intrachaine du complexe  $\beta$ -cétoester/lanthanide, ce qui est significatif pour la formation et la fonction de ces nanoparticules. La caractérisation des SCNPs a été réalisée par différentes approches : chromatographie d'exclusion de taille (SEC), diffusion dynamique de la lumière (DLS), spectrométrie de masse à plasma à couplage inductif (ICP-MS) et spectroscopie de fluorescence. Les SCNPs ont été formés avec succès et sont capables de sensibiliser les ions cuivre ( $\text{Cu}^{2+}$ ).

Les résultats semblent indiquer clairement que les SCNPs à base de Eu, Tb et Dy peuvent être très utiles pour une détection directe et visuelle d'un excès de concentration de  $\text{Cu}^{2+}$  dans l'eau à l'œil nu, en raison des changements de couleur respectifs de rouge à transparent, vert à transparent et jaune à transparent sous lumière UV. En résumé, ce travail apporte une avancée importante dans la technologie de surveillance environnementale avec la présentation de SCNPs à base de lanthanides comme capteurs efficaces et faciles à utiliser pour une tâche importante : fournir de l'eau potable sûre. Cette approche contribuera non seulement à la santé publique et à la protection de l'environnement, mais ouvrira également la voie à de nouveaux développements en termes de capteurs similaires pour d'autres contaminants.

Le **chapitre 3** est basé sur le développement d'une idée novatrice comprenant la synthèse de nanoclusters d'or (Au-NCs) au sein de nanoparticules à chaîne unique (SCNPs) et l'application de ces derniers comme nanoréacteur en catalyse aqueuse. L'efficacité et la sélectivité des métalloenzymes dans les environnements cellulaires ont suscité l'intérêt de la présente étude, qui doit être imitée par des catalyseurs naturels utilisant des nano-objets mimétiques de métalloenzymes simplifiés. Contrairement à la plupart des SCNPs contenant des métaux rapportés jusqu'à présent, où les ions métalliques sont complexés, dans ce travail, l'objectif était l'encapsulation de nanoclusters métalliques, plus précisément des Au-NCs de taille inférieure à 5 nm, au sein des SCNPs, afin d'exploiter leurs propriétés catalytiques émergentes.

Pour la synthèse des Au-NCs/SCNPs, un copolymère aléatoire amphiphile de poly (OEGMA-co-AEMA) a été utilisé pour s'auto-assembler dans l'eau et former des SCNPs, réduisant les ions Au(III) en Au(0). Les groupes bêta-cétoester situés dans les unités AEMA le long de la chaîne du copolymère ont agi comme réducteurs et agents stabilisants très efficaces pour les Au-NCs. D'autre part, des caractérisations par TEM, DLS et spectroscopie UV-Vis ont établi une bonne conformation des Au-NCs/SCNPs formés et stables.

L'étude a révélé de nouvelles utilités de ces nanostructures en tant que nanoréacteurs catalytiques pour la réduction de 4-nitrophénol, nitrobenzène et 3-(4-nitrophényl)-1,3-

oxazolidin-2-one par borohydrure ( $\text{BH}_4^-$ ) dans l'eau à température ambiante. Ces réactions représentent bien des points de référence pour l'évaluation de l'activité catalytique des Au-NCs/SCNPs synthétisés dans l'eau et ouvrent donc une nouvelle perspective d'applications potentielles en catalyse, biomédecine, énergie et électronique.

Ces résultats ouvrent ainsi de nouvelles voies pour la synthèse et l'incorporation de nanoclusters métalliques au sein des SCNPs pour une catalyse avancée en milieu aqueux. Le fait que les systèmes à base de polymères et de nanoclusters métalliques parviennent effectivement à imiter l'activité des métalloenzymes ouvre donc des promesses de développement de systèmes catalytiques efficaces, stables et sélectifs dans un large champ d'applications.

Le **chapitre 4** introduit une nouvelle approche de la catalyse avec des nanoparticules polymères à chaîne unique hétérobimétalliques Pt(II)/Cu(II) (SCNPs), introduisant stratégiquement des groupes fonctionnels  $\alpha$ -dialzo- $\beta$ -cétoester et  $\beta$ -cétoester nus dans la structure des SCNPs. Cela implique la génération de carbène photoactivée avec une lumière de longueur d'onde de 365 nm et des ions Pt(II), en sélectionnant le dichloro(1,5-cyclooctadiène)Pt(II) pour son affinité avec les groupements carbène générés. Par la suite, le Cu(II) est introduit par des réactions avec l'acétate de Cu(II), résultant en une structure polymérique de complexes Cu(II)-( $\beta$ -cétoester)<sub>2</sub>. Cette incorporation duale de métaux est essentielle pour le repliement du précurseur polymérique en la structure nanoscopique finale, comme en témoignent la spectroscopie infrarouge, la chromatographie d'exclusion de taille et la diffusion dynamique de la lumière, indiquant la formation de SCNPs Pt(II)/Cu(II) bien définis. La nouveauté de cette investigation réside dans le développement et l'application de ces nouveaux SCNPs.



# **1. Introduction**



## 1.1. Nanoscience and Soft Matter

Since the advent of nanoscience and nanotechnology, as pioneered by Nobel laureate Richard P. Feynman in his seminal 1959 lecture, "There's Plenty of Room at the Bottom",<sup>1</sup> the scientific community has witnessed a plethora of transformative developments across the disciplines of physics, chemistry, and biology. These advancements have materialized Feynman's visionary concepts of manipulating matter at the most diminutive scale, specifically at the molecular and atomic levels, herein referred to as the nanoscale.

The term "nanotechnology," albeit subject to varied interpretations across different scientific domains and geographical regions, is frequently employed as an umbrella term to encapsulate technologies that operate on an exceedingly minute scale. Nonetheless, nanotechnology is principally delineated as the scientific endeavor encompassing the comprehensive understanding, precise manipulation, and strategic restructuring of matter at dimensions on the order of nanometers (notably, less than 100 nm).<sup>2</sup>

Whitesides (2004) highlights that at this scale, the properties of materials undergo a fundamental shift, distinguishing them markedly from their bulk counterparts.<sup>3</sup> This field has witnessed an exponential growth over recent decades, leading to the emergence of groundbreaking disciplines such as nanomedicine, as elucidated by Mishra (2013),<sup>4</sup> nanoelectronics, described by Puers et al. (2017),<sup>5</sup> and nanocatalysis, as discussed by Bahadur-Singh and Kumar-Tandon (2014).<sup>6</sup> The surge in nanoscience research and investment is well-documented by Velmurugan and Radhakrishnan (2016).<sup>7</sup>

Solid-state physics and electronics have ventured into the realm of nanostructures through the employment of lithography and etching processes, denoted as the "topdown" approach. This methodology facilitates the creation of structures with dimensions not less than approximately 20 nanometers. Conversely, nature exemplifies an alternative paradigm for the assembly of diminutive structures. In this context,

individual molecules are amalgamated into larger functional entities and intricate structural hierarchies through a process of self-organization, a strategy referred to as the "bottom-up" approach.<sup>8</sup>

In nature, dynamic individual biomacromolecules self-assemble into a variety of functional nanoentities on various scales,<sup>9</sup> giving rise to complex materials like viruses or DNA. Seen from this angle, the natural world serves as a model for the design of small buildings. Fundamental to the creation of nanostructures is the nanoparticle, a fundamental unit that is larger than atoms or simple molecules, which are subject to quantum mechanics, but much smaller than macroscopic objects governed by Newtonian mechanics.<sup>10</sup>

Nanoparticles are classified into two varieties based on composition: "**hard nanoparticles**", which are usually made of inorganic materials, and "**soft nanoparticles**", which are made of organic components. Exceptional control over size and shape has been achieved in the creation of hard nanoparticles, such as metal oxide nanoparticles, quantum dots, and gold nanoclusters.

Macromolecular architecture modification has made tremendous strides in the last several decades in the field of artificial soft nano-objects. The development of effective Controlled Radical Polymerization (CRP) methods is primarily responsible for these improvements. Many complicated macromolecular structures, including star polymers, comb-like copolymers, and hyperbranched macromolecules, have been developed by using CRP methodologies.<sup>11, 12</sup> The materials produced as a result of these processes differ significantly from their linear analogs with similar molecular weights in terms of their characteristics (Figure 1). Within this spectrum of artificial soft nano-objects, a notable category is represented by **Single-Chain Nanoparticles (SCNPs)**.

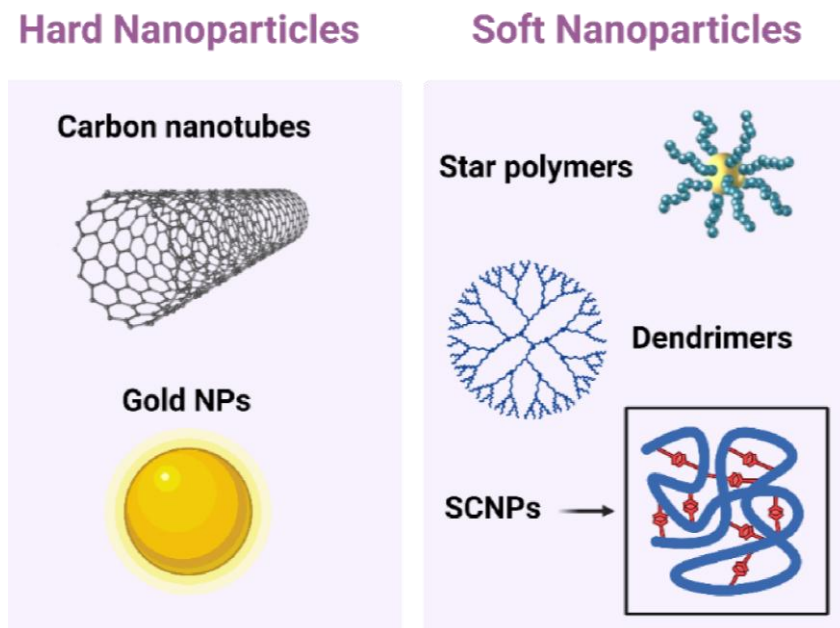


**Figure 1.** Different examples of hard-nanoparticles and soft-nanoparticles classified by type and morphology.

## 1.2. Single-Chain Nanoparticles

The development of Single-Chain Polymer Nanoparticles (SCNPs) constitutes a vibrant area within the realm of macromolecular chemistry, aimed at replicating the precision of natural polymeric models. Analogous to the configuration of proteins, SCNPs are crafted through the intramolecular folding of synthetic linear polymer precursors (Figure 2). This innovative approach positions SCNPs as viable candidates for a wide array of applications across diverse fields such as catalysis,<sup>13,14</sup> microelectronics,<sup>15</sup> nanomedicine,<sup>16</sup> DNA delivery mechanisms,<sup>17</sup> sensory technologies<sup>16</sup> or imaging agents.<sup>18</sup>

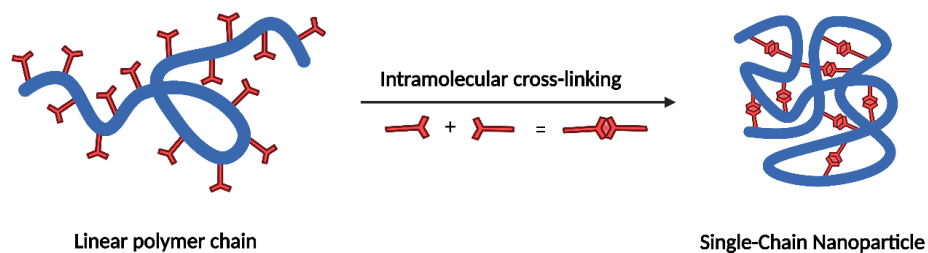


**Figure 2.** Schematic illustration of a linear polymer precursor and a single-chain nanoparticle (SCNP) obtained through intra-chain folding/collapse of individual polymer chains at very dilute conditions.

The notion of Single-Chain Nanoparticles (SCNPs) formed through the intra-molecular cross-linking of individual linear polymer chains was first posited 22 years prior.<sup>19</sup> Presently, research within the domain of SCNPs resides at the intersection of polymer science, nanotechnology, and biology. The process by which individual polymer chains fold into functional SCNPs bears similarity to the folding of proteins into their functional, native states, albeit with the acknowledgment that current SCNPs do not exhibit the sequence perfection, size uniformity, and precise morphology characteristic of natural biomacromolecules.<sup>20</sup>

Specifically, the dimensional characteristics of nanoparticles (NPs) are complexly tuned in relation to the molecular length of the precursor polymer, a parameter whose fine control has been assured with an increase in polymerization developments throughout the recent decades.<sup>21</sup> Additionally, the density of crosslinking implemented is a critical factor in dictating the size of the NPs. A prototype for polymers in terms of intramolecular crosslinking was initiated in 1962,<sup>22</sup> while its advancement to a level enabling well-controlled processes on a larger scale only came in 2002.<sup>23</sup> Since then, a variety of methodologies have been developed for the intramolecular crosslinking of precursor polymer chains which enabled preparation of functional Single-Chain Nanoparticles (SCNPs).<sup>24</sup>

### **1.2.1. Design and synthesis of SCNPs**

The degree of functionalization and the molecular weight of the Single-Chain Nanoparticle (SCNP) precursor polymer are important factors that control SCNP size. This is related to the kind of interactions that help the folding/collapse process together with the solvent's quality (e.g., excellent solvent, selective solvent).<sup>25,26</sup> The manufacture of single-chain nanoparticles involves three main processes, as shown in Figure 3.<sup>27</sup>

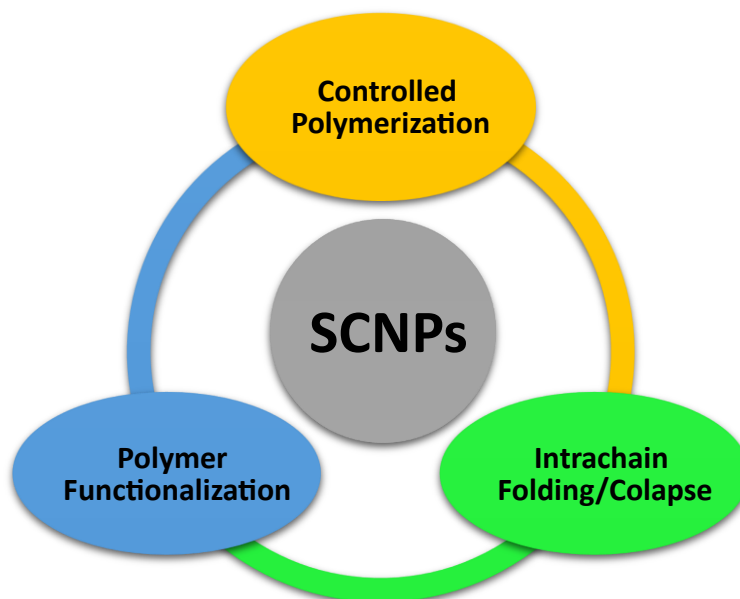


**Figure 3.** Illustration of the different techniques involved in the construction of single-chain nanoparticles (SCNPs): controlled polymerization, polymer functionalization and polymer folding/collapse.

#### 1.2.1.1. Precursor synthesis

The development of controlled radical polymerization (CRP) techniques has led to an exponential increase in the use of specialty polymers made by CRP in the fields of nanoscience and nanotechnology. These techniques can easily produce polymers that closely resemble the polydispersity properties of well-defined anionic "living" polymers with controlled architectures like stars, combs, and dendrimers, and they also show robust compatibility with a wide range of monomer functional groups.<sup>28</sup> Reversible addition-fragmentation chain transfer (RAFT) polymerization,<sup>29</sup> atom transfer radical polymerization (ATRP),<sup>30</sup> nitroxide-mediated radical polymerization (NMP),<sup>31</sup> and, more recently, ring-opening metathesis polymerization (ROMP) using second (or higher) generation Grubbs catalysis have become popular CRP techniques.<sup>32</sup>

From the previously indicated range of controlled polymerization techniques, **RAFT polymerization** is used in this Thesis because it provides precise control over the molecular weight distribution of the precursor single-chain nanoparticles. Moreover,

RAFT polymerization is unique in that it may be applied to monomers containing a wide variety of functional groups and does so without requiring the use of a metal catalyst.

## **RAFT POLYMERIZATION**

Reversible Addition-Fragmentation Chain Transfer polymerization (RAFT) is a reversible deactivation radical polymerization, defined as having a paradigm that gives the process of radical polymerization living features. The chain transfer agent is principally a thiocarbonylthio compound, *via* which the molecular weights and polydispersity indices are controlled very efficiently throughout the process of free-radical polymerization.<sup>33</sup> RAFT polymerization is an operative mechanism based on six principal phases as illuminated in Figure 4.

In effect, the process begins with the initiation phase wherein the initiator, represented as a split into two reactive fragments (I) inside the figure, reacts with a monomer (M) to give a radical (denoted as P1 to indicate its unit length). This new radical then goes on to react with another monomer unit in a similar fashion, increasing the length of the polymer chain in an additive way (changing from  $P_n$  to  $P_{n+1}$ ) in a process called propagation. The third phase is indicated as the realization of a pre-equilibrium state occasioned when the nascent polymer chain interacts with the CTA (chain transfer agent) leading to the release of the radical (R) which will consequently arrest the chain's elongation. This results in the next stage where the free radical enters a new reaction with other monomer units, hence forming the synthesis of a new polymer chain. The process finally moves ahead to the state of true equilibrium, with the help of the CTA through its mediation, and guarantees the reciprocal exchange of radicals between different chains and providing equal growth opportunities for all the chains.

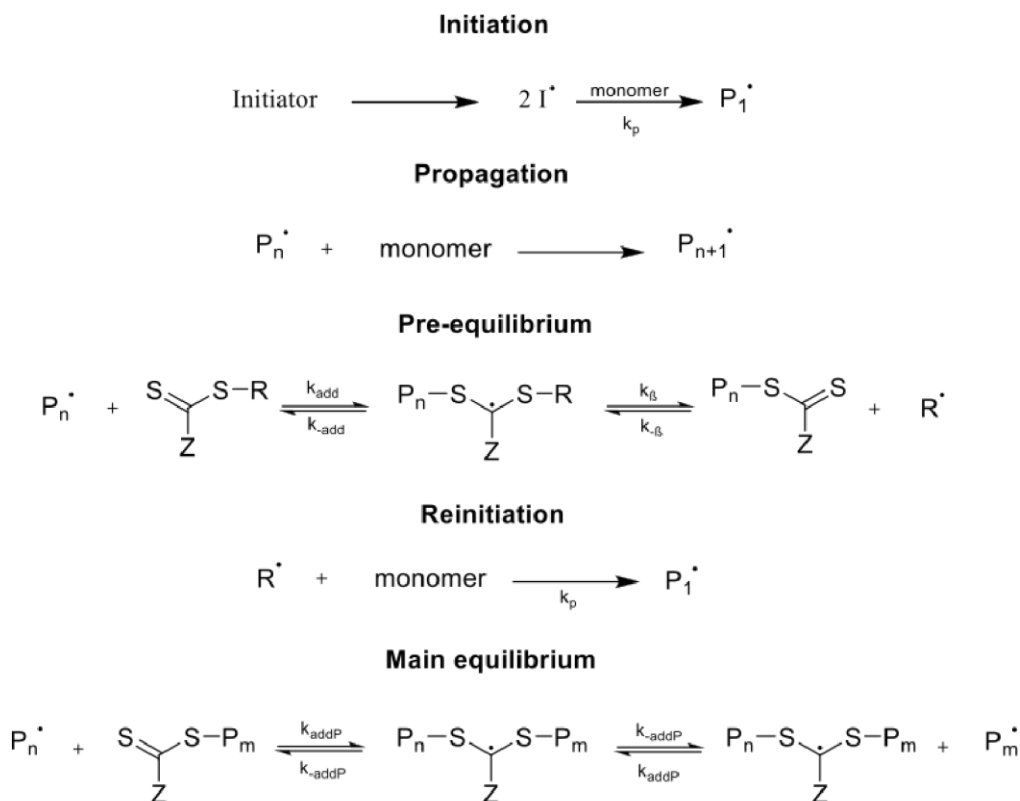


**Figure 4.** Mechanism of RAFT polymerization with a thiocarbonylthio compound as chaintransfer agent.

### 1.2.1.2. Precursor functionalization

Polymer functionalization is concerned with the quantitative and selective alteration of polymers under conditions that are relatively mild and devoid of side reactions. This process, also referred to as post-polymerization modification or polymer analogous modification, occupies a significant niche within the annals of polymer science.<sup>34</sup> The advent of controlled/living radical polymerization techniques such as RAFT (Reversible Addition-Fragmentation Chain Transfer), ATRP (Atom Transfer Radical Polymerization), and NMP (Nitroxide Mediated Polymerization) since the mid-1990s has markedly expanded the repertoire of chemical reactions suitable for post-polymerization modification, demonstrating enhanced functional group tolerance in comparison to traditional living anionic or cationic polymerization methodologies.

Among the most efficacious and prevalently employed reactions for polymer functionalization are: thiol-ene/thiol-yne additions (categorized as click reactions), modification of epoxides, anhydrides, oxazolines, and isocyanates through reactions with amines/alcohols/thiols (also recognized as click reactions), alteration of active esters via amine reactions, thiol-disulfide exchange, Diels-Alder reaction (identified as a click reaction), Michael-type addition, Copper-catalyzed azide-alkyne cycloaddition (CuAAC) (acknowledged as a click reaction), and modification of ketones and aldehydes with amines, alkoxyamines, or hydrazines.

Within the scope of this doctoral thesis, it is noteworthy to emphasize that extensive endeavors pertaining to the functionalization of the precursor materials have not been undertaken, as elucidated in the forthcoming chapters. Nevertheless, it is pivotal to underscore that in **Chapter 4**, a pivotal facet of the research pertained to the diazotransformation of the polymer precursor, which assumed a critical role in the synthesis of Single-Chain Nanoparticles (SCNPs).

### **1.2.1.3. Intrachain Folding/Collapse**

Significantly, three distinct methodologies have been devised for the fabrication of single-chain nanoparticles: 1) intrachain homocoupling, 2) intrachain heterocoupling, and 3) crosslinker-induced compaction.

#### **1) Intrachain Homocoupling**

Through homo-functional chain-collapse, the copolymer strand is endowed with reactive, self-complementary 'R' groups (i.e., vinyl double bonds) which undergo intramolecular reactions under dilute conditions (illustrated in Figure 5).

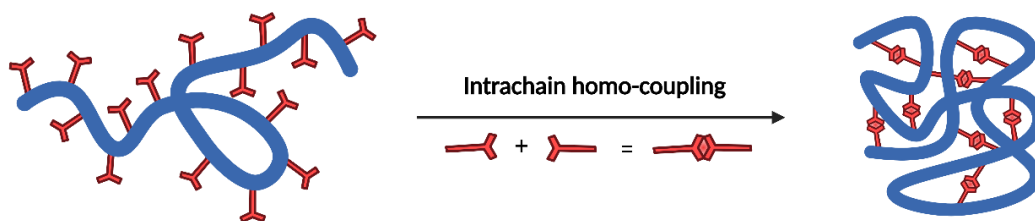


**Figure 5.** Illustration of intra-chain homocoupling technique employed for the construction of SCNPs.

## 2) Intrachain Heterocoupling

This hetero-coupling chain collapse modality is akin to its predecessor, albeit necessitating two complementary functionalities, 'R' and 'X', on the identical polymer strand (Figure 6), also requiring dilute reaction conditions.

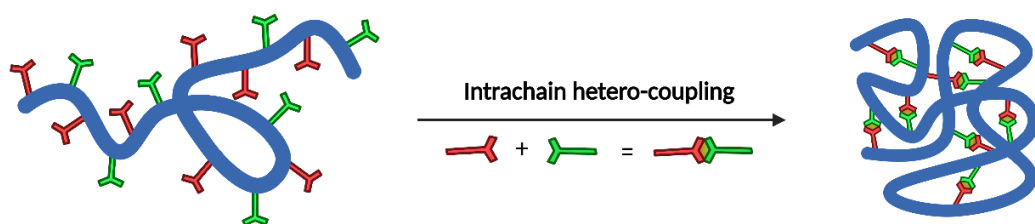


**Figure 6.** Illustration of intra-chain heterocoupling technique employed for the construction of SCNPs.

## 3) Crosslinker-Induced Compaction

Utilizing a crosslinker, this strategy facilitates the synthesis of unimolecular nanoparticles. The polymer strand, functionalized with an appropriate 'R' group, is compacted through reaction with the two 'X' terminal groups of the crosslinker (Figure 7), with intermolecular crosslinking commonly mitigated by gradual addition of one reactant to the other. Principal advantages include simplified precursor polymer synthesis and enhanced functionality *via* the crosslinking agent.

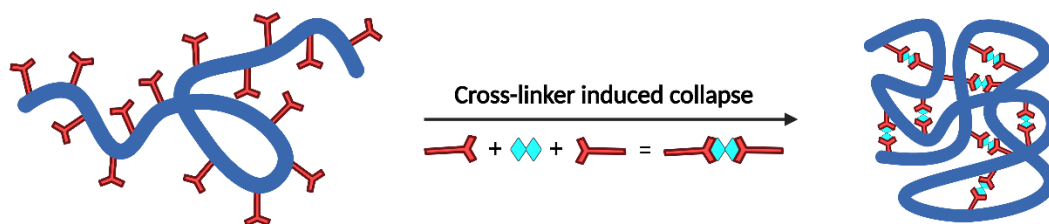


**Figure 7.** Illustration of cross-linker induced collapse technique employed for the construction of SCNPs.

Regarding the bonding interactions utilized, single-chain nanoparticles are synthesized through **intrachain covalent bonds** (yielding irreversible SCNPs) or *via* **intrachain noncovalent** and **dynamic-covalent bonds** (yielding reversible SCNPs).

### A) Irreversible Single-Chain Polymer Nanoparticle Systems

#### Covalent bonding

The synthesis of irreversible single-chain nanoparticles (SCNPs) is facilitated through covalent bonding, utilizing both conventional organic and "click" chemistry reactions for the effective creation of robust unimolecular soft nanoparticles. It's imperative to note that the covalent stabilization of polymer geometry negates the dynamic nature of single-chain entities, thus restricting their application in dynamic biomimetic systems, such as protein folding/unfolding mechanisms.

Initial disclosures of irreversible single-chain nanoparticle synthesis *via* the intrachain homocoupling method under highly diluted conditions by Mecerreyes et al. utilized poly(styrene)-, poly(alkyl methacrylate)-, and poly( $\epsilon$ -caprolactone)-based precursors with vinyl reactive groups.<sup>19</sup> Jiang et al. and Cherian et al. respectively utilized unsaturated groups for poly(4-N-Boc-aminostyrene)- and poly(carbonate)-based single-chain nanoparticles.<sup>35</sup> Subsequently, Harth et al. synthesized benzosulfone-decorated precursors for individual unimolecular nanoparticle creation via quinodimethane

formation under similar conditions.<sup>36</sup> Poly(methyl methacrylate)-based SCNPs were obtained by Zhu et al. through intramolecular Bergman cyclization at lower temperatures (150 °C).<sup>37</sup> The synthesis of poly(styrene) and poly(alkyl methacrylate)based unimolecular nanoparticles via intramolecular cross-linking of sulfonyl azide<sup>38</sup> and benzoxazine<sup>39</sup> functionalized polymers required elevated temperatures (190–200 °C). Additionally, Dirlam et al. recently prepared poly(styrene)-based unimolecular nanoparticles via intrachain crosslinking through oxidative polymerization of 3,4propylenedioxythiophene functional groups at 50 °C.<sup>40</sup>

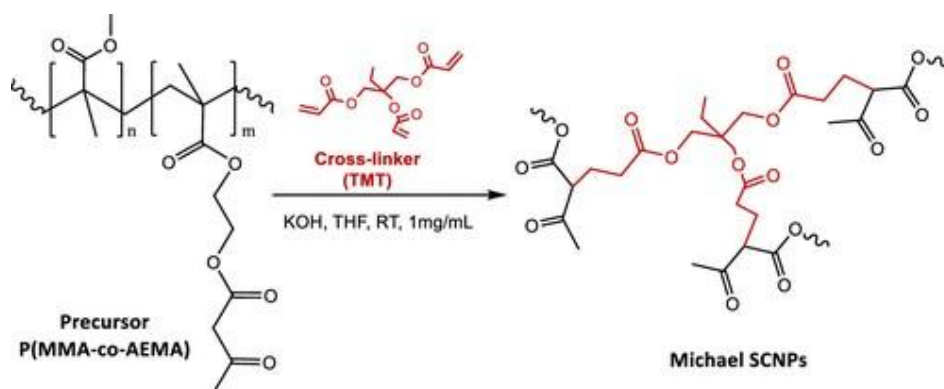


Figure 8. Scheme of the Michael synthesis route followed by Sanchez-Sanchez et al.<sup>41</sup> for the formation of the SCNPs.

Colmenero et al. presented a study using small-angle neutron scattering (SANS) and neutron spin echo (NSE) techniques to explore the structure and dynamics of irreversible single-chain nanoparticles (SCNPs) in a dilute solution. These SCNPs were obtained through Michael addition-mediated multidirectional self-assembly (Figure 8). Trimethylolpropane triacrylate acted as the intrachain cross-linking agent. Precursors were random copolymers of methyl methacrylate (MMA) and (2-acetoacetoxy)ethyl methacrylate (AEMA).<sup>41</sup>

The intrachain heterocoupling technique has been employed for the fabrication of irreversible single-chain nanoparticles using efficient azide-alkyne "click" chemistry (i.e., copper-catalyzed [3+2] cycloaddition of alkynes and azides (CuAAC)).<sup>42</sup> Ruiz de Luzuriaga et al. synthesized biofunctionalized poly(methyl methacrylate) unimolecular

nanoparticles at room temperature and high yield utilizing azide- and protected alkyne-decorated polymer precursors.<sup>43</sup> Pomposo et al. simplified this technique, employing copolymers with protected alkyne and chloromethyl groups, converting them to azidomethyl groups via a straightforward substitution reaction with sodium azide.<sup>44</sup> The intrachain hetero-coupling method has also facilitated the creation of thermoresponsive single-chain nanoparticles.<sup>45</sup> Nitrile imine mediated tetrazole-ene cycloaddition (NITEC) has been applied for the synthesis of well-defined fluorescent single-chain nanoparticles.<sup>18</sup>

The crosslinker-mediated collapse of polymer chains represents another efficient methodology for obtaining SCNPs. Poly( $\gamma$ -glutamic acid)-based single-chain nanoparticles were produced through the crosslinker-induced collapse method using a biosynthetic poly( $\gamma$ -glutamic acid) precursor and 2,2'-(ethylenedioxy)diethylamine as the bifunctional crosslinker in the presence of carbodiimide.<sup>46</sup>

## **B) Reversible Single-Chain Polymer Nanoparticle Systems**

Two principal types of reversible interactions, i.e., non-covalent interactions and dynamic covalent bonds, enable the synthesis of responsive, structurally dynamic single-chain nanoparticles (SCNPs).

### **Non-covalent Interactions**

The concept of non-covalent bonds has captivated researchers across various fields since Linus Pauling's seminal work on hydrogen bonding in the 1930s.<sup>47</sup> Jean Marie Lehn's introduction of "supramolecular chemistry"<sup>48</sup> has facilitated the exploration of non-covalent bonds in constructing advanced artificial architectures, including supramolecular polymers. The susceptibility of main-chain supramolecular polymers to environmental variations, manifesting in solvent polarity and concentration-dependent molecular weights, underscores the influence of factors such as temperature, pressure, and concentration on non-covalent bond strengths and the equilibrium between bonded and unbonded species.

Non-covalent, or supramolecular, interactions are categorized into three classes based on bond strength: i) weak interactions (0-15 kcal/mol), including van der Waals forces, hydrophobic interactions,  $\pi$ - $\pi$  stacking interactions, and hydrogen bonds; ii) medium strength interactions (15-60 kcal/mol), such as multiple hydrogen bonds and weaker metal coordination complexes; and iii) strong interactions (>60 kcal/mol), encompassing ionic interactions, host-guest interactions, and robust metal coordination or chelate complexation (Figure 9).

The strength of non-covalent bonds is contingent on external factors like solvent type, temperature, and concentration, precluding a strict categorization.<sup>49</sup> Non-covalent or supramolecular interactions have facilitated the creation of complex architectures involving side-chain supramolecular polymers,<sup>50</sup> multi-block supramolecular polymers,<sup>51</sup> and multi-arm self-assembled stars.<sup>52</sup>

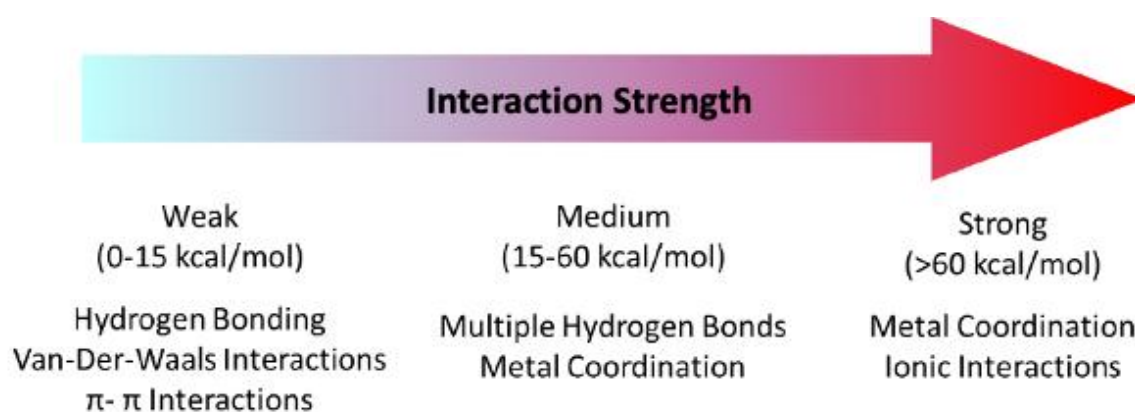


Figure 9. Organization of non-covalent interactions by bond strength.<sup>49</sup>

### Dynamic Covalent Bonds

Dynamic covalent chemistry encompasses reversible covalent reactions that enable the exchange of molecular components to reach the system's thermodynamic equilibrium.<sup>53</sup> Dynamic covalent bonds, exhibiting the robustness of covalent bonds, are only disruptable and reformable under specific external conditions (e.g., catalyst presence). Furthermore, dynamic covalent chemistry has successfully contributed to dynamic combinatorial libraries,<sup>54</sup> drug discovery,<sup>55</sup> and controlled fragrance delivery.<sup>56</sup>

Hawker, Kim, and their colleagues' pioneering efforts in 2008 demonstrated an efficient approach to supramolecular single-chain nanoparticles via benzamide dimerization, forming quadruple hydrogen bonds between benzamide motifs.<sup>57</sup> Subsequent extensive research by Meijer, Palmans, and their teams advanced the field of metastable noncovalent bonded single-chain nanoparticles through the introduction of orthogonal techniques based on ureidopyrimidinone (UPy)<sup>58</sup> and benzene-1,3,5-tricarboxamide (BTA)<sup>59</sup> hydrogen bonding motifs. Meijer's group recently showcased sequential supramolecular nanoparticle synthesis through complementary self-assembly of UPy and BTA units.<sup>60</sup> Host-guest interactions involving cucurbit[n]uril complexation<sup>61</sup> and hydrophobic L-phenylalanine Phe-Phe interactions<sup>62</sup> have been leveraged to fabricate water-borne supramolecular single-chain nanoparticles.

#### **1.2.1.4. Morphology of Single-Chain Nanoparticles (SCNPs) in Solution**

Understanding and controlling the morphology of SCNPs overall is a necessity to properly utilize their properties in a wide variety of applications including drug delivery, sensing, and the development of new nanomaterials. Being able to extract the precise SCNPs out of precursor polymer synthesis will be critical in the future of how we can effectively predict the final morphology type for a well-designed SCNPs for a desired application.

As illustrated in Figure 10, it all begins in the synthetic selection of the precursor: choosing block copolymers and enabling mostly Janus SCNPs with generally self-assembly behaviors enabling complex multi-molecular structures such as micelles and lamellae, or random copolymers with mostly isolated/sparse or globular morphologies without self-assembly behaviors in general.

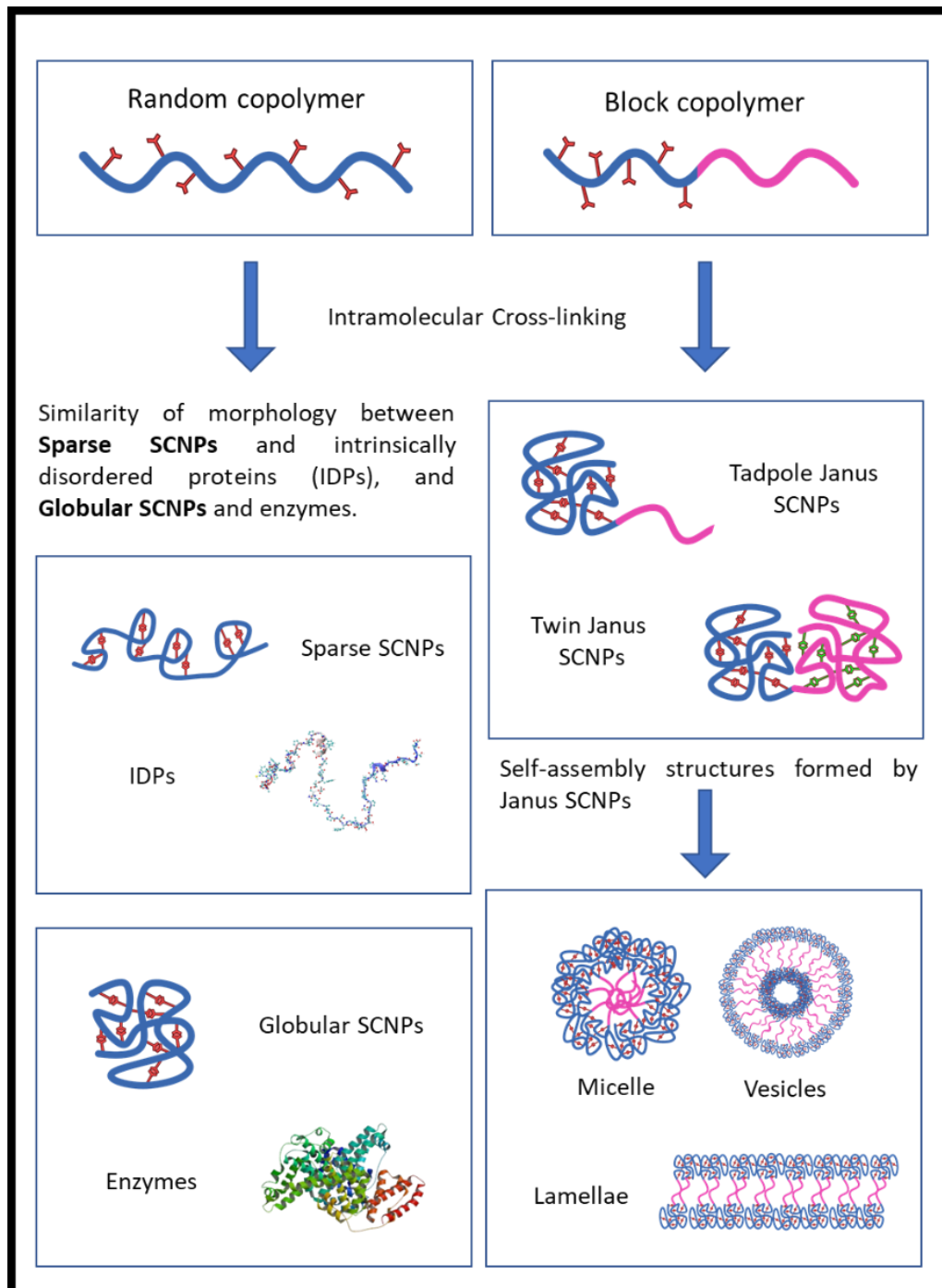


**Figure 10.** Scheme of the different morphologies of SCNPs from block copolymer precursor and from random copolymer precursor. It showed some self-assembly structures formed by Janus SCNPs and the similarity of morphology between sparse SCNPs and intrinsically disordered proteins (IDPs), and globular SCNPs and enzymes.

Amphiphilic block copolymers self-assemble into nanostructures due to block incompatibility. Janus Single-Chain Nanoparticles (SCNPs)<sup>63</sup> have bifacial properties, leading to twin or tadpole morphologies, and can form micelles, lamellae, or vesicles.<sup>64</sup>

Random copolymers, in contrast, are formed from two or more monomers polymerized in a random sequence, resulting in a statistical distribution of monomers along the polymer chain. These random copolymers can give rise to either sparse or globular SCNPs. Sparse SCNPs are morphologically analogous to Intrinsically Disordered Proteins (IDPs), while globular SCNPs resemble enzymes.

In good solvents, sparse SCNPs exhibit a morphology with extended linear sections and compact regions, driven by the interplay between intra-chain cross-linking and a preference for short-range loop formation, as demonstrated by Molecular Dynamics (MD) simulations.<sup>65,66</sup> Globular SCNPs, on the other hand, possess a homogeneous core-shell structure akin to that of native proteins, such as enzymes. The synthesis of globular SCNPs often involves complex synthetic routes. Techniques such as the utilization of long cross-linkers and bifunctional groups have been employed to enhance loop formation and compaction within these structures.<sup>67,68</sup>

### **1.3. Applications of SCNPs**

The versatility of single-chain nanoparticles (SCNPs) encompasses a broad spectrum of applications, including catalysis, sensing, and nanomedicine, as depicted in Figure 11. The efficacy of SCNP technology across these domains stems primarily from the nanoparticles' minute dimensions and their adaptability tailored to specific functionalities. Although research endeavors pertaining to SCNPs have predominantly delved into fundamental investigations, these materials have manifested practical utility in various contexts. Intrinsically, the interior composition of the nanoparticle furnishes a conducive chemical milieu, characterized by tunable hydrophobic or hydrophilic properties, alongside controlled size modulation achievable through manipulation of intra-chain cross-linking densities and the molecular weight of the precursor polymer. Moreover, the integration of selective functional sites within the nanoparticle structure is facilitated by controlled polymerization methodologies and post-polymerization modification techniques. Subsequent sections encapsulate recent applied research endeavors elucidating the diverse applications of SCNPs.

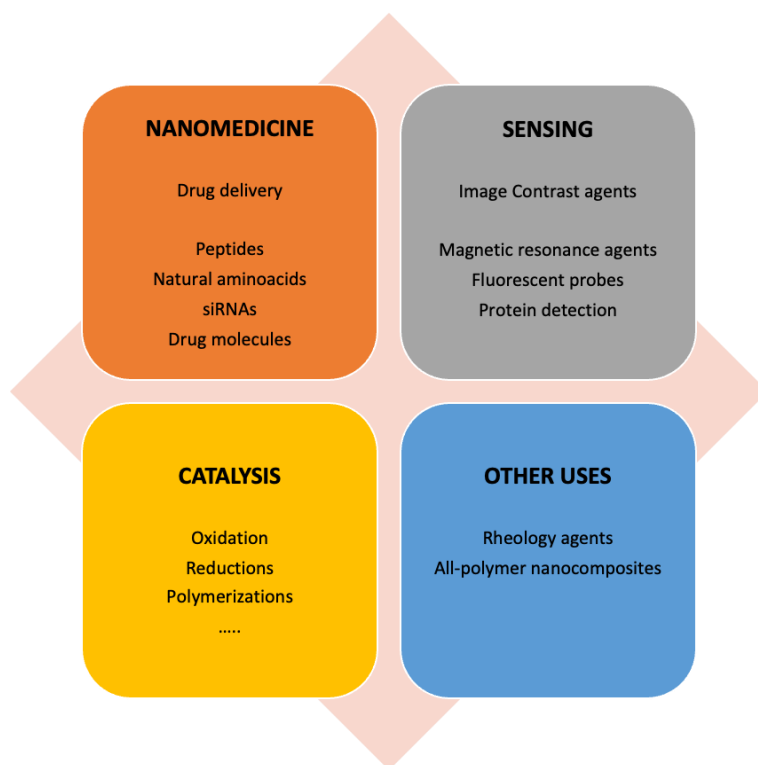


Figure 11. Illustration of some examples of potential applications of SCNPs.

### 1.3.1. Catalysis

The development of catalytically active single-chain nanoparticles is considered an essential approach in polymer chemistry, creating new ways for the design of catalysts seamlessly integrating the advantages of both homogeneous and heterogeneous catalysis systems. The PhD thesis regards the concept of polymer chains serving as spatially demanding supports for metal-ions in catalytic systems and the effects of such configurations on the catalytic efficiency. Substitution of molecular ligands by polymer chains in organometallic catalysts is an event that inflicts large changes which may influence catalytic activity either by diffusional limitations or because of dense catalytic pockets, which hinder substrate access. This phenomenon noted by the group led by Pomposo underscores the challenge for ensuring the free diffusion within the SCNP nanoreactors in order to maintain activity but, at the same time, recognizing that selective substrate access should sharpen reaction specificity.

The initial development of SCNPs focused on structural models, using intramolecular crosslinking to induce chain collapse into nanoparticle form. Earlier studies on such systems were aimed at understanding changes in intrinsic viscosity and the radius of gyration upon chain collapse.<sup>69</sup> This era of discovery offered us critical knowledge of the physical behaviour of SCNPs, but at that time, did not yet leverage their catalytic potential. Significant advancements came in the early 2010s with new polymer synthesis and crosslinking methodologies, reviving interest in SCNPs and paving the way for their application in catalysis.<sup>70</sup>

The concept of SCNPs as functional nanoreactors began to take shape, leveraging the idea of intramolecular crosslinking to fold polymer chains into discrete, stable nanostructures. These nanostructures could be tailored to incorporate catalytic sites, mimicking the active sites found in natural enzymes. This approach allowed for the development of SCNPs with highly specific substrate binding and catalytic efficiency, similar to that of enzymes.

One pioneering study in this area was conducted by Pomposo et al., who explored the catalytic site distribution within 'clickase' SCNPs. They show that SCNPs with clustered catalytic sites had significantly higher activity than those with homogeneous catalytic site distribution, which suggested that precise internal morphology control can give rise to enhancements in catalytic performance to a much greater extent than was realized at the beginning of the discoveries about SCNPs.<sup>71</sup> This discovery underscored the potential of SCNPs to achieve enzyme-like efficiency through synthetic means.

The incorporation of metal ions into SCNPs was particularly fruitful. Barner-Kowollik and Roesky teams reported bimetallic configurations in SCNPs. Platinum and europium metals were combined, leading to the development of multifunctional nanoreactors. Such SCNPs offered high catalytic activity, ease of recoverability, and reusability—the two limitations highly relevant for conventional homogeneous catalysts.<sup>72</sup> In an illustrative example, Knöfel et al. reported the synthesis of phosphine-functionalized polymer chain-bearing SCNPs and their use as homogeneous catalysts in the amination

of allyl alcohol. Pt(II)-SCNPs, depending on the polarity of the solvent, could be separated from the reaction mixture and recycled in additional cycles with good potential in terms of high catalytic efficiency and ease of recoverability. They also worked on the synthesis and the catalytic applications of SCNPs that contain both Au and Y. The researchers synthesized SCNPs chemically by trapping Au(I) and Y(III) ions into the polymer matrix. Such NPs were observed to exhibit recyclable and very high catalytic behavior. Research gave much attention to the recovery and reusing of SCNPs over several catalytic cycles by keeping the efficiency and stability of the same. This alluded to the possible uses of the new heterobimetallic SCNPs in sustainable catalysis, toughness, and application to chemical reactions.<sup>73</sup>

Further advancements were made adding additional functionalities into SCNPs. Maag et al. developed SCNPs that exhibit fluorescence, facilitating easy tracking and recycling of the catalysts. This novelty highlighted the possibility to combine catalytic function with optical properties in SCNPs, meaning a broader potential application field.<sup>74</sup> A library of zinc porphyrin cores was prepared based on poly (methyl methacrylate-co-anthracene methacrylate) polymers by Patenaude, Berda, and Pazicni. These SCNPs were equipped with different functional groups, and showed enhanced reactivity and substrate specificity, emphasizing the importance of secondary coordination spheres in SCNP catalysis.<sup>75</sup>

The structural design of SCNPs was inspired by natural enzymes, particularly their ability to create a specified microenvironment for the catalytic reaction. Researchers have imitated those structural attributes of natural enzymes during the design of SCNPs to attain high catalytic efficiency and substrate specificity. For example, Palmans and Meijer developed a concept of ruthenium-based catalysts, dispersed in amphiphilic block copolymers, to synthesize SCNPs with central hydrophobic cores similar to enzyme active sites. Such strategy provided an improvement not only in terms of substrate binding but also in the protection of the catalytic sites from deactivation. As a result, operational life of the catalyst was extended in this design.<sup>76</sup>

Current studies have focused on creating dynamic SCNP systems that can respond to external stimuli, such as light, temperature or pH, to control catalytic activity. Frisch et al. synthesized SCNPs with photo-switchable groups for on-demand catalytic activity control, which opened a new direction for the development of "smart" catalysts that can tune their functionality depending on the environmental conditions.<sup>77</sup>

Recent advance in catalytic nanotechnology was brought forward by a contribution from Daniel Taton's group, reporting on an original study on the thermolysis-driven release of catalytically active N-heterocyclic carbenes (NHC) from SCNPs. Accordingly, Arno, O'Reilly, and Taton developed a processing protocol where controlled thermal unfolding is used for silver ion crosslinked SCNPs, creating a method for stepwise, targeted release of NHCs. All these nanoparticles open the pore-opening mechanism and exhibit activity on catalytic sites. This, therefore, describes the application of SCNPs in temperature-impacted catalytic reactions, which bounds to have a promising future with a new dimension with respect to control and efficiency of the catalysis process, as described in case studies.<sup>78</sup> This new approach indeed opened the functional scopes of SCNPs and paves the way for designing new applications of advanced catalytic systems for targeted reactions, with numerous contributions accruing in the fields of sustainable and efficient catalysis.

In another recent work, the group of researchers working under the supervision of Daniel Taton also managed to move the development of metal-conjugated single-chain nanoparticles toward the advanced level and a step higher. An illustrative study in terms of the synthesis of SCNPs is by Taton et al. This new methodology used the unique properties of SCNPs to design highly effective catalytic systems in aqueous environments. The robust characteristics of SCNPs in different catalytic reactions, for the first time, are demonstrated in this application in green and sustainable processes. They doped the polymer backbone with palladium (II) to make the catalytic activity and the nanoparticles' stability generalizable for most future studies in the field of optimization in catalytic nanotechnology.<sup>79</sup>

Revolutionary changes have been noticed in SCNP catalysis from 2020 to the present as a more significant understanding of polymer chemistry and the development of advanced characterization techniques. More effort is directed towards practical applications of SCNPs in industrial catalysis, environmental clean-up, and biomedical applications. Advanced characterization techniques, such as SANS, XPS, and molecular dynamics simulation, have given detailed insight into the internal morphology and catalytic mechanisms of SCNPs. This has made it possible to tailor the structure and function of SCNPs, leading to optimized catalytic performance. Patel et al. employed molecular dynamics simulations in combination with machine learning, leading to the generation of a diverse library of SCNPs, with which they gained insights into how structural parameters affect the morphology and catalytic performances.<sup>80</sup>

In addition to enhancing catalytic efficiency and substrate specificity, researchers have been working on fine-tuning the internal structures and incorporating multifunctional catalytic sites into SCNPs. Pomposo's group investigated the impact of the intra-chain distribution of catalytic sites on the catalytic performance of metallo-folded single-chain nanoparticles (SCNPs). The findings demonstrate that optimizing the spatial arrangement of catalytic sites within SCNPs significantly enhances their catalytic efficiency and specificity, paving the way for the development of more effective catalytic systems.<sup>81</sup> Other study made by Zimmerman et al. Demonstrated the catalytic activity of copper-containing single-chain nanoparticles, with further emphasis on their enzyme-like activity. It experimentally proved that these SCNPs would increase catalytic efficiency and selectivity through effective coordination of substrates, as in the case of natural enzymes. The internal structure and the layout of copper ions within the SCNPs were fine-tuned for catalytic performances. SCNPs were able to catalyze a broad range of reactions and, hence, be useful for complicated biological systems. These results showed the potential of SCNPs as advanced catalytic materials, which have the unyielding platform for developing next-generation catalysts with enhanced performance toward industrial and biomedical applications.<sup>82</sup>

Nevertheless, there are still some challenges in the development and application of SCNPs despite the significant progress. Achieving enzyme-like catalytic activity and

specificity remains a formidable task. While SCNPs offer greater flexibility in terms of different metal incorporation and functionalization, replicating the complex interactions within natural enzyme active sites requires further complex innovation. The use of sequence-defined polymers could have the potential to offer enzymatic-like precision for SCNPs, in a way that, it would allow the copolymer chain to bear a sequence of polar and nonpolar monomers in a site-specific manner along that copolymer chain.<sup>83</sup>

Additionally, future efforts of the research work will focus on improving the understanding of the morphology of the interior of the SCNPs and its effect on the catalytic performance. In this regard, the above-advanced characterization techniques, i.e., SANS and simulations, come into the forefront of this score. The techniques will give further insight into the nature of the 3-D structures of the SCNPs and internal configurations regarding catalysis activity.<sup>84</sup>

Recent efforts have also explored the potential applications of SCNPs in energy applications. They have been examined concerning their possible use in fuel cells and batteries because of their unique catalytic properties for effective energy conversion and storage. The new course of investigation, in this respect, can offer an opening toward developing sustainable energy technology. Comanescu explored the nanoconfinement of hydrides and SCNPs in relation to advanced energy storage solutions. With this potential being said, the paper focused on improving the efficiency of hydrogen storage and energy conversion processes, such as hydrogen fuel cells. Because of such unique properties of SCNPs, more significantly, their catalytic activities and precision in structure, the study showed improvements at a very significant level in fuel cell technology and energy storage systems. The current work thus zeroes in on the relevance of SCNPs in coming up with newer, more effective, and sustainable energy solutions.<sup>85</sup>

In terms of novel works and innovation, scalability and multifunctionality of SCNPs synthesis is another critical issue. It is an important brainteaser in this Thesis because today's approaches are so complex and time-consuming that it makes them not very attractive for industry. The development of a much more effective scalable synthesis and

multifunctional applications could play a vital role in the future of SCNPs. Tao Chen explored polymer-based nanoreactors capable of facily performing efficient acid/base cascade catalysis using SCNPs. Generally, this study demonstrated the successful implementation of tandem catalysis and showed several strategies for site isolation that enhance reaction efficiency and result in better scalability. These advancements have been crucial to large-scale application of SCNP catalytic reactions, which stand a good chance before the eventual overall catalytic processes.<sup>86</sup>

The total synthesis of some value-added fine chemicals was reported by K. Ghosh et al. using continuous flow cascade catalysis. He developed similar concepts for generating an organic porous solid, which has both acid and base catalytic sites simultaneously. The authors performed consecutive catalytic reactions without isolating the intermediates to raise the efficiency of the process in a completely single reactor. The process was carried out continuously in a flow reactor using a continuously feeding reactant and continuously discharging product. They optimized the conditions of temperature, pressure, and flow rate to get the maximum yield and selectivity of the reaction. The continuous flow system allowed a scale-up of the process, showing significant improvements in SCNP catalytic reactions.<sup>87</sup>

In conclusion, single-chain nanoparticles represent a groundbreaking approach in catalysis, combining the precision and efficiency of natural enzymes with the versatility and tunability of synthetic polymers. The advancements reviewed by all these different researchers underscore the transformative potential of SCNPs in both academic and industrial contexts. Continued research and innovation promise even greater breakthroughs, paving the way for more efficient, sustainable, and versatile catalytic systems.

### 1.3.2. Sensing

Single-chain polymer nanoparticles (SCNPs) present promising opportunities for the advancement of sensors and biosensors. This potential has been demonstrated through proof-of-concept experiments, specifically in the areas of: i) metal ion sensing, and ii) protein sensing.

The first study by Gillissen et al. explored SCNPs developed for metal ion sensing. The researchers made 3,30-bis(acylamino)-2,20-bipyridine substituted benzene-1,3,5-tricarboxamide (BiPy-BTA) grafted polynorbornene polymers using a ring-opening metathesis polymerization of norbornene monomers. The compact conformation adopted by the SCNPs changed with functionalization degree of BiPy-BTA and with solvent polarity, directly influencing its fluorescence intensity. Such property was exploited for metal ion's detection, especially copper, since the metal ions were reported to have a powerful interaction with the bipyridine units. Compartmentalization inherently enhances the efficiency of SCNPs as sensors and controlled microenvironments also improved their sensitivity and selectivity (Figure 12).<sup>88</sup>

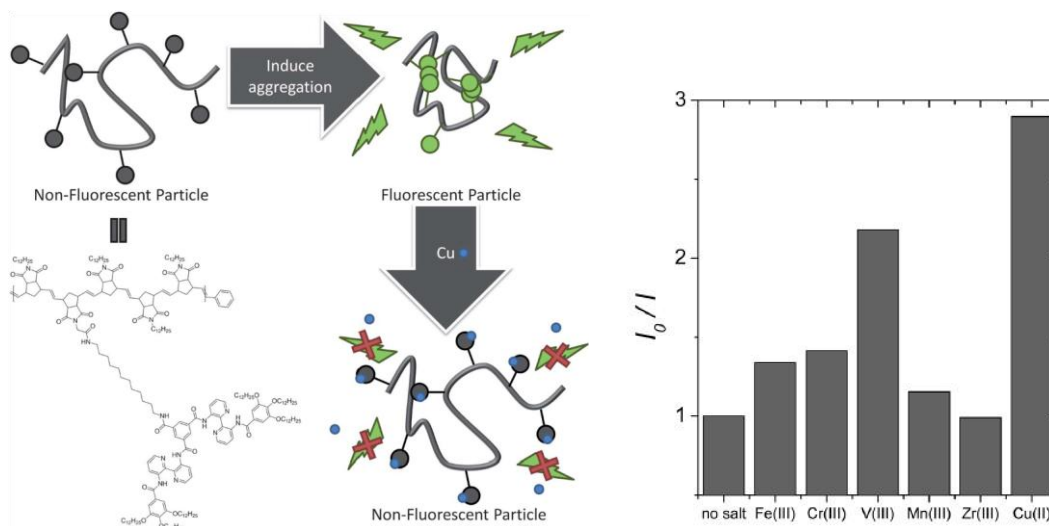


Figure 12. Schematic representation of the sensing function of the BiPy-BTA functional polymers and illustration of the response of fluorescent bipyridine-containing single-chain nanoparticles towards different metal ions.<sup>88</sup>

The group of Pomposo described a straightforward, fast, susceptible, and robust colorimetric method for detecting zein protein in aqueous ethanol. Detection was based on the formation of gold nanoparticles in the presence of pyridine-functionalized single-chain nanoparticles (SCNPs). In the absence of zein, the reduction of  $\text{NaAuCl}_4$  by hydrazine in the presence of pyridine-functionalized SCNPs leads to steric-stabilizing-induced gold nanoparticles of about 8 nm in size, manifested by a red-colored solution. Though, in the presence of zein, the abundant affinity of the zein residues towards the pyridine moieties hinders steric stabilization of the growing gold nanoparticles. This leads to larger nanoparticles ( $\sim 100$  nm) and a blue solution. This way, the operating principle behind this colorimetric sensor originated from the delicate balance of zein-pyridine-gold interaction, which could be utilized for the detection of zein up to a concentration range of 12 to 3000  $\mu\text{g}/\text{mL}^{-1}$  by the naked eye, as shown in Figure 13.<sup>89</sup>



Figure 13. Photographs of the sensing system in the presence of decreasing concentrations of zein.<sup>89</sup>

Recently, Lu et al. demonstrated an effective way to design aggregation-induced emission (AIE)-functionalized SCNPs suitable for detecting  $\text{H}_2\text{O}_2$ . Herein, the SCNPs were prepared by ring-opening copolymerization and, subsequently, by intramolecular cross-linking through olefin metathesis. The above two kinds of SCNPs were encapsulated with an  $\text{H}_2\text{O}_2$ -responsive polymer as a carrier and fluorescent switch. In the presence of  $\text{H}_2\text{O}_2$ , the hydrophobic segment of the responsive polymer chain became hydrophilic, which made the distance from the SCNPs larger and the fluorescence intensity lower. The

changes in fluorescence changed SCNPs potential activity, making them applicable to high-sensitivity and stable fluorescent detection of trace levels of  $\text{H}_2\text{O}_2$ .<sup>90</sup>

SCNPs have been developed with outstanding sensitivity, selectivity, and versatility as sensing systems. The development of SCNPs for metal ion detection, protein sensing, and hydrogen peroxide detection symbolizes the broad applicability and innovative potential of these nanostructures. With inevitable progress in research, SCNPs will likely find their applications broadened even further and firmly claim their place in advanced sensing technologies.

### **1.3.3. Nanomedicine**

Nanomedicine is a discipline leveraging the particular characteristics of nanoparticles for purposes of diagnosis, monitoring, therapy, and control of biological systems. The use of SCNPs in conveying all such purposes outplays those played by traditional small molecules and other nanoparticle systems due to more prolonged circulation times, lower degradation, and facility of targeting of specific tissues or cellular markers to enhance delivery and therapeutic agent efficacy.<sup>91</sup>

#### **Cytotoxicity Studies**

Biocompatibility is one of the most critical aspects a nanomaterial should possess when it has been designed for biomedical applications SCNPs. Biocompatible SCNPs were synthesized using the strategy of organo-catalyzed ring-opening polymerization by Qiao et al.<sup>92</sup> The synthesized SCNPs showed low toxicity to human embryonic kidney cells (HEK293T). Their study revealed that these SCNPs, covalently cross-linked by biodegradable polyester linkages, were nontoxic at concentrations up to 100  $\mu\text{g}/\text{mL}$ , showing promise for safe biomedical applications.

Further investigations by Lemcoff and Zimmerman explored the influence of molecular weight on cell viability using fluorescein-containing SCNPs. They found that SCNPs with molecular weights ranging from 50 to 100 kDa exhibited high HeLa cell viability ( $\geq 80\%$ ) at a concentration of 10  $\mu\text{M}$ . This study highlighted the potential of SCNPs to serve as

non-toxic carriers for imaging agents or therapeutic drugs.<sup>93</sup> Additional research by Loinaz et al. (2016), combined in vitro and in vivo toxicity research toward SCNPs from poly(methacrylic acid) and they observed minimal toxicity in pancreatic adenocarcinoma cell lines at concentrations up to 50 µg/mL and no acute toxicity in mice at a dose of 100 mg/kg, underscoring the safety of SCNPs for potential clinical use.<sup>94</sup>

### **Controlled Drug Delivery Systems**

SCNPs have been extensively studied as nanocarriers for the controlled delivery of therapeutic agents, including chiral amino acid derivatives, peptides, vitamins, and small molecule drugs. The precise control over SCNPs morphology and functionality enables tailored drug release profiles, enhancing therapeutic efficacy while minimizing side effects.

For instance, Hamilton and Hard developed SCNPs-based nanocarriers for the intracellular delivery of peptide therapeutics. These SCNPs were decorated with dendritic molecular transporters and fluorescent probes, facilitating efficient cellular uptake and controlled peptide release while preserving the biological activity of the peptides.<sup>95</sup> This approach has significant potential for delivering therapeutic peptides to intracellular targets, which are often challenging to reach with conventional delivery systems.

Pomposo et al. synthesized SCNPs designed for the dermal delivery of vitamin B9. These SCNPs showed a progressive and controlled release of the vitamin following a Fickian diffusion mechanism, with complete release observed within six hours.<sup>96</sup> In a subsequent study, they explored the simultaneous delivery of hinokitiol and vitamin B9, achieving efficient release profiles at different pH levels. This dual-delivery system demonstrated the versatility of SCNPs in administering multiple therapeutic agents with distinct release kinetics.

Cheng and Zimmerman developed stimuli-responsive SCNPs capable of encapsulating the anticancer drug 5-fluorouracil (5-FU). These SCNPs exhibited excellent thermo/pH-

responsive behavior, with the highest drug release observed under conditions mimicking the tumor microenvironment (lower pH and higher temperature). This specificity reduces the risk of premature drug release and enhances the therapeutic targeting of cancer cells.<sup>97</sup>

### **Image Contrast Agents**

SCNPs have also been evaluated as potential agents for various imaging techniques, including magnetic resonance imaging (MRI), single photon emission computerized tomography (SPECT), and fluorescence imaging. These applications leverage the unique optical and magnetic properties of SCNPs, enhancing the sensitivity and specificity of imaging modalities.

For example, Loinaz and Odriozola synthesized gadolinium ( $Gd^{3+}$ )-decorated SCNPs that demonstrated enhanced relaxivity compared to traditional gadolinium chelates. These SCNPs, with an average relaxivity value of  $6.8 \text{ mM}^{-1}\text{s}^{-1}$ , offered improved contrast in MRI scans, making them promising candidates for advanced diagnostic imaging.<sup>98</sup> Similarly, Harth et al. developed water-soluble SCNPs with dual MRI and fluorescence imaging capabilities, enhancing their multifunctionality for diagnostic applications.<sup>99</sup> Fluorescent SCNPs have also been developed with reduced photobleaching and enhanced emission properties. Zimmerman et al. demonstrated the use of fluorescein-loaded SCNPs for long-term bioimaging, showing strong fluorescence signals inside HeLa cells.<sup>100</sup>

As a conclusion, The potential of SCNPs in nanomedicine is vast, with promising applications in drug delivery, imaging, and sensing. Their unique properties, such as controlled morphology, biocompatibility, and the ability to functionalize with various therapeutic and diagnostic agents, position SCNPs as versatile tools in the advancement of nanomedicine. Future research is expected to further explore and optimize these applications, paving the way for innovative therapeutic and diagnostic solutions. The development of SCNPs offers a glimpse into the future of personalized medicine, where treatments are tailored to individual patients' needs, enhancing efficacy and reducing side effects.

### 1.3.4. Other applications

Beyond the primary applications previously delineated, Single-Chain Nanoparticles (SCNPs) are poised to revolutionize the creation of new materials endowed with tailored properties. By strategically engineering polymer chain architectures, it is now possible to synthesize materials demonstrating customized mechanical, thermal, or electrical characteristics. These materials are destined to find application in everything from standard coatings to advanced composite materials. While these represent more specialized applications currently under investigation, SCNPs have been used to engineer nanostructures,<sup>101</sup> enhance oil recovery processes,<sup>102</sup> and synthesize plasmonic nanoparticles.<sup>103</sup> The use of these materials has also been expanded to design hydrophobic coatings<sup>104</sup> and realize hydrophobic cotton with greatly improved resistance,<sup>105, 106</sup> underscoring the pervasive utility of SCNPs in the field of material science and engineering.

## 1.5. References

1. Feynman, R. P. *Plenty of Room at the Bottom*.
2. *THE NATIONAL NANOTECHNOLOGY INITIATIVE Strategic Plan*. www.nano.gov. (2007).
3. Whitesides, G. M. Nanoscience, Nanotechnology, and Chemistry. *Small* **1**, 172–179 (2005).
4. Mishra, A. K. *Nanomedicine for Drug Delivery and Therapeutics*. (John Wiley & Sons, 2013).
5. Front Matter. in *Nanoelectronics* i–xlviii (2017).  
doi:<https://doi.org/10.1002/9783527800728.fmatter>.
6. Singh, S. & Tandon, P. Catalysis: A brief review on Nano-Catalyst. *Journal of Energy and Chemical Engineering(JECE)* **2**, 106–115 (2014).
7. Velmurugan, C. & Radhakrishnan, N. *Visualizing Global Nanotechnology Research on Publication Deeds, 1989-2014*.  
<http://digitalcommons.unl.edu/libphilprac><http://digitalcommons.unl.edu/libphilprac/1372> (1989).
8. Drexler, E., Peterson, C. & Pergamit, G. *Unbounding the Future: The Nanotechnology Revolution*. (1991).
9. Gonzalez-Burgos, M., Latorre-Sanchez, A. & Pomposo, J. A. Advances in single chain technology. *Chem Soc Rev* **44**, 6122–6142 (2015).
10. Contents. in *Soft Nanoparticles for Biomedical Applications* (eds. Chemistry, R. S. of, Callejas-Fernández, J., Estelrich, J., Quesada-Pérez, M. & Forcada, J.) 0 (The Royal Society of Chemistry, 2014). doi:10.1039/9781782625216-FP011.
11. Taton, D. *et al.* Controlled polymerizations as tools for the design of star-like and dendrimer-like polymers. *Polym Int* **55**, 1138–1145 (2006).
12. Gregory, A. M. & Stenzel, M. H. Complex polymer architectures via RAFT polymerization: From fundamental process to extending the scope using click chemistry and nature’s building blocks. *Prog Polym Sci* **37**, 38–105 (2012).
13. Sanchez-Sanchez, A. *et al.* “Michael” Nanocarriers Mimicking Transient-Binding Disordered Proteins. *ACS Macro Lett* **2**, 491–495 (2013).

14. Garmendia, S., Dove, A. P., Taton, D. & O'Reilly, R. K. Reversible ionically-crosslinked single chain nanoparticles as bioinspired and recyclable nanoreactors for N-heterocyclic carbene organocatalysis. *Polym Chem* **9**, 5286–5294 (2018).
15. Yang, S. *et al.* Molecular Templating of Nanoporous Ultralow Dielectric Constant ( $\approx 1.5$ ) Organosilicates by Tailoring the Microphase Separation of Triblock Copolymers. *Chemistry of Materials* **13**, 2762–2764 (2001).
16. Hamilton, S. K. & Harth, E. Molecular Dendritic Transporter Nanoparticle Vectors Provide Efficient Intracellular Delivery of Peptides. *ACS Nano* **3**, 402–410 (2009).
17. Niemeyer, C. M. Nanoparticles, Proteins, and Nucleic Acids: Biotechnology Meets Materials Science. *Angewandte Chemie International Edition* **40**, 4128–4158 (2001).
18. Willenbacher, J. *et al.* Photochemical Design of Functional Fluorescent Single-Chain Nanoparticles. *ACS Macro Lett* **3**, 574–579 (2014).
19. Mecerreyes, D. *et al.* A Novel Approach to Functionalized Nanoparticles: Self-Crosslinking of Macromolecules in Ultradilute Solution. *Advanced Materials* **13**, 204–208 (2001).
20. Latorre-Sánchez, A. & Pomposo, J. A. Recent bioinspired applications of single-chain nanoparticles. *Polym Int* **65**, 855–860 (2016).
21. Liu, C., Hong, C.-Y. & Pan, C.-Y. Polymerization techniques in polymerization-induced self-assembly (PISA). *Polym Chem* **11**, 3673–3689 (2020).
22. Scott, K. W., Lorenz, O. & Parks, C. R. Network degradation accompanying the vulcanization of natural rubber with a sulfur–diphenylguanidine system. *J Appl Polym Sci* **8**, 2909–2922 (1964).
23. Harth, E. *et al.* A Facile Approach to Architecturally Defined Nanoparticles via Intramolecular Chain Collapse. *J Am Chem Soc* **124**, 8653–8660 (2002).
24. Hamelmann, N. M. & Paulusse, J. M. J. Single-chain polymer nanoparticles in biomedical applications. *Journal of Controlled Release* **356**, 26–42 (2023).
25. De-La-Cuesta, J. *et al.* Size of Elastic Single-Chain Nanoparticles in Solution and on Surfaces. *Macromolecules* **50**, 6323–6331 (2017).
26. Pomposo, J. A. *et al.* Folding Single Chains to Single-Chain Nanoparticles via Reversible Interactions: What Size Reduction Can One Expect? *Macromolecules* **50**, 1732–1739 (2017).

27. Sanchez-Sanchez, A., Pérez-Baena, I. & Pomposo, J. A. Advances in Click Chemistry for Single-Chain Nanoparticle Construction. *Molecules* **18**, 3339–3355 (2013).
28. Destarac, M. Controlled Radical Polymerization: Industrial Stakes, Obstacles and Achievements. *Macromol React Eng* **4**, 165–179 (2010).
29. Chiefari, J. *et al.* Living Free-Radical Polymerization by Reversible Addition–Fragmentation Chain Transfer: The RAFT Process. *Macromolecules* **31**, 5559–5562 (1998).
30. Wang, J.-S. & Matyjaszewski, K. Controlled/"living" radical polymerization. atom transfer radical polymerization in the presence of transition-metal complexes. *J Am Chem Soc* **117**, 5614–5615 (1995).
31. Hawker, C. J., Bosman, A. W. & Harth, E. New Polymer Synthesis by Nitroxide Mediated Living Radical Polymerizations. *Chem Rev* **101**, 3661–3688 (2001).
32. Lynn, D. M., Kanaoka, S. & Grubbs, R. H. Living Ring-Opening Metathesis Polymerization in Aqueous Media Catalyzed by Well-Defined Ruthenium Carbene Complexes. *J Am Chem Soc* **118**, 784–790 (1996).
33. Perrier, S. 50th Anniversary Perspective: RAFT Polymerization—A User Guide. *Macromolecules* **50**, 7433–7447 (2017).
34. Arda Günay, K., Theato, P. & Klok, H.-A. *History of Post-Polymerization Modification*. (2013).
35. Jiang, J. & Thayumanavan, S. Synthesis and Characterization of Amine-Functionalized Polystyrene Nanoparticles. *Macromolecules* **38**, 5886–5891 (2005).
36. Adkins, C. T., Muchalski, H. & Harth, E. Nanoparticles with Individual Site-Isolated Semiconducting Polymers from Intramolecular Chain Collapse Processes. *Macromolecules* **42**, 5786–5792 (2009).
37. Huang, Z.-D. *et al.* Microscopically porous, interconnected single crystal LiNi<sub>1/3</sub>Co<sub>1/3</sub>Mn<sub>1/3</sub>O<sub>2</sub> cathode material for Lithium ion batteries. *J Mater Chem* **21**, 10777–10784 (2011).
38. Jiang, X., Pu, H. & Wang, P. Polymer nanoparticles via intramolecular crosslinking of sulfonyl azide functionalized polymers. *Polymer (Guildf)* **52**, 3597–3602 (2011).

39. Wang, P., Pu, H. & Jin, M. Single-chain nanoparticles with well-defined structure via intramolecular crosslinking of linear polymers with pendant benzoxazine groups. *J Polym Sci A Polym Chem* **49**, 5133–5141 (2011).
40. Dirlam, P. T. *et al.* Single chain polymer nanoparticles via sequential ATRP and oxidative polymerization. *Polym Chem* **4**, 3765–3773 (2013).
41. González-Burgos, M. *et al.* Structure and Dynamics of Irreversible Single-Chain Nanoparticles in Dilute Solution. A Neutron Scattering Investigation. *Macromolecules* **53**, 8068–8082 (2020).
42. Sanchez-Sanchez, A. & Pomposo, J. A. Efficient Synthesis of Single-Chain Polymer Nanoparticles *via* Amide Formation. *J Nanomater* **2015**, 723492 (2015).
43. de Luzuriaga, A. R. *et al.* Intramolecular Click Cycloaddition: An Efficient Room-Temperature Route towards Bioconjugable Polymeric Nanoparticles. *Macromol Rapid Commun* **29**, 1156–1160 (2008).
44. Oria, L., Aguado, R., Pomposo, J. A. & Colmenero, J. A Versatile “Click” Chemistry Precursor of Functional Polystyrene Nanoparticles. *Advanced Materials* **22**, 3038–3041 (2010).
45. Ormategui, N. *et al.* Synthesis of single chain thermoresponsive polymer nanoparticles. *Soft Matter* **8**, 734–740 (2012).
46. Radu, J. É. F. *et al.* Structural and dynamical characterization of poly-gamma-glutamic acid-based cross-linked nanoparticles. *Colloid Polym Sci* **286**, 365–376 (2008).
47. INGOLD, C. K. The Nature of the Chemical Bond and the Structure of Molecules and Crystals. *Nature* **145**, 644–645 (1940).
48. Front Matter. in *Supramolecular Chemistry I–X* (1995).  
doi:<https://doi.org/10.1002/3527607439.fmatter>.
49. Pollino, J. M. & Weck, M. Non-covalent side-chain polymers: design principles, functionalization strategies, and perspectives. *Chem Soc Rev* **34**, 193–207 (2005).
50. Kato, T. & Frechet, J. M. J. Stabilization of a liquid-crystalline phase through noncovalent interaction with a polymer side chain. *Macromolecules* **22**, 3818–3819 (1989).
51. Yang, X. *et al.* Supramolecular AB Diblock Copolymers. *Angewandte Chemie International Edition* **43**, 6471–6474 (2004).

52. Todd, E. M. & Zimmerman, S. C. Bis-ureidodeazapterin (Bis-DeAP) as a general route to supramolecular star polymers. *Tetrahedron* **64**, 8558–8570 (2008).
53. Jin, Y., Wang, Q., Taynton, P. & Zhang, W. Dynamic Covalent Chemistry Approaches Toward Macrocycles, Molecular Cages, and Polymers. *Acc Chem Res* **47**, 1575–1586 (2014).
54. Corbett, P. T. *et al.* Dynamic Combinatorial Chemistry. *Chem Rev* **106**, 3652–3711 (2006).
55. Ramström, O. & Lehn, J.-M. Drug discovery by dynamic combinatorial libraries. *Nat Rev Drug Discov* **1**, 26–36 (2002).
56. Levrand, B., Ruff, Y., Lehn, J.-M. & Herrmann, A. Controlled release of volatile aldehydes and ketones by reversible hydrazone formation – “classical” profragrances are getting dynamic. *Chemical Communications* 2965–2967 (2006) doi:10.1039/B602312F.
57. Seo, M., Beck, B. J., Paulusse, J. M. J., Hawker, C. J. & Kim, S. Y. Polymeric Nanoparticles via Noncovalent Cross-Linking of Linear Chains. *Macromolecules* **41**, 6413–6418 (2008).
58. Foster, E. J., Berda, E. B. & Meijer, E. W. Metastable Supramolecular Polymer Nanoparticles via Intramolecular Collapse of Single Polymer Chains. *J Am Chem Soc* **131**, 6964–6966 (2009).
59. Mes, T., van der Weegen, R., Palmans, A. R. A. & Meijer, E. W. Single-Chain Polymeric Nanoparticles by Stepwise Folding. *Angewandte Chemie International Edition* **50**, 5085–5089 (2011).
60. Hosono, N. *et al.* Orthogonal Self-Assembly in Folding Block Copolymers. *J Am Chem Soc* **135**, 501–510 (2013).
61. Appel, E. A., Dyson, J., del Barrio, J., Walsh, Z. & Scherman, O. A. Formation of Single-Chain Polymer Nanoparticles in Water through Host–Guest Interactions. *Angewandte Chemie International Edition* **51**, 4185–4189 (2012).
62. Akagi, T., Piyapakorn, P. & Akashi, M. Formation of Unimer Nanoparticles by Controlling the Self-Association of Hydrophobically Modified Poly(amino acid)s. *Langmuir* **28**, 5249–5256 (2012).
63. Ji, X., Zhang, Y. & Zhao, H. Amphiphilic Janus Twin Single-Chain Nanoparticles. *Chemistry – A European Journal* **24**, 3005–3012 (2018).

64. M, ter H. G., A, P. A. R. & Meijer, E. W. Supramolecular Single-Chain Polymeric Nanoparticles. *CCS Chemistry* **1**, 64–82 (2019).
65. Pomposo, J. A. *et al.* How Far Are Single-Chain Polymer Nanoparticles in Solution from the Globular State? *ACS Macro Lett* **3**, 767–772 (2014).
66. Moreno, A. J. *et al.* Advantages of Orthogonal Folding of Single Polymer Chains to Soft Nanoparticles. *Macromolecules* **46**, 9748–9759 (2013).
67. Perez-Baena, I. *et al.* Efficient Route to Compact Single-Chain Nanoparticles: Photoactivated Synthesis via Thiol–Yne Coupling Reaction. *Macromolecules* **47**, 8270–8280 (2014).
68. Terashima, T., Sugita, T., Fukae, K. & Sawamoto, M. Synthesis and Single-Chain Folding of Amphiphilic Random Copolymers in Water. *Macromolecules* **47**, 589–600 (2014).
69. Lyon, C. K. *et al.* A brief user's guide to single-chain nanoparticles. *Polymer Chemistry* vol. 6 181–197 Preprint at <https://doi.org/10.1039/c4py01217h> (2015).
70. Hanlon, A. M., Lyon, C. K. & Berda, E. B. What Is Next in Single-Chain Nanoparticles? *Macromolecules* **49**, 2–14 (2016).
71. Sanchez-Sanchez, A., Arbe, A., Colmenero, J. & Pomposo, J. A. Metallo-folded single-chain nanoparticles with catalytic selectivity. *ACS Macro Lett* **3**, 439–443 (2014).
72. Knöfel, N. D. *et al.* Heterobimetallic Eu(iii)/Pt(ii) single-chain nanoparticles: a path to enlighten catalytic reactions. *Chem Sci* **11**, 10331–10336 (2020).
73. Bohlen, J. L., Kulendran, B., Rothfuss, H., Barner-Kowollik, C. & Roesky, P. W. Heterobimetallic Au(i)/Y(iii) single chain nanoparticles as recyclable homogenous catalysts. *Polym Chem* **12**, 4016–4021 (2021).
74. Maag, P. H., Feist, F., Frisch, H., Roesky, P. W. & Barner-Kowollik, C. Fluorescent and Catalytically Active Single Chain Nanoparticles. *Macromolecules* **55**, 9918–9924 (2022).
75. Patenaude, B. F., Berda, E. B. & Pazicni, S. Probing secondary coordination sphere interactions within porphyrin-cored polymer nanoparticles. *Polym Chem* **13**, 677–683 (2022).

76. Terashima, T. *et al.* Single-chain folding of polymers for catalytic systems in water. *J Am Chem Soc* **133**, 4742–4745 (2011).
77. Frisch, H., Marschner, D. E., Goldmann, A. S. & Barner-Kowollik, C. Wellenlängengesteuerte dynamische kovalente Chemie. *Angewandte Chemie* **130**, 2054–2064 (2018).
78. Garmendia, S. *et al.* Catalytically Active N-Heterocyclic Carbene Release from Single-Chain Nanoparticles Following a Thermolysis-Driven Unfolding Strategy. *Macromol Rapid Commun* **40**, (2019).
79. Lambert, R. *et al.* Pd(ii)-NHC coordination-driven formation of water-soluble catalytically active single chain nanoparticles. *Polym Chem* **9**, 3199–3204 (2018).
80. Tao, L., Chen, G. & Li, Y. Machine learning discovery of high-temperature polymers. *Patterns* **2**, (2021).
81. Asenjo-Sanz, I., Claros, T., González, E., Verde-Sesto, E. & Pomposo, J. A. ‘Clickase’ Single-Chain Nanoparticles: Effect of Intra-Chain Distribution of Catalytic Sites on Catalytic Activity. (2021)  
doi:10.20944/preprints202101.0613.v1.
82. Chen, J. *et al.* Enzyme-like Click Catalysis by a Copper-Containing Single-Chain Nanoparticle. *J Am Chem Soc* **140**, 13695–13702 (2018).
83. Shi, Q., Zhang, Z. & Liu, S. Precision Sequence-Defined Polymers: From Sequencing to Biological Functions. *Angewandte Chemie - International Edition* vol. 63 Preprint at <https://doi.org/10.1002/anie.202313370> (2024).
84. Arbe, A. *et al.* Structure and dynamics of single-chain nano-particles in solution. *Polymer (Guildf)* **105**, 532–544 (2016).
85. Comanescu, C. Recent Development in Nanoconfined Hydrides for Energy Storage. *International Journal of Molecular Sciences* vol. 23 Preprint at <https://doi.org/10.3390/ijms23137111> (2022).
86. Zhu, X. *et al.* Design of polymer-based nanoreactors for efficient acid/base cascade catalysis: A comparative study of site isolation strategies. *J Mol Struct* **1285**, (2023).
87. Let, S., K. Dam, G., Fajal, S. & Ghosh, S. K. Organic porous heterogeneous composite with antagonistic catalytic sites as a cascade catalyst for continuous flow reaction. *Chem Sci* **14**, 10591–10601 (2023).

88. Gillissen, M. A. J., Voets, I. K., Meijer, E. W. & Palmans, A. R. A. Single chain polymeric nanoparticles as compartmentalised sensors for metal ions. *Polym Chem* **3**, 3166–3174 (2012).
89. Latorre-Sanchez, A. & Pomposo, J. A. A simple, fast and highly sensitive colorimetric detection of zein in aqueous ethanol via zein-pyridine-gold interactions. *Chemical Communications* **51**, 15736–15738 (2015).
90. Lu, Z., Zhang, J., Yin, W., Guo, C. & Lang, M. Preparation of AIE Functional Single-Chain Polymer Nanoparticles and Their Application in H<sub>2</sub>O<sub>2</sub> Detection through Intermolecular Heavy-Atom Effect. *Macromol Rapid Commun* **43**, (2022).
91. Pomposo, J. A., Moreno, A. J., Arbe, A. & Colmenero, J. Local Domain Size in Single-Chain Polymer Nanoparticles. *ACS Omega* **3**, 8648–8654 (2018).
92. Wong, E. H. H., Lam, S. J., Nam, E. & Qiao, G. G. Biocompatible single-chain polymeric nanoparticles via organo-catalyzed ring-opening polymerization. *ACS Macro Lett* **3**, 524–528 (2014).
93. Bai, Y. *et al.* Practical synthesis of water-soluble organic nanoparticles with a single reactive group and a functional carrier scaffold. *Chem Sci* **5**, 2862–2868 (2014).
94. Benito, A. B. *et al.* Functional Single-Chain Polymer Nanoparticles: Targeting and Imaging Pancreatic Tumors in Vivo. *Biomacromolecules* **17**, 3213–3221 (2016).
95. Hamilton, S. K. & Harth, E. Molecular dendritic transporter nanoparticle vectors provide efficient intracellular delivery of peptides. *ACS Nano* **3**, 402–410 (2009).
96. Sanchez-Sanchez, A. *et al.* Design and preparation of single-chain nanocarriers mimicking disordered proteins for combined delivery of dermal bioactive cargos. *Macromol Rapid Commun* **34**, 1681–1686 (2013).
97. Li, Y. *et al.* Crosslinked dendronized polyols as a general approach to brighter and more stable fluorophores. *Chemical Communications* **52**, 3781–3784 (2016).
98. Perez-Baena, I. *et al.* Single-chain polyacrylic nanoparticles with multiple Gd(III) centres as potential MRI contrast agents. *J Mater Chem* **20**, 6916–6922 (2010).
99. Adkins, C. T., Dobish, J. N., Brown, S. & Harth, E. Water-soluble semiconducting nanoparticles for imaging. *ACS Macro Lett* **2**, 710–714 (2013).
100. Li, Y. *et al.* Crosslinked dendronized polyols as a general approach to brighter and more stable fluorophores. *Chemical Communications* **52**, 3781–3784 (2016).

101. He, H., Shen, X. & Nie, Z. Engineering interactions between nanoparticles using polymers. *Prog Polym Sci* **143**, 101710 (2023).
102. Paternina, C. A., Quintero, H. & Mercado, R. Improving the interfacial performance and the adsorption inhibition of an extended-surfactant mixture for enhanced oil recovery using different hydrophobicity nanoparticles. *Fuel* **350**, 128760 (2023).
103. Distaso, M. & Peukert, W. A biphasic batch and continuous flow synthesis of hydrophobic gold and silver nanoparticles. *React Chem Eng* **8**, 1855–1867 (2023).
104. Yu, B. *et al.* A wear and heat-resistant hydrophobic fluoride-free coating based on modified nanoparticles and waterborne-modified polyacrylic resin. *RSC Adv* **13**, 4542–4552 (2023).
105. Zhang, S. *et al.* Polymethylhydrosiloxane and ZIF-8/color nanoparticles enhanced the UV-resistance, antibacterial and hydrophobicity performance of cotton fabrics. *Prog Org Coat* **182**, 107702 (2023).
106. Zhang, S. *et al.* Enhanced hydrophobicity and UV resistance of cotton fabrics through the synergistic effect of raspberry-shaped colored nanoparticles and polymethylhydrosiloxane. *Appl Surf Sci* **637**, 157849 (2023).

## **2. Outline and objectives of the Thesis**



The general objective of this doctoral thesis is to develop innovative metallic single-chain nanoparticles (SCNPs) through novel synthesis methods, addressing contemporary challenges in environmental monitoring, catalysis and green chemistry. The research focuses on creating lanthanide-based SCNPs, gold nanocluster encapsulated SCNPs, and heterobimetallic SCNPs. By emphasizing groundbreaking synthesis techniques, this thesis aims to contribute significantly to public health and environmental sustainability through efficient and eco-friendly solutions.

On one hand, **Chapter 2** aims to design and synthesize lanthanide-based single-chain nanoparticles (SCNPs) that serve as visual sensors for detecting copper ( $\text{Cu}^{2+}$ ) ions in drinking water. The goal is to develop a simple, efficient, and selective method for monitoring  $\text{Cu}^{2+}$  levels, which are toxic at high concentration limits set by the WHO and EPA. The objective will be to achieve easy and rapid detection without the need for sophisticated instrumentation.

In **Chapter 3**, objective will be to synthesize gold nanoclusters (Au-NCs) encapsulated within SCNPs, exploring their use as catalytic nanoreactors in aqueous environments. The aim will be to enhance the catalytic efficiency of gold nanoclusters by embedding them within SCNPs, adhering to green chemistry principles. The catalytic efficacy of these nanoclusters will be evaluated in reducing nitroaromatic compounds in water, to study their potential for scalable, environmentally friendly industrial applications.

The objective of the project in **Chapter 4** will be to synthesize and apply heterobimetallic Pt(II)/Cu(II) single-chain nanoparticles (SCNPs) as efficient, soft nanocatalysts for performing consecutive one-pot alkyne semihydrogenation and alkene dioxygenation reactions within a green solvent, N-butylpyrrolidone (NBP). The project will aim to address the challenges associated with multistep chemical processes and the reliance on toxic organic solvents by offering a sustainable alternative.

In summary, through the innovative design and synthesis of SCNPs, this research contributes significantly to public health and environmental sustainability. This work aims to advance nanotechnology and catalysis principles to develop novel, efficient, and sustainable solutions for water quality monitoring and green chemistry applications.



### **3. Lanthanide-based Single-Chain Nanoparticles as “Visual” Pass/Fail Sensors of Maximum Permissible Concentration of Cu<sup>2+</sup> Ions in Drinking Water**



### 3.1 Motivation

The maximum permissible concentration (m.p.c.) of Cu<sup>2+</sup> ions in drinking water, as set by the World Health Organization (WHO) is  $m.p.c.(Cu^{2+})_{WHO} = 30 \mu M$ , whereas the US Environmental Protection Agency (EPA) establishes a more restrictive value of  $m.p.c.(Cu^{2+})_{EPA} = 20 \mu M$ . Herein, we develop -for the first time ever- a family of  $m.p.c.(Cu^{2+})$  “visual” pass/fail sensors based on water-soluble lanthanide-containing single-chain nanoparticles (SCNPs) exhibiting an average hydrodynamic diameter below 10 nm. Both europium (Eu)- and terbium (Tb)-based SCNPs allow excessive Cu<sup>2+</sup> concentration to be readily detected in water, as can be naked-eye monitored by red-to-transparent and green-to-transparent color changes under ultra-violet (UV) light irradiation, respectively, taking place at *ca.* 30  $\mu M$  of Cu<sup>2+</sup> ions in both cases. Complementary, dysprosium (Dy)-based SCNPs show a yellow-to-transparent color transition under UV light irradiation at *ca.* 15  $\mu M$  of Cu<sup>2+</sup> ions. Eu-, Tb- and Dy-containing SCNPs prove to be selective for Cu<sup>2+</sup> ions as they do not respond against other metal ions, such as Fe. These new  $m.p.c.(Cu^{2+})$  “visual” pass/fail sensors are thoroughly characterized by a combination of techniques including size exclusion chromatography (SEC), dynamic light scattering (DLS), inductively coupled plasma mass spectrometry (ICP-MS), infra-red (IR), UV and fluorescence spectroscopy.

### 3.2 Introduction

Copper is an essential trace element for animals and plants.<sup>1</sup> In fact, Cu<sup>2+</sup> -the 3<sup>th</sup> most important metal ion present in biological system- is involved as cofactor of numerous metalloenzymes.<sup>2,3</sup> Cu<sup>2+</sup> ions are also essential for the human body and defect of this crucial micronutrient can impart cytopenia (a reduction in the number of mature blood cells) and profound neurological deficits.<sup>4,5</sup> On the contrary, an excessive Cu<sup>2+</sup> intake from occupational exposure or contaminated water can cause gastrointestinal problems, liver and kidney damage, hemolytic anemia and impaired immune function, among other effects.<sup>6,7</sup> Thus, Cu<sup>2+</sup> ions act as one of the environment pollutants to control due

### 3. Lanthanide-based Single-Chain Nanoparticles as “Visual” Pass/Fail Sensors of Maximum Permissible Concentration of Cu<sup>2+</sup> Ions in Drinking Water

to their increased use at several levels (home, industrial, and agricultural operations), as well as environmental persistency.<sup>8</sup>

Different regulatory Organisms have established the maximum permissible concentration (m.p.c.) of Cu<sup>2+</sup> ions in drinking water. The m.p.c. of Cu<sup>2+</sup> ions in drinking water by the World Health Organization (WHO) is m.p.c.(Cu<sup>2+</sup>)WHO = 30 μM, whereas the US Environmental Protection Agency (EPA) establishes a more restrictive value of m.p.c.(Cu<sup>2+</sup>)EPA = 20 μM.<sup>9,10</sup> Although different analytical techniques are available to accurately determine the concentration of Cu<sup>2+</sup> ions in drinking water (e.g., atomic absorption spectroscopy, ion chromatography, inductively coupled plasma mass spectrometry), these techniques often involve sophisticated instrumentation and require skilled users. Consequently, alternative methods based on “visual” pass/fail sensors providing operational simplicity, sensitivity and selectivity are highly desirable.

To tackle that challenge, we envisioned to design single-chain polymer nanoparticles (SCNPs) incorporating lanthanide metal ions as a versatile platform towards a new generation of m.p.c.(Cu<sup>2+</sup>) operating as “visual” pass/fail sensors. SCNPs are individual polymeric chains that are intramolecularly folded through intra-chain interactions.<sup>11</sup> The folding of discrete synthetic polymer chains into SCNPs attempts to mimic the natural folding of biomacromolecules, such as proteins.<sup>12</sup> The chain folding process leads to locally compact domains within SCNPs, which can be of practical use to bind active species (e.g., metal ions,<sup>13</sup> luminophores,<sup>14</sup> drugs<sup>15</sup>). Consequently, SCNPs offer interesting opportunities for the development of improved sensors<sup>16</sup>, innovative drug delivery vehicles<sup>17</sup> and biomimetic catalysts,<sup>18</sup> among other practical applications. On the other hand, a variety of complexes based on lanthanide ions<sup>19-22</sup> have been investigated as fluorescent “turn-off” sensors of Cu<sup>2+</sup> ions.

However, most of these molecular sensors are not directly operative in water, but instead, in organic solvent/water mixtures. We hypothesized that, by using an amphiphilic random copolymer featuring beta-ketoester functional groups able to complex with lanthanide ions, water-soluble lanthanide containing SCNPs could be

achieved via intra-chain beta-ketoester/lanthanide complexation. The resulting lanthanide based SCNPs were thus employed as innovative m.p.c.(Cu<sup>2+</sup>) “visual” pass/fail sensors in drinking water. Here we report the rational design of europium (Eu)-, terbium (Tb)- and dysprosium (Dy)-based SCNPs, as well as their use -for the first time ever- as efficient “visual” pass/fail sensors of maximum permissible concentration of Cu<sup>2+</sup> ions in water.

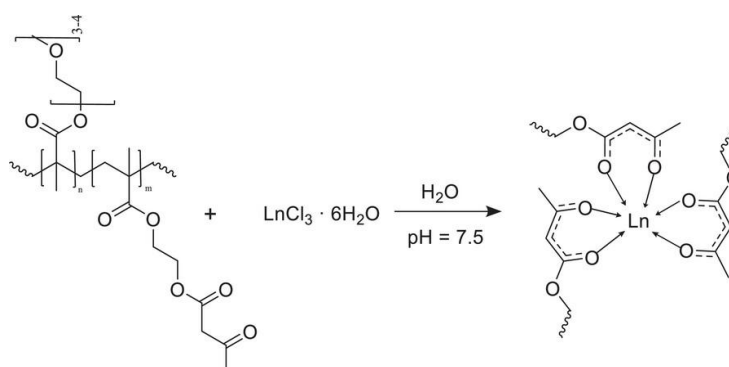
### 3.3. Materials, techniques and methods

#### 3.3.1. Materials

Oligo(ethylene glycol) methyl ether methacrylate (OEGMA) (average  $M_n \sim 300$  g/mol), (2-acetoacetoxy)ethyl methacrylate (AEMA) (95%), 2,2-azobis(2-methylpropionitrile) (AIBN) ( $\geq 98\%$ ), triethylamine (Et<sub>3</sub>N) ( $>99\%$ ), methyl acetoacetate 99%, 1,4-dioxane (anhydrous, 99.8%), hexane (anhydrous, 95 %), 4-cyano-4-(thiobenzoylthio)pentanoic acid ( $\geq 97\%$ ), europium trichloride hexahydrate (EuCl<sub>3</sub> x 6 H<sub>2</sub>O) (99.99% trace metals basis), terbium trichloride hexahydrate (TbCl<sub>3</sub> x 6 H<sub>2</sub>O) (99.99% trace metals basis), dysprosium trichloride hexahydrate (DyCl<sub>3</sub> x 6 H<sub>2</sub>O) (99.99% trace metals basis), copper (II) acetate (98%), iron (II) acetate (95%), cobalt (II) acetate tetrahydrate (99%), barium acetate (99%), nickel (II) acetate tetrahydrate (99%), mercury (II) acetate ( $\geq 98.0\%$ ), lead (II) acetate tetrahydrate (99%) zinc (II) acetate dehydrate (99%), iron (III) acetylacetonate (97%), calcium acetate monohydrate (99%), manganese (II) acetylacetonate (98%), magnesium chloride (98%) and chromium(III) acetate (98%) were supplied by Merck (SigmaAldrich). Potassium hydroxide (KOH) ( $\geq 85\%$ , pellets) was supplied by PanReac AppliChem (ITW Reagents). Silver(I) acetate (99%) was supplied by ITW Reagents (Acros Organics). Deionized water was obtained from a Thermo Scientific apparatus (Barnstead TII Pure Water System). Tetrahydrofuran (THF) was supplied by Scharlab. Deuterated chloroform (CDCl<sub>3</sub>) (99.8 atom % D) was supplied by Merck.

### 3.3.2. Techniques

<sup>1</sup>H nuclear magnetic resonance (NMR) spectra were obtained at room temperature (r.t.) using a Bruker spectrometer operating at 400 MHz with CDCl<sub>3</sub> as the solvent. Size exclusion chromatography (SEC) measurements were conducted at 30 °C in an Agilent 1200 system that was equipped with PLgel 5 μm Guard and PLgel 5 μm MIXED-C columns. The measurements employed a triple detection system, which included a differential refractive index detector (Optilab Rex, Wyatt), a multi-angle laser light scattering (MALLS) detector (MiniDawn Treos, Wyatt), and a viscosimetric (VIS) detector (ViscoStar-II, Wyatt). SEC data were analysed using Wyatt's ASTRA Software (version 6.1). Tetrahydrofuran (THF) was used as the eluent with a flow rate of 1 mL/min. For both the precursor and the single-chain nanoparticles, a value of dn/dc = 0.1150 was applied. Dynamic Light Scattering (DLS) measurements were carried out at r.t. on a Malvern Zetasizer Nano ZS apparatus. Metal content in the single-chain nanoparticles was determined by inductively coupled plasma mass spectrometry (ICP-MS). Fourier transform infrared (FTIR) spectra were recorded at r.t. on a JASCO 3600 FTIR spectrometer. UV spectroscopy was carried out in an Agilent 8453A spectrometer. Photoluminescence (PL) spectra were recorded at r.t. on an Agilent Cary Eclipse spectrometer. Horiba Laquatwin-pH-33 compact pH-meter was used for pH measurements.



**Scheme 1.** Schematic illustration of the synthesis of lanthanide (Ln)-based single-chain polymer nanoparticles (SCNPs) using an amphiphilic random copolymer decorated with beta-ketoester functional groups, namely, poly(OEGMA-co-AEMA).

### 3.3.3.Methods

#### Synthesis of amphiphilic random copolymer featuring beta-ketoester functional groups

OEGMA (1.54 mL, 5.6 mmol), AEMA (0.26 mL, 1.38 mmol), 4-cyano-4-(thiobenzoylthio) pentanoic acid (18.3 mg, 0.065 mmol), and AIBN (2.15 mg, 0.013 mmol) were dissolved at r.t. in 1,4-dioxane (3 mL). The resulting mixture was degassed by purging with argon for 15 min. Then, the mixture was subjected to reversible addition fragmentation chain-transfer (RAFT) copolymerization at 70 °C for 24 h. The resulting poly(OEGMA-co-AEMA) copolymer, a pink oil, was isolated by precipitation in hexane. Subsequently, the product was dissolved in a minimal amount of THF and added to an excess of hexane (twice). After removal of volatile organic solvents, further drying was carried out at r.t. under vacuum and confirmed by <sup>1</sup>H NMR (Figure 1).

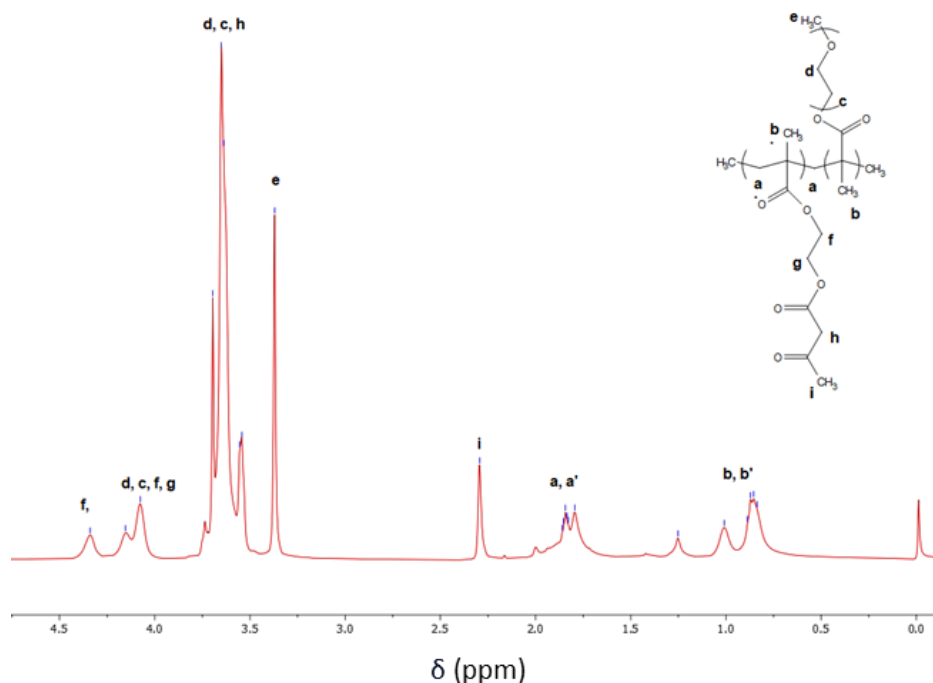


**Figure 1.** <sup>1</sup>H NMR spectrum of poly(OEGMA-co-AEMA).

### Synthesis of lanthanide-based single-chain polymer nanoparticles (SCNPs)

Poly(OEGMA-co-AEMA) (15 mg, 0.03 mmol) and the corresponding lanthanide trichloride hexahydrate (LnCl<sub>3</sub> x 6 H<sub>2</sub>O; Ln = Eu, Tb, Dy) (30 μM) were dissolved in water (15 mL) at r.t. and pH = 7.5 for 24 h. The resulting lanthanide-containing SCNPs were purified by dialysis against deionized water. ICP-MS data about the lanthanide content in the SCNPs are provided in Table 1. Successful formation of SCNPs was confirmed by SEC and DLS measurements, according to well-established literature procedures.<sup>11</sup> To mitigate possible interference from molecular oxygen, all lanthanide-based SCNPs were subjected to an extensive degassing (N<sub>2</sub>) process before performing the fluorescence measurements.

**Table 1.** SEC and ICP-MS data of Ln-SCNPs.

Ln-SCNPs	<i>M<sub>w</sub></i> (MALLS) (kDa)	<i>D</i>	Ln <sup>3+</sup> content (μg/mg) <sup>a</sup>	Ln <sup>3+</sup> content (μg/mg) <sup>b</sup>
Eu-SCNPs	85.0	1.12	4.6	2.7
Tb-SCNPs	88.9	1.36	4.8	2.0
Dy-SCNPs	-	-	4.9	-

<sup>a</sup>Theoretical value. <sup>b</sup>Experimental value determined from ICP-MS measurements.

## 3.4. Results and discussion

### 2.4.1. Eu-SCNPs as m.p.c.(Cu<sup>2+</sup>) “visual” pass/fail sensors

Europium-based single-chain nanoparticles (Eu-SCNPs) were prepared at a concentration of 1 mg/mL, following the procedure depicted in Scheme 1. A linear amphiphilic random copolymer, namely, poly(OEGMA-co-AEMA) was first synthesized by

### 3. Lanthanide-based Single-Chain Nanoparticles as “Visual” Pass/Fail Sensors of Maximum Permissible Concentration of Cu<sup>2+</sup> Ions in Drinking Water

RAFT copolymerization of the hydrophilic monomer OEGMA and the hydrophobic monomer AEMA. Poly(OEGMA-co-AEMA) was found to contain 35 mol% of betaketoester functional groups, as determined by <sup>1</sup>H NMR spectroscopy (Figure 1). Poly(OEGMA-co-AEMA) showed a weight-average molecular weight of  $M_w = 80.7$  kDa and relatively low dispersity,  $\mathcal{D} = 1.11$  (Table 1). Eu-SCNPs resulted from the complexation of Eu<sup>3+</sup> ions in solution by beta-ketoester functional groups of poly(OEGMA-co-AEMA) (see Scheme 1).

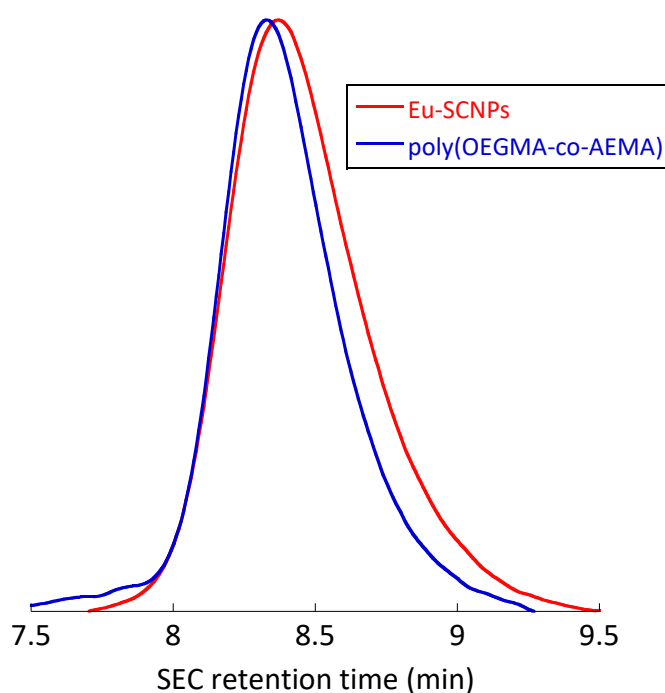


**Figure 2.** SEC traces of the precursor, poly(OEGMA-co-AEMA), and the Eu-SCNPs

The formation of Ln<sup>3+</sup>/beta-ketoester complexes involving low molecular weight organic compounds is well documented.<sup>23-25</sup> To the best of our knowledge, however, there are no precedents of single-chain polymer nanoparticle formation *via* intra-chain lanthanide/beta-ketoester complex formation. Successful preparation of Eu-SCNPs was confirmed by a combination of structural and size characterization techniques. Hence, SEC results confirmed a shift of the SEC elution time at peak maximum towards longer retention time and, hence, smaller hydrodynamic size for Eu-SCNPs when compared to

the parent poly(OEGMA-co-AEMA) (Figure 2). Eu-SCNPs showed  $M_w = 85.0$  kDa and  $\bar{D} = 1.12$ , suggesting the folding of individual copolymer chains and the absence of multichain aggregates by intermolecular crosslinking.<sup>11</sup>

Dynamic light scattering measurements confirmed the changes in the size of the Eu-SCNPs. Two peaks in Figure 3 indicates the presence of particles with different hydrodynamic diameters. The shift from a larger peak to a smaller one suggests that the average hydrodynamic diameter of the nanoparticles decreased from 8.3 nm to 7.3 nm. This decrease in size is attributed to the intra-chain complexation of Eu<sup>3+</sup> ions with betaketoester functional groups within the polymer chains, effectively causing the chains to fold into a more compact structure and form the Eu-SCNPs.

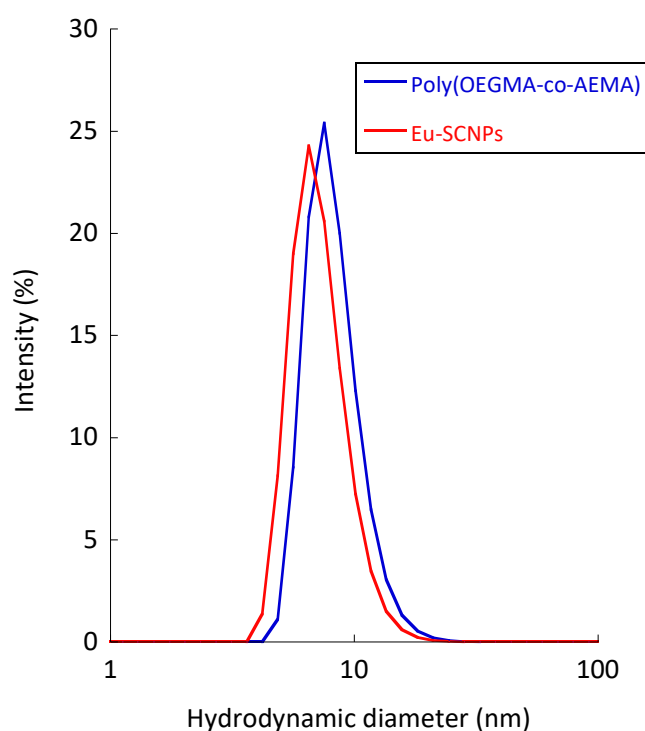


**Figure 3.** DLS size distribution of the precursor, poly(OEGMA-co-AEMA) (blue colour), and the Eu-SCNPs (red colour).

Eu-SCNPs display remarkable fluorescent properties when exposed to UV light at an excitation wavelength of 254 nm. This fluorescence is observable within a pH range of 7.5 to 11 as shown in Figure 4 which represents the relative photoluminescence intensity

### 3. Lanthanide-based Single-Chain Nanoparticles as “Visual” Pass/Fail Sensors of Maximum Permissible Concentration of Cu<sup>2+</sup> Ions in Drinking Water

at various pH levels, indicating the stability of fluorescence under these conditions. In Figure 5, practical demonstration of this fluorescence, where Eu-SCNPs exhibit a vivid red glow under UV irradiation, affirming their potential use in applications such as bioimaging and sensing within the specified pH range. This pH-dependent fluorescence could be critical for developing pH sensors or for applications where the pH could affect the fluorescence-based detection.

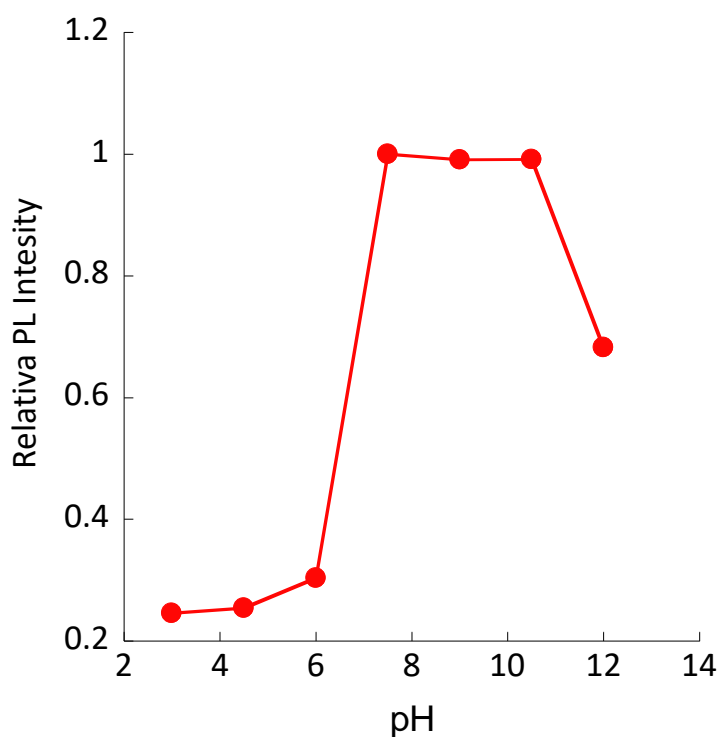


**Figure 4.** Illustration of the redish fluorescent Eu-SCNPs under UV light irradiation ( $\lambda_{exc} = 254$  nm), at various pH levels.

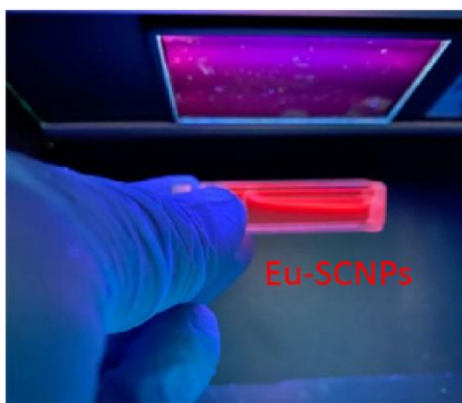


**Figure 5.** Relative photoluminescence (PL) of Eu-SCNPs.

Figure 6 shows a parameter labeled as "Stokes shift" ( $\Delta\lambda$ ), which is typically the difference in wavelength between the peaks of the absorbance and emission spectra. The Stokes shift is an important feature in fluorescent materials as it provides information about the energy loss between the absorption and emission of light. In practical terms, a larger Stokes shift is often advantageous because it minimizes the reabsorption of emitted light, improving the efficiency of fluorescence. Two distinct peaks can be observed, one related to absorbance and another sharper peak for emission. The Stokes shift would be the wavelength difference between these two peaks: 367 nm.

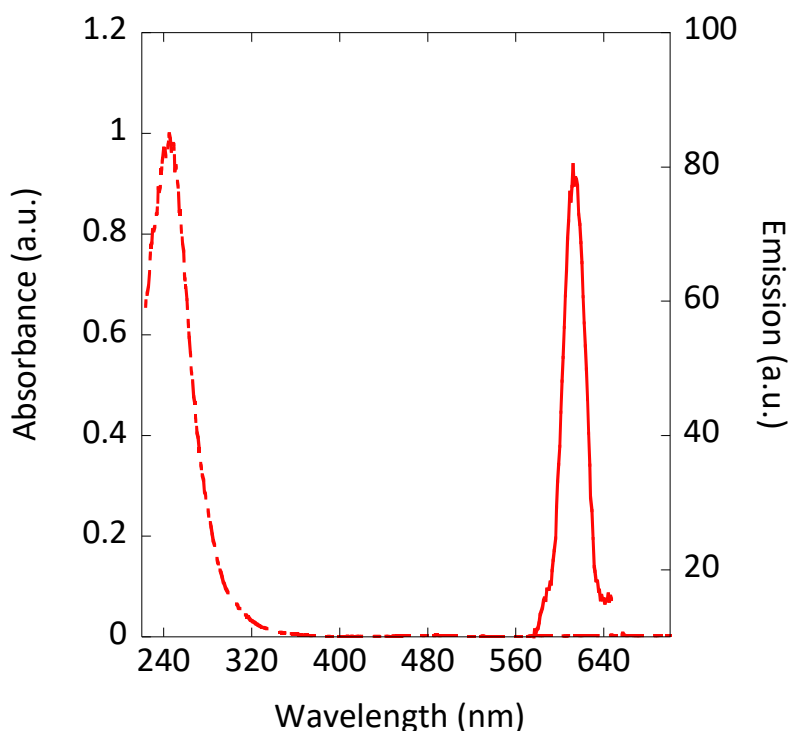


**Figure 6.** Absorbance (dotted) vs emission (continuous) and Stokes shift ( $\Delta\lambda$ ) of Eu-SCNPs.

3D and 2D fluorescence studies were carried out to know the complete relationships between excitation and emission of the Eu-SCNPs. In the 3D representation (Figure 7 and 8), the intensity of emission is visualized as peaks, with height corresponding to intensity at various excitation wavelengths. The 2D contour plot simplifies this by projecting the data onto a plane, making it easier to discern the wavelengths at which Eu-SCNPs exhibit

3. Lanthanide-based Single-Chain Nanoparticles as “Visual” Pass/Fail Sensors of Maximum Permissible Concentration of Cu<sup>2+</sup> Ions in Drinking Water

maximum fluorescence. These plots are critical for determining the optimal excitation-emission pairs for analytical applications of Eu-SCNPs.

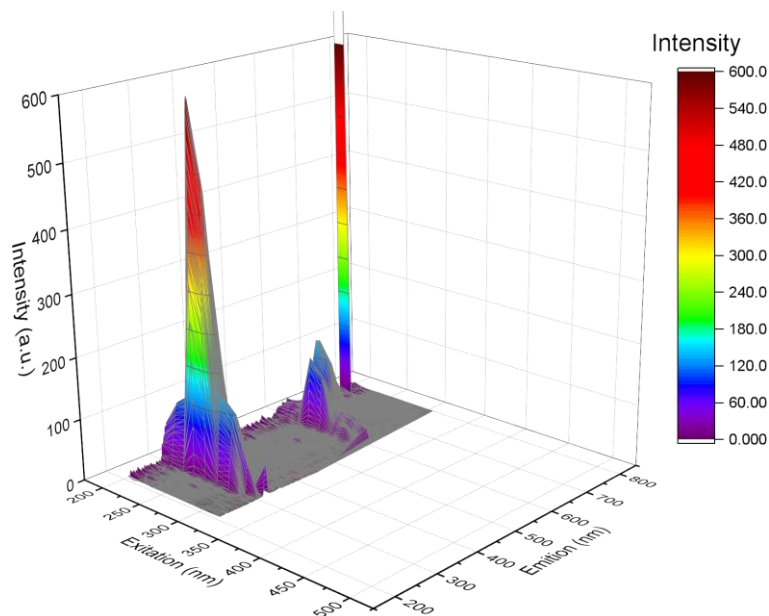


**Figure 7.** 3D study of excitation vs. emission for Eu-SCNPs.

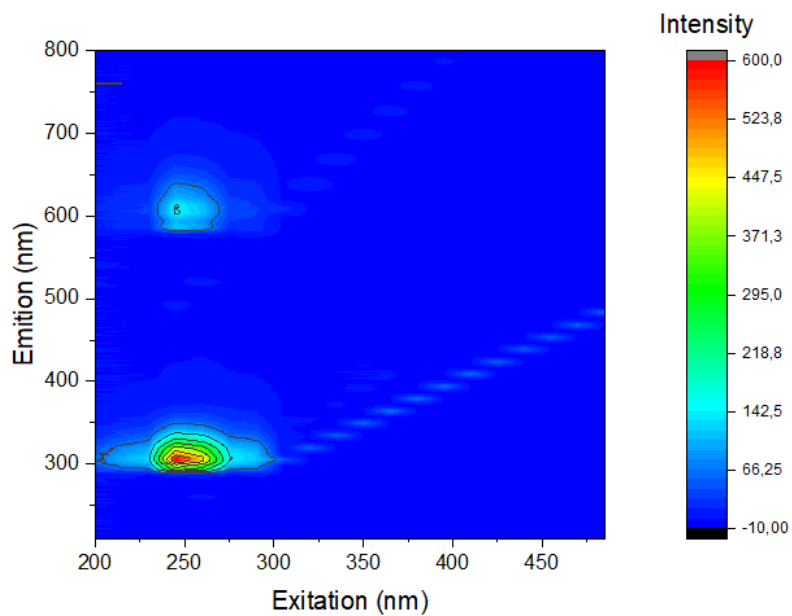


**Figure 8.** 2D study of excitation vs. emission for Eu-SCNPs.

### 3. Lanthanide-based Single-Chain Nanoparticles as “Visual” Pass/Fail Sensors of Maximum Permissible Concentration of Cu<sup>2+</sup> Ions in Drinking Water

Fluorescence intensity of Eu-SCNPs over time, specifically at intervals of 10 minutes, 1 hour, 1 day, and 1 month was studied to know the stability of nanoparticles (Figure 9). The overlapping curves suggest that the Eu-SCNPs maintain their fluorescence intensity quite well over the period observed. The minimal change in peak height over these different time points indicates that the Eu-SCNPs are chemically stable and do not undergo significant degradation or quenching that would otherwise affect their fluorescence.

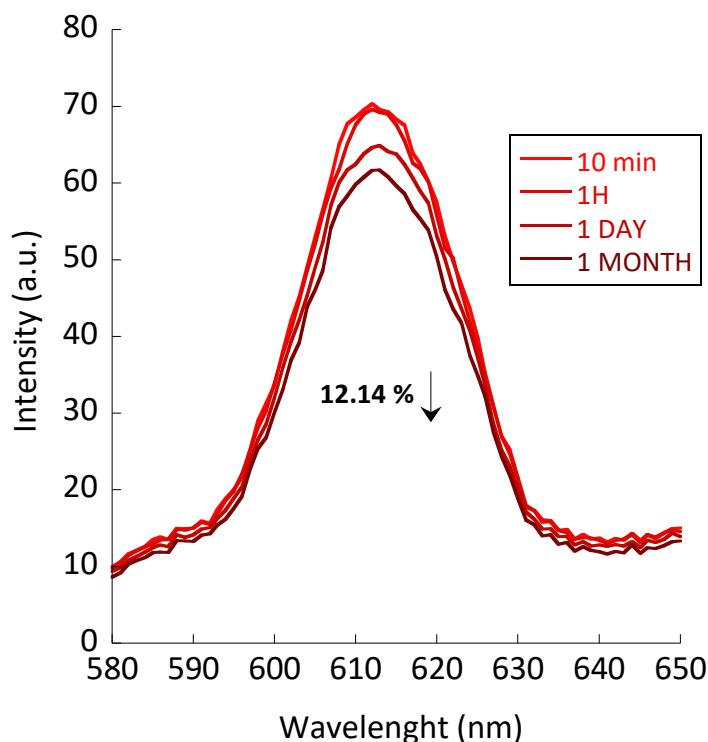


**Figure 9.** Stability of the fluorescence intensity over time for Eu-SCNPs.

Figure 10 demonstrates the photoluminescence (PL) intensity variation of Eu-SCNPs when subjected to changes in pH levels from neutral (pH 7.5) to acidic (pH 4). The distinct patterns of PL intensity at these two pH values indicate that the nanoparticles' fluorescence is pH-sensitive. At pH 7.5, the PL intensity is significantly higher compared to pH 4, where a marked decrease in fluorescence is observed. As can be seen in Figure 10, 3-4 cycles of pH change were supported by the Eu-SCNPs until the fluorescence completely disappeared.

3. Lanthanide-based Single-Chain Nanoparticles as “Visual” Pass/Fail Sensors of Maximum Permissible Concentration of Cu<sup>2+</sup> Ions in Drinking Water

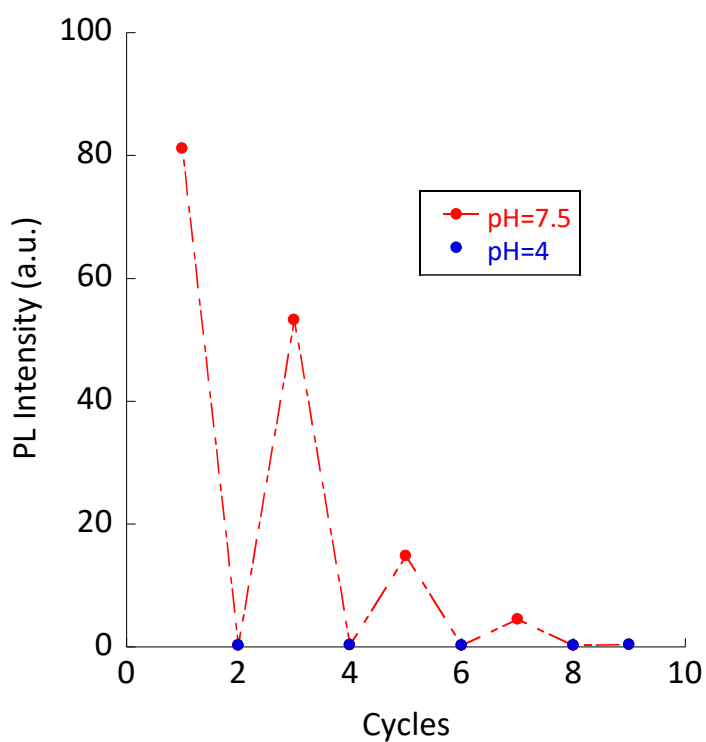


**Figure 10.** Evolution of the PL intensity of Eu-SCNPs upon consecutive pH changes between 7.5 and 4.

FTIR spectroscopy provided further evidence of the presence of Eu<sup>3+</sup>/beta-ketoester complexes in Eu-SCNPs. As illustrated in Figure 11, a new band located at 1632.4 cm<sup>-1</sup> indeed appeared in the FTIR spectrum of the Eu-SCNPs, which could be assigned to the stretching vibration of the enol tautomer of the beta-ketoester groups bonded to Eu<sup>3+</sup>.

3. Lanthanide-based Single-Chain Nanoparticles as “Visual” Pass/Fail Sensors of Maximum Permissible Concentration of Cu<sup>2+</sup> Ions in Drinking Water

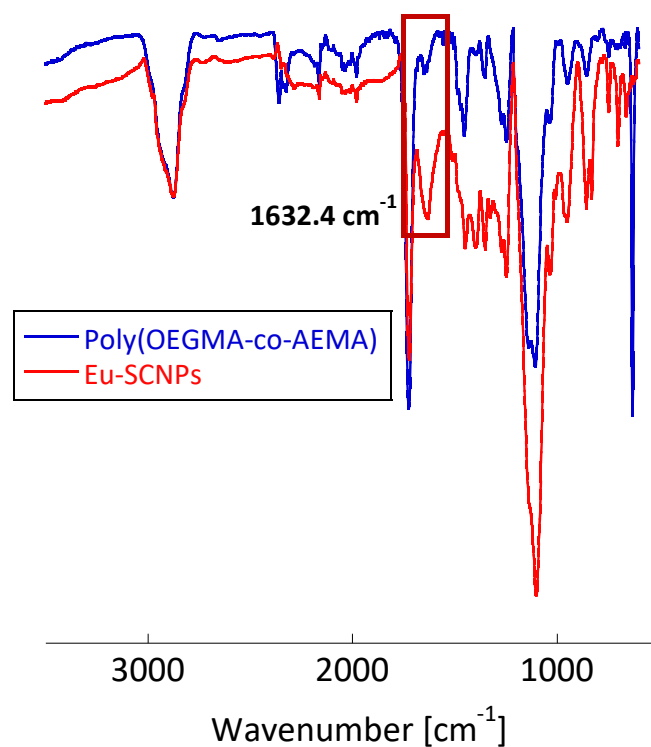


**Figure 11.** FTIR spectra of poly(OEGMA-co-AEMA) (blue colour) and Eu-SCNPs (red colour)

Figure 12 shows the PL spectra of Eu-SCNPs in water in the presence of increasing amounts of Cu<sup>2+</sup> ions ( $\lambda_{\text{exc}} = 254 \text{ nm}$ ). As shown in Figure 13, Eu-SCNPs can be used as “visual” pass/fail sensors of m.p.c. of Cu<sup>2+</sup> ions in water, according to the WHO criterion (m.p.c.(Cu<sup>2+</sup>)<sub>WHO</sub> = 30  $\mu\text{M}$ ).<sup>9</sup> A clear red-to-transparent colour change under UV light ( $\lambda_{\text{exc}} = 254 \text{ nm}$ ) is indeed observed also in Figure 13 on passing from [Cu<sup>2+</sup>]  $\leq 27.5 \mu\text{M}$  to [Cu<sup>2+</sup>] = 30  $\mu\text{M}$ .

3. Lanthanide-based Single-Chain Nanoparticles as “Visual” Pass/Fail Sensors of Maximum Permissible Concentration of Cu<sup>2+</sup> Ions in Drinking Water

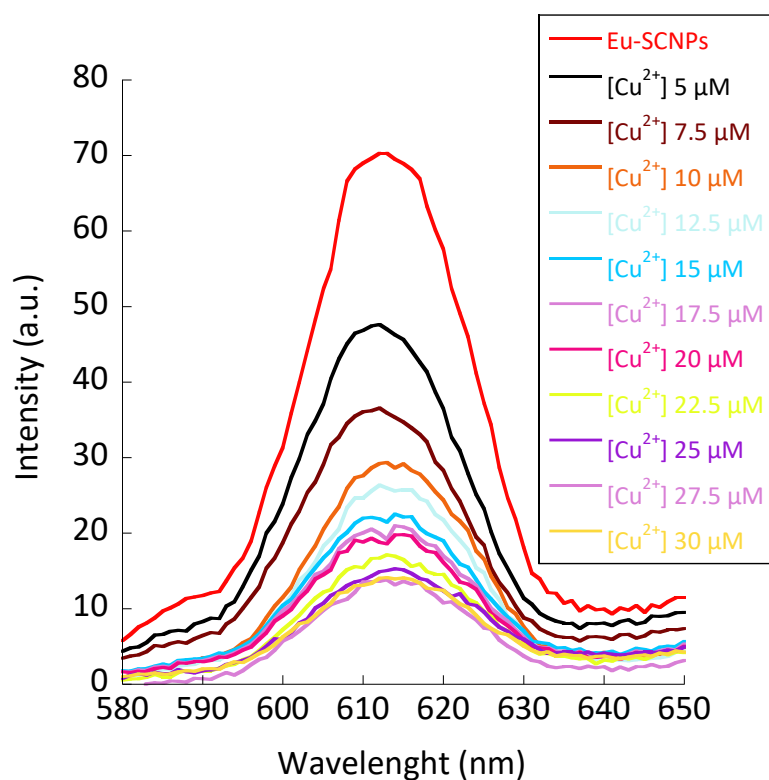


**Figure 12.** PL spectra of Eu-SCNPs in water in the presence of increasing amounts of Cu<sup>2+</sup> ions.



**Figure 13.** (e) demonstration of the utility of Eu-SCNPs as “visual” pass/fail sensors of m.p.c. of Cu<sup>2+</sup> ions in water according to the WHO criterion (i: 5 μM, ii: 10 μM, iii: 15 μM, iv: 22.5 μM, v: 25 μM, vi: 27.5 μM and vii: 30 μM).

Analysis of the data in Figure 14 using the Stern-Volmer equation ( $I_0/I = 1 + K_{SV}[Cu^{2+}]$ ) provided a value of  $K_{SV} = 1.4 \times 10^5 M^{-1}$  and a squared coefficient of linear regression of  $R^2 = 0.99$ .

3. Lanthanide-based Single-Chain Nanoparticles as “Visual” Pass/Fail Sensors of Maximum Permissible Concentration of Cu<sup>2+</sup> Ions in Drinking Water

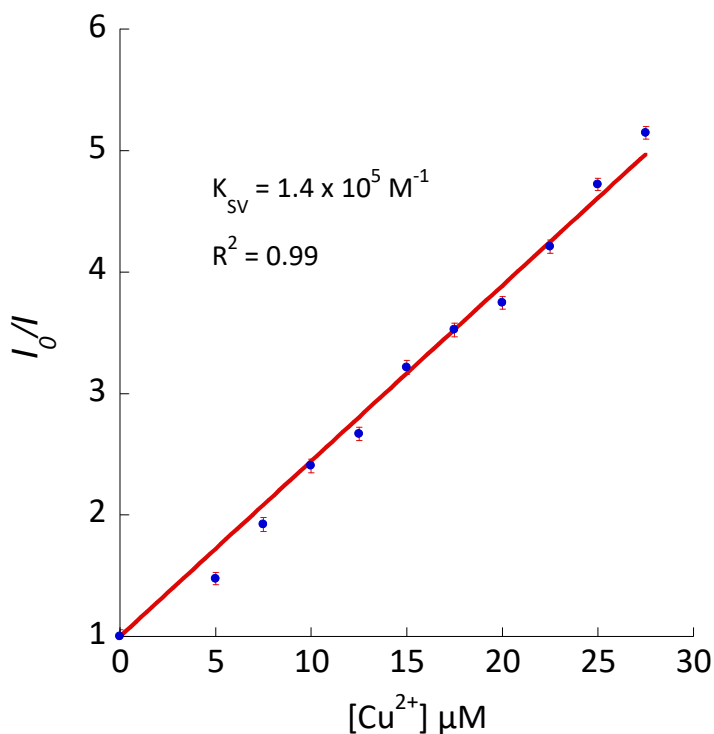


**Figure 14.** Stern-Volmer plot ( $I_0/I = 1 + K_{SV}[Cu^{2+}]$ ) of Eu-SCNPs (error bars estimated from triple measurements)

Remarkably, Eu-SCNPs proved highly selective for Cu<sup>2+</sup> ions against other metal ions, such as Fe<sup>2+</sup>, Ag<sup>+</sup>, Co<sup>2+</sup>, Ba<sup>2+</sup>, Ni<sup>2+</sup>, Hg<sup>2+</sup>, Pb<sup>2+</sup>, Zn<sup>2+</sup>, Fe<sup>3+</sup>, Ca<sup>2+</sup>, Mn<sup>2+</sup>, Mg<sup>2+</sup> and Cr<sup>3+</sup>. From the bar chart (Figure 15), it's clear that the response of Eu-SCNPs to Cu<sup>2+</sup> is significantly higher than to other metal ions, indicated by the towering peak for Cu<sup>2+</sup>. This suggests that Eu-SCNPs have a high selectivity for Cu<sup>2+</sup> ions. The line graph (Figure 16) shows the photoluminescence (PL) spectra of Eu-SCNPs in the presence of different metal ions, including Cu<sup>2+</sup>. The spectra for Cu<sup>2+</sup> shows a pronounced quenching of Eu<sup>3+</sup> emission, which is not observed with other metal ions. This quenching is attributed to energy transfer from Eu<sup>3+</sup> to Cu<sup>2+</sup> ions, followed by nonradiative relaxation to the ground state of the Cu<sup>2+</sup> ions,<sup>27,28</sup> confirming the selectivity of Eu-SCNPs for Cu<sup>2+</sup> ions over others. This property is particularly valuable for the development of selective sensors for Cu<sup>2+</sup> in various applications.

3. Lanthanide-based Single-Chain Nanoparticles as “Visual” Pass/Fail Sensors of Maximum Permissible Concentration of  $\text{Cu}^{2+}$  Ions in Drinking Water

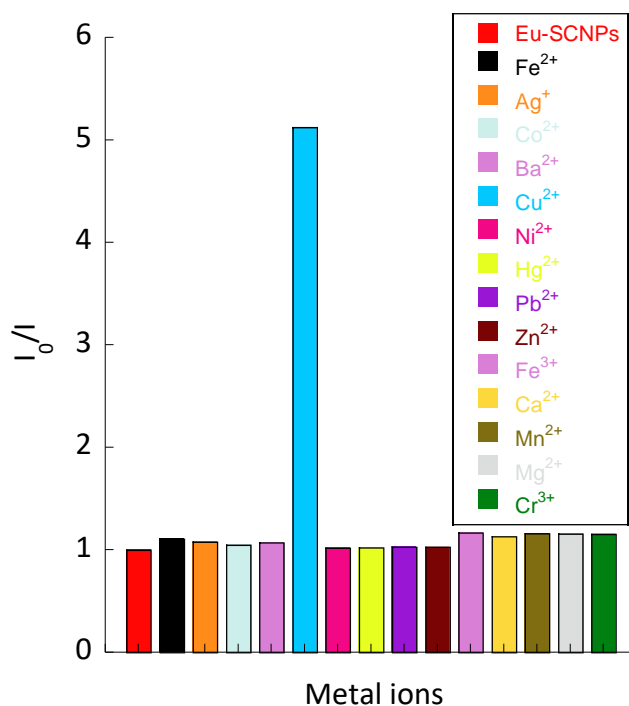


**Figure 15.** PL intensity of Eu-SCNPs in the presence of different metal ions at a concentration of 27.5  $\mu\text{M}$ .

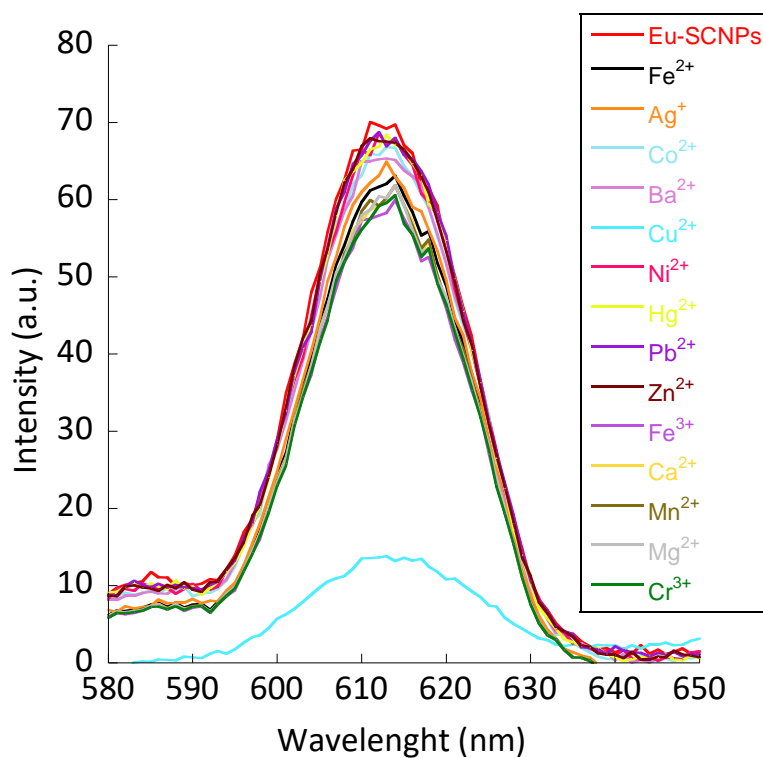


**Figure 16.** Selectivity of Eu-SCNPs for  $\text{Cu}^{2+}$  ions against other metal ions.

### 3.4.2. Tb-SCNPs as m.p.c.(Cu<sup>2+</sup>) “visual” pass/fail sensors

Tb-SCNPs were obtained from the complexation of Tb<sup>3+</sup> ions in solution by beta-ketoester functional groups of poly(OEGMA-co-AEMA), as displayed in Scheme 1. The average hydrodynamic diameter of the Tb-SCNPs was 7.2 nm (Figure 17), a value smaller than that of the poly(OEGMA-co-AEMA) precursor (8.3 nm). The SEC trace of Tb-SCNPs (M<sub>w</sub> = 88.9 kDa, Đ = 1.36, see ESI) confirmed the absence of multi-chain aggregates, in accordance with DLS results.

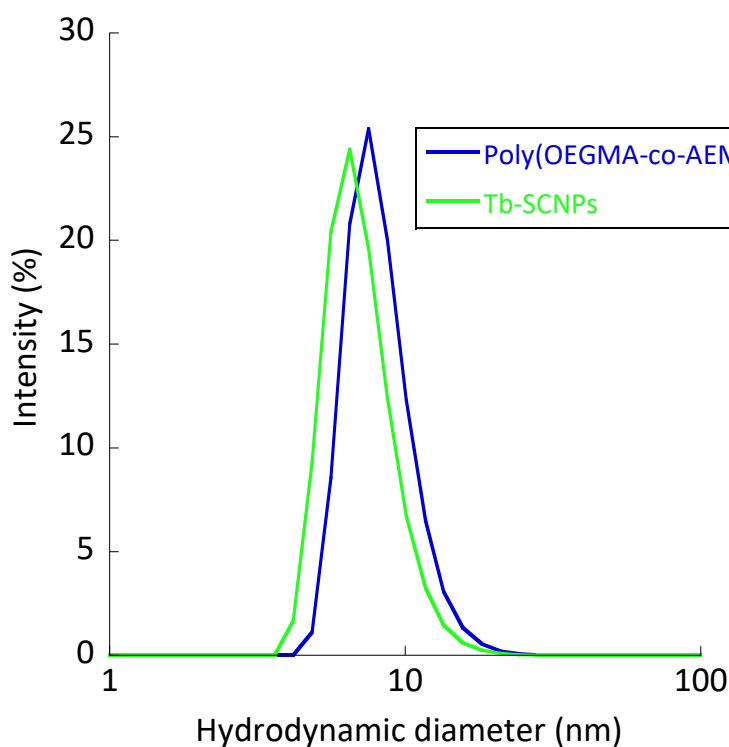


**Figure 17.** DLS size distribution of the precursor, poly(OEGMA-co-AEMA), and the Tb-SCNPs.

The Tb-based SCNPs were visualized as greenish fluorescent nanomaterials under UV light irradiation ( $\lambda_{\text{exc}} = 254 \text{ nm}$ ) in a range of pH between 7.5 and 9 (see Figure 18). Under strong acidic conditions the fluorescence disappeared due to the disruption of Tb<sup>3+</sup>/beta-ketoester complexes, whereas under high basic pH a decrease in fluorescence was noted, as a consequence of aggregation of the Tb-SCNPs. In this way, the bright

3. Lanthanide-based Single-Chain Nanoparticles as “Visual” Pass/Fail Sensors of Maximum Permissible Concentration of Cu<sup>2+</sup> Ions in Drinking Water

green glow of the Tb-SCNPs under UV irradiation was clearly visible in Figure 19, indicating that they could be used in sensing within a pH range of 7.5-9.

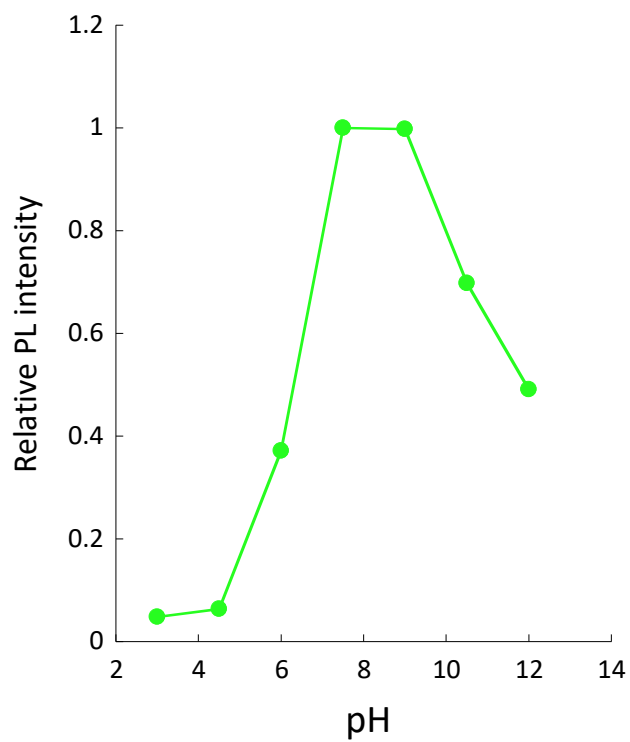


**Figure 18.** Relative PL intensity vs. pH for Tb-SCNPs.

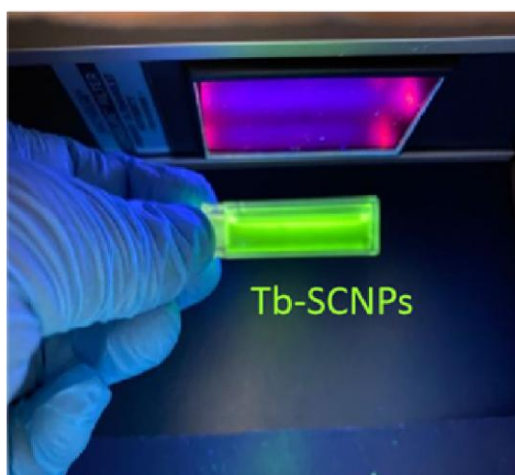


**Figure 19.** Illustration of the greenish fluorescent Tb-SCNPs under UV light irradiation ( $\lambda_{\text{exc}} = 254$  nm)

Shown in Figure 20 is the "Stokes shift" ( $\Delta\lambda$ ). This is how the wavelength contrast between the peaks of the absorbance and emission spectra are defined. For fluorescent materials, this is an all-important shift because the larger it is, the more energy is lost from light absorption to emission and the less emitted light will be re-absorbed. As a result, fluorescence efficiency is increased. What you are looking at is a peak for absorbance and a sharper peak for emission. The Stokes shift is obviously the difference in wavelength between those two peaks: 302 nm.

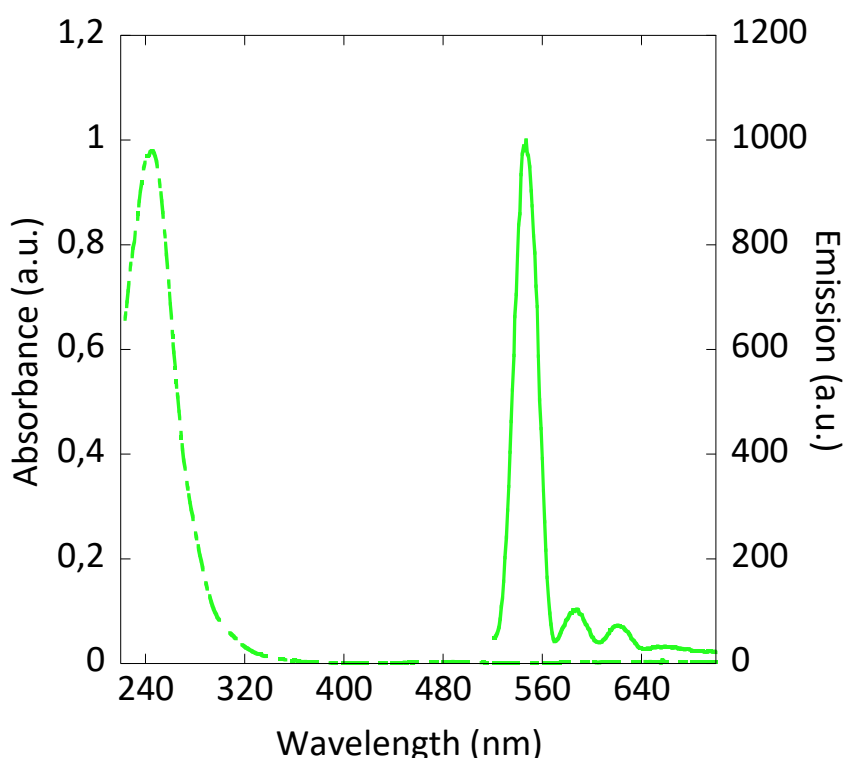


**Figure 20.** Absorbance (dotted) vs emission (continuous) and Stokes shift ( $\Delta\lambda$ ) of Tb-SCNPs.

Tb-SCNP fluorescence in 3D and 2D excitation-emission landscapes is shown in Figure 21 and 22. 3D fluorescence analysis (Figure 21) offers an intuitive presentation. Emission intensities are shown as peaks and interpretation through one height is possible at the different excitation wavelengths. A 2D contour plot (Figure 22) provides a correlated projection on a plane and simplifies the identification of the wavelengths where Tb-SCNPs display peak fluorescence. These visualization tools are essential for the

3. Lanthanide-based Single-Chain Nanoparticles as “Visual” Pass/Fail Sensors of Maximum Permissible Concentration of Cu<sup>2+</sup> Ions in Drinking Water

identification of the excitation-emission pair most suitable for Tb-SCNPs’ analytical applications.

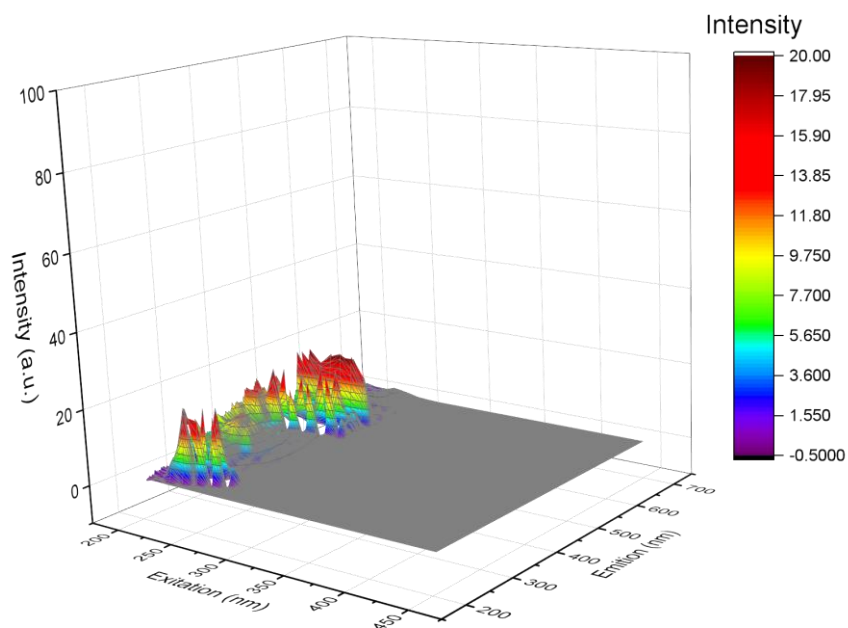


**Figure 21.** 3D study of excitation vs. emission for Tb-SCNPs.

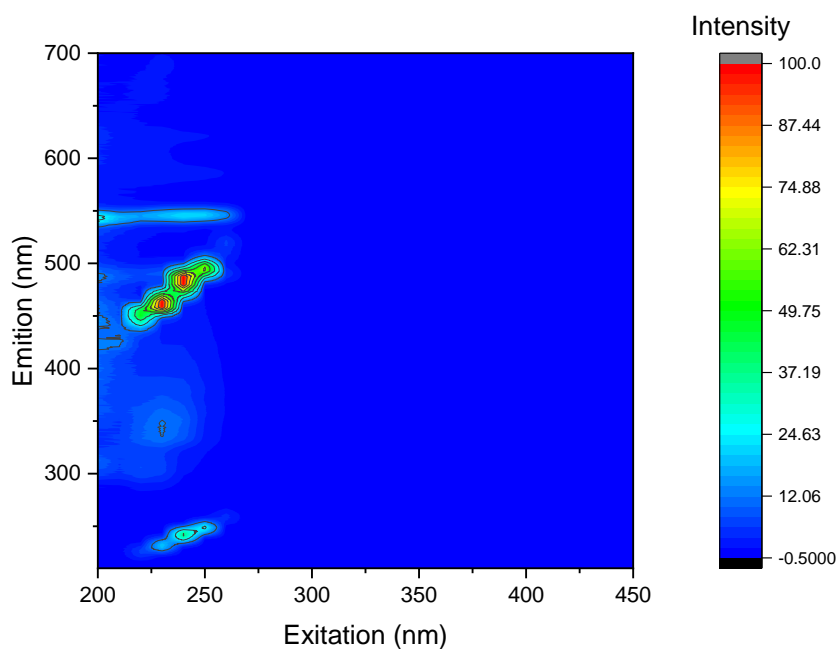


**Figure 22.** 2D study of excitation vs. emission for Tb-SCNPs.

### 3. Lanthanide-based Single-Chain Nanoparticles as “Visual” Pass/Fail Sensors of Maximum Permissible Concentration of Cu<sup>2+</sup> Ions in Drinking Water

As in the case of Tb-SCNPs, the stability results closely aligned with the previous findings. The study focused on the fluorescence intensity of Tb-SCNPs at intervals of 10 minutes, 1 hour, 1 day, and 1 month to assess the nanoparticles' stability. The nearly identical curves from both sets of experiments indicate that the Tb-SCNPs consistently maintain their fluorescence intensity over the examined period (see Figure 23).

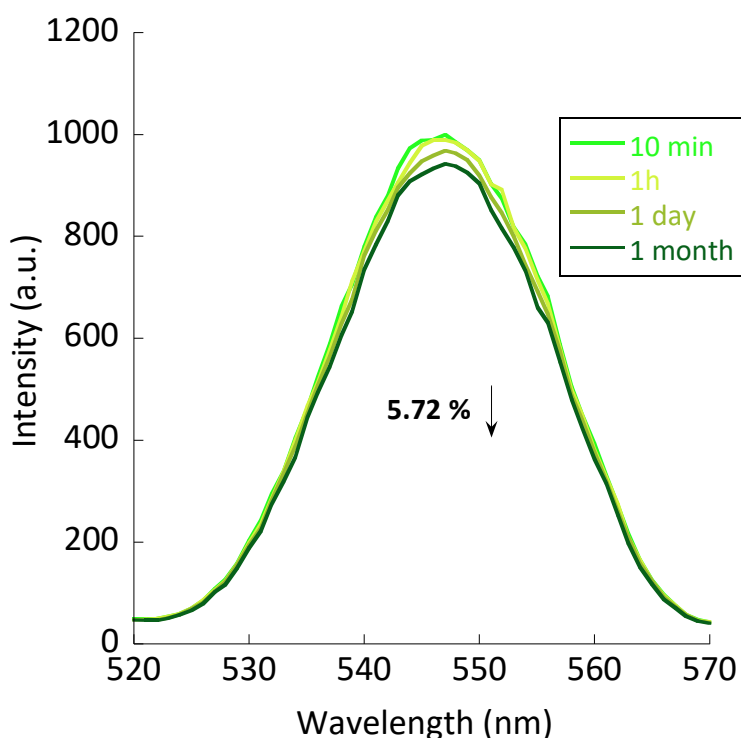


**Figure 23.** Stability of the fluorescence intensity over time for Tb-SCNPs.

The pH adjustment coral test is shown in Figure 24, which demonstrates the variation of the photoluminescence (PL) intensity of Tb-SCNPs with pH alterations between neutral (pH 7.5) and acidic (pH 4) environments. The marked distinctions in PL intensity as a function of pH show the pH-dependency of the nanoparticles' fluorescence. Their fluorescence intensity is far greater at pH 7.5 than at pH 4, where a striking reduction in fluorescence is evident. In addition, as shown in Figure 24, Tb-SCNPs endure 3-4 cycles of pH alterations until their fluorescence entirely disappears.

3. Lanthanide-based Single-Chain Nanoparticles as “Visual” Pass/Fail Sensors of Maximum Permissible Concentration of Cu<sup>2+</sup> Ions in Drinking Water

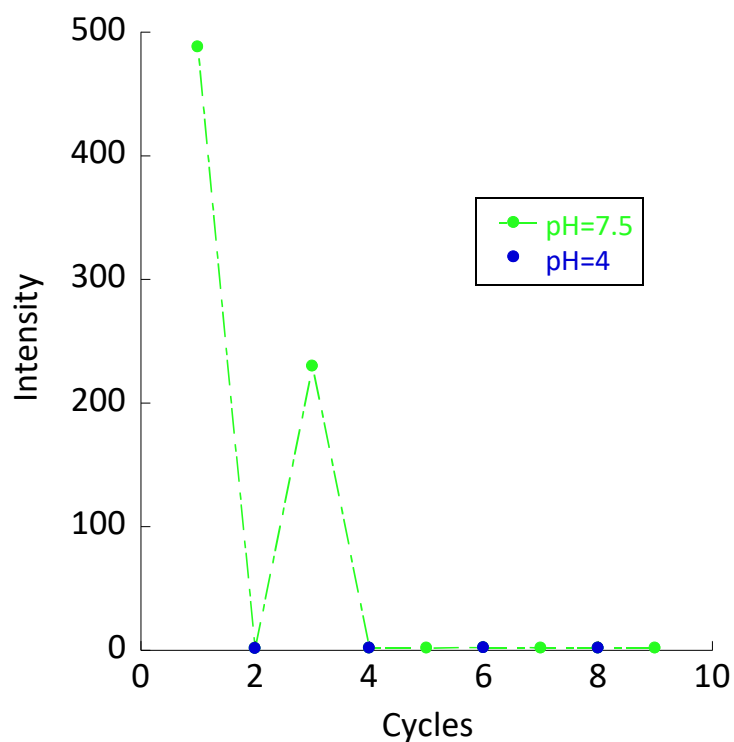


**Figure 24.** Evolution of the PL intensity of Tb-SCNPs upon consecutive pH changes between 7.5 and 4.

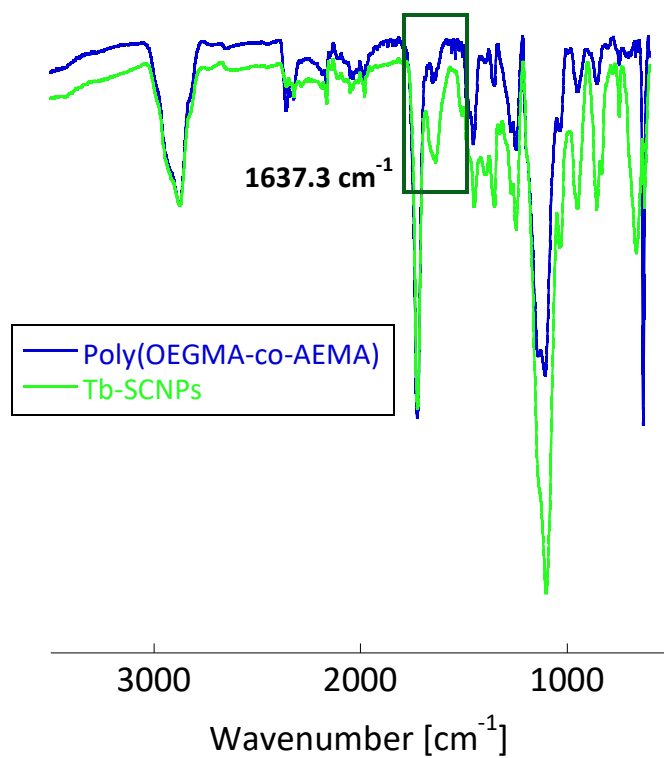


**Figure 25.** FTIR spectra of poly(OEGMA-co-AEMA) (blue colour) and Tb-SCNPs (green colour).

3. Lanthanide-based Single-Chain Nanoparticles as “Visual” Pass/Fail Sensors of Maximum Permissible Concentration of Cu<sup>2+</sup> Ions in Drinking Water

FTIR spectroscopy provided further evidence of the presence of Tb<sup>3+</sup>/beta-ketoester complexes in Tb-SCNPs. As illustrated in Figure 25, a new band located at 1637.3 cm<sup>-1</sup> indeed appeared in the FTIR spectrum of the Tb-SCNPs, which could be assigned to the stretching vibration of the enol tautomer of the beta-ketoester groups bonded to Tb<sup>3+</sup>. PL spectra of Tb-SCNPs in water in the presence of increasing amounts of Cu<sup>2+</sup> ions ( $\lambda_{\text{exc}} = 254 \text{ nm}$ ) are given in Figure 26. A clear green-to-transparent colour change under UV light ( $\lambda_{\text{exc}} = 254 \text{ nm}$ ) was thus observed by the naked-eye, on passing from [Cu<sup>2+</sup>]  $\leq 27.5 \mu\text{M}$  to [Cu<sup>2+</sup>] = 30  $\mu\text{M}$  or above (see Figure 27).

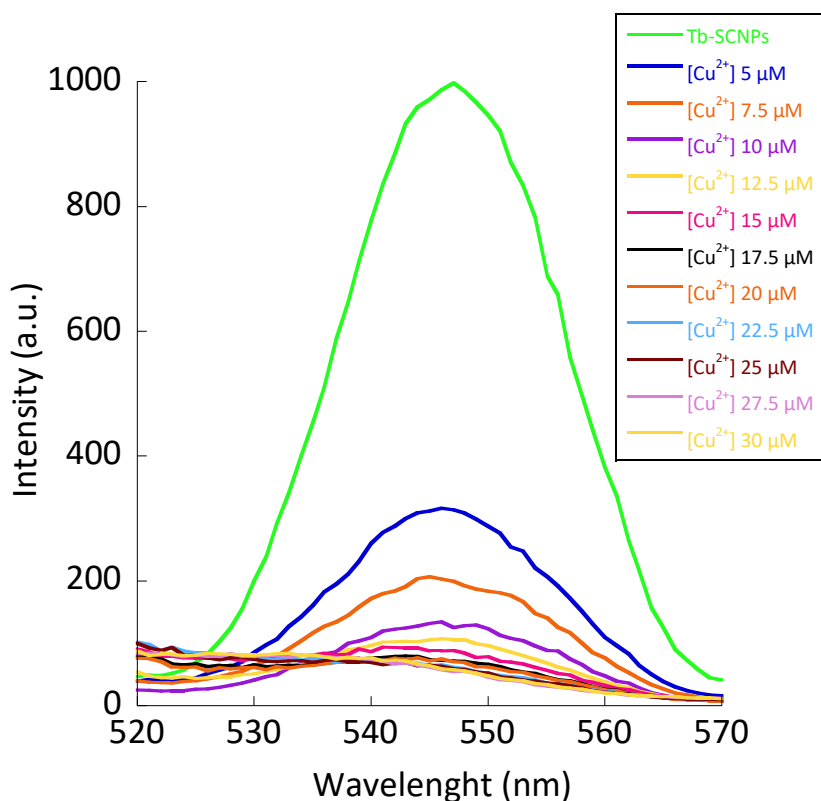


**Figure 26.** PL spectra of Tb-SCNPs in water in the presence of increasing amounts of Cu<sup>2+</sup> ions.

3. Lanthanide-based Single-Chain Nanoparticles as “Visual” Pass/Fail Sensors of Maximum Permissible Concentration of Cu<sup>2+</sup> Ions in Drinking Water



**Figure 17.** demonstration of the utility of Tb-SCNPs as “visual” pass/fail sensors of m.p.c. of Cu<sup>2+</sup> ions in water according to the WHO criterion (i: 2.5 μM, ii: 5 μM, iii: 15 μM, iv: 22.5 μM, v: 25 μM, vi: 27.5 μM and vii: 30 μM).

In other words, Tb-SCNPs proved very useful as “visual” pass/fail sensors of m.p.c. of Cu<sup>2+</sup> ions in water, according to the WHO criterion ( $m.p.c.(Cu^{2+})_{WHO} = 30 \mu M$ ).<sup>9</sup> Analysis of the data in Figure 28 using the Stern-Volmer equation provided  $K_{SV} = 8.2 \times 10^5 M^{-1}$  and  $R^2 = 0.98$ . The higher value of  $K_{SV}$  for Tb-SCNPs relatively to Eu-SCNPs indicates a strong sensing ability of Tb-SCNPs when compared to Eu-SCNPs. Moreover, Tb-based SCNPs display high selectivity for Cu<sup>2+</sup> ions against a variety of other metal ions (Figure 29 and 30).

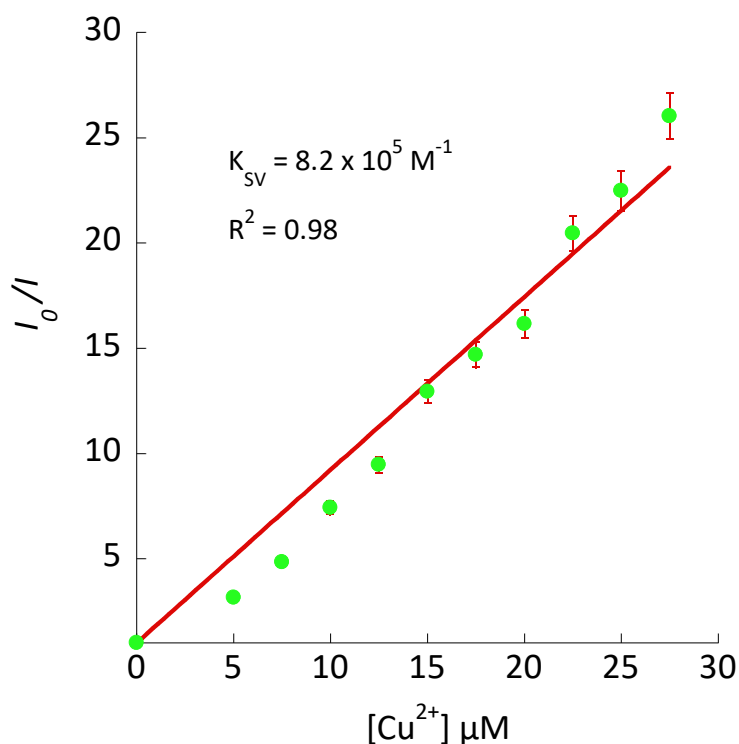


**Figure 28.** Stern-Volmer plot of Tb-SCNPs (error bars estimated from triple measurements).

3. Lanthanide-based Single-Chain Nanoparticles as “Visual” Pass/Fail Sensors of Maximum Permissible Concentration of Cu<sup>2+</sup> Ions in Drinking Water

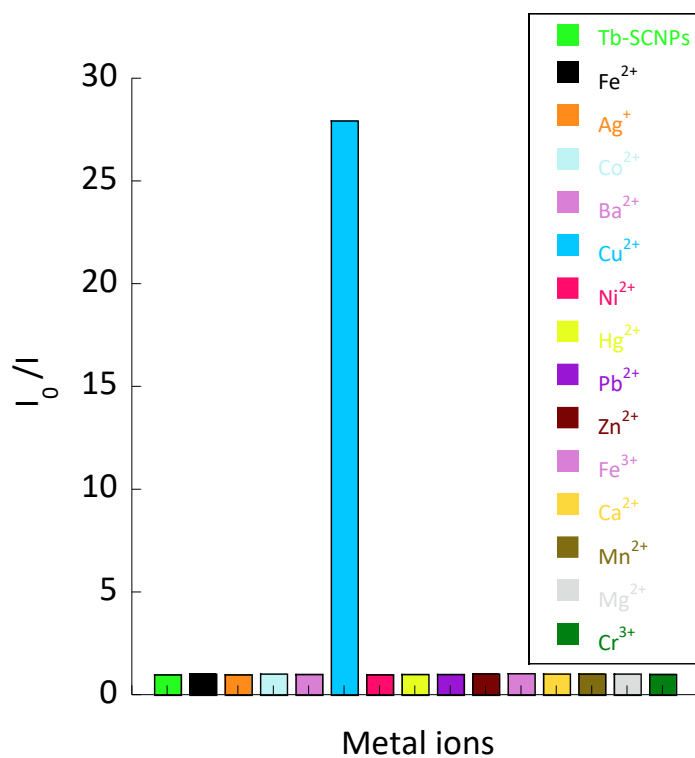


**Figure 29.** Selectivity of Tb-SCNPs for Cu<sup>2+</sup> ions against other metal ions.

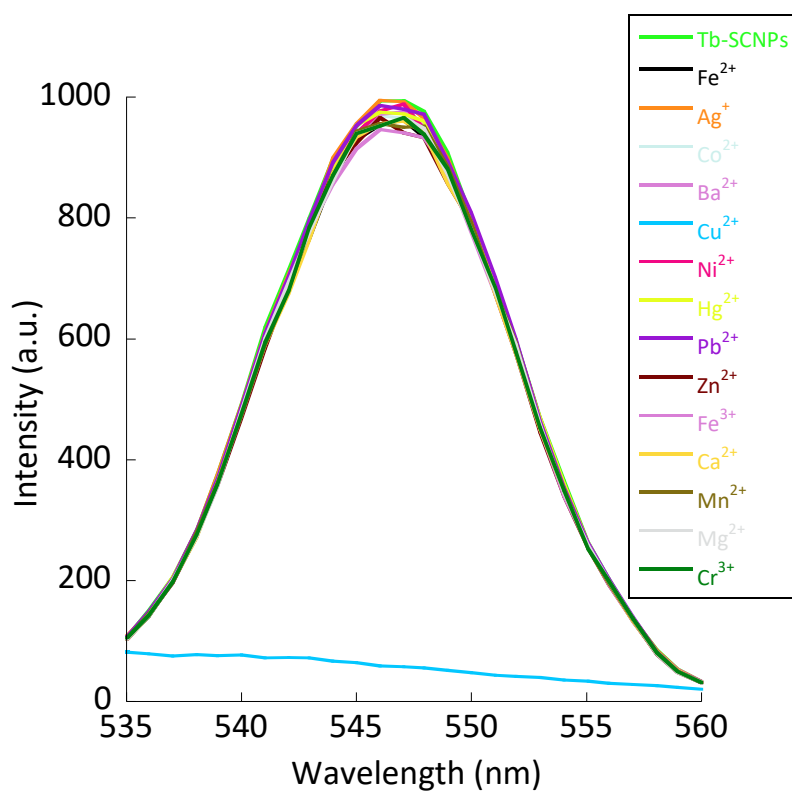


**Figure 30.** PL intensity of Tb-SCNPs in the presence of different metal ions at a concentration of 30 μM.

### 3.4.3. Dy-SCNPs as m.p.c.(Cu<sup>2+</sup>) “visual” pass/fail sensors

Dy-SCNPs synthesized via complexation of Dy<sup>3+</sup> ions in solution by beta-ketoester functional groups of poly(OEGMA-co-AEMA) showed an average hydrodynamic diameter of 7.6 nm, a value smaller than that of the poly(OEGMA-co-AEMA) precursor (Figure 31).

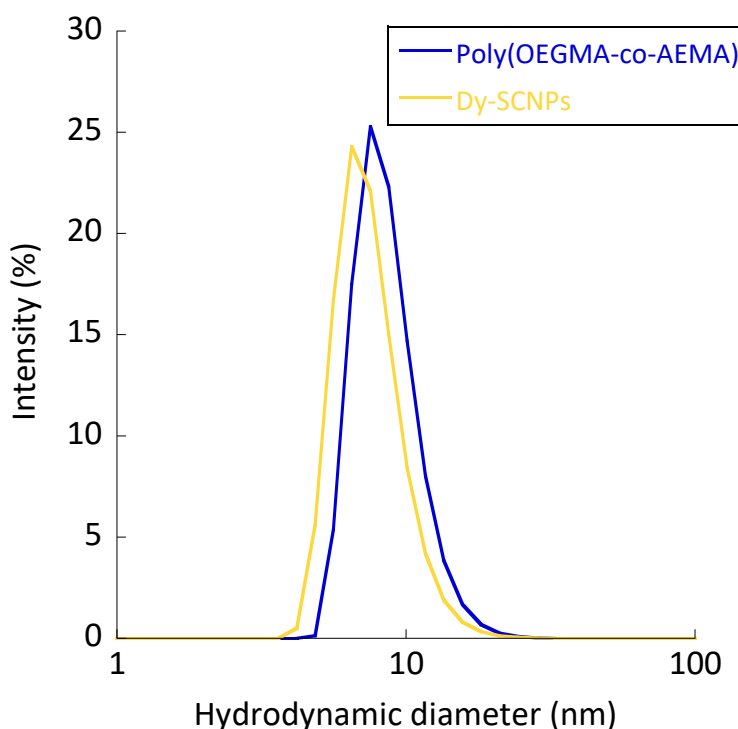


**Figure 31.** DLS size distribution of the precursor, poly(OEGMA-co-AEMA) and the Dy-SCNPs. Dy-SCNPs displayed yellowish fluorescence under UV light irradiation ( $\lambda_{exc} = 254$  nm) in a pH range between 7.5 and 9. Similar to the case of Eu-SCNPs and Tb-SCNPs, the fluorescence of Dy-based SCNPs could be switched-off at very low pH, owing to rupture of Dy<sup>3+</sup>/beta-ketoester complexes or high pH (because of the appearance of aggregation and precipitation phenomena). Dy-based SCNPs were found to display yellowish fluorescence by the naked eye under UV light irradiation at  $\lambda_{exc} = 254$  nm (Figure 32 and 33).

3. Lanthanide-based Single-Chain Nanoparticles as “Visual” Pass/Fail Sensors of Maximum Permissible Concentration of Cu<sup>2+</sup> Ions in Drinking Water

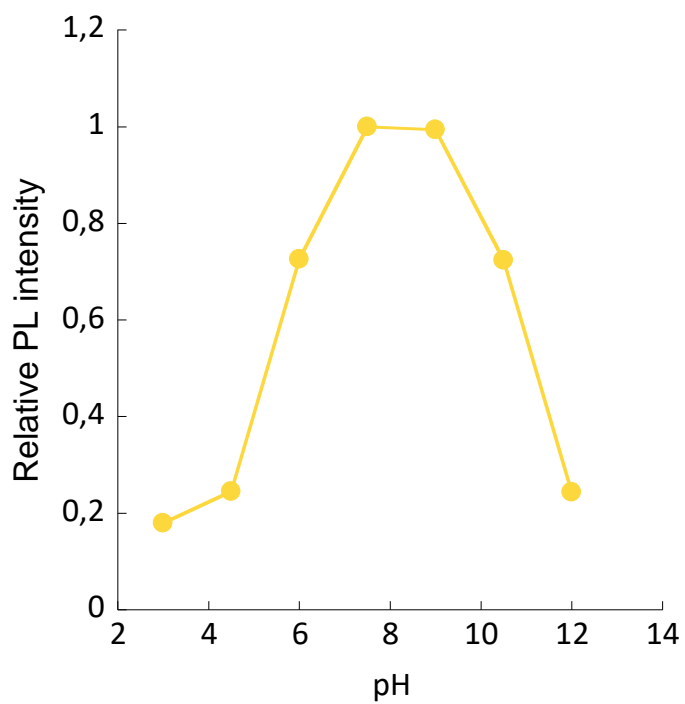
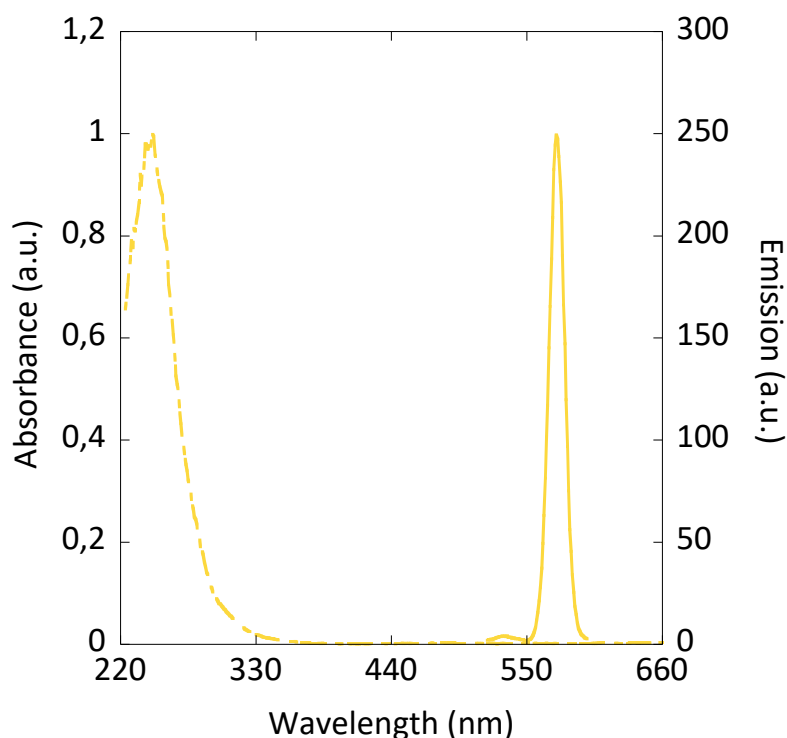


**Figure 32.** Relative PL intensity vs. pH for Dy-SCNPs.



**Figure 33.** Illustration of the yellowish fluorescent Dy-SCNPs under UV light irradiation ( $\lambda_{exc} = 254$  nm) .

3. Lanthanide-based Single-Chain Nanoparticles as "Visual" Pass/Fail Sensors of Maximum Permissible Concentration of Cu<sup>2+</sup> Ions in Drinking Water



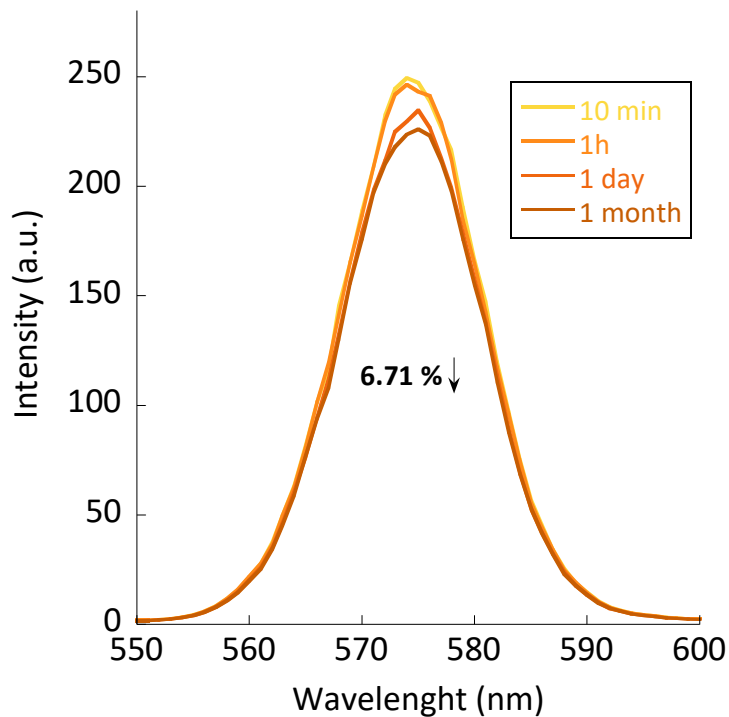
**Figure 34.** Absorbance (dotted) vs emission (continuous) and Stokes shift ( $\Delta\lambda$ ) of Dy-SCNPs.

Figure 34 shows a parameter labeled as "Stokes shift" ( $\Delta\lambda$ ), which is typically the difference in wavelength between the peaks of the absorbance and emission spectra. The Stokes shift is an important feature in fluorescent materials as it provides information about the energy loss between the absorption and emission of light. In practical terms, a larger Stokes shift is often advantageous because it minimizes the reabsorption of emitted light, improving the efficiency of fluorescence. Two distinct peaks can be observed, one related to absorbance and another sharper peak for emission. The Stokes shift would be the wavelength difference between these two peaks: 329 nm.

Fluorescence intensity of Eu-SCNPs over time, specifically at intervals of 10 minutes, 1 hour, 1 day, and 1 month was studied to know the stability of nanoparticles (Figure 35). The overlapping curves suggest that the Eu-SCNPs maintain their fluorescence intensity quite well over the period observed. The minimal change in peak height over these different time points indicates that the Eu-SCNPs are chemically stable and do not

### 3. Lanthanide-based Single-Chain Nanoparticles as “Visual” Pass/Fail Sensors of Maximum Permissible Concentration of Cu<sup>2+</sup> Ions in Drinking Water

undergo significant degradation or quenching that would otherwise affect their fluorescence.



**Figure 35.** Stability of the fluorescence intensity over time for Dy-SCNPs.

The pH adjustment coral test is shown in Figure 36, which demonstrates the variation of the photoluminescence (PL) intensity of Eu-SCNPs with pH alterations between neutral (pH 7.5) and acidic (pH 4) environments. The marked distinctions in PL intensity as a function of pH show the pH-dependency of the nanoparticles' fluorescence. Their fluorescence intensity is far greater at pH 7.5 than at pH 4, where a striking reduction in fluorescence is evident. In addition, as shown in Figure 36, Eu-SCNPs endure 3-4 cycles of pH alterations until their fluorescence entirely disappears.

3. Lanthanide-based Single-Chain Nanoparticles as “Visual” Pass/Fail Sensors of Maximum Permissible Concentration of Cu<sup>2+</sup> Ions in Drinking Water

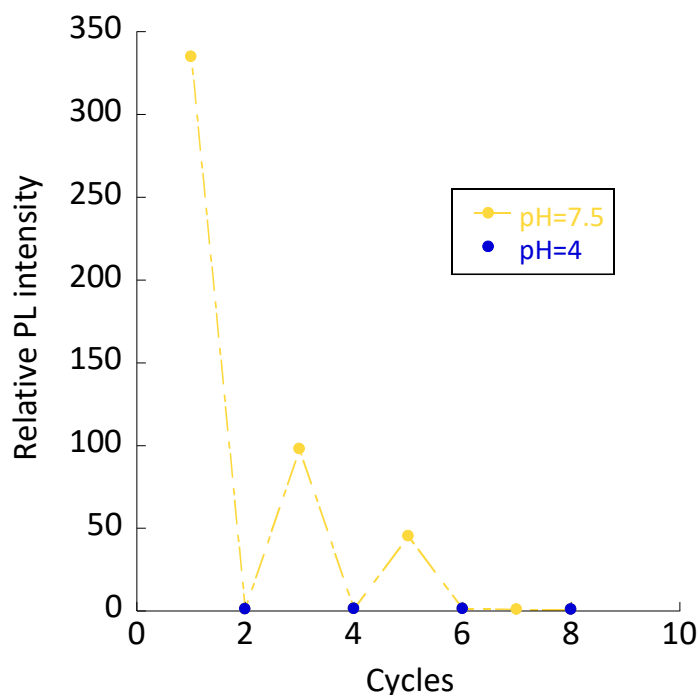


**Figure 36.** Evolution of the PL intensity of Dy-SCNPs upon consecutive pH changes between 7.5 and 4.

In the FTIR spectrum of the Dy-based SCNPs, the stretching vibration of the enol tautomer of the beta-ketoester groups bonded to Dy<sup>3+</sup> was observed at 1642.1 cm<sup>-1</sup>, which could be assigned to the stretching vibration of the enol tautomer of the betaketoester groups bonded to Dy<sup>3+</sup> (Figure 37).

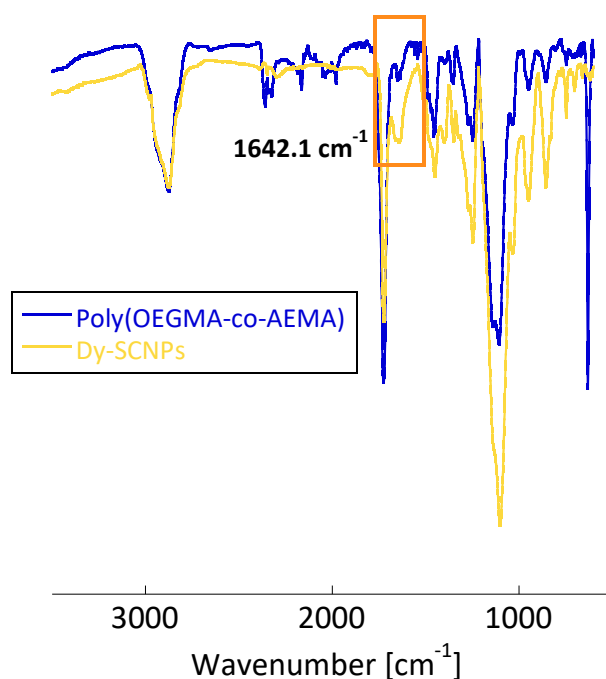


**Figure 37.** FTIR spectra of poly(OEGMA-co-AEMA) (blue colour) and Dy-SCNPs (yellow colour)

3. Lanthanide-based Single-Chain Nanoparticles as “Visual” Pass/Fail Sensors of Maximum Permissible Concentration of Cu<sup>2+</sup> Ions in Drinking Water

Dy-SCNPs show a yellow-to-transparent color transition under UV light irradiation at ca. 15  $\mu\text{M}$  of Cu<sup>2+</sup> ions (Figure 38) -very close to the US-EPA criterion (m.p.c.(Cu<sup>2+</sup>)<sub>EPA</sub> = 20  $\mu\text{M}$ )- making these Dy-based SCNPs practical “visual” pass/fail sensors of m.p.c. of Cu<sup>2+</sup> ions in water according to the EPA regulation.

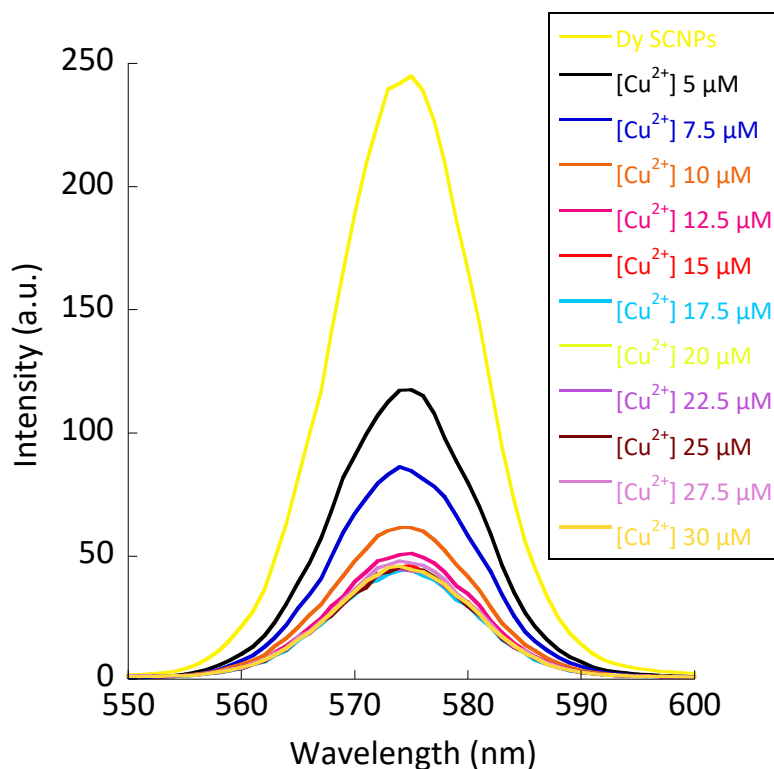


**Figure 38.** PL spectra of Dy-SCNPs in water in the presence of increasing amounts of Cu<sup>2+</sup> ions.

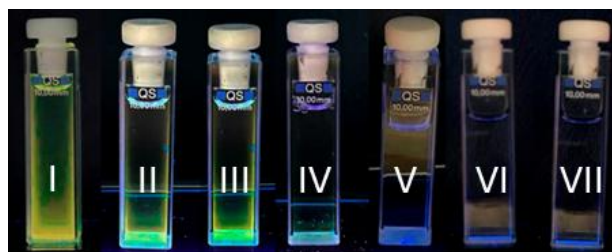


**Figure 39.** Demonstration of the utility of Dy-SCNPs as “visual” pass/fail sensors of m.p.c. of Cu<sup>2+</sup> ions in water according to the EPA criterion (i: 1  $\mu\text{M}$ , ii: 2.5  $\mu\text{M}$ , iii: 10  $\mu\text{M}$ , iv: 15  $\mu\text{M}$ , v: 20  $\mu\text{M}$ , and vi: 30  $\mu\text{M}$ ),

3. Lanthanide-based Single-Chain Nanoparticles as “Visual” Pass/Fail Sensors of Maximum Permissible Concentration of Cu<sup>2+</sup> Ions in Drinking Water

A Stern-Volmer plot for Dy-SCNPs provided  $K_{SV} = 2.9 \times 10^5 \text{ M}^{-1}$  and  $R^2 = 0.99$  (see Figure 40). Similarly, to Eu-based and Tb-based SCNPs, Dy-based SCNPs proved selective for Cu<sup>2+</sup> ions against other metal ions in solution (see Figure 41 and 42).

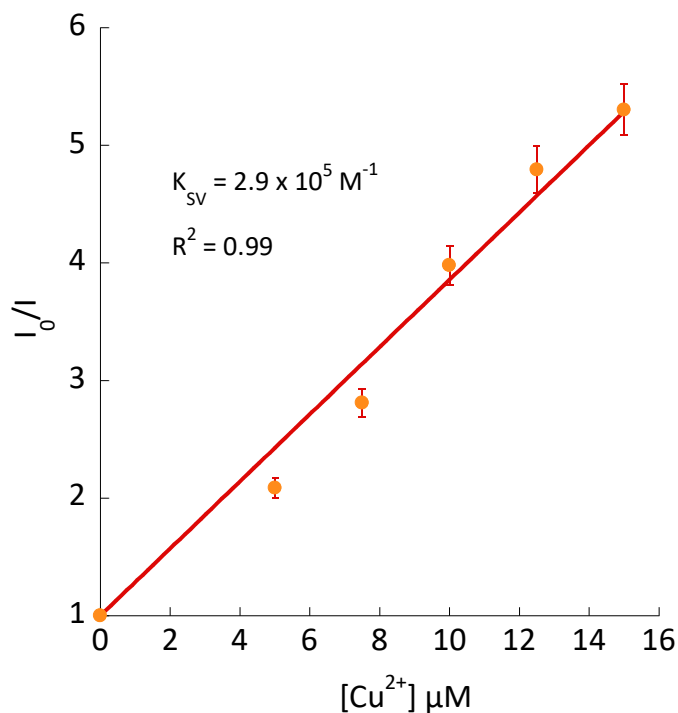


Figure 40. Stern-Volmer plot of Dy-SCNPs (error bars estimated from triple measurements)

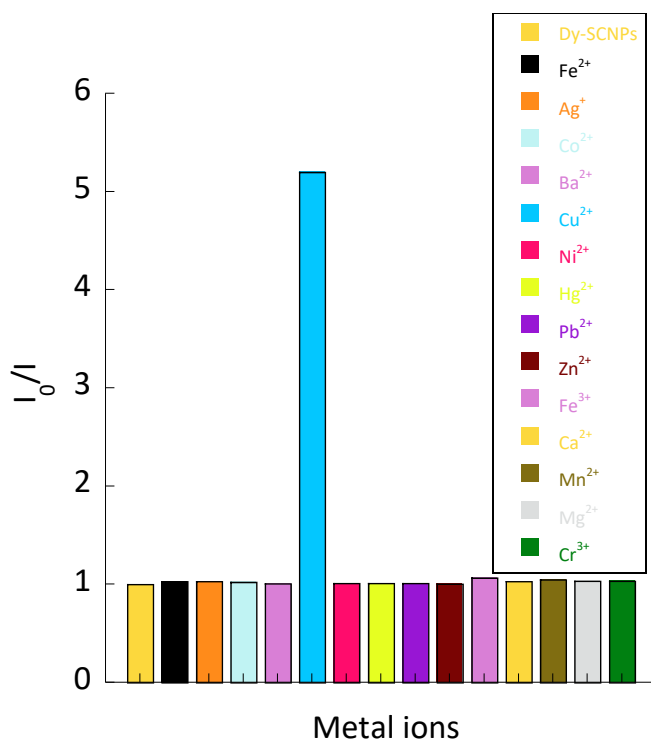
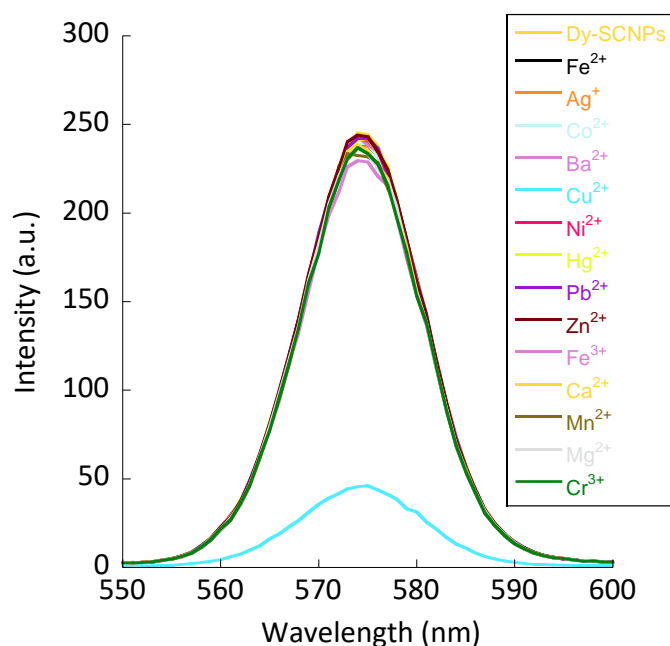


Figure 41. Selectivity of Dy-SCNPs for Cu<sup>2+</sup> ions against other metal ions.

### 3. Lanthanide-based Single-Chain Nanoparticles as “Visual” Pass/Fail Sensors of Maximum Permissible Concentration of Cu<sup>2+</sup> Ions in Drinking Water



**Figure 42.** PL intensity of Dy-SCNPs in the presence of different metal ions at a concentration of 15  $\mu\text{M}$ .

### 3.5. Conclusions

We introduced a new generation of m.p.c.(Cu<sup>2+</sup>) “visual” pass/fail sensors based on water-soluble lanthanide (Eu, Tb, or Dy)-containing SCNPs of sub-10 nm size range. Under UV light irradiation at  $\lambda_{\text{exc}} = 254 \text{ nm}$ , Eu-SCNPs and Tb-SCNPs showed a naked-eye red-to-transparent and green-to-transparent colour transitions, respectively, near [Cu<sup>2+</sup>] = 30  $\mu\text{M}$  in water at pH = 7.5. As for Dy-based SCNPs, they displayed a yellow to transparent colour change at ca. [Cu<sup>2+</sup>] = 15  $\mu\text{M}$ . The characteristic FTIR stretching vibration of the enol tautomer of the beta-ketoester groups bonded to Eu<sup>3+</sup>, Tb<sup>3+</sup> and Dy<sup>3+</sup> ions in Eu-SCNPs, Tb-SCNPs and Dy-SCNPs was located at 1632.4, 1637.3 and 1642.1  $\text{cm}^{-1}$ , respectively. These “visual” pass/fail sensors show high selectivity towards Cu<sup>2+</sup> ions against a variety of other metal ions (Fe<sup>2+</sup>, Ag<sup>+</sup>, Co<sup>2+</sup>, Ba<sup>2+</sup>, Ni<sup>2+</sup>, Hg<sup>2+</sup>, Pb<sup>2+</sup>, Zn<sup>2+</sup>, Fe<sup>3+</sup>, Ca<sup>2+</sup>, Mn<sup>2+</sup>, Mg<sup>2+</sup> and Cr<sup>3+</sup>). Consequently, Eu-SCNPs and Tb-SCNPs can be used as “visual” pass/fail sensors of m.p.c. of Cu<sup>2+</sup> ions in water according to the WHO criterion (m.p.c.(Cu<sup>2+</sup>)<sub>WHO</sub> = 30  $\mu\text{M}$ ). Complementary, Dy-SCNPs can be useful as “visual” pass/fail sensors of m.p.c. of Cu<sup>2+</sup> ions in water according to the EPA regulation (m.p.c.(Cu<sup>2+</sup>)<sub>EPA</sub> = 20  $\mu\text{M}$ ).

### 3.6. References

1. R. A. Muttkowski, Copper in Animals and Plants, *Science*, 1921, 53, 453-454.
2. W. Kaim and J. Rall, J. Copper - A “Modern” Bioelement, *Angew. Chem. Int. Ed.*, 1996, 35, 43-60.
3. B.-E. Kim, T. Nevitt and D. J. Thiele, Mechanisms for copper acquisition, distribution and regulation, *Nat. Chem. Biol.*, 2008, 4, 176-185.
4. T. R. Halfdanarson, N. Kumar, C. Y. Li, R. L. Phyllyk and W. J. Hogan, Hematological manifestations of copper deficiency: a retrospective review, *Eur. J. Haematol.*, 2008, 80, 523-531.
5. M. C. Linder, Copper homeostasis in mammals, with emphasis on secretion and excretion. A review, *Int. J. Mol. Sci.*, 2020, 21, 4932.
6. F. Pizarro, M. Olivares, R. Uauy, Contreras, P. Contreras, A. Rebelo and V. Gidi, Acute gastrointestinal effects of graded levels of copper in drinking water, *Environ. Health Perspect.*, 1999, 107, 117-121.
7. G. Brewer, Copper toxicity in the general population, *Clin. Neurophysiol.*, 2010, 121, 459-460.
8. P. G. Georgopoulos, A. Roy, M. J. Yonone-Lioy, R. E. Opiekun and P. J. Lioy, Environmental copper: its dynamics and human exposure issues, *J. Toxicol. Env. Heal. B Crit Rev.* 2001, 4, 341394.
9. Copper in Drinking-water, World Health Organization (WHO), 2004.
10. Copper Facts, US Environmental Protection Agency (EPA), 2008.
11. Single-Chain Polymer Nanoparticles: Synthesis, Characterization, Simulations and Applications, ed. J. A. Pomposo, Wiley-VCH, Weinheim, 2017.
12. A. Latorre-Sánchez and J. A. Pomposo, Recent bioinspired applications of single-chain nanoparticles, *Polym. Int.*, 2016, 65, 855-860.
13. M. A. J. Gillissen, I. K. Voets, E. W. Meijer and A. R. A. Palmans, Single chain polymeric nanoparticles as compartmentalised sensors for metal ions, *Polym. Chem.*, 2012, 3, 3166-3174.

3. Lanthanide-based Single-Chain Nanoparticles as “Visual” Pass/Fail Sensors of Maximum Permissible Concentration of Cu<sup>2+</sup> Ions in Drinking Water
14. J. De-La-Cuesta, E. Verde-Sesto, A. Arbe and J. A. Pomposo, Self-Reporting of Folding and Aggregation by Orthogonal Hantzsch Luminophores Within a Single Polymer Chain, *Angew. Chem. Int. Ed.*, 2021, 60, 3534-3539.
15. C. C. Cheng, D. J. Lee, Z. S. Liao and J. J. Huang, Stimuliresponsive single-chain polymeric nanoparticles towards the development of efficient drug delivery systems, *Polym. Chem.*, 2016, 7, 6164-6169.
16. A. Latorre-Sánchez and J. A. Pomposo, A simple, fast and highly sensitive colorimetric detection of zein in aqueous ethanol via zein-pyridine-gold interactions, *Chem. Commun.*, 2015, 51, 15736-15738.
17. N. M. Hamelmann, J. W. D. Paats, Y. Avalos-Padilla, E. Lantero, I. Siden-Kiamos, L. Spanos, X. Fernandez-Busquets and J. M. J. Paulusse, Single-Chain Polymer Nanoparticles Targeting the Ookinete Stage of Malaria Parasites, *ACS Infect. Dis.*, 2023, 9, 56-64.
18. S. Garmendia, S. B. Lawrenson, M. C. Arno, R. K. O'Reilly, D. Taton and A. P. Dove, Catalytically Active N-Heterocyclic Carbene Release from Single-Chain Nanoparticles Following a Thermolysis-Driven Unfolding Strategy, *Macromol. Rapid Commun.*, 2019, 40, 1900071.
19. T. Gunnlaugsson, J. P. Leonard, K. Sénéchal and A. J. Harte, Eu(III)–cyclen–phen conjugate as a luminescent copper sensor: the formation of mixed polymetallic macrocyclic complexes in water, *Chem. Commun.*, 2004, 782-783.
20. A. Nonat, A. J. Harte, K. Senechal-David, J. P. Leonard and T. Gunnlaugsson, Luminescent sensing and formation of mixed f–d metal ion complexes between a Eu(III)cyclen-phen conjugate and Cu(II), Fe(II), and Co(II) in buffered aqueous solution, *Dalton Trans.*, 2009, 4703-4711.
21. Z. Ekmekci, Highly selective fluorescence ‘turn-off’ sensors for Cu<sup>2+</sup> in aqueous environments, *Tetrahedron Lett.*, 2015, 56, 1878-1881.
22. L. M. Aroua, R. Ali, A. E. A. E. Albadri, S. Messaoudi, F. M. Alminderej and S. M. Saleh, A New, Extremely Sensitive, TurnOff Optical Sensor Utilizing Schiff Base for Fast Detection of Cu(II), *Biosensors*, 2023, 13, 359.

3. Lanthanide-based Single-Chain Nanoparticles as “Visual” Pass/Fail Sensors of Maximum Permissible Concentration of Cu<sup>2+</sup> Ions in Drinking Water

23. B.S. Sankha and R.N. Kapoor, Organic compounds of samarium. II. Reactions of samarium isopropoxide with ethyl acetoacetate, *Can. J. Chem.*, 1966, 44, 1369-1372.
24. N.K. Dutt and S. Rahut, Chemistry of lanthanons-XXIII. The formation constants of the ethyl acetoacetate complexes of rare earth, *J. Inorg. Nucl. Chem.* 1969, 31, 3177-3179.
25. A. M. Mishchenko, E. K. Trunova and A. S. Berezhnytska, Lanthanide Complexes with Allyl Acetoacetate in Mixed Water–Organic Media: Formation, Stability and Bonding, *J. Solution Chem.*, 2015, 44, 2117-2128.
26. O. Stern and M. Volmer, Über die Abklingzeit der Fluoreszenz, *Zeitschrift für Physik*, 1919, 20, 183-188.
27. M. L. Aulsebrook, B. Graham, M. R. Grace and K. L. Tuck, Lanthanide complexes for luminescence-based sensing of low molecular weight analytes, *Coord. Chem. Rev.*, 2018, 375, 191220.
28. K. Szyszka, S. Targońska, A. Lewińska, A. Watras and R. J. Wiglusz, Quenching of the Eu<sup>3+</sup> Luminescence by Cu<sup>2+</sup> Ions in the Nanosized Hydroxyapatite Designed for Future BioDetection, *Nanomaterials*, 2021, 11, 464.



#### **4. Gold Nanoclusters Synthesized within Single-Chain Nanoparticles as Catalytic Nanoreactors in Water**



## 4.1. Motivation

Metalloenzymes are able to catalyze complex biochemical reactions in cellular (aqueous) media with high efficiency. In recent years, a variety of metal-containing single-chain nanoparticles (SCNPs) have been synthesized as simplified metalloenzymemimetic nano-objects. However, most of the metal-containing SCNPs reported so far contained complexed metal ions but not metal nanoclusters (NCs) with diameter  $< 5$  nm, which could be used as powerful, emerging catalysts. Herein, we report the synthesis of gold nanoclusters (Au-NCs) within SCNPs and the further use of Au-NCs/SCNPs as catalytic nanoreactors in water. We demonstrate that a common motif contained in several drugs (i.e., the aminophenyl–oxazolidinone fragment present in Rivaroxaban, Sutezolid, and Linezolid) can be efficiently prepared in water from a hydrophobic precursor compound by using the Au-NCs/SCNPs as efficient catalytic nanoreactors. In summary, this work paves the way for the synthesis of metal–NCs/SCNPs for advanced catalysis in aqueous media.

## 4.2. Introduction

Metalloenzymes contain metal ions as co-factors for a variety of biochemical reactions that take place in the cellular environment.<sup>1</sup> The precise outer coordination sphere offered by the metalloenzyme is critical for its catalytic activity and substrate selectivity. Hence, metalloenzyme activity is substantially reduced when the polypeptide 3D structure is altered due to, e.g., a severe pH change or heating. Consequently, many attempts have been performed to endow synthetic polymers with metalloenzymemimetic activity, trying to capitalize on the stability of polymers and the efficient catalytic activity of metal ions as co-factors.<sup>2,3</sup> Moreover, the folding of discrete synthetic polymer chains to singlechain nanoparticles (SCNPs) has introduced the additional advantage of the presence of local pockets within which metal ions could find

an appropriate coordination sphere for efficient catalysis.<sup>4–6</sup> Several recent reviews disclose the potential advantage of SCNPs as metalloenzyme-mimetic catalysts.<sup>7–11</sup> However, most of the metal-containing SCNPs reported so far contained complexed metal ions but not entrapped metal nanoclusters (NCs) with diameter < 5 nm, which could be used as powerful, emerging catalysts. Interestingly, a pioneering work by Zhao et al.<sup>12</sup> reported the kinetics of the formation of gold nanoparticles (Au-NPs) using SCNPs decorated with tertiary amines without the involvement of any other additional reductants. In a subsequent work, the CO<sub>2</sub>-responsiveness of these SCNPs was used to produce gas-tunable nanoreactors for Au-NPs synthesis.<sup>13</sup> However, even if the localized surface plasmon resonance (LSRP) band characteristic of Au-NPs was observed by ultraviolet–visible (UV-Vis) spectroscopy, these authors did not investigate the catalytic properties of the resulting Au-NPs/SCNPs.

Metal nanoclusters offer unique advantages over complexed metal ions, including their small size, enhanced stability, and tunable properties for a wide range of applications in fields such as catalysis, biomedicine, energy, and electronics. In this work, we report the synthesis of gold nanoclusters (Au-NCs) with diameter < 5 nm within SCNPs and the further use of Au-NCs/SCNPs as catalytic nanoreactors in water. Gold nanoclusters have recently attracted great interest due to their small size and atomically precise number of atoms per nanocluster that offer interesting possibilities for a range of applications, including cancer phototherapy<sup>14</sup>, bioimaging<sup>15</sup>, sensing<sup>16</sup>, and catalysis<sup>17</sup>. Ligand protected Au-NCs with a size between 2 and 5 nm are often used in catalysis<sup>18</sup>. The first use of Au-NCs for catalysis was reported by Haruta et al.<sup>19</sup> for the oxidation of CO even at very low temperatures (–70 °C). Since then, the catalytic properties of naked and ligand-protected Au-NCs have been investigated in a wide number of chemical transformations.<sup>20–23</sup> When compared to Au-NPs, the larger surface-to-volume ratio of Au-NCs explains their enhanced reactivity and superior catalytic properties. Moreover, the chemical inertness of gold nanoclusters compared to other metallic nanoclusters makes them highly stable in various environments and ensures long-term performance and durability in catalysis.<sup>20–23</sup> However, to the best of our knowledge, Au-NCs have not been synthesized within SCNPs, nor have the resulting SCNPs-protected Au-NCs been employed as catalytic nanoreactors yet. Herein, we use an amphiphilic random

copolymer self-assembled as SCNPs featuring beta-ketoester units as a template to generate and stabilize Au-NCs with diameter < 5 nm. The precise morphology of AuNCs/SCNPs was revealed by transmission electron microscopy (TEM), whereas the hydrodynamic size in water was determined by dynamic light scattering (DLS) measurements. As proof-of-concept experiments of the catalytic activity of AuNCs/SCNPs in water, we illustrate the fast reduction of nitrophenol to aminophenol as well as the conversion of nitrobenzene to aniline with an excellent yield. Finally, we carry out the efficient transformation in water of 3-(4-nitrophenyl)-1,3-oxazolidin-2-one to 3(4-aminophenyl)-1,3-oxazolidin-2-one—a common motif contained in several drugs like Rivaroxaban, Sutezolid, and Linezolid— using the Au-NCs/SCNPs as catalytic nanoreactors.

### 4.3. Materials and Methods

#### 4.3.1. Materials

Oligo(ethylene glycol) methyl ether methacrylate (OEGMA) (average  $M_n \sim 300$  Da), (2-acetoacetoxy)ethyl methacrylate (AEMA) (95%), 2,2-azobis(2-methylpropionitrile) (AIBN) ( $\geq 98\%$ ), triethylamine ( $\text{Et}_3\text{N}$ ) ( $> 99\%$ ), 1,4-dioxane (anhydrous, 99.8%), n-hexane (anhydrous, 95%), ethyl acetate (anhydrous, 99.8%), deuterated dimethyl sulphoxide ( $\text{DMSO-d}_6$ ) (99.9 atom % D), 4-cyano-4-(thiobenzoylthio)pentanoic acid ( $\geq 97\%$ ), 4-nitrophenol ( $\geq 99\%$ ), nitrobenzene ( $\geq 99\%$ ), 3-(4-nitrophenyl)-1,3-oxazolidin-2-one (95%), chloroform ( $\text{CHCl}_3$ ) ( $\geq 99\%$ ), and deuterated chloroform ( $\text{CDCl}_3$ ) (99.8 atom % D) were supplied by Merck (Sigma-Aldrich) (Madrid, Spain). Tetrachloroauric (III) acid trihydrate (99%) was supplied by Thermo Scientific (Eindhoven, The Netherlands). Methanol ( $\text{MeOH}$ , analytical grade) and tetrahydrofuran (THF, GPC grade) were supplied by Scharlau (Barcelona, Spain). Deionized water was obtained from a Thermo Scientific apparatus (Barnstead TII Pure Water System) (Eindhoven, The Netherlands).

#### 4.3.2. Techniques

Size exclusion chromatography (SEC) measurements were conducted at a temperature of  $30^\circ\text{C}$  in an Agilent 1200 system that was equipped with PLgel 5  $\mu\text{m}$  Guard and PLgel

5  $\mu\text{m}$  MIXED-C columns. The measurements employed a triple detection system, which included a differential refractive index detector (Optilab Rex, Wyatt, Toulouse, France), a MALLS detector (MiniDawn Treos, Wyatt, Toulouse, France), and a viscosimetric (VIS) detector (ViscoStar-II, Wyatt, Toulouse, France). The data obtained were analyzed using Wyatt's ASTRA Software (version 6.1). THF was used as eluent with a flow rate of 1 mL/min. For both poly(OEGMA-co-AEMA) and the SCNPs, a value of  $dn/dc = 0.115$  was used.  $^1\text{H}$  Nuclear Magnetic Resonance (NMR) spectra were obtained at room temperature (r.t.) in a Bruker (Madrid, Spain) spectrometer operating at 400 MHz using  $\text{CDCl}_3$  as solvent. Infrared (IR) spectra were recorded at r.t. on a JASCO 3600 (Madrid, Spain) FTIR spectrometer. Dynamic light scattering (DLS) measurements were carried out at r.t. on a Malvern Zetasizer Nano ZS (Cambridge, UK) apparatus. Ultraviolet-visible (UV-Vis) spectra were recorded in an Agilent 8453A (Madrid, Spain) UV-Vis spectrometer with a Peltier thermostatic cell holder T-controller 89096A. Transmission electron microscopy (TEM) experiments were conducted in a TECNAI G220 TWIN (Eindhoven, The Netherlands) high-resolution transmission electron microscope. The measurements were carried out with a 200 kV accelerating voltage, employing low dose conditions.

## 4.4. Procedures

### 4.4.1. Procedure for the Synthesis of Poly(OEGMA-co-AEMA)

OEGMA (1.54 mL, 5.6 mmol), AEMA (0.26 mL, 1.38 mmol), 4-cyano-4-(thiobenzoylthio) pentanoic acid (18.3 mg, 0.065 mmol), and AIBN (2.15 mg, 0.013 mmol) were dissolved in 1,4-dioxane (3 mL), and the resulting mixture was degassed with argon for 15 min. The copolymerization reaction took place at 70 °C for 24 h, yielding poly(OEGMA-co-AEMA) as a pink oil product that was isolated by precipitation in hexane. Subsequently, the copolymer was redissolved in a minimal amount of THF and added to an excess of hexane (twice), followed by solvent removal and further drying at r.t. under vacuum. The content of AEMA units in poly(OEGMA-co-AEMA) was 35 mol%, as determined by  $^1\text{H}$  NMR spectroscopy as shown in Figure 43.

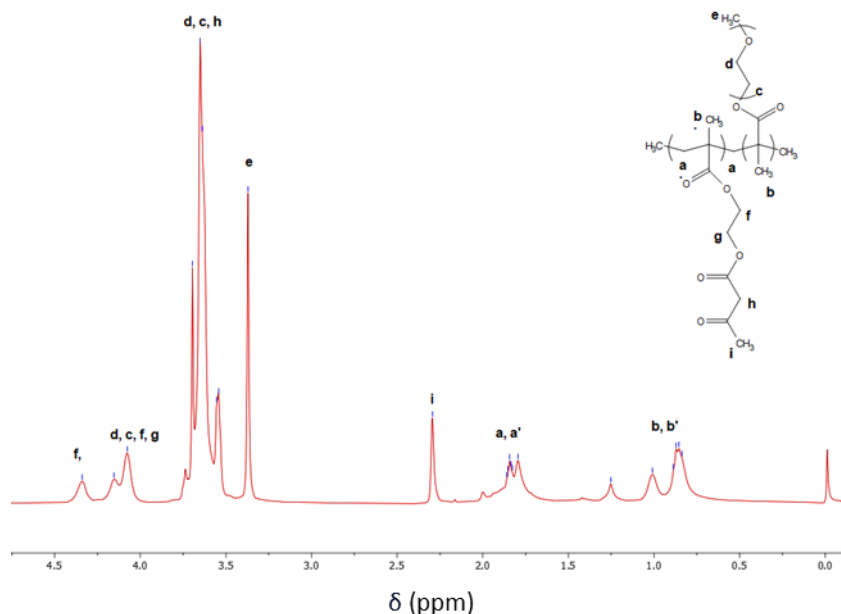


**Figure 43.** <sup>1</sup>H NMR spectrum of poly(OEGMA-co-AEMA).

#### 4.4.2. Procedure for the Synthesis of Gold Nanoclusters (Au-NCs) within Poly(OEGMA-co-AEMA) Single-Chain Nanoparticles (SCNPs)

In a typical reaction, poly(OEGMA-6co-AEMA) (15 mg, 0.03 mmol) and tetrachloroauric (III) acid trihydrate (0.00245 mmol) were dissolved in water (15 mL) under argon at r.t. for 1 h. The reaction was followed by DLS, confirming that there was no significant change in hydrodynamic size of the poly(OEGMA-co-AEMA) SCNPs under such conditions. TEM measurements confirmed the presence of Au-NCs within the SCNPs. Additionally, UV-Vis measurements showed that the Au-NCs synthesized within the SCNPs did not have the localized surface plasmon resonance (LSPR) absorbance signal characteristic of gold nanoparticles (Au-NPs).

#### 4.4.3. Procedure for the Reduction of 4-Nitrophenol Catalyzed by AuNCs/SCNPs

The Au-NC/SCNPs were used as catalyst for the reduction at r.t. of 4-nitrophenol (0.2 mmol) to 4-aminophenol in the presence of NaBH<sub>4</sub> (0.8 mmol). In a typical experiment, a solution of 2 mL of Au-NC/SCNPs aqueous solution (1 mg/mL) was prepared and 18.8

$\mu\text{L}$  of 4-nitrophenol and 30.35 mg of  $\text{NaBH}_4$  were sequentially added under argon into a vial at  $0^\circ\text{C}$ . The 4-nitrophenol reduction reaction was then monitored via UV-Vis spectrophotometry. Absorbance was recorded by taking  $1\ \mu\text{L}$  of crude at a given reaction time, which was then diluted in 2 mL of deionized water. After reaction, 4-aminophenol was purified *via* preparative thin-layer chromatography (TLC) (n-hexane/ethyl acetate 1:1), with a yield of 95%.  $^1\text{H}$  NMR (400 MHz,  $\text{DMSO-d}_6$ , ppm):  $\delta$  4.36 (s, 2H), 6.42–6.46 (m, 4H), 8.34 (s, 1H).

#### **4.4.4. Procedure for the Reduction of Nitrobenzene Catalyzed by AuNCs/SCNPs**

The Au-NC/SCNPs were used as catalysts for the reduction at r.t. of nitrobenzene (0.2 mmol) to aniline in the presence of  $\text{NaBH}_4$  (0.8 mmol). The same procedure described in Section 3.4.3. was followed. Absorbance was recorded by taking  $2\ \mu\text{L}$  of crude at a given reaction time, which was then diluted in 4 mL of deionized water. After reaction, aniline was purified *via* preparative TLC (n-hexane/ethyl acetate 1:1), with a yield of 96%.  $^1\text{H}$  NMR (400 MHz,  $\text{DMSO-d}_6$ , ppm):  $\delta$  3.65 (s, 2H), 6.67–6.70 (m, 2H), 6.73–6.77 (m, 1H), 7.13–7.17 (m, 2H).

#### **4.4.5. Procedure for the Reduction of 3-(4-Nitrophenyl)-1,3-oxazolidin-2-one Catalyzed by Au-NCs/SCNPs**

The Au-NC/SCNPs were used as catalysts for the reduction at r.t. of 3-(4-nitrophenyl)-1,3-oxazolidin-2-one (0.2 mmol) to 3-(4-aminophenyl)-1,3-oxazolidin-2-one in the presence of  $\text{NaBH}_4$  (0.8 mmol). The same procedure described in Section 3.4.3. was followed. Absorbance was recorded by taking  $2\ \mu\text{L}$  of crude at a given reaction time, which was then diluted in 10 mL of deionized water. It is worth noting that due to the heterogenous character of the reaction and to the vigorous generation of molecular hydrogen gas, aliquots for analysis were prepared ensuring only the aqueous phase was taken. The product, 3-(4-aminophenyl)oxazolidin-2-one, was purified *via* preparative TCL

(n-hexane/ethyl acetate 1:1), with a yield of 89%.  $^1\text{H}$  NMR (400 MHz,  $\text{CDCl}_3$ ), ppm):  $\delta$  4.63 (s, 2H), 3.97–4.01 (dd, 2H), 4.43–4.47 (dd, 2H), 6.68–6.71 (d, 2H), 7.27–7.30 (d, 2H).

## 4.5. Results and Discussion

### 4.5.1. Synthesis of Gold Nanoclusters within Single-Chain Nanoparticles (Au-NCs/SCNPs)

We targeted an amphiphilic poly(OEGMA-co-AEMA) random copolymer featuring hydrophilic oligo(ethyleneglycol) methyl ether methacrylate (OEGMA) and hydrophobic (2-acetoacetoxy)ethyl methacrylate (AEMA) units as a template for the synthesis of AuNCs. Based on the literature data of low-molecular-weight ligands,<sup>24</sup> we surmised that the beta-ketoester group of AEMA could be used as a reductant of Au(III) ions, as well as a stabilizing and structure-directing agent, to generate the Au-NCs. Poly(OEGMA-coAEMA) was synthesized by means of reversible addition fragmentation chain-transfer (RAFT) polymerization (see Figure 44).

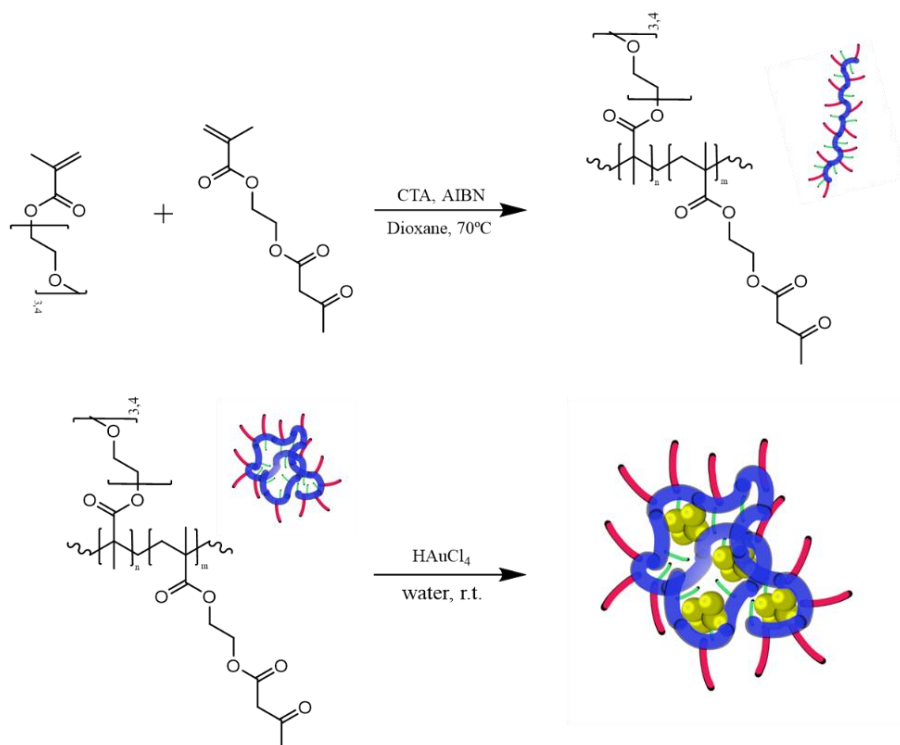


**Figure 44.** Synthesis of an amphiphilic poly(OEGMA-co-AEMA) random copolymer featuring hydrophilic oligo(ethyleneglycol) methyl ether methacrylate (OEGMA) and hydrophobic (2-

#### 4. Gold Nanocluster Synthesized within Single-Chain Nanoparticles as Catalytic Nanoreactors in Water

acetoacetoxy)ethyl methacrylate (AEMA) repeat units via reversible addition fragmentation chaintransfer (RAFT) polymerization. Schematic illustration of the synthesis of Au-NCs/SCNPs from poly(OEGMA-co-AEMA) self-assembled in water in the form of SCNPs.

The copolymer showed a weight-average molecular weight ( $M_w$ ) of 80.7 kDa and a low dispersity ( $D$ ) value of 1.12, as determined by SEC. The content of AEMA units in the copolymer was 35 mol%, as estimated from  $^1\text{H}$  NMR spectroscopy. It is well-known from previous works that amphiphilic poly(OEGMA-co-AEMA) random copolymers with this AEMA content are able to self-assemble intramolecularly in water at high dilution (1 mg/mL) into discrete core-shell-like SCNPs.<sup>25,26</sup> In agreement with previous results, DLS measurements of poly(OEGMA-co-AEMA) in water at 1 mg/mL revealed an average hydrodynamic diameter of  $D_h = 11.0$  nm corresponding to discrete, individual SCNPs without any sign of the presence of multi-chain aggregates (see Table 2 and Figure 44).

**Table 2.** Evolution of average nanoparticle sizes during the synthesis of Au-NCs/SCNPs.

Material Type	Reaction Time, $t$	DLS Hydrodynamic Diameter, $D_h$ (nm) <sup>2</sup>
Poly(OEGMA-co-AEMA) <sup>1</sup>	0 min.	11.0
Au-NCs/SCNPs	1 min.	11.0
Au-NCs/SCNPs	15 min.	10.7
Au-NCs/SCNPs	1 h	11.3
Au-NCs/SCNPs	1 day	11.2
Au-NCs/SCNPs	1 week	11.6

<sup>1</sup> Self-assembled in water in the form of core-shell-like SCNPs. <sup>2</sup> Standard deviation ca.  $\pm 0.3$  nm.

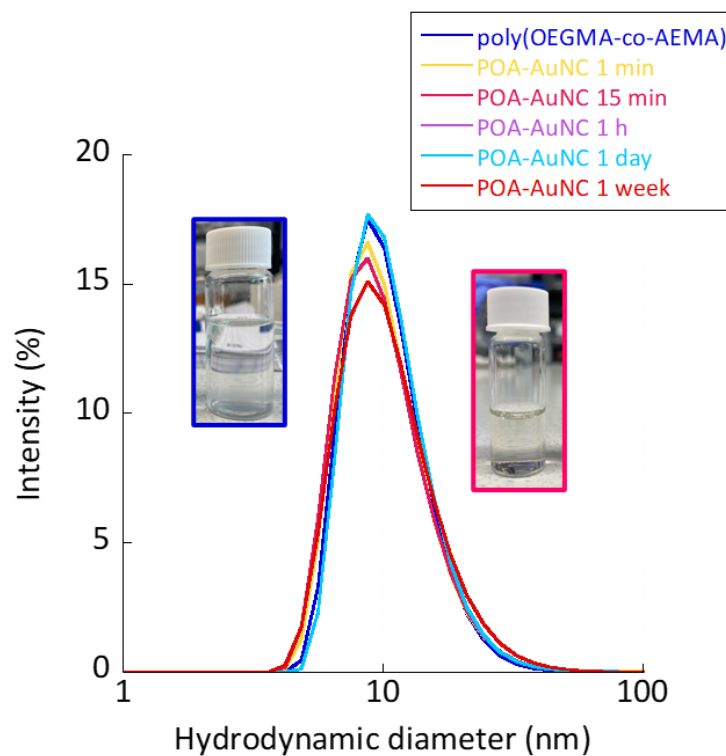


**Figure 44.** DLS size distribution of poly(OEGMA-co-AEMA) SCNPs and Au-NCs/SCNPs.

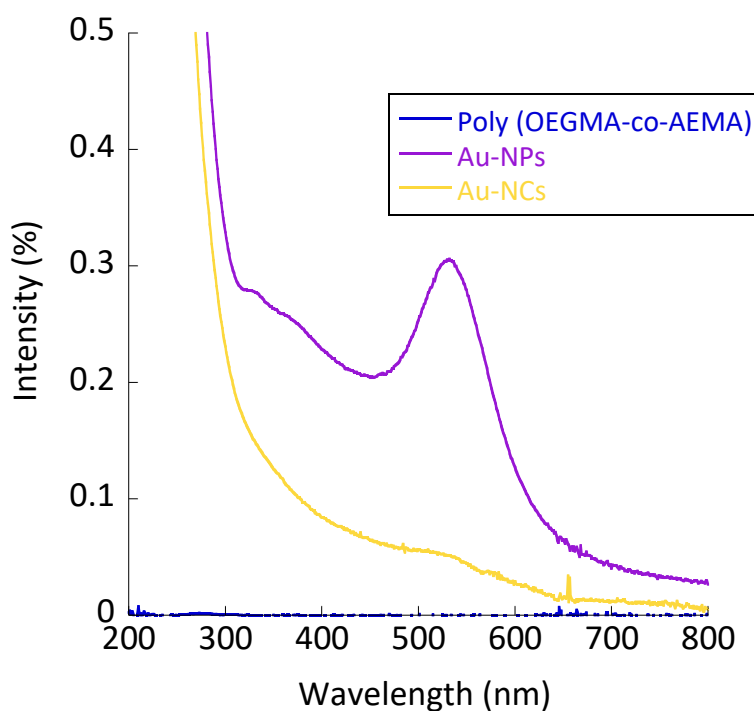


**Figure 45.** Comparison of the UV-Vis spectra of Au-NPs synthesized in the presence of poly(OEGMA-co-AEMA) SCNPs at a (Au(III))/(beta-ketoester (AEMA)) ratio of 1 vs Au-NCs synthesized within poly(OEGMA-co-AEMA) SCNPs at a (Au(III))/(beta-ketoester (AEMA)) ratio of 0.08.

For the synthesis of Au-NCs within the SCNPs through beta-ketoester-mediated Au(III) reduction (Figure 45), we found control of the (Au(III))/(beta-ketoester (AEMA)) ratio to be critical. Hence, by using a (Au(III))/(beta-ketoester (AEMA)) ratio of 1, we obtained gold nanoparticles (Au-NPs) instead of Au-NCs, as revealed by the intense localized surface plasmon resonance (LSPR) UV-Vis absorbance signal characteristic of Au-NPs (Figure 45). Interestingly, by lowering the (Au(III))/(beta-ketoester (AEMA)) ratio to 0.08, we observed *via* TEM the presence of Au-NCs (diameter < 5 nm) within individual poly(OEGMA-coAEMA) SCNPs (Figure 46), as well as the total absence of the LSPR band typical of larger Au-NPs (Figure 45). No significant differences were found between the IR spectra of neat poly(OEGMA-co-AEMA) and the Au-NCs/SCNPs, as illustrated in Figure 47, which we attribute to the relatively low (Au(III))/(beta-ketoester (AEMA)) ratio employed. Notably, the size of the Au-NCs/SCNPs was found to be very stable over time, as illustrated in Table 2 and Figure 44, showing the notorious stabilizing effect of the SCNPs against Au-NCs aggregation over time. Conversely, by using a (Au(III))/(betaketoester (AEMA)) ratio of 1, the diameter of the resulting Au-NPs was found to grow with time, as illustrated in Figure 48 by the associated color changes. After 1 day, the DLS hydrodynamic diameter of the Au-NPs was found to be 67.1 nm.

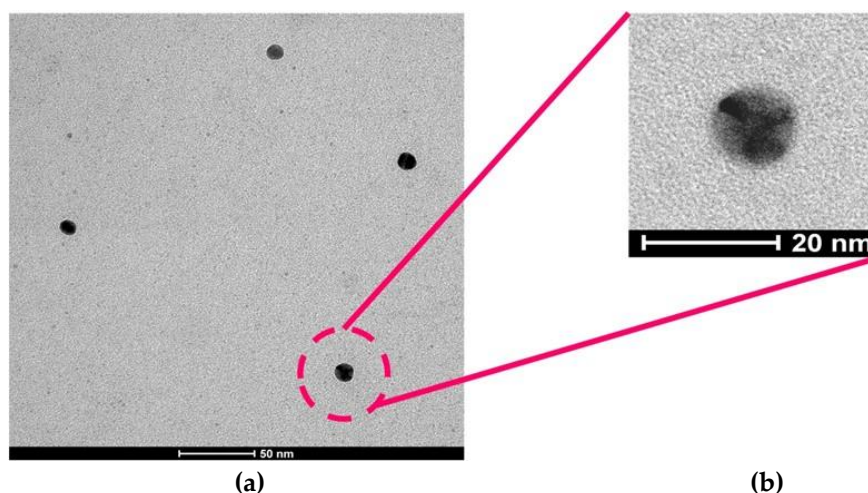


**Figure 46.** (a) TEM picture of Au-NCs synthesized within poly(OEGMA-co-AEMA) SCNPs at a (Au(III))/(beta-ketoester (AEMA)) ratio of 0.08. (b) Illustration of the presence of (darker) AuNCs with a diameter < 5 nm within a representative single-chain nanoparticle of ca. 11 nm in diameter.

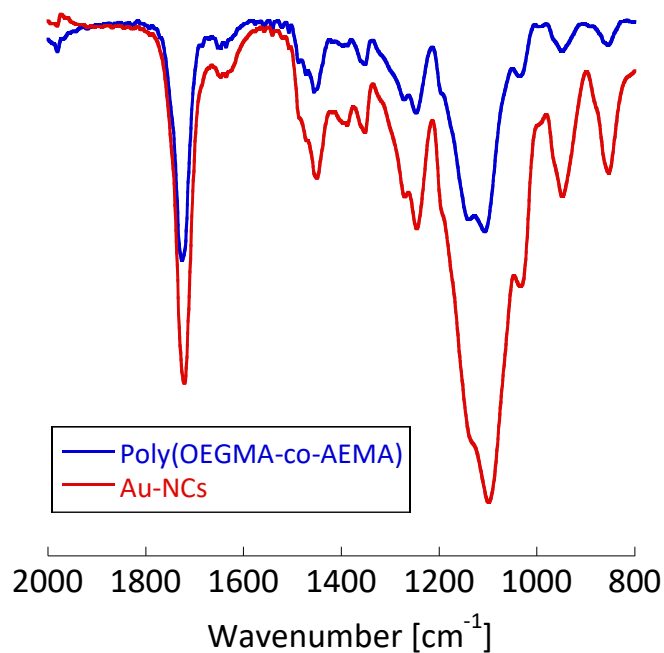


**Figure 47.** IR spectra of neat poly(OEGMA-co-AEMA) SCNPs (blue color) and Au-NCs/SCNPs (red color).

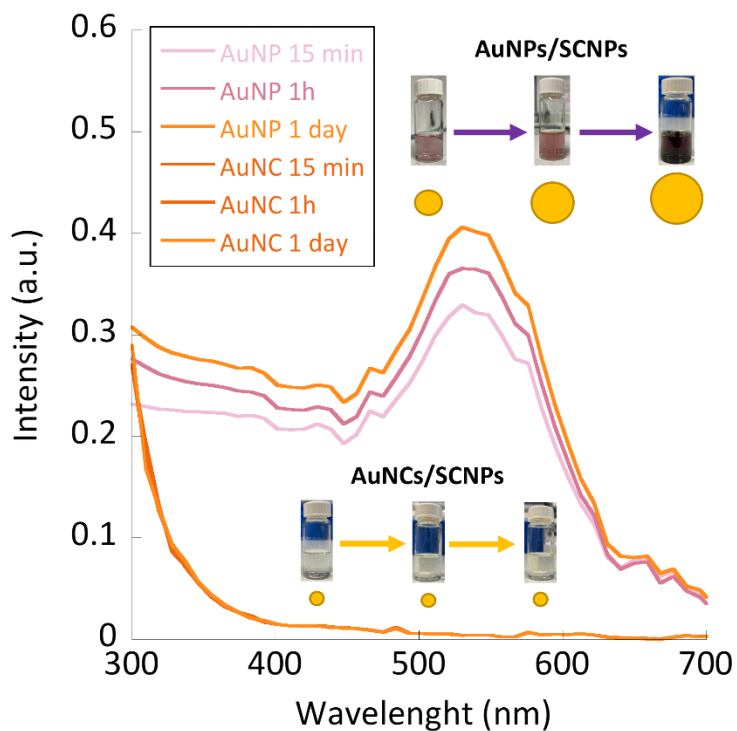


**Figure 48.** Au-NPs synthesized in the presence of poly(OEGMA-co-AEMA) SCNPs at a (Au(III))/(beta-ketoester (AEMA)) ratio of 1 vs Au-NCs synthesized at a ratio of 0.08.

Taken together, the above results demonstrate the efficient synthesis of stabilized Au-NCs with size < 5 nm within discrete poly(OEGMA-co-AEMA) SCNPs of ca. 11 nm in diameter. Key to the access to stabilized Au-NCs within SCNPs, instead of to larger AuNPs that grow in size over time, is the control of the (Au(III))/(beta-ketoester (AEMA)) ratio employed during the synthesis.

#### **4.5.2. Gold Nanoclusters within Single-Chain Nanoparticles (AuNCs/SCNPs) as Catalytic Nanoreactors**

We report herein the results of the use of Au-NCs within SCNPs as catalytic nanoreactors for the reduction of 4-nitrophenol, nitrobenzene, and 3-(4-nitrophenyl)-1,3-oxazolidinone by borohydride ( $\text{BH}_4^-$ ) in water at r.t.

##### **4.5.2.1. Reduction of 4-Nitrophenol to 4-Aminophenol Catalyzed by Au-NCs/SCNPs**

Paracetamol (a popular analgesic and antipyretic agent used to treat fever and mild to moderate pain) can be typically synthesized from 4-nitrophenol as an intermediate *via* its reduction to 4-aminophenol and subsequent acetylation with acetic anhydride. 4-nitrophenol is highly soluble in water (11.6 mg/mL at 20 °C). We investigated the reduction of 4-nitrophenol (4-NP) to 4-aminophenol (4-AP) by  $\text{BH}_4^-$  in water at r.t. by using the Au-NCs/SCNPs as highly efficient catalytic nanoreactors. This transformation has emerged as an important model reaction for assessing the catalytic activity of metallic nanoparticles in water. Section 3.4.3. details the experimental procedure that followed, which is depicted schematically in Figure 49.

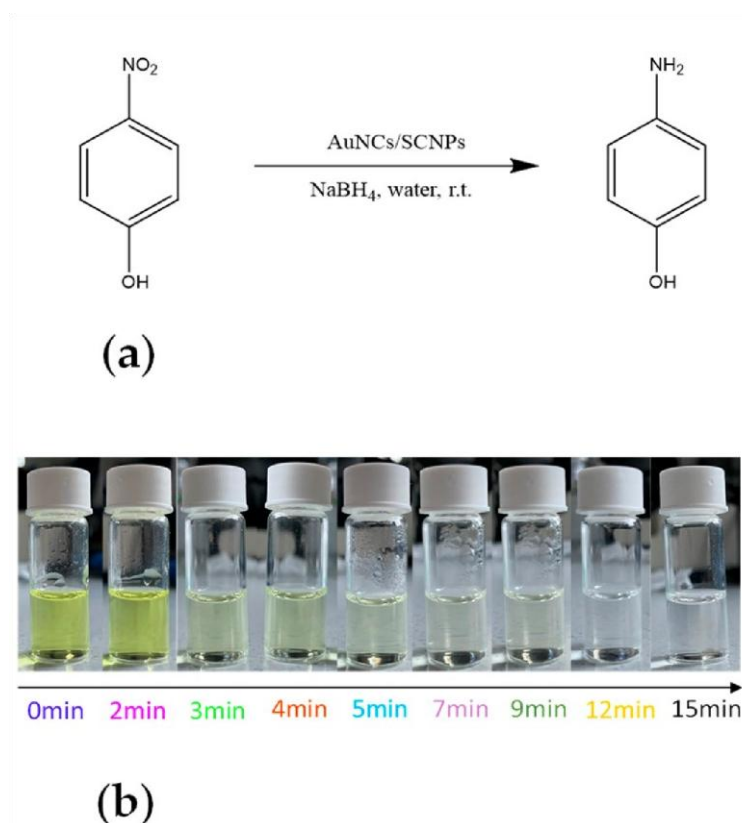


**Figure 49.** (a) Reduction of 4-nitrophenol to 4-aminophenol in water at r.t. by using the AuNCs/SCNPs as highly efficient catalytic nanoreactors. (b) Color changes observed during the reduction of 4-nitrophenol ( $\lambda_{\max} \approx 400$  nm) to 4-aminophenol ( $\lambda_{\max} \approx 300$  nm) catalyzed by AuNCs/SCNPs.

The conversion of 4-nitrophenol to 4-aminophenol was followed by UV-Vis spectrometry due to the different, well-separated absorption bands of the reactant and product, as illustrated in Figure 49(b) and Figure 50. Interestingly, under our reaction conditions, an isosbestic point located at ca.  $\lambda = 325$  nm was observed in the UV-Vis spectra during the reduction of 4-nitrophenol ( $\lambda_{\max} \approx 400$  nm) to 4-aminophenol ( $\lambda_{\max} \approx 300$  nm). This fact suggests the major involvement of a direct route mechanisms in the reduction of 4-nitrophenol to 4-aminophenol in water at r.t. with Au-NCs/SCNPs.<sup>27</sup> No reaction was observed in a model experiment lacking the Au-NCs/SCNPs catalyst.

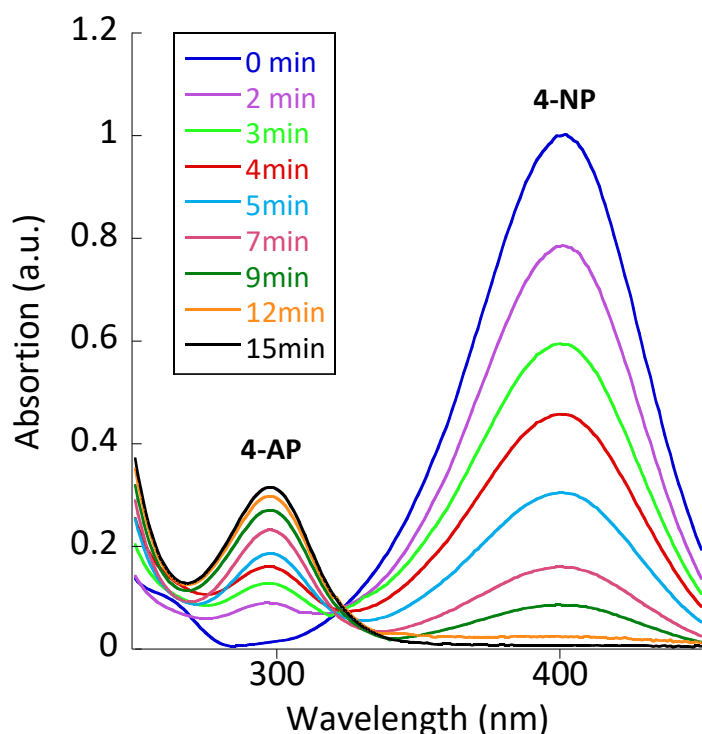


**Figure 50.** Kinetics of the reduction of 4-nitrophenol to 4-aminophenol catalyzed by AuNCs/SCNPs as determined by UV-Vis spectroscopy.

The purified product's chemical structure was confirmed using  $^1\text{H}$  nuclear magnetic resonance spectroscopy ( $^1\text{H}$  NMR). The spectrum shows numerous proton environments within the molecule. A singlet at  $\delta$  4.36 (s, 2H) suggests the presence of a pair of equivalent protons, the amino group. The multiplet from  $\delta$  6.42-6.46 (m, 4H) signifies an aromatic system with protons which experience slightly different electronic environments, likely due to the influence of an adjacent substituent, such as the  $-\text{NH}_2$  and  $-\text{OH}$  groups. Finally, the singlet at  $\delta$  8.34 for the remaining proton (s, 1H) is typical of an aromatic proton that is deshielded, typically due to an electronegative group (such as a nitro or carbonyl) nearby or, in this case, this singlet signifies the influence of a hydroxyl group in -para to the amino group. This spectrum indicates a clean product with no significant impurities, in that only the expected signals are observed.

#### 4. Gold Nanocluster Synthesized within Single-Chain Nanoparticles as Catalytic Nanoreactors in Water

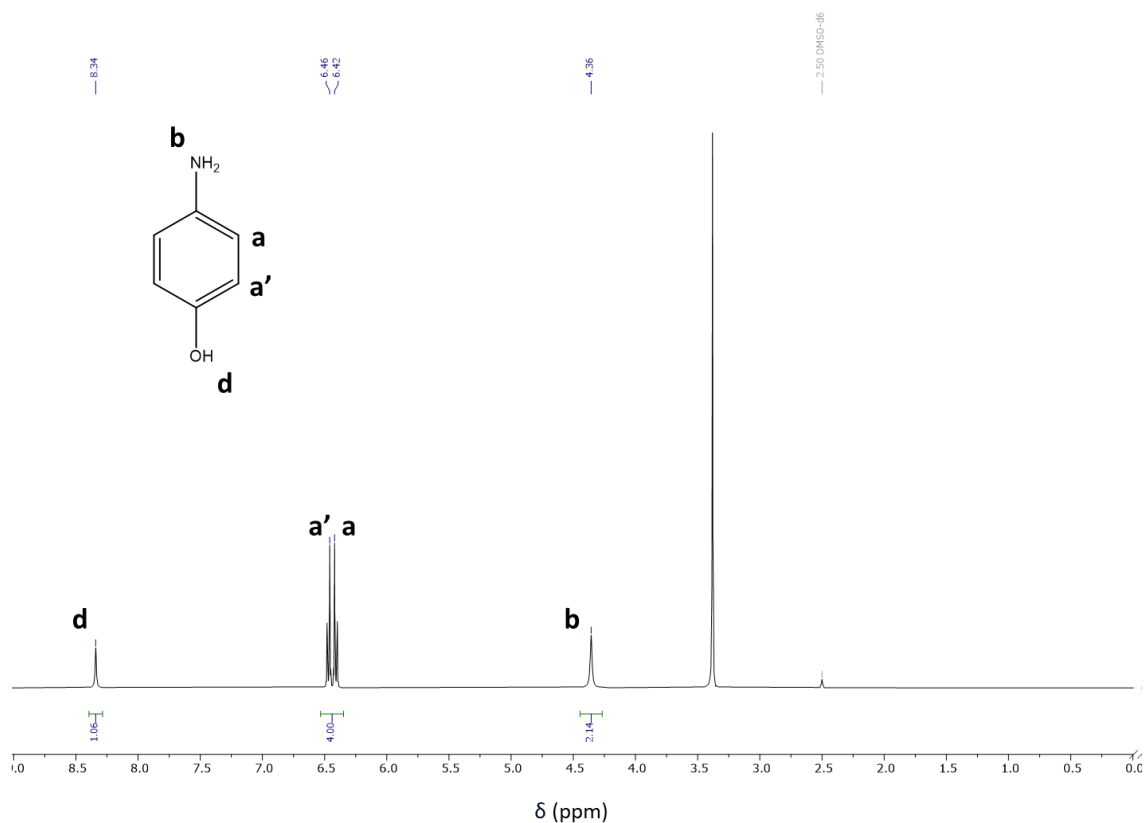


**Figure 51.**  $^1\text{H}$  MNR spectrum after isolation *via* preparative TLC of the 4-aminophenol product.

Meticulously constructed calibration curves were done for all compounds via UV-visible spectroscopy. The goal of this effort was to determine the molar extinction coefficients for each compound. This parameter is critical for quantitating the ability of a compound to absorb light at a particular wavelength. The process of creating a calibration curve involves making a series of standard solutions with accurately known concentrations of the target compound. Each set of standards is then subjected to UV-vis spectroscopy, where we record the absorbance at the wavelength where the compound exhibits maximum absorption. The relationship between absorbance and concentration for these standards should be linear, according to the Beer-Lambert law, over the range of concentrations used.

The molar extinction coefficient,  $\epsilon$ , refers to the absorbance of a one molar (1 M) solution of the compound in a cuvette of cross-section 1 cm. Plotting the absorbance values versus the concentrations of the standards generates a calibration curve. The slope of

the straight-line portion of this plot is the molar extinction coefficient, and the linearity of the relationship is embodied in the Beer-Lambert law, given by:

$$A = \varepsilon l C$$

Here, A is the absorbance, l is the path length of the cuvette and c is the concentration of the compound in the solution. The law suggests that the absorbance is directly proportional to both the concentration and the path length and requires that other experimental conditions be kept constant, in addition to assuming the system follows ideal behavior.

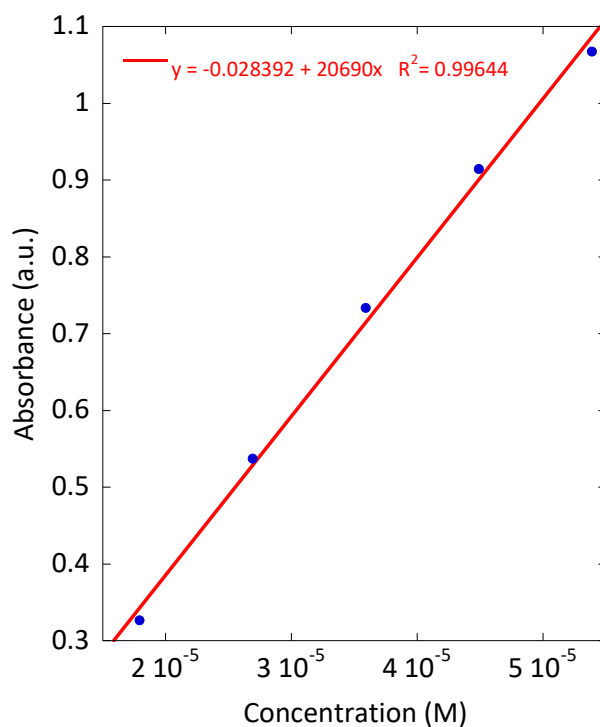


**Figure 52.** Calibration curve for determination of the UV-Vis molar extinction coefficient of 4-nitrophenol in water at r.t.:  $\varepsilon (\lambda_{\max} = 400 \text{ nm}) \approx 20239 \text{ M}^{-1}\text{cm}^{-1}$ . Literature value:  $\varepsilon (\lambda_{\max} = 400 \text{ nm}) \approx 18900 \text{ M}^{-1}\text{cm}^{-1}$  (Coiffier A. *et al. J. Mater. Chem.* **2001**, *11*, 2039).

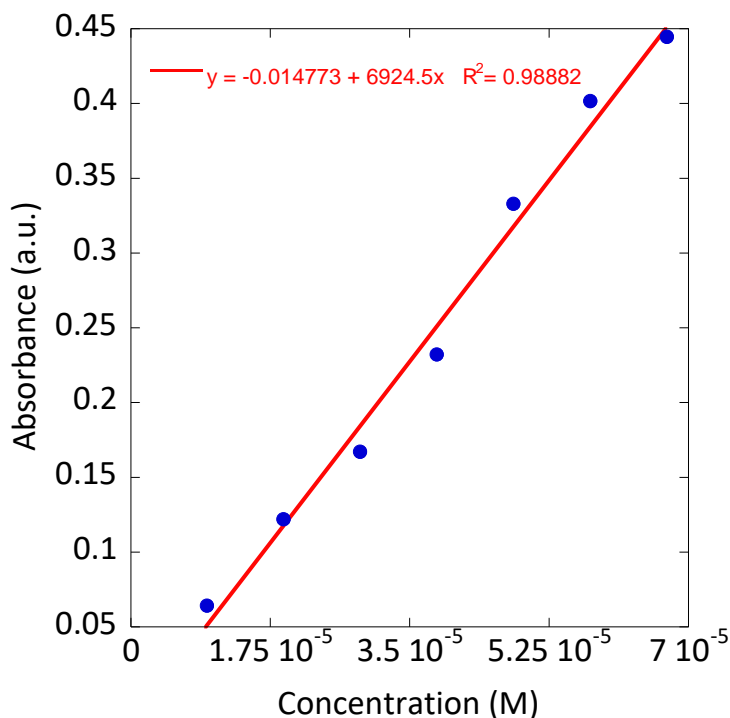


**Figure 53.** Calibration curve for determination of the UV-Vis molar extinction coefficient of 4-aminophenol in water at r.t.:  $\epsilon (\lambda_{\max} = 300 \text{ nm}) \approx 6925 \text{ M}^{-1}\text{cm}^{-1}$ .

The importance of determining the molar extinction coefficient goes beyond mere quantification. It has been particularly critical in this work for tracking chemical reaction progress. Figure 54 shows the evolution of the concentration of the reactant and the product over time as estimated from data in Figure 50. A reaction yield of 95% was achieved in 15 min. of reaction time, where the amount of 4-nitrophenol was totally consumed. As illustrated in Figure 55, the apparent kinetic constant ( $k_{\text{app}}$ ) of the reaction was estimated to be  $k_{\text{app}} = 5.96 \times 10^{-3} \text{ s}^{-1}$ , which is a value between those reported by Yamamoto et al. for *N,N*-dimethylformamide-stabilized Au-NCS ( $k_{\text{app}} \approx 3 \times 10^{-3} \text{ s}^{-1}$ ) and atomically monodisperse glutathione-stabilized Au-NCS ( $k_{\text{app}} \approx 8 \times 10^{-3} \text{ s}^{-1}$ ).<sup>28</sup>

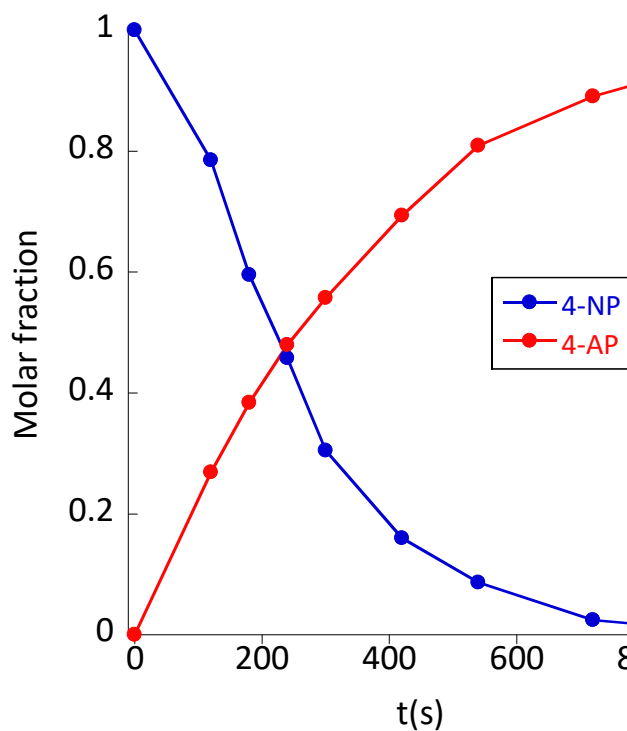


**Figure 54.** Evolution of the concentration of reactant (blue) and product (red) over time ( $t$ ) during the reduction of 4-nitrophenol (4-NP) to 4-aminophenol (4-AP) catalyzed by AuNCs/SCNPs.

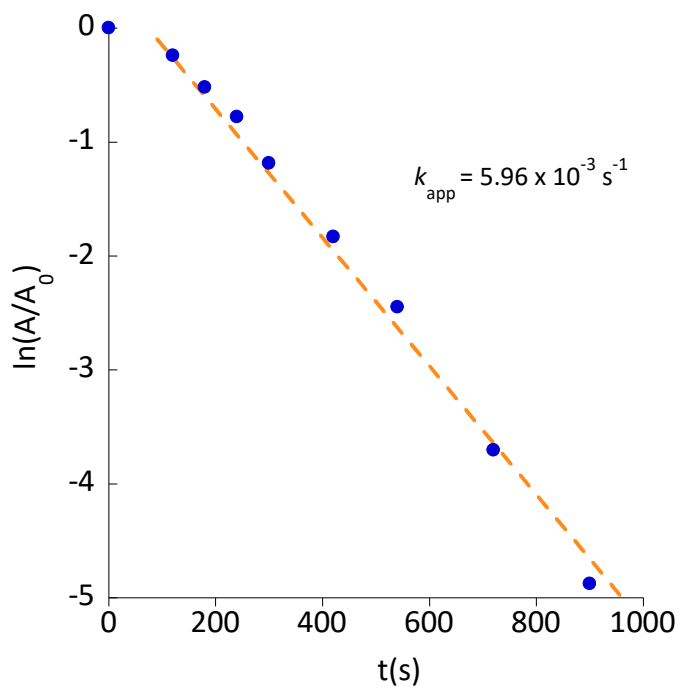


**Figure 55.** Determination of the apparent kinetic constant of the reduction of 4-NP to 4-AP catalyzed by Au-NCs/SCNPs ( $A/A_0$  is the 4-NP absorbance normalized to the absorbance at the start of the reaction).

#### 4.5.2.2. Reduction of Nitrobenzene to Aniline Catalyzed by Au-NCs/SCNPs

We also investigated the reduction in water at r.t. of nitrobenzene (which is sparingly water-soluble (1.9 mg/mL at 20 °C)) to aniline by  $\text{BH}_4^-$  using the Au-NCs/SCNPs as catalytic nanoreactors. Figure 56 shows the UV-Vis spectra recorded at different reaction times during the nitrobenzene reduction reaction. Initially, the main UV-Vis absorption band of nitrobenzene is observed at  $\lambda_{\text{max}} \approx 265$  nm. The intensity of this band decreases with reaction time, and after 90 min., only the UV-Vis absorption peaks of aniline were clearly visible at  $\lambda_{\text{max}} \approx 230$  nm and 280 nm. However, during the reduction reaction process, the presence of a new UV-Vis absorption band centered at ca.  $\lambda_{\text{max}} \approx 330$  nm is clearly seen in Figure 56. Based on the literature data,<sup>29</sup> we attribute this new band to the generation of *cis*-azobenzene as an intermediate species that progressively transform to the aniline product. Consequently, in the case of the reduction in water at r.t. of nitrobenzene to aniline by  $\text{BH}_4^-$  using the Au-NCs/SCNPs as catalytic nanoreactors, both the direct route and the condensation route mechanisms are involved.<sup>30</sup> Figure 63 provides the evolution of the concentration of nitrobenzene, *cis*-azobenzene, and aniline over time, as estimated from data in Figure 56. After 90 min. of reaction time, the reaction yield was 96% (see Figure 63).

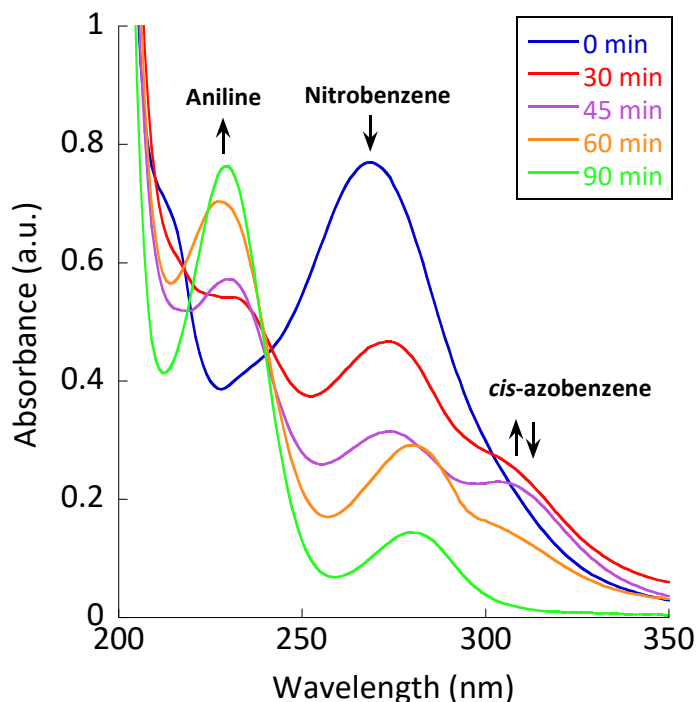


**Figure 56.** Kinetics of the reduction of nitrobenzene to aniline catalyzed by Au-NCs/SCNPs as determined by UV-Vis spectroscopy.

Proton nuclear magnetic resonance ( $^1\text{H}$  NMR) spectroscopy played a central role in the comprehensive mechanistic investigation, as it was implemented to discern structural evolution from reactants to products. The  $^1\text{H}$  NMR spectra of *cis*-azobenzene, the intermediate of interest, was expected to display separate proton environments associated with the phenyl groups flanking the *azo*-bridge. The *cis* arrangement of the azobenzene imparts discrete chemical shifts to aryl protons, as the orientation of these atoms is intricately linked to the electron-withdrawing influence of the azo linkage on aromatic protons as shown in Figure 57.

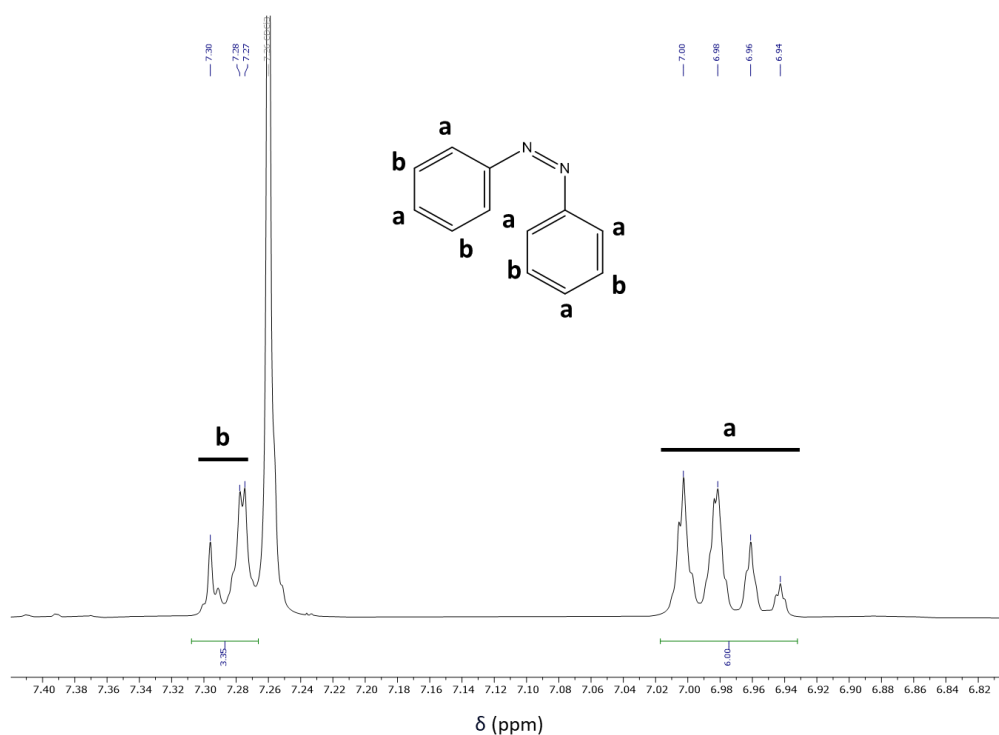


**Figure 57.**  $^1\text{H}$  NMR spectrum after isolation *via* preparative TLC of the *cis*-azobenzene intermediate species.

Meanwhile, the  $^1\text{H}$  NMR spectrum of aniline, the final product, was carefully recorded in  $\text{DMSO-d}_6$  and revealed (Figure 58). A singlet at  $\delta$  3.65 (s, 2H) is indicative of the amino group protons ( $-\text{NH}_2$ ). These protons are not coupling in a solvent system of this type and therefore occur as a singlet. Multiplets in the region  $\delta$  6.67–6.70 and  $\delta$  6.73–6.77 are indicative of the complexity of the aromatic region. The former set of signals are characteristic of protons in the ortho position to the amino group while the latter are in the para position. The slight upfield and downfield shifts over this small range of

chemical shifts are consistent with the electron-donating resonance effect which the amino substituent exerts on the aromatic ring. The last set of multiplets ( $\delta$  7.13–7.17) reflect the protons in the meta position to the amino group. The complexity of the splitting pattern in this region is consistent with the expected magnetic environment of protons that are three bonds away from the substituent, in this case, the amino group. The precise identification of aniline NMR signals and the interpretative insights into cisazobenzene they revealed were major contributions to our overall understanding of the reaction mechanism as shown in Figure 59. These spectroscopic snapshots finally not only offered proof of the continued structural integrity of the intermediate and final product, but also a dynamic view of the stepwise transformations that occurred within the reaction milieu.

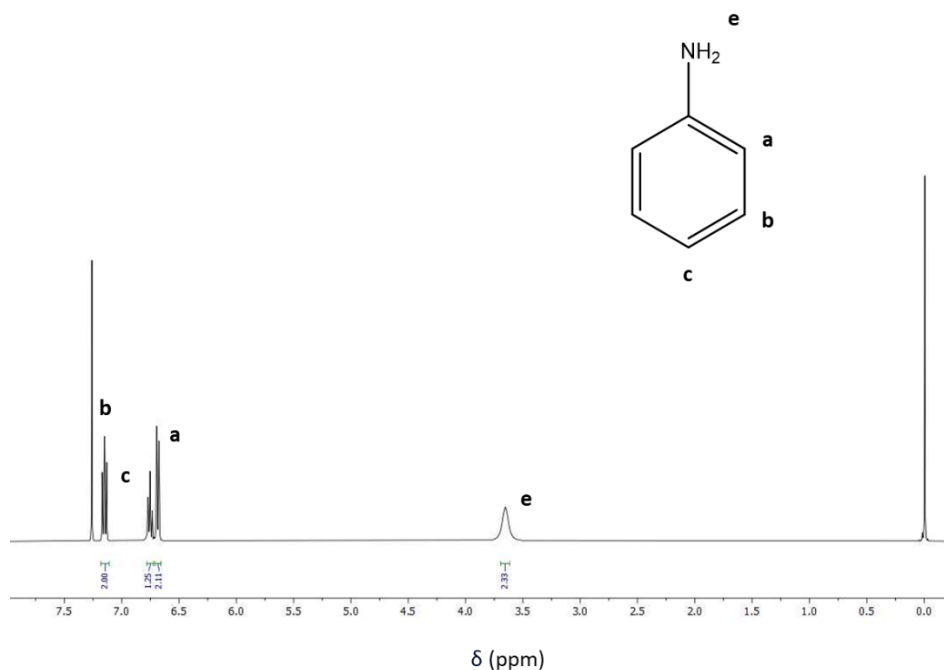


**Figure 58.**  $^1\text{H}$  NMR spectrum after isolation *via* preparative TLC of the aniline

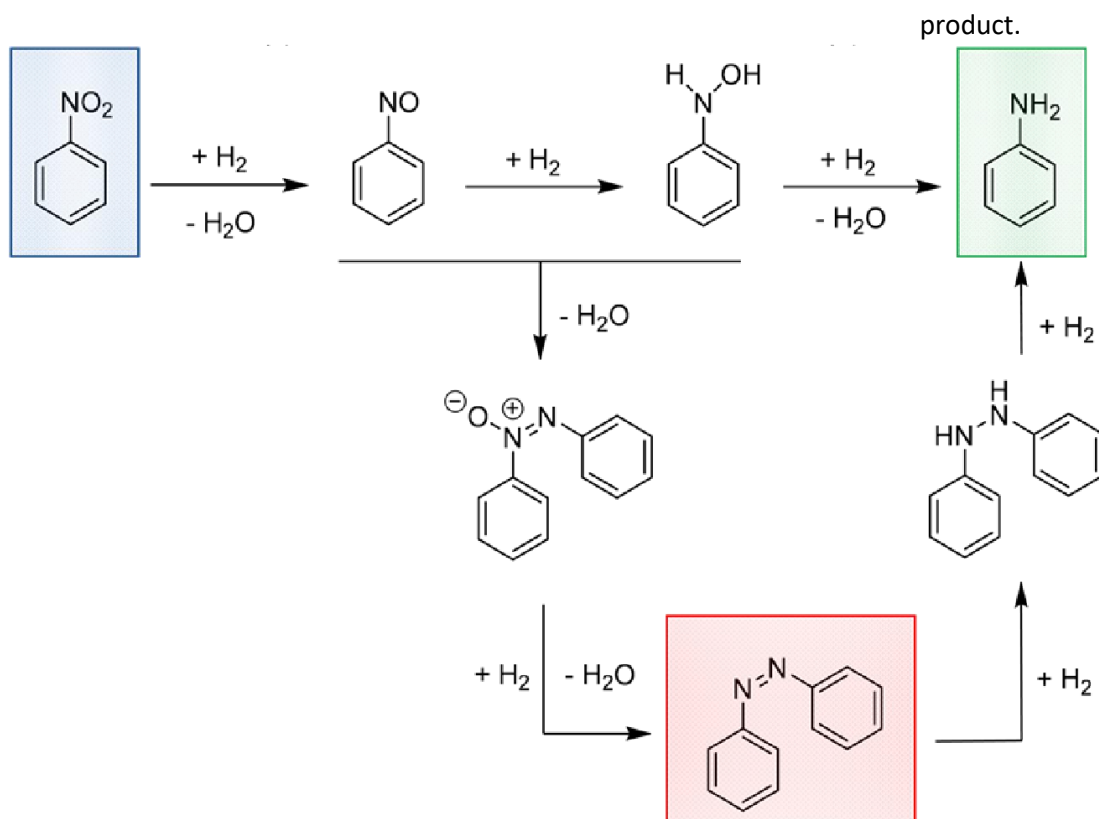


**Figure 59.** Experimental data point to the involvement of both the direct route (**upper**) and the condensation route (**bottom**) mechanisms.

It was imperative to quantify the molar extinction coefficients so that we could understand how the system evolves in terms of the molar fractions of the constituent species as well as the mechanistic progression and the kinetics of the reaction. Once again, the molar extinction coefficients were deduced through UV-visible spectroscopic analysis (Figure 60,61 and 62) where calibration curves were constructed. Molar extinction coefficients furnished a crucial foundation for our kinetic analysis, allowing us to quantify the molar fractions of the reactants, intermediates, and products throughout the course of the reaction, thus providing a window into the intricate molecular interactions and transformations that dictate the course of the chemistry of the reaction under study.

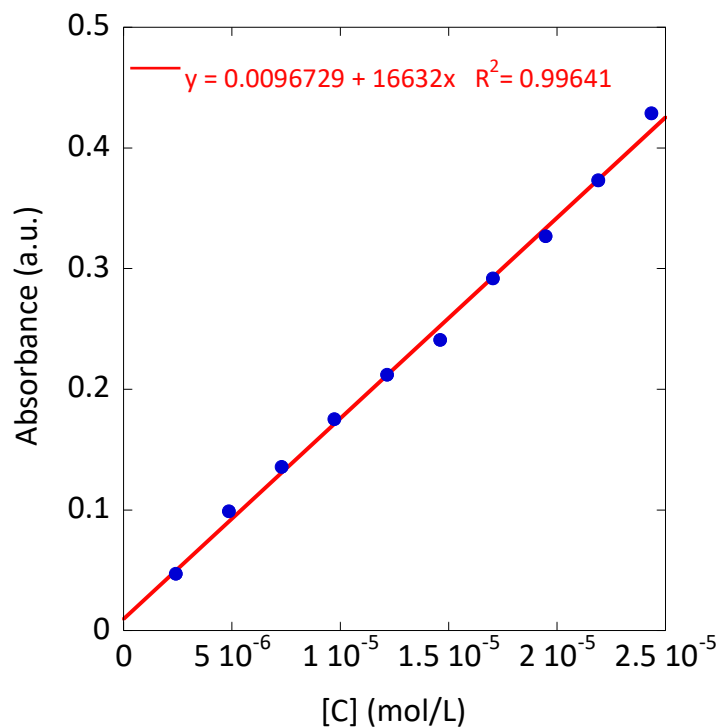


**Figure 60.** Calibration curve for determination of the UV-Vis molar extinction coefficient of nitrobenzene in water at r.t.:  $\epsilon$  ( $\lambda_{\max} = 265 \text{ nm}$ )  $\approx 16632 \text{ M}^{-1}\text{cm}^{-1}$ .

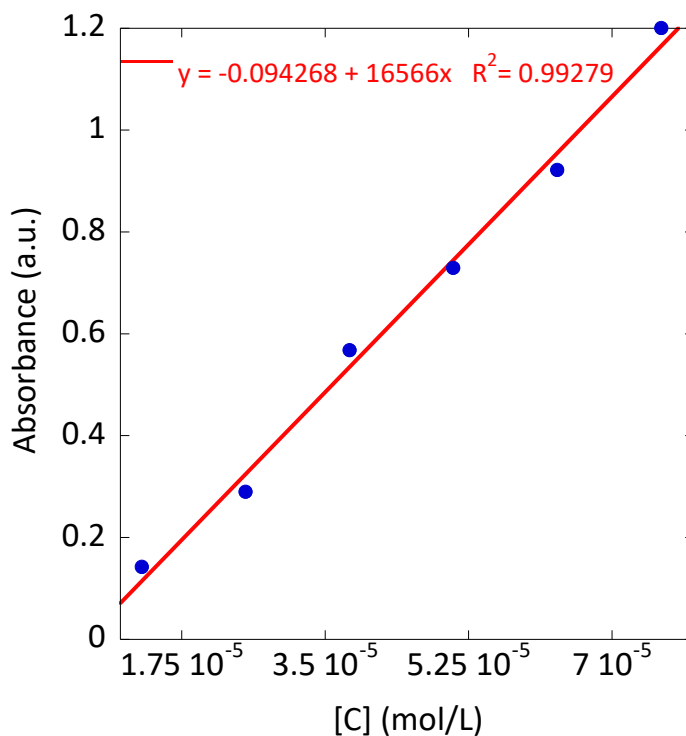


**Figure 61.** Calibration curve for determination of the UV-Vis molar extinction coefficient of azobenzene in water at r.t.:  $\epsilon$  ( $\lambda_{\max} = 230 \text{ nm}$ )  $\approx 16566 \text{ M}^{-1}\text{cm}^{-1}$ .

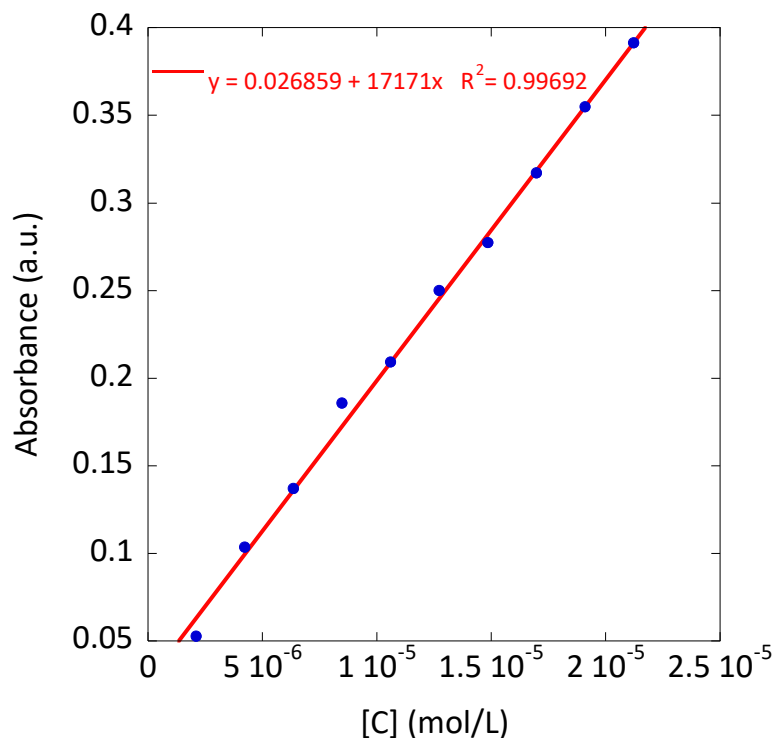


**Figure 62.** Calibration curve for determination of the UV-Vis molar extinction coefficient of aniline in water at r.t.:  $\epsilon$  ( $\lambda_{\max} = 230 \text{ nm}$ )  $\approx 20239 \text{ M}^{-1}\text{cm}^{-1}$ .

Figure 63 shows the evolution of the concentration of the reactant and the product over time as estimated from data in Figure 56. A reaction yield of 96% was achieved in 90 min. of reaction time, where the amount of nitrobenzene was totally consumed. As illustrated in Figure 55, the apparent kinetic constant ( $k_{\text{app}}$ ) of the reaction was estimated to be  $k_{\text{app}} = 3.8 \times 10^{-4} \text{ s}^{-1}$ .

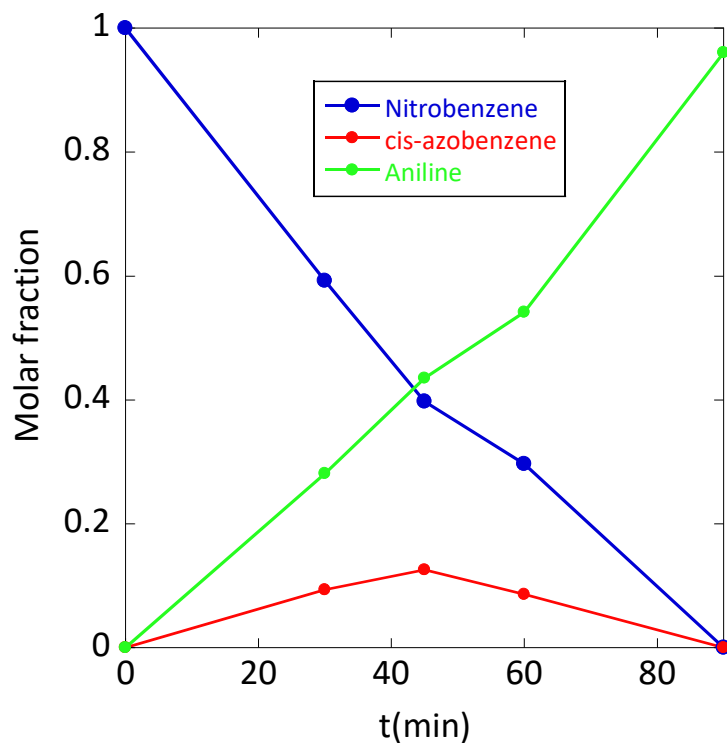


**Figure 63.** Evolution of the concentration of nitrobenzene (blue), *cis*-azobenzene (red) and aniline (green) over time during the reduction of nitrobenzene to aniline catalyzed by AuNCs/SCNPs.

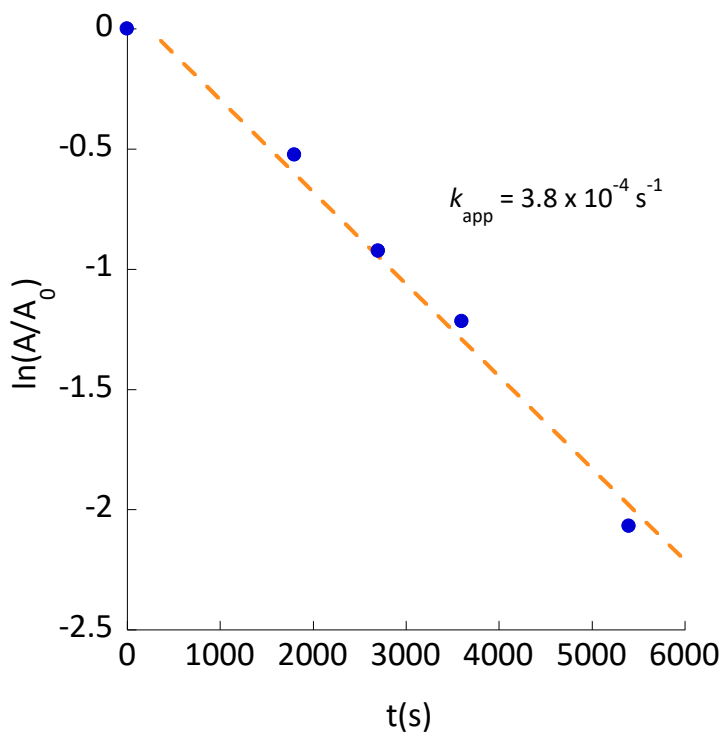


**Figure 64.** Apparent kinetic constant ( $k_{app}$ ) of the reduction of nitrobenzene to aniline catalyzed by Au-NCs/SCNPs.

#### 4.5.2.3. Reduction of 3-(4-Nitrophenyl)-1,3-oxazolidin-2-one to 3-(4-Aminophenyl)-1,3-oxazolidin-2-one Catalyzed by Au-NCs/SCNPs

Motivated by the high conversion observed during the Au-NCs/SCNPs-catalyzed reduction of both 4-nitrophenol and nitrobenzene, we additionally investigated the reduction of 3-(4-nitrophenyl)-1,3-oxazolidin-2-one to 3-(4-aminophenyl)-1,3-oxazolidin-2-one catalyzed by Au-NCs/SCNPs. In this sense, the aminophenyl– oxazolidinone fragment is a common motif contained in several drugs like Rivaroxaban, Sutezolid, and Linezolid (see Figure 65).

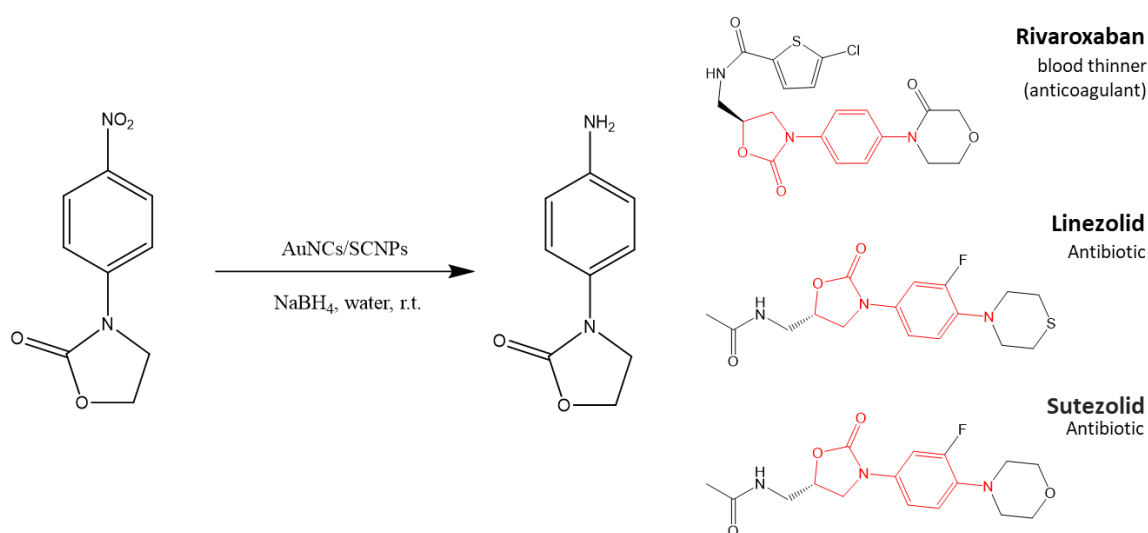


**Figure 65.** Illustration of the reduction of 3-(4-nitrophenyl)-1,3-oxazolidin-2-one to 3-(4aminophenyl)- 1,3-oxazolidin-2-one by BH<sub>4</sub> – in water at r.t. catalyzed by Au-NCs/SCNPs. The aminophenyl– oxazolidinone fragment is a common motif contained in several drugs like Rivaroxaban, Linezolid, and Sutezolid.

We found the Au-NCs/SCNPs-catalyzed reduction of 3-(4-nitrophenyl)-1,3-oxazolidin-2-one to proceed in two steps (fast and slow, respectively), as summarized in Figure 66.

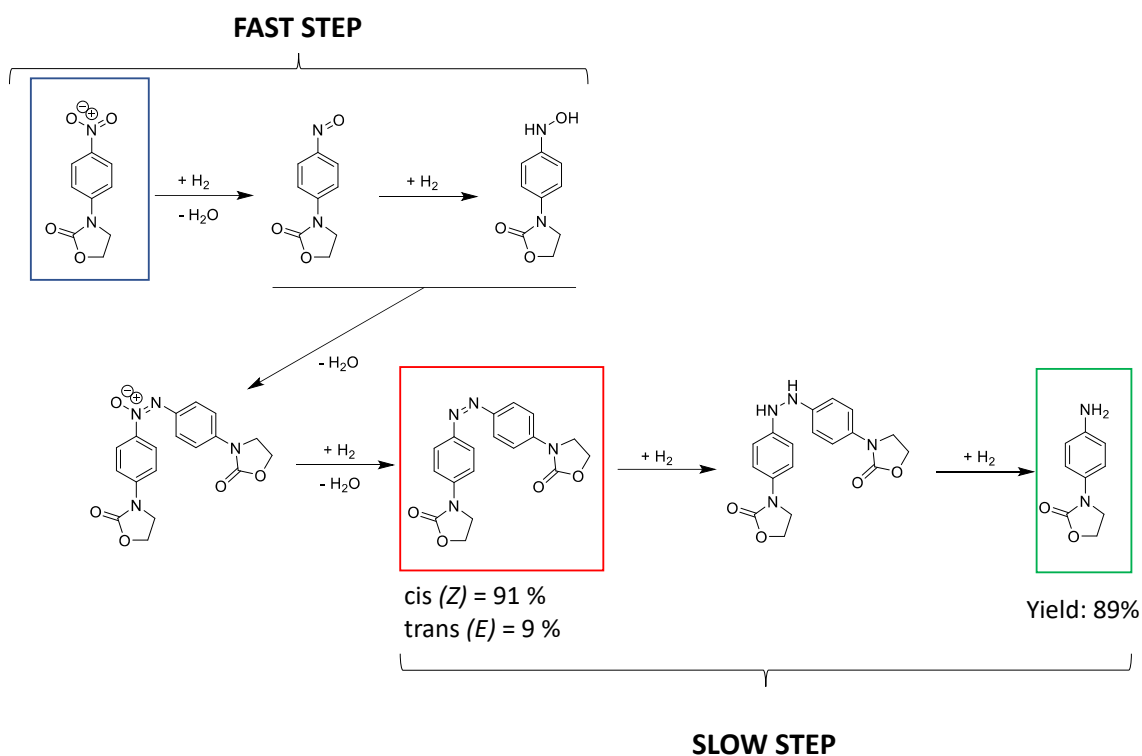


**Figure 66.** Reduction of 3-(4-nitrophenyl)-1,3-oxazolidin-2-one (in blue) to 3-(4-aminophenyl)-1,3-oxazolidin-2-one (in green) catalyzed by Au-NCs/SCNPs. The fast step corresponds to the formation of the diazene intermediate (in red), and the slow step to the generation of the aminophenylloxazolidinone product.

Figure 67 shows the UV-Vis spectra recorded at different reaction times corresponding to the fast step. We observed the complete disappearance of the UV-Vis absorption peak of 3-(4-nitrophenyl)-1,3-oxazolidin-2-one ( $\lambda_{\max} \approx 320$  nm) in 15 min. and then the appearance of a new UV-Vis absorption peak ( $\lambda_{\max} \approx 360$  nm), which can be attributed to the generation of the diazene intermediate ((*Z*)-3,3'-(diazene-1,2-diylbis(4,1phenylene))bis(oxazolidin-2-one)) in 3 h of reaction time. The intensity of this new band was stable after 3 h of reaction time, and it did not change until 9 h of additional reaction time. Then, during the slow step, a progressive disappearance of the UV-Vis peak of the diazene intermediate at  $\lambda_{\max} \approx 360$  nm was found, as well as the concomitant appearance of a new UV-Vis absorption band at  $\lambda_{\max} \approx 250$  nm corresponding to the 3-(4-aminophenyl)-1,3-oxazolidin-2-one product (see Figure 67). Figure 73 illustrates the evolution of the concentration of 3-(4-nitrophenyl)-1,3-oxazolidin-2-one, (*Z*)-3,3'-(diazene-1,2-diylbis(4,1phenylene))bis(oxazolidin-2-one), and 3-(4-aminophenyl)-1,3-oxazolidin-2-one over time, as estimated from data in Figure 67,

and the corresponding calibration curves are provided in the Supporting Information. After 20 h of reaction time, the reaction yield was 89%.

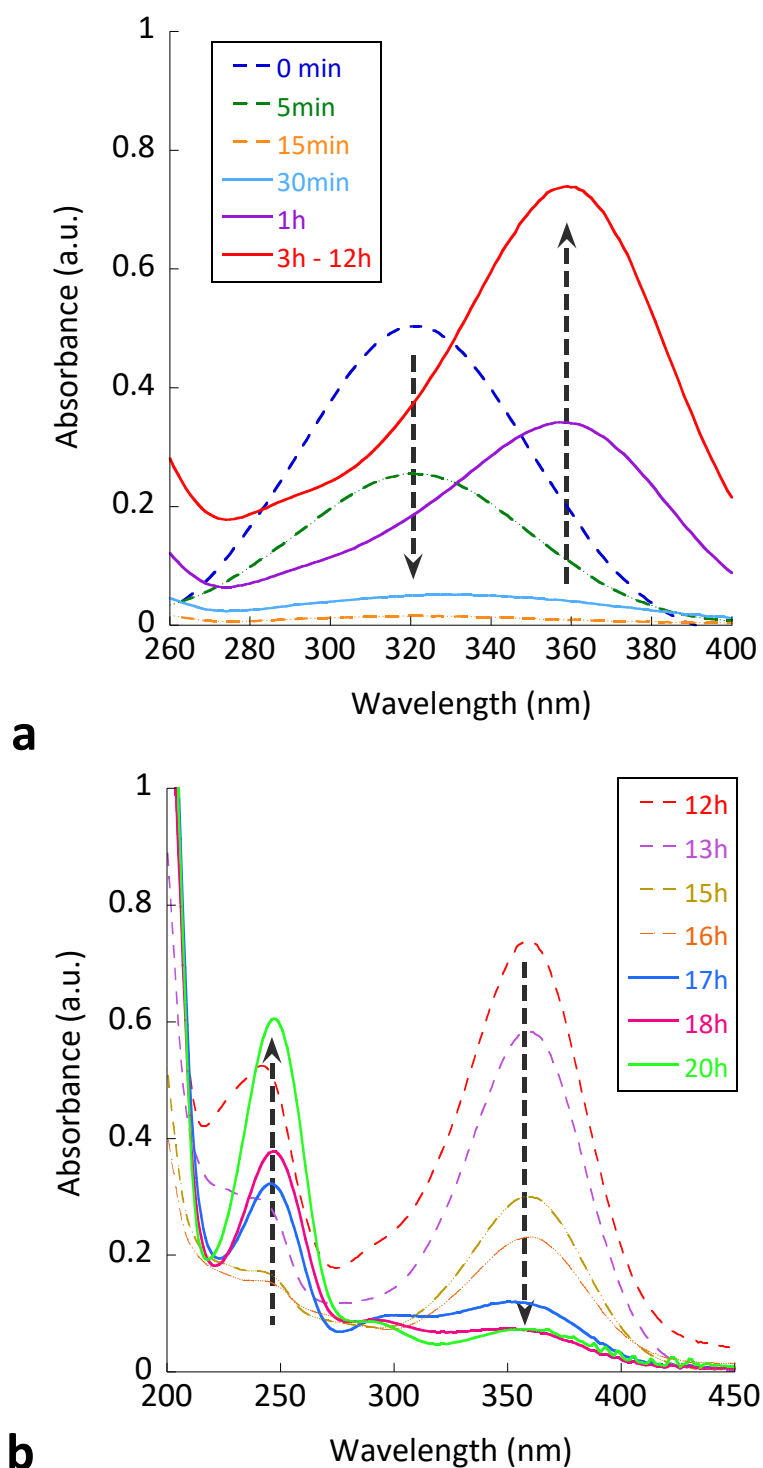


**Figure 67.** Kinetics of the reduction of 3-(4-nitrophenyl)-1,3-oxazolidin-2-one to 3-(4aminophenyl)-1,3-oxazolidin-2-one catalyzed by Au-NCs/SCNPs as determined by UV-Vis spectroscopy corresponding to the fast step (a) and the slow step (b) of the reaction.

In this case, a clear intermediate was observed again in the reaction, so as in the Reduction of nitrobenzene to aniline, both the intermediate and the final product were characterized by  $^1\text{H}$  NMR as can be seen in Figure 68 and Figure 69.

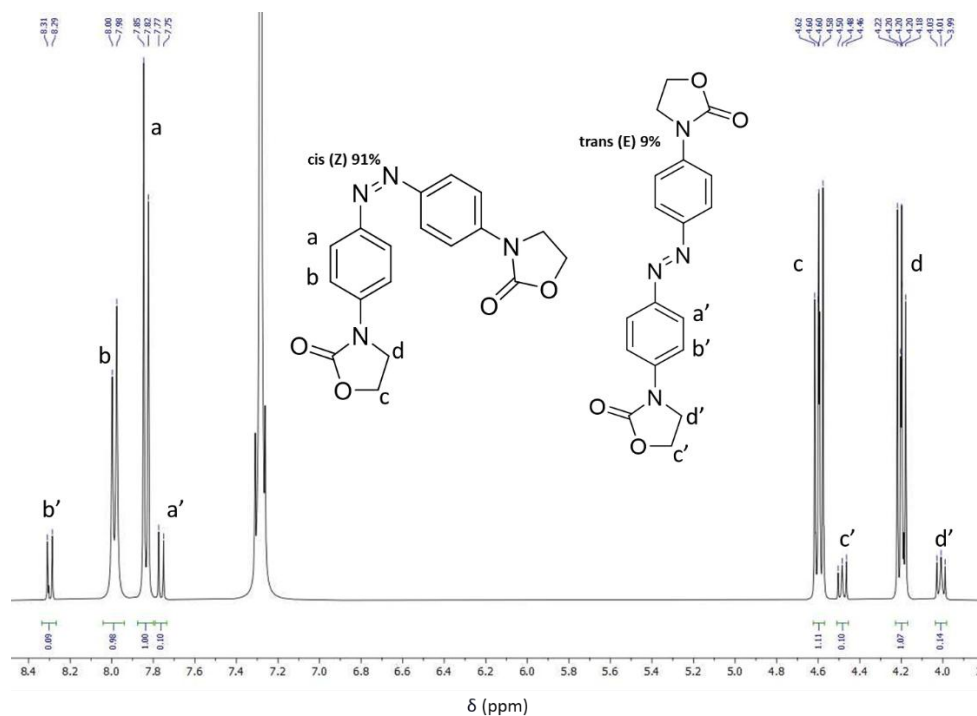


**Figure 68.**  $^1\text{H}$  MNR spectrum after isolation *via* preparative TLC of the (Z)-3,3'-(diazene-1,2-diylbis(4,1-phenylene))bis(oxazolidin-2-one) intermediate species.

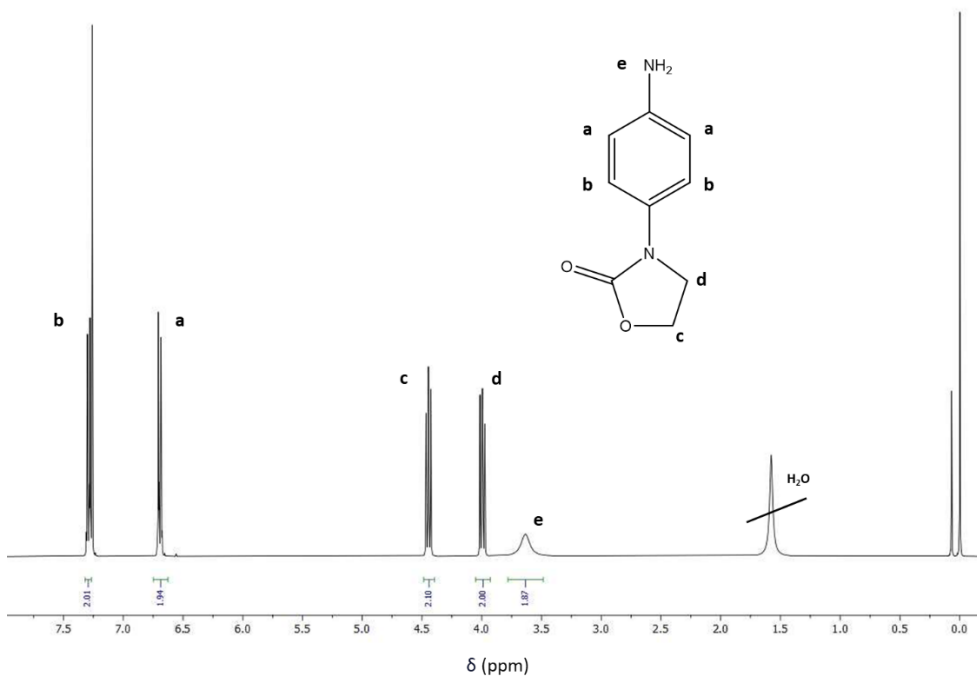


**Figure 69.**  $^1\text{H}$  MNR spectrum after isolation *via* preparative TLC of the 3-(4-aminophenyl)-1,3-oxazolidin-2-one product.

Accordingly, in order to ensure that our monitoring was reliable and accurate, calibration curves were constructed to obtain molar extinction coefficients for the substances involved in our reaction. This was necessary in our case because the molar extinction coefficient is highly specific to each chemical species and depends on a number of parameters that are directly related to the experimental conditions. This monitoring is crucial for being able to obtain the full picture of what is happening during a chemical reaction. It can show us the reaction kinetics, so we can optimize the conditions in which we perform the reaction for the greatest yield, and also to maintain the consistency and quality of product from batch to batch.

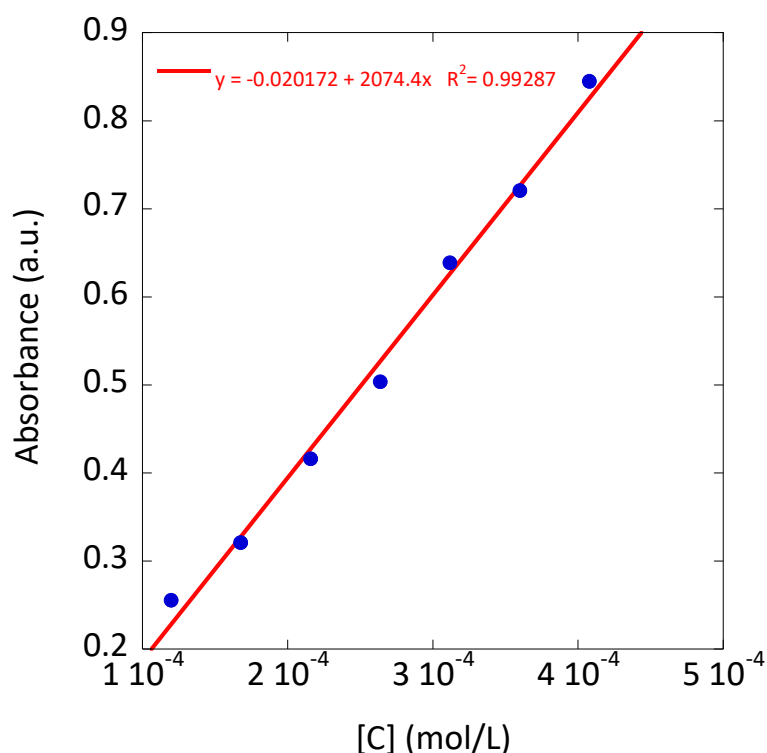


**Figure 70.** Calibration curve for determination of the UV-Vis molar extinction coefficient of 3-(4-nitrophenyl)-1,3-oxazolidin-2-one in water at r.t.:  $\epsilon$  ( $\lambda_{\max} = 320 \text{ nm}$ )  $\approx 2074 \text{ M}^{-1}\text{cm}^{-1}$ .

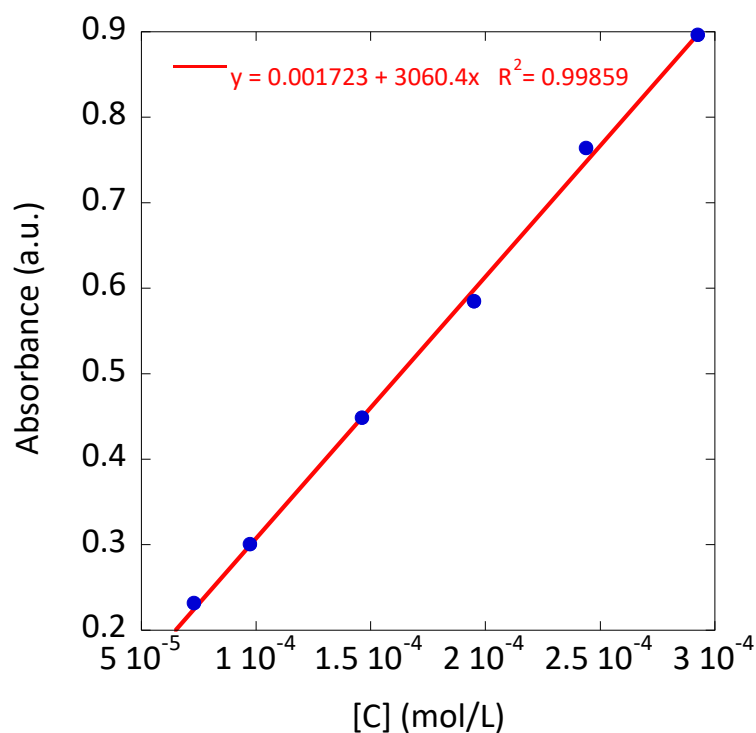


**Figure 71.** Calibration curve for determination of the UV-Vis molar extinction coefficient of (Z)3,3'-(diazene-1,2-diylbis(4,1-phenylene))bis(oxazolidin-2-one) in water at r.t.:  $\epsilon$  ( $\lambda_{\max} = 360$  nm)  $\approx 3060 \text{ M}^{-1}\text{cm}^{-1}$ .

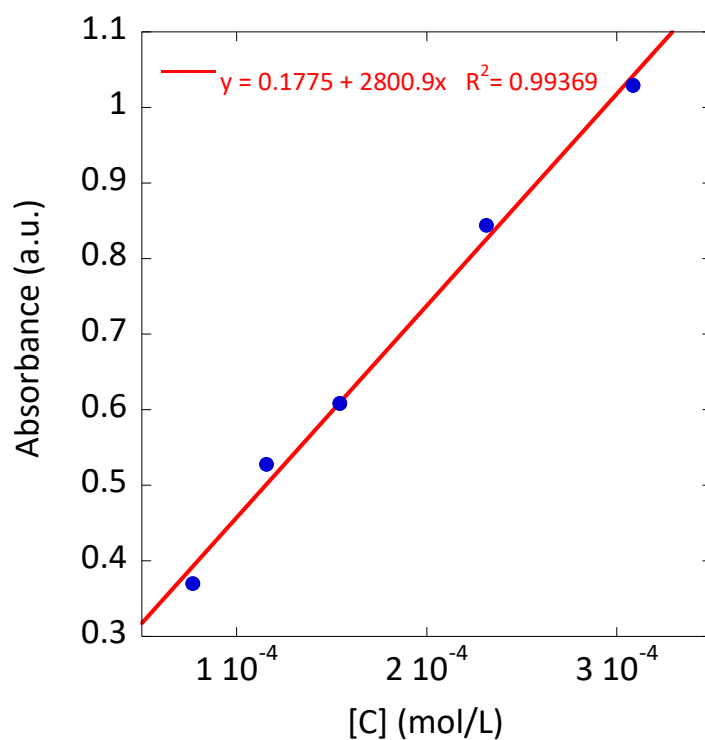


**Figure 72.** Calibration curve for determination of the UV-Vis molar extinction coefficient of 3-(4-aminophenyl)-1,3-oxazolidin-2-one in water at r.t.:  $\epsilon$  ( $\lambda_{\max} = 250$  nm)  $\approx 2801 \text{ M}^{-1}\text{cm}^{-1}$ .

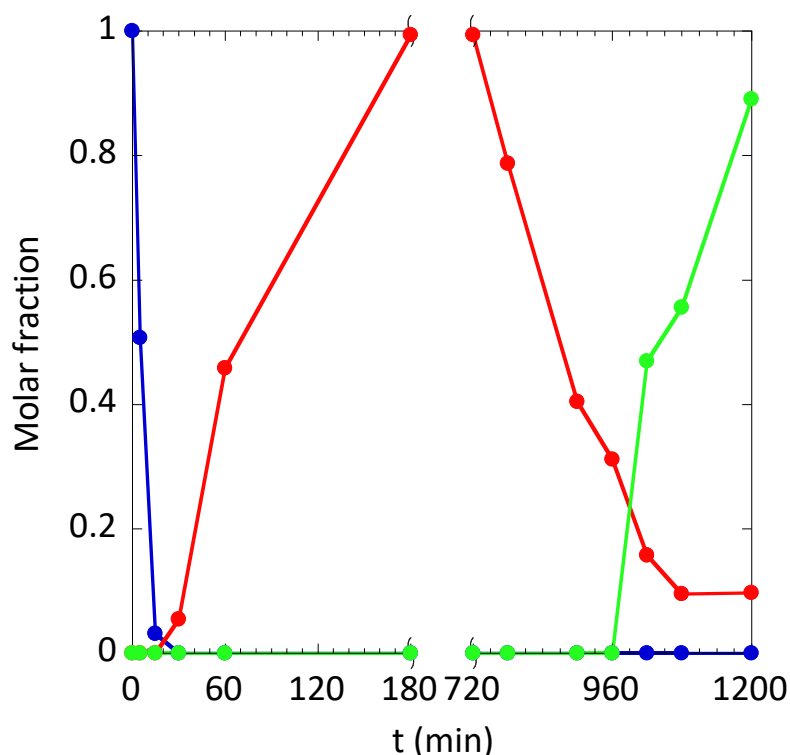


**Figure 73.** Evolution of the concentration of 3-(4-nitrophenyl)-1,3-oxazolidin-2-one (blue color), (Z)-3,3'-(diazene-1,2-diylbis(4,1phenylene))bis(oxazolidin-2-one) (red color), and 3-(4aminophenyl)-1,3-oxazolidin-2-one (green color) over time.

## 4.6. Conclusions

We report the synthesis of gold nanoclusters (Au-NCs) with diameter < 5 nm (as revealed *via* TEM) within discrete single-chain polymeric nanoparticles (SCNPs) of poly(OEGMAcoAEMA) with a diameter of around 11 nm (as revealed *via* DLS and TEM) and its further use as efficient catalytic nanoreactors for the reduction of model nitroaromatic compounds in water at r.t. We show that the key to the access to stabilized Au-NCs within SCNPs, instead to larger Au-NPs that grow in size over time, is the control of the (Au(III))/(betaketoester (AEMA)) ratio employed during the synthesis. As proof-of-concept of the catalytic activity of Au-NCs/SCNPs in water at r.t., we illustrate the fast reduction of nitrophenol to aminophenol, as well as the conversion of nitrobenzene to aniline in excellent yield. Finally, we show the efficient transformation in water of 3-(4nitrophenyl)-1,3-oxazolidin-2-one to 3-(4-aminophenyl)-1,3-oxazolidin-2-one—a

#### 4. Gold Nanocluster Synthesized within Single-Chain Nanoparticles as Catalytic Nanoreactors in Water

common motif contained in several drugs like Rivaroxaban, Sutezolid, and Linezolid—using the Au-NCs/SCNPs as catalytic nanoreactors. We hope this work will inspire the synthesis of other metal-NCs/SCNPs for advanced catalysis in aqueous media.

## 4.7. References

1. Valdez, C.E.; Smith, Q.A.; Nechay, M.R.; Alexandrova, A.N. Mysteries of metals in metalloenzymes. *Acc. Chem. Res.* **2014**, *47*, 3110–3117.
2. Götz, S.; Zechel, S.; Hager, M.D.; Newkome, G.R.; Schubert, U.S. Versatile Applications of Metallopolymers. *Prog. Polym. Sci.* **2021**, *119*, 101428.
3. Womble, C.T.; Kuepfert, M.; Cohen, A.E.; Weck, M. Multicompartment Polymeric Nanoreactors for Non-Orthogonal Cascade Catalysis. *Macromol. Rapid Commun.* **2019**, *40*, 1800580.
4. Latorre-Sánchez, A.; Pomposo, J.A. Recent bioinspired applications of single-chain nanoparticles. *Polym. Int.* **2016**, *65*, 855–860.
5. Pomposo, J.A.; Moreno, A.J.; Arbe, A.; Colmenero, J. Local Domain Size in SingleChain Polymer Nanoparticles. *ACS Omega* **2018**, *3*, 8648–8654.
6. Xiong, T.M.; Garcia, E.S.; Chen, J.F.; Zhu, L.Y.; Alzona, A.J.; Zimmerman, S.C. Enzymelike catalysis by single chain nanoparticles that use transition metal cofactors. *Chem. Commun.* **2022**, *58*, 985–988.
7. Rubio-Cervilla, J.; González, E.; Pomposo, J.A. Advances in Single-Chain Nanoparticles for Catalysis Applications. *Nanomaterials* **2017**, *7*, 341.
8. Rothfuss, H.; Knöfel, N.D.; Roesky, P.W.; Barner-Kowollik, C. Single-Chain Nanoparticles as Catalytic Nanoreactors. *J. Am. Chem. Soc.* **2018**, *140*, 5875–5881.
9. ter Huurne, G.M.; Palmans, A.R.A.; Meijer, E.W. Supramolecular Single-Chain Polymeric Nanoparticles. *CCS Chem.* **2019**, *1*, 64–82.
10. Verde-Sesto, E.; Arbe, A.; Moreno, A.J.; Cangialosi, D.; Alegría, A.; Colmenero, J.; Pomposo, J.A. Single-chain nanoparticles: Opportunities provided by internal and external confinement. *Mater. Horiz.* **2020**, *7*, 2292–2313.
11. Mundsinger, K.; Izuagbe, A.; Tuten, B.; Roesky, P.; Barner-Kowollik, C. Single Chain Nanoparticles in Catalysis. *Angew. Chem. Int. Ed.* **2023**, e202311734.
12. He, J.; Tremblay, L.; Lacelle, S.; Zhao, Y. Preparation of Polymer Single Chain Nanoparticles Using Intramolecular Photodimerization of Coumarin. *Soft Matter* **2011**, *7*, 2380–2386.

4. Gold Nanocluster Synthesized within Single-Chain Nanoparticles as Catalytic Nanoreactors in Water
13. Fan, W.Z.; Tong, X.; Farnia, F.; Yu, B.; Zhao, Y. CO<sub>2</sub>-Responsive Polymer Single-Chain Nanoparticles and Self-Assembly for Gas-Tunable Nanoreactors. *Chem. Mater.* **2017**, *29*, 5693–5701.
14. Yang, Z.R.; Yang, X.; Guo, Y.H.; Kawasaki, H. A Review on Gold Nanoclusters for Cancer Phototherapy. *ACS Appl. Bio Mater.* **2023**, *6*, 4504–4517.
15. Mordini, D.; Mavridi-Printezi, A.; Menichetti, A.; Cantelli, A.; Li, X.K.; Montalti, M. Luminescent Gold Nanoclusters for Bioimaging: Increasing the Ligand Complexity. *Nanomaterials* **2023**, *13*, 648.
16. He, Z.; Shu, T.; Su, L.; Zhang, X.J. Strategies of Luminescent Gold Nanoclusters for Chemo-/Bio-Sensing. *Molecules* **2019**, *24*, 3045.
17. Li, S.H.; Tian, W.J.; Liu, Y.Y. The ligand effect of atomically precise gold nanoclusters in tailoring catalytic properties. *Nanoscale* **2021**, *13*, 16847–16859.
18. Casteleiro, B.; Martinho, J.M.G.; Farinha, J.P.S. Encapsulation of gold nanoclusters: Stabilization and more. *Nanoscale* **2021**, *13*, 17199–17217.
19. Haruta, M.; Yamada, N.; Kobayashi, T.; Iijima, S. Gold catalysts prepared by coprecipitation for low-temperature oxidation of hydrogen and of carbon monoxide. *J. Catal.* **1989**, *115*, 301–309.
20. Nasaruddin, R.R.; Chen, T.K.; Yan, N.; Xie, J.P. Roles of thiolate ligands in the synthesis, properties and catalytic application of gold nanoclusters. *Coord. Chem. Rev.* **2018**, *368*, 60–79.
21. Shi, Q.; Qin, Z.; Sharma, S.; Li, G. Recent progress in heterogeneous catalysis by atomically and structurally precise metal nanoclusters. *Chem. Rec.* **2021**, *21*, 879–892.
22. Biswas, S.; Das, S.; Negishi, Y. Advances in Cu nanocluster catalyst design: Recent progress and promising applications. *Nanoscale Horiz.* **2023**, *8*, 1509–1522.
23. Matus, M.F.; Häkkinen, H. Understanding ligand-protected noble metal nanoclusters at work. *Nature Rev. Mater.* **2023**, *8*, 372–389.
24. Zhang, L.; Zheng, H.C.; Gan, Y.H.; Wu, B.D.; Chen, Z.H.; Wei, S.S.; Zhang, G.Y.; Zhang, S.J.; Pan, B.C.; Chen, C.C. An all-in-one approach for synthesis and functionalization of nano colloidal gold with acetylacetone. *Nanotechnology* **2022**, *33*, 075605.

4. Gold Nanocluster Synthesized within Single-Chain Nanoparticles as Catalytic Nanoreactors in Water
25. Sanchez-Sanchez, A.; Arbe, A.; Kohlbrecher, J.; Colmenero, J.; Pomposo, J.A. Efficient Synthesis of Single-Chain Globules Mimicking the Morphology and Polymerase Activity of Metalloenzymes. *Macromol. Rapid Commun.* **2015**, *36*, 1592–1597.
26. Robles-Hernández, B.; González, E.; Pomposo, J.A.; Colmenero, J.; Alegría, A. Water dynamics and self-assembly of single-chain nanoparticles in concentrated solutions. *Soft Matter* **2020**, *16*, 9738–9745.
27. Gu, S.; Wunder, S.; Lu, Y.; Ballauff, M.; Fenger, R.; Rademann, K.; Jaquet, B.; Zaccone, A. Kinetic Analysis of the Catalytic Reduction of 4-Nitrophenol by Metallic Nanoparticles. *J. Phys. Chem. C* **2014**, *118*, 18618–18625.
28. Yamamoto, H.; Yano, H.; Kouchi, H.; Obora, Y.; Arakawa, R.; Kawasaki, H. N,N-Dimethylformamide-stabilized gold nanoclusters as a catalyst for the reduction of 4-nitrophenol. *Nanoscale* **2012**, *4*, 4148–4154.
29. Vetráková, L.; Ladányi, V.; Al Anshori, J.; Dvorák, P.; Wirz, J.; Heger, D. The absorption spectrum of cis-azobenzene. *Photochem. Photobiol. Sci.* **2017**, *16*, 1749–1756.
30. Noschese, A.; Buonerba, A.; Canton, P.; Milione, S.; Capacchione, C.; Grassi, A. Highly efficient and selective reduction of nitroarenes into anilines catalyzed by gold nanoparticles incarcerated in a nanoporous polymer matrix: Role of the polymeric support and insight into the reaction mechanism. *J. Catal.* **2016**, *340*, 30–40.

**5. Consecutive One-Pot Alkyne Semihydrogenation/  
Alkene Dioxygenation Reactions by Pt(II)/Cu(II)  
Single-Chain Nanoparticles in Green Solvent**



## 5.1. Motivation

This work was sparked by the pressing need for sustainable progresses in catalysis, particularly for the design of nanocatalysts that can carry out multi-step chemical reactions all in one reaction vessel. Realizing these environmental and economic drawbacks of using toxic solvents and the difficulties that are accompanied by purifying processes in the classical multi-step synthesis, we could focus on overcoming these challenges. Here, we developed a facile methodology that afforded heterobimetallic Pt(II)/Cu(II) single-chain polymer nanoparticles (SCNPs) in a sequential manner, capitalizing both on metal-ligand coordination for intramolecular folding and their synergistic catalytic activity. Thus, this strategy is greener in N-butylpyrrolidone use as a nontoxic solvent and displays the efficiency and selectivity of such bimetallic SCNPs in consecutive one-pot alkyne semihydrogenation and alkene dioxygenation reactions. This work, through this contribution, tries to make a successful attempt at making its contribution to the larger goal of sustainable chemistry, as the above-said complex multi-metallic SCNPs may open new vistas in the synthesis and application of these highly versatile and multi-functional nanocatalysts.

## 5.2. Introduction

Metal-ligand coordination allows intramolecularly folding of ligand-decorated discrete synthetic polymer chains to metallofolded single-chain polymer nanoparticles (SCNPs).<sup>1</sup> SCNPs are intra-chain cross-linked single polymer chains with manifold promising applications, mainly as catalysts, nanosensors and drug nanocarriers.<sup>2</sup> In general, intramolecular folding of the isolated synthetic chains generates locally compact zones within the SCNPs for efficient immobilization of catalytic active species, luminophores or drugs.<sup>3</sup> To some extent, the intrachain folding of discrete synthetic polymer chains to SCNPs resembles the folding of certain proteins to their precise functional conformation (*i.e.*, native state).<sup>4</sup> In particular, metallo-folded SCNPs leverage the dual role played by the metal: as a folding element *via* intra-chain metal-ligand coordination, and as an immobilized functional center for subsequent catalysis.<sup>5</sup> The number and catalytic

applications of metallo-folded SCNPs as enzyme-mimetic nanoentities have grown significantly in recent years.<sup>6,7</sup> In a seminal work, Terashima *et al.* reported Ru-containing amphiphilic SCNPs to catalyze the reduction of cyclohexanone to cyclohexanol in water.<sup>8</sup> Pomposo *et al.* pioneered the introduction of metallo-folded Cu(II)-containing SCNPs showing catalytic selectivity in alkyne homocoupling reactions,<sup>5</sup> and single-chain globules mimicking the morphology and polymerase activity of metalloenzymes.<sup>9</sup> He *et al.* prepared metallo-folded SCNPs containing Ni-thiolate complexes showing excellent thermal stability under aerobic conditions and excellent activity and selectivity during the photocatalytic reduction of CO<sub>2</sub> to CO.<sup>10</sup> Zimmerman *et al.* developed “clickase” SCNPs displaying enzyme-like “click” catalysis *in vivo* and enabling efficient cell surface glycan editing.<sup>11</sup> Taton *et al.* reported SCNPs containing Ag(I)-*N*-heterocyclic carbene (NHC) linkages as NHC pre-catalysts for the benzoin condensation reaction.<sup>12</sup> Yang *et al.* synthesized metal-containing SCNPs in concentrated solutions at room temperature (r.t.) by introducing electrostatic repulsion and intra-chain crosslinking by coordination with Cu(II) or Fe(II) or Fe(III) ions.<sup>13</sup> Tan *et al.* synthesized enzyme-mimetic SCNPs with chiral Fe(II)-oxazoline complexes for efficient asymmetric sulfa-Michael addition of thiols to  $\alpha,\beta$ -unsaturated ketones in water at r.t.<sup>14</sup> More recently, Pomposo *et al.* developed a method to upcycling poly(vinyl chloride) (PVC) waste to efficient catalytic Cu(II)-containing SCNPs.<sup>15</sup> Current advances in catalysis utilizing SCNPs have been recently reviewed by the Barner-Kowollik team.<sup>16</sup>

However, introduction of at least two distinct metal species in SCNPs although highly desirable is still synthetically challenging. In a pioneering work, Lemcoff *et al.* synthesized Rh(I)/Ir(I) SCNPs although their catalytic properties were not evaluated.<sup>17</sup> Subsequently, Barner-Kowollik *et al.* synthesized heterobimetallic Eu(III)/Pt(II)-SCNPs<sup>18</sup> and Au(I)/Y(III)-SCNPs<sup>19</sup> in which only one of the two metal ions, Pt(II) or Au(I), was used for catalysis, while the other was employed for sensing or intrachain folding (Eu(III) or Y(III), respectively). More recently, the same group decorated SCNPs folded through ferrocene units with Pd(II) atoms, which proved to be an active catalyst for the intramolecular hydroamination of an aminoalkyne.<sup>20</sup>

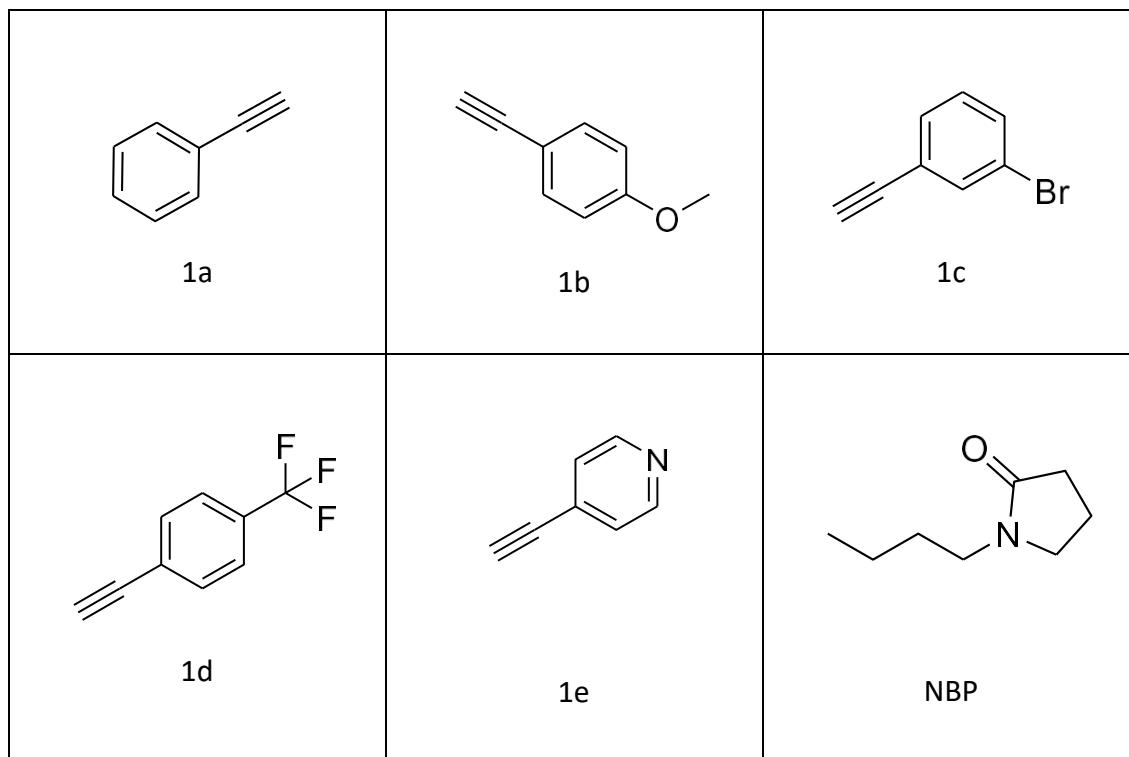
Advanced heterobimetallic nanocatalysts for carrying out multistep chemical processes in a single reaction vessel are currently of great interest in academia and industry.<sup>21</sup> Often, however, major costs of many consumer products synthesized in multistep processes are incurred in the purification and isolation of intermediates.<sup>22</sup> Additionally, replacement of toxic organic solvents by green solvents has attracted significant interest.<sup>23</sup> To the best of our knowledge, bimetallic SCNPs that would allow consecutive one-pot reactions to be performed in a green solvent have not been reported. To fill this gap, we report herein the proof of concept of heterobimetallic SCNPs through the synthesis of Pt(II)/Cu(II)-SCNPs. We show that these can serve as advanced soft nanocatalysts to perform consecutive one-pot alkyne semihydrogenation / alkene dioxygenation reactions in *N*-butylpyrrolidone (NBP) as a green solvent.

### 5.3. Materials and methods

#### 5.3.1. Materials

Methyl methacrylate (MMA) (99%), (2-acetoacetoxy)ethyl methacrylate (AEMA) (95%), 2,2'-azo(2-methylpropionitrile) (AIBN) ( $\geq 98\%$ ), *p*-carboxybenzenesulfonazide (*p*-CBSA) (97%), triethylamine (Et<sub>3</sub>N) (>99%), dichloromethane (CH<sub>2</sub>Cl<sub>2</sub>) (anhydrous,  $\geq 99.8\%$ ), ethyl acetate (EtOAc) (anhydrous, 99.8%), diethyl ether (Et<sub>2</sub>O) (ACS reagent, anhydrous, >99.0%), deuterated chloroform (CDCl<sub>3</sub>) (99.96 atom % D, containing 0.03% (v/v) tetramethylsilane), *N,N*-dimethylformamide (DMF) ( $\geq 99.9\%$ ), *n*-hexane (Hex) (>95%), *N*-butylpyrrolidinone (NBP) ( $\geq 99.5\%$ ), (1,5-cyclooctadiene)platinum(II) dichloride (Pt(COD)Cl<sub>2</sub>), copper (II) acetate (Cu(OAc)<sub>2</sub>) (98%), magnesium sulphate (Mg<sub>2</sub>SO<sub>4</sub>) (anhydrous,  $\geq 99.5\%$ ), phenylacetylene (1a) (98%) were purchased from Sigma-Aldrich and used, unless specified, as received. 2-Cyanoprop-2-ylidithiobenzoate (CPDB) ( $\geq 97\%$ ) was purchased from Strem Chemicals. Methanol (MeOH) (synthesis grade) and THF (HPLC grade) were purchased from Scharlab. 1-Ethynyl-4-methoxybenzene (1b) (>98.0% by GC), 3-bromophenylacetylene (1c) (>98.0% by GC), 4-ethynylbenzotrifluoride (1d) (>98.0% by GC), 4-Pyridylacetylene (1e) (>98.0% by GC) were purchased from TCI Chemicals. *N*-Hydroxyphthalimide (NHPI) (98%) was purchased from BLDPharm. Purified

water was obtained from a Thermo Scientific apparatus (Barnstead TII Pure Water System). AIBN was recrystallized from methanol. MMA was purified by distillation before use. AEMA was purified by passing through alumina.



### 5.3.2. Techniques

$^1\text{H}$  nuclear magnetic resonance (NMR) spectra were obtained at room temperature (r.t.) using a Bruker spectrometer operating at 400 MHz with  $\text{CDCl}_3$  as the solvent. Size exclusion chromatography (SEC) data were acquired using a PL-GPC 50 instrument from Agilent Technologies, which integrates differential refractive index (DRI) and multi-angle light scattering (MALS) detectors. DMF containing 0.1% of LiBr with a flow of 1.0 mL/min was used as an eluent. A PLgel MIXED, 7.5 x 50 mm, 10  $\mu\text{m}$ , guard column, and a PLgel 500  $\text{\AA}$ , 7.5 x 300 mm, 5  $\mu\text{m}$ , or a PL PolarGel-M, 7.5 x 300 mm, 8  $\mu\text{m}$ , HPLC columns were used. The molecular weights of the different samples were determined using a  $dn/dc$  value of 0.0608. SEC data were analysed using Wyatt's ASTRA Software (version 8.1). Dynamic light scattering (DLS) measurements were carried out at r.t. on a Malvern

Zetasizer Nano ZS apparatus. Metal content in the single-chain nanoparticles was determined by inductively coupled plasma-mass spectrometry (ICP-MS). Fourier transform infrared (IR) spectra were recorded at r.t. on a JASCO 3600 FTIR spectrometer. Elemental analysis (EA) were performed in a Euro EA3000 elemental analyzer (CHNS).

## 5.4. Procedures

### 5.4.1. Synthesis of P0

In a typical procedure, MMA (3 mL, 28.2 mmol), AEMA (2.63 mL, 15.58 mmol), CPDB (22.2 mg, 0.1 mmol) and AIBN (16.5 mg, 1 mmol) were dissolved in EtOAc (10.45 mL). The solution was degassed by bubbling N<sub>2</sub> for 15 min. The copolymerization reaction was carried at 65 °C for 24 h. After isolation of the resulting copolymer P0 by precipitation in MeOH, it was dried under dynamic vacuum until constant weight. Yield: 94.0%.  $\beta$ -ketoester content (<sup>1</sup>H NMR): 30 mol%. *M*<sub>w</sub> (SEC) = 73.6 kDa,  $\bar{D}$  (SEC) = 1.17.

### 5.4.2. Synthesis of P1

The synthesis of P1 was conducted under light-protected conditions. The process involved dissolving 300 mg (0.47 mmol) of P0 in 10 mL of CH<sub>2</sub>Cl<sub>2</sub> at r.t. Next, *p*-CBSA (12.25 mg, 0.35 eq.) and Et<sub>3</sub>N (0.4 mL, 2.87 mmol) were added to the solution, which was then stirred for 24 h protected from light. Upon completion of the reaction, the resulting solution was concentrated and precipitated in MeOH, and the functionalized copolymer, P1, was dried in a vacuum oven in the absence of light. Yield: 76%.  $\alpha$ -diazo- $\beta$ -ketoester content (EA): 19 mol%. *M*<sub>w</sub> (SEC) = 75.3 kDa,  $\bar{D}$  (SEC) = 1.15, *R*<sub>h</sub> (DLS) = 12.5 nm.

**Table 3.** Elemental analysis (EA) results of P0 and P1

Sample	C (%)	H (%)	N (%)
P0	57.41	7.51	-
P1	55.62	6.65	4.16

### 5.4.3. Synthesis of P1-SCNPs (as a control)

The synthesis of P1-SCNPs from P1 was achieved *via* irradiation with ultraviolet light. 15 mg (0.07 mmol) of P1 were dissolved in 15 mL of DMF and the solution was exposed to UV light irradiation (365 nm) for 1 h. Subsequently, the reaction was quenched by the addition of liquid nitrogen. The resulting P1-SCNPs were precipitated with diethyl ether and dried under dynamic vacuum. Yield: 92%.  $M_w$  (SEC) = 75.6 kDa,  $\bar{D}$  (SEC) = 1.11,  $R_h$  (DLS) = 10.0 nm.

### 5.4.4. Synthesis of Pt(II)-SCNPs

The synthesis of Pt(II)-SCNPs from P1 was achieved *via* irradiation with ultraviolet light. Specifically, 15 mg (0.07 mmol) of P1 and 1.96 mg (0.00525 mmol) Pt(COD)Cl<sub>2</sub> were dissolved in 15 mL of DMF and the solution was exposed to UV light irradiation (365 nm) for 1 h. Subsequently, the reaction was quenched by the addition of liquid nitrogen. The resulting Pt(II)-SCNPs were precipitated with diethyl ether and dried under dynamic vacuum. Yield: 86%. Pt(II) content (ICP-MS): 0.13 mol%.  $M_w$  (SEC) = 78.4 kDa,  $\bar{D}$  (SEC) = 1.15,  $R_h$  (DLS) = 9.9 nm.

### 5.4.5. Synthesis of Pt(II)/Cu(II)-SCNPs

P1 (15 mg, 0.07 mmol) and Pt(COD)Cl<sub>2</sub> (1.96 mg, 0.00525 mmol) were dissolved in 15 mL of DMF and the solution was exposed to UV light irradiation (365 nm) for 1 h. The reaction was promptly quenched by the addition of liquid nitrogen. A concentrated solution of Cu(OAc)<sub>2</sub> in DMF (0.954 mg, 0.00525 mmol of Cu) was then added dropwise and the reaction mixture was stirred for 24 h. The resulting Pt(II)/Cu(II)-SCNPs were precipitated with diethyl ether and dried under dynamic vacuum. Yield: 79%. Pt(II) content (ICP-MS): 0.14 mol%. Cu(II) content (ICP-MS): 0.43 mol%.  $M_w$  (SEC) = 81.6 kDa,  $\bar{D}$  (SEC) = 1.18,  $R_h$  (DLS) = 8.6 nm.

**Table 4.** Inductively coupled plasma-mass spectrometry (ICP-MS) results of Pt(II)-SCNPs, Cu(II)SCNPs and Pt(II)/Cu(II)-SCNPs

Sample	Pt(II) content (g/mg)	Cu(II) content (g/mg)
Pt(II)-SCNPs	9.29	-
Cu(II)-SCNPs	-	9.11
Pt(II)/Cu(II)-SCNPs	9.73	9.54

#### 5.4.6. Synthesis of Cu(II)-SCNPs (as a control).

P1-SCNPs (15 mg, 0.07 mmol) was dissolved in DMF (15 ml) at r.t. A solution of Cu(OAc)<sub>2</sub> in DMF (0.954 mg, 0.00525 mmol) was then added dropwise, and the reaction mixture was stirred for 24 h. The resulting Cu(II)-SCNPs were precipitated with diethyl ether and dried under dynamic vacuum. Yield: 95%. Cu(II) content (ICP-MS): 0.41 mol%. *M<sub>w</sub>* (SEC) = 77.1 kDa, *D* (SEC) = 1.21, *R<sub>h</sub>* (DLS) = 10.0 nm.

#### 5.4.7. General procedure for the consecutive one-pot alkyne semihydrogenation/alkene dioxygenation reactions catalysed by Pt(II)/Cu(II)-SCNPs in NBP at r.t.

In a 10 mL round bottomed, oven-dried flask, which was previously equipped of magnetic stir bar, 2 mL of Pt(II)/Cu(II)-SCNPs solution in NBP ([polymer] = 1 mg mL<sup>-1</sup>) were added, followed by 0.07 mmol of the alkyne compound (1a-1e) and the system was sealed with rubber septum. The solution was then degassed by purging argon flow for 5 min. After displacement of atmospheric oxygen, the flask was equipped of a security elastic balloon to ensure both no extra-pressure in the system and, simultaneously, to reduce volatility of solvents and substrates. A low-pressure molecular hydrogen flow was then bubbled in the reaction mixture at r.t. at definite interval of times (10 min bubbling each 20 min until reaction completion). The progress of the reaction was monitored by thin layer chromatography (TLC) using EtOAc and Hex as eluents. After the semihydrogenation reaction was complete, 13.68 mg (0.084 mmol) of *N*-hydroxyphthalimide was added to the solution at r.t. and under air (open flask). The

progress of the reaction was monitored by TLC using EtOAc and *n*-hexane as eluents. After reaction completion, 10 mL of water was added to the solution. The resultant mixture was extracted with EtOAc (3 x 5 mL) and successively washed with water (3 x 5 mL). The organic solution was dried over anhydrous Mg<sub>2</sub>SO<sub>4</sub>, filtered and evaporated to give a residue that was purified on silica gel column chromatography using Hex and EtOAc as eluents to afford the corresponding  $\beta$ -Keto-*N*-alkoxyphthalimide product (3a3e).

## 5.5. Results and discussion

The synthetic procedure followed in this work to produce Pt(II)/Cu(II)-SCNPs is depicted schematically in Figure 74. Initially, the monomers (2-acetoacetoxy)ethyl methacrylate (AEMA) and methyl methacrylate (MMA), which functions as a spacer, were copolymerized *via* reversible addition fragmentation chain-transfer (RAFT) polymerization<sup>5</sup> yielding the random copolymer P0 (Figure 74A). Subsequently, P0 with a content of  $\beta$ -ketoester functional groups of 30 mol%, a weight-average molecular weight of  $M_w = 73.6$  kDa and a narrow dispersity of  $\mathcal{D} = 1.17$  was decorated with 19 mol% of  $\alpha$ -diazo- $\beta$ -ketoester functional groups -using *p*-carboxybenzenesulfonazide (*p*-CBSA) as the diazo transfer reagent<sup>-23</sup> leaving 11 mol%  $\beta$ -ketoester functional groups unreacted (see Figure 74B).

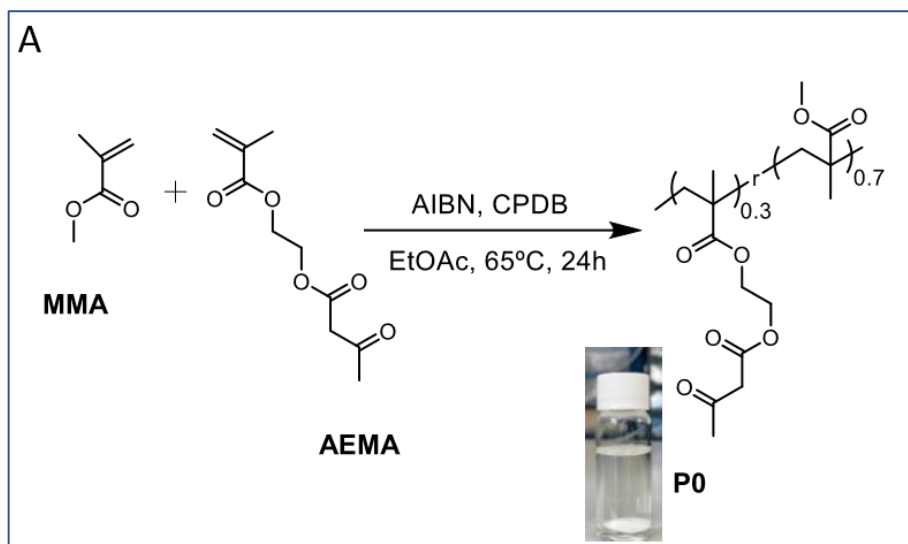


**Figure 74A.** Preparation of a random copolymer P0 containing naked  $\beta$ -ketoester functional groups (30 mol%) *via* reversible addition fragmentation chain-transfer (RAFT) polymerization (MMA = methyl methacrylate; AEMA = (2-acetoacetoxy)ethyl methacrylate; AIBN = azobisisobutyronitrile; CPDB = 2-cyanoprop-2-ylidithiobenzoate; EtOAc = ethyl acetate).

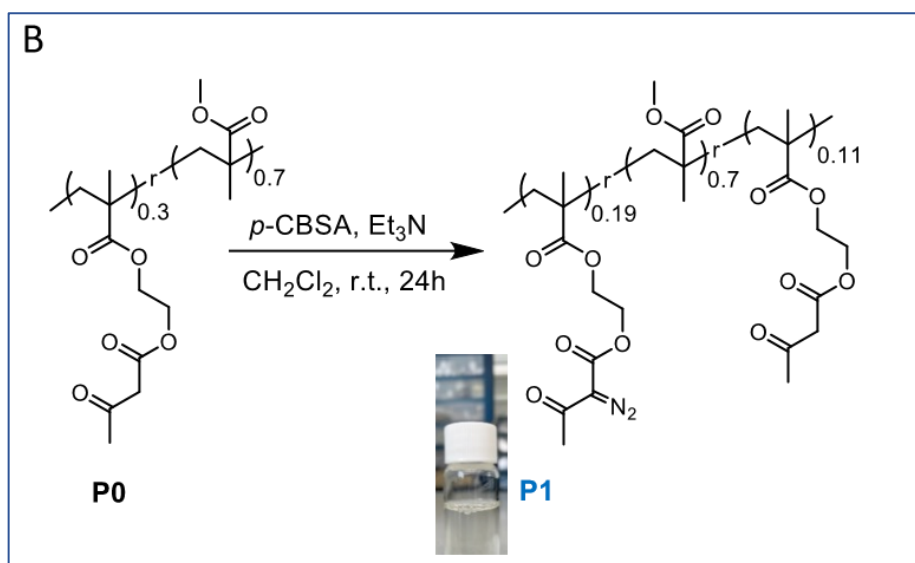


**Figure 74B.** Decoration of P0 with  $\alpha$ -diazo- $\beta$ -ketoester functional groups (19 mol%) to give polymeric precursor P1 (*p*-CBSA = *p*-carboxybenzenesulfonazide; Et<sub>3</sub>N = trimethylamine; CH<sub>2</sub>Cl<sub>2</sub> = dichloromethane).

5. Consecutive One-Pot Alkyne Semihydrogenation/Alkene Dioxygenation Reactions by Pt(II)/Cu(II) Single-Chain Nanoparticles in Green Solvent

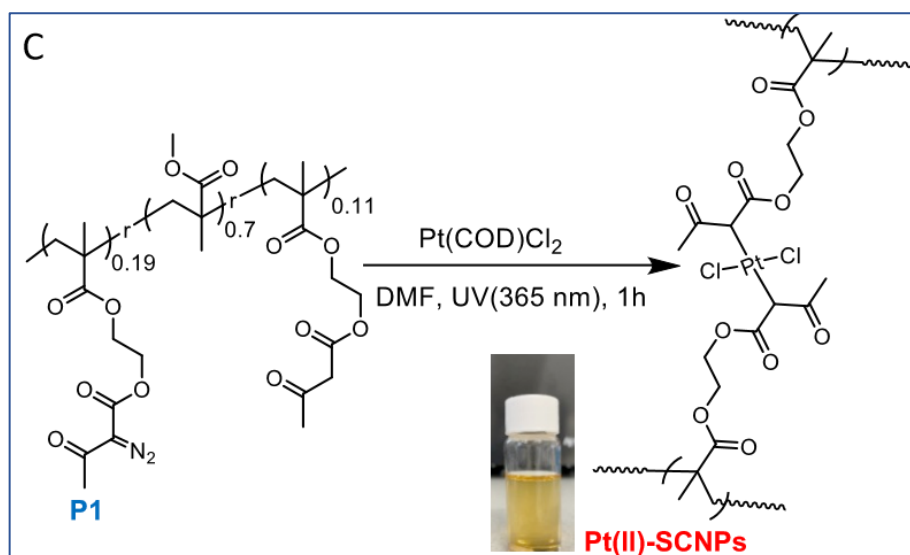


**Figure 74C.** Folding of precursor P1 at high dilution *via* photoactivated carbene generation at  $\lambda_{\text{exc}} = 365 \text{ nm}$  in the presence of dichloro(1,5cyclooctadiene)Pt(II) (Pt(COD)Cl<sub>2</sub>) to generate Pt(II)-SCNPs (DMF = dimethylformamide).

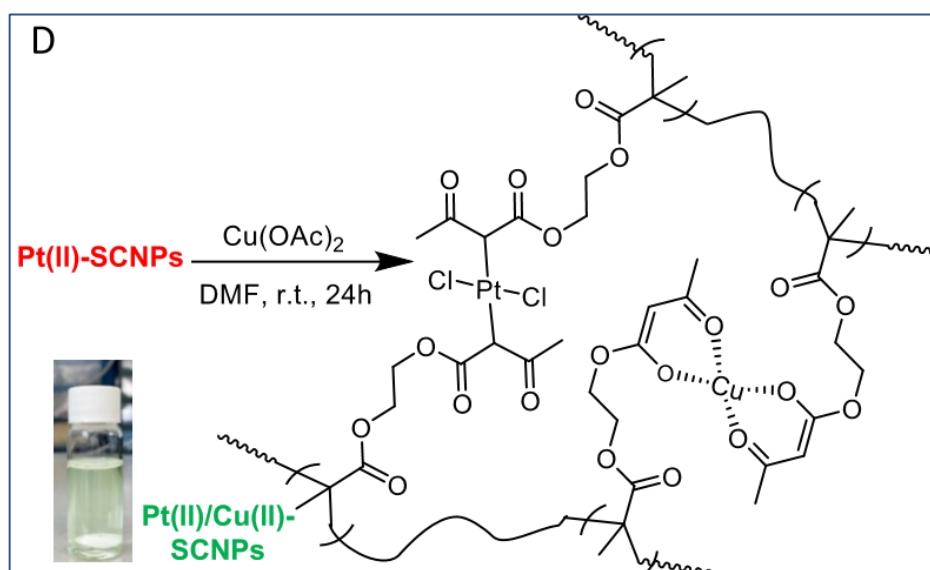


**Figure 74D.** Schematic illustration of the synthesis of Pt(II)/Cu(II)-SCNPs: (D) Additional folding of Pt(II)-SCNPs at high dilution *via* Cu(II) complexation by residual  $\beta$ -ketoester functional groups of Pt(II)-SCNPs (11 mol%) to give heterobimetallic Pt(II)/Cu(II)-SCNPs (Cu(OAc)<sub>2</sub> = Cu(II) acetate).

Upon the diazo transfer reaction, the resulting polymeric precursor P1 showed  $M_w = 75.3 \text{ kDa}$  and  $\mathcal{D} = 1.11$ , in very good agreement with the expected  $M_w$  (75.1 kDa) based on its chemical composition. Infrared (IR) spectroscopy measurements confirmed the appearance of the characteristic infrared vibration band of the diazo moieties centred at

$\nu \approx 2200 \text{ cm}^{-1}$  (Figure 75). Next, heterobimetallic Pt(II)/Cu(II)-SCNPs were sequentially synthesized from P1 containing both  $\alpha$ -diazo- $\beta$ -ketoester and unreacted  $\beta$ -ketoester functional groups. Thus, P1 was first irradiated with UV light at  $\lambda_{\text{exc}} = 365 \text{ nm}$  at high dilution in the presence of dichloro(1,5-cyclooctadiene)Pt(II) (Pt(COD)Cl<sub>2</sub>) to generate the highly reactive carbene species from the  $\alpha$ -diazo- $\beta$ -ketoester functional groups and to promote intrachain cross-linking *via* Pt(II) bonding. Successful folding of P1 to Pt(II)-SCNPs was confirmed through size exclusion chromatography (SEC) and dynamic light scattering (DLS) measurements whereas the IR spectrum of Pt(II)-SCNPs showed the disappearance of the characteristic diazo IR vibration band after 1h of UV irradiation (see Figure 75).

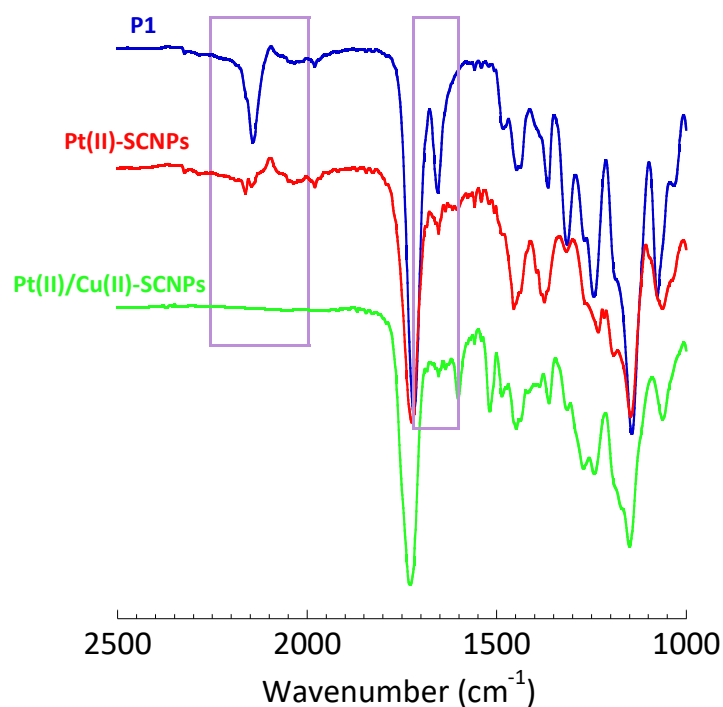


**Figure 75.** Infrared (IR) spectra of polymeric precursor P1, Pt(II)-SCNPs and Pt(II)/Cu(II)-SCNPs.

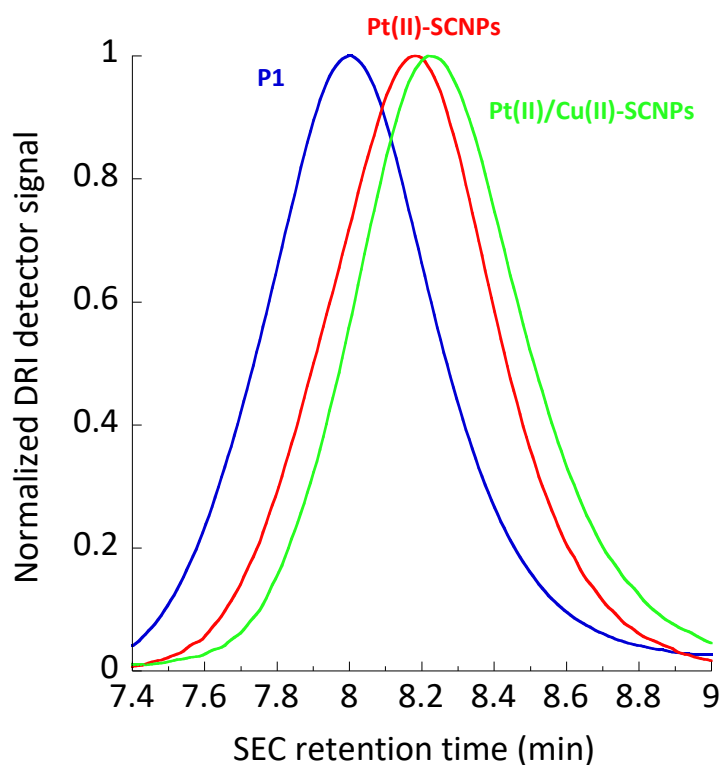


**Figure 76.** Size exclusion chromatography (SEC) traces (differential refractive index (DRI) detector, DMF, 1 mL min<sup>-1</sup>) of P1, Pt(II)-SCNPs and Pt(II)/Cu(II)-SCNPs.

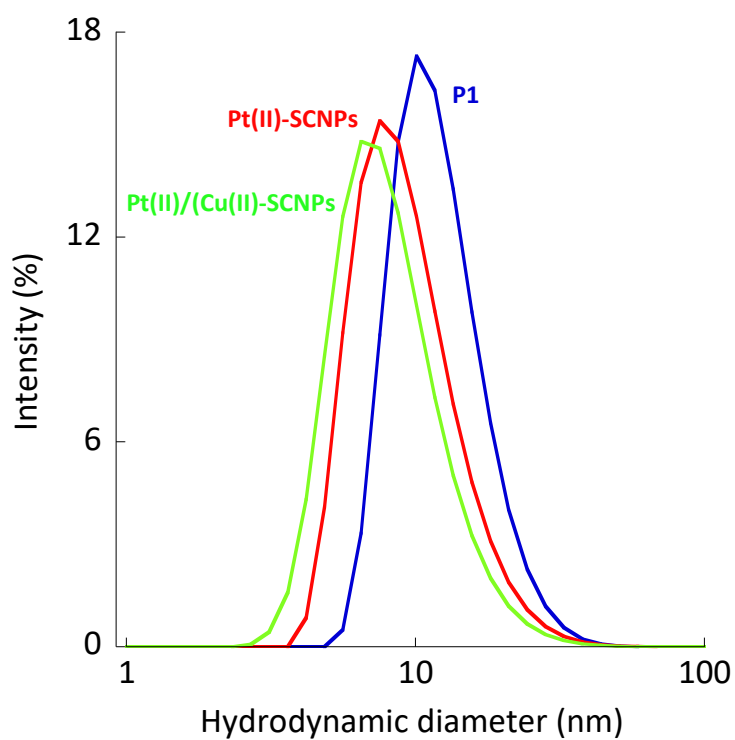


**Figure 77.** Dynamic light scattering (DLS) size distributions of P1, Pt(II)-SCNPs and Pt(II)/Cu(II)-SCNPs.

**Table 5.** Dynamic light scattering<sup>a</sup> (DLS) and size exclusion chromatography<sup>b</sup> (SEC) results.

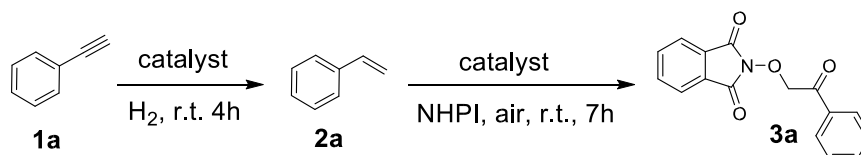
Sample	<sup>a</sup> Particle Size (nm)	%	St. Dev.	PDI	<sup>b</sup> Mw (kDa)	$\bar{D}$
<b><i>α</i>-dialdo-PMA</b>	<b>12.54</b>	99.4	4.9	0.406	75.3	1.105
PMA-SCNPs	10.01	99.8	4.7	0.409	75.6	1.110
<b>Pt(II)-SCNPs</b>	<b>9.87</b>	99.6	4.6	0.257	78.4	1.145
Cu(II)-SCNPs	9.98	99.9	2.4	0.518	77.1	1.210
<b>Pt(II)/Cu(II)-SCNPs</b>	<b>8.62</b>	99.8	4.2	0.291	81.6	1.184

<sup>a</sup>Determined by DLS in DMF

<sup>b</sup>Determined by SEC in DMF with poly(methyl methacrylate)  $dn/dn = 0.0608$

SEC results showed an increase in retention time and, hence, a reduction in hydrodynamic size for the Pt(II)-SCNPs when compared to P1 (Figure 76). The average hydrodynamic diameter of P1,  $D_h = 12.5$  nm as determined by DLS, was found to decrease to  $D_h = 9.9$  nm upon formation of the Pt(II)-SCNPs (Fig. 2C). In a final step, Cu(II) ions were incorporated via Cu(II)-( $\beta$ -ketoester)<sub>2</sub> complex formation from Cu(II) acetate<sup>5</sup> and the naked  $\beta$ -ketoester functional groups of the Pt(II)-SCNPs (11 mol%) affording the heterobimetallic Pt(II)/Cu(II)-SCNPs (see Figure 74D). Confirmation of the successful (additional) folding of Pt(II)-SCNPs to Pt(II)/Cu(II)-SCNPs was obtained from SEC (Figure 76) and DLS (Figure 77) measurements. The average hydrodynamic diameter of Pt(II)/Cu(II)SCNPs was found to be  $D_h = 8.6$  nm. The less pronounced reduction in hydrodynamic size upon the second folding event can be attributed to the reduced degrees of freedom available after the first Pt(II)-induced compaction.<sup>24</sup> Confirmation of the complexation of Cu(II) ions by the residual  $\beta$ -ketoester groups was obtained from the IR spectrum of the Pt(II)/Cu(II)-SCNPs. As illustrated in Figure 75A, it shows the characteristic vibration bands located at *ca.* 1600  $\text{cm}^{-1}$  (stretching C=O vibration, enol tautomer bonded to Cu) and *ca.* 1515  $\text{cm}^{-1}$  (stretching C=C vibration, enol tautomer bonded to Cu).<sup>5</sup> Inductively coupled plasma-mass spectrometry (ICP-MS) measurements showed a content of Pt(II) and Cu(II) ions in the Pt(II)/Cu(II)-SCNPs of 9.7  $\mu\text{g}/\text{mg}$  and 9.5  $\mu\text{g}/\text{mg}$ , respectively.

**Table 6.** Comparison of Pt(II)/Cu(II)-SCNPs to different control catalysts for consecutive alkyne semihydrogenation / alkene dioxygenation reactions at r.t. (see ESI).



Entry	Catalyst	Solvent	Conv. of 1a (%)	Yield of 2a (%)	Yield of 3a (%)
1	Pt(COD)Cl <sub>2</sub>	DMF	91	60	-
2	Cu(OAc) <sub>2</sub>	DMF	-	-	-
3	Pt(COD)Cl <sub>2</sub> + Cu(OAc) <sub>2</sub>	DMF	91	58	62
4	P1-SCNPs <sup>a</sup>	DMF	-	-	-
5	Pt(II)-SCNPs	DMF	≥ 99	90	-
6	Cu(II)-SCNPs <sup>b</sup>	DMF	-	-	-
7	Pt(II)-SCNPs + Cu(II)-SCNPs	DMF	≥ 99	93	82
8	Pt(II)/Cu(II)-SCNPs	DMF	≥ 99	95	84
9	Pt(II)/Cu(II)-SCNPs	NBP	≥ 99	95	80

<sup>a</sup>Synthesized-as a control-from P1 without Pt(COD)Cl<sub>2</sub>

<sup>b</sup>Synthesized-as a control-from P1-SCNPs

With the Pt(II)/Cu(II)-SCNPs in hand, we envisioned the use of these heterobimetallic SCNPs as advanced soft nanocatalysts for consecutive one-pot (incompatible) reactions. In this sense, we selected the preparation of  $\beta$ -Keto-*N*-alkoxyphthalimides as intermediates of great utility for the pharmaceutical and agricultural industries<sup>25</sup> by starting from phenylacetylene substrates. Table 1 shows a comparison of Pt(II)/Cu(II)SCNPs to different control catalysts for consecutive one-pot phenylacetylene (1a) semihydrogenation / styrene (2a) dioxygenation with air and *N*-hydroxyphthalimide (NHPI) at r.t. to give the  $\beta$ -keto-*N*-alkoxyphthalimide 3a as the target product. With Pt(COD)Cl<sub>2</sub> (1 mol% Pt(II)) 1a was transformed to 2a in DMF with a yield of 60%, with a large portion of 1a completely hydrogenated to ethylbenzene (Table 1, entry 1). As expected, Cu(OAc)<sub>2</sub> (1 mol% Cu(II)) was found to be inefficient for the semihydrogenation of 1a (Table 1, entry 2). A combination of Pt(COD)Cl<sub>2</sub> for the

semihydrogenation reaction, and subsequently adding  $\text{Cu}(\text{OAc})_2$  for the dioxygenation reaction gives a yield of 2a and 3a of 58% and 62%, respectively (Table 1, entry 3). Pt(II)SCNPs (0.13 mol% Pt(II)) provided 2a in 90% yield (Table 1, entry 5) whereas both P1SCNPs synthesized as a control from P1 without  $\text{Pt}(\text{COD})\text{Cl}_2$  and Cu(II)-SCNPs synthesized also as a control from P1-SCNPs were totally inefficient (Table 1, entries 4 and 6). A combination of Pt(II)-SCNPs for the semihydrogenation reaction, and subsequently addition of Cu(II)-SCNPs (0.41 mol% Cu(II)) for the dioxygenation reaction provided 2a and 3a in 93% and 82% yield, respectively (Table 1, entry 7). Pleasingly, the heterobimetallic Pt(II)/Cu(II)-SCNPs (0.14 mol% Pt(II) and 0.43 mol% Cu(II)) allowed the consecutive one-pot semihydrogenation / dioxygenation reaction to be carried out in DMF with exceptional selectivity and yield (Table 1, entry 8). Moreover, a similar efficiency and selectivity was found for the heterobimetallic Pt(II)/Cu(II)-SCNPs when the consecutive one-pot semihydrogenation of 1a / dioxygenation of 2a with air and NHPI was carried out in NBP as a green solvent to replace toxic DMF.

Figure 78A shows the consumption of 1a and the production of 2a over time during the semihydrogenation reaction in NBP, as determined by  $^1\text{H}$  NMR spectroscopy. The kinetics of this reaction was followed through the disappearance of the alkyne proton of 1a denoted as a in Fig. 3B and the concomitant appearance of the vinylic protons denoted as b, c and d of 2a (Figure 78B). In the late stages, after 210 min. of reaction time, hydrogenation of 2a to ethylbenzene (secondary product) takes place (see Figure 78B). After 4h of reaction time, the conversion of 1a was found to be complete and the yield of 2a of 95%. The turnover number (moles of product per mole of catalyst, TON) of the Pt(II)/Cu(II)-SCNPs in the semihydrogenation reaction was  $\text{TON} = 665$  (a value 10 times higher than that of  $\text{Pt}(\text{COD})\text{Cl}_2$  at 1 mol% Pt(II)).

5. Consecutive One-Pot Alkyne Semihydrogenation/Alkene Dioxygenation Reactions by Pt(II)/Cu(II) Single-Chain Nanoparticles in Green Solvent

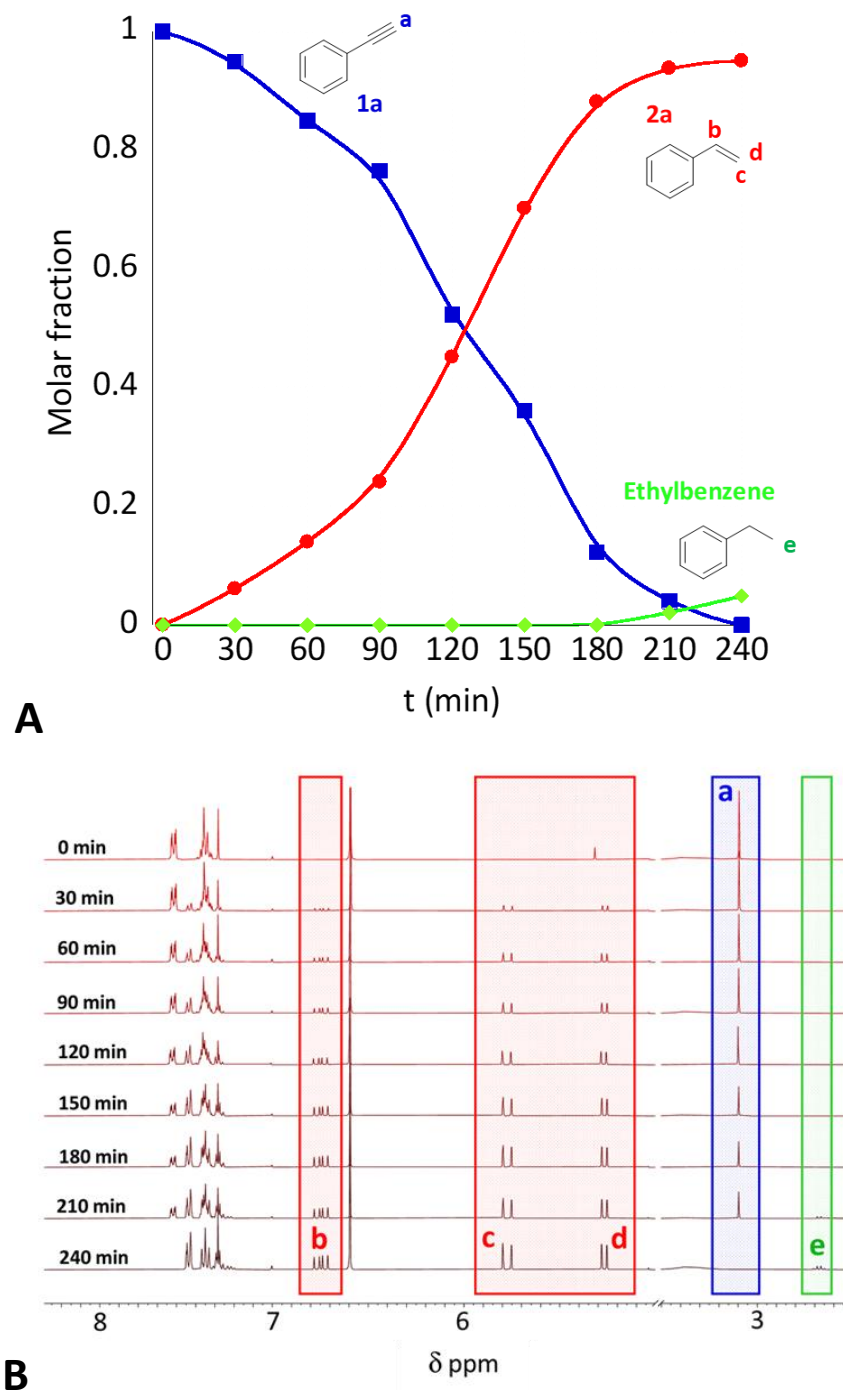


**Figure 78.** Consecutive one-pot alkyne semihydrogenation / alkene dioxygenation reactions catalysed by Pt(II)/Cu(II)-SCNPs in NBP at r.t.: (A) Evolution of the concentration of phenylacetylene (1a), styrene (2a) and ethylbenzene (secondary product) during the alkyne semihydrogenation reaction. (B) Reaction kinetics of the semihydrogenation reaction as followed by  $^1\text{H}$  NMR spectroscopy through the disappearance of alkyne proton of 1a denoted as a, and the concomitant appearance of the vinylic protons denoted as b, c and d of 2a. Notice the presence of a small peak (denoted as e) coming from ethylbenzene after 210 min of reaction time.

5. Consecutive One-Pot Alkyne Semihydrogenation/Alkene Dioxygenation Reactions by Pt(II)/Cu(II) Single-Chain Nanoparticles in Green Solvent

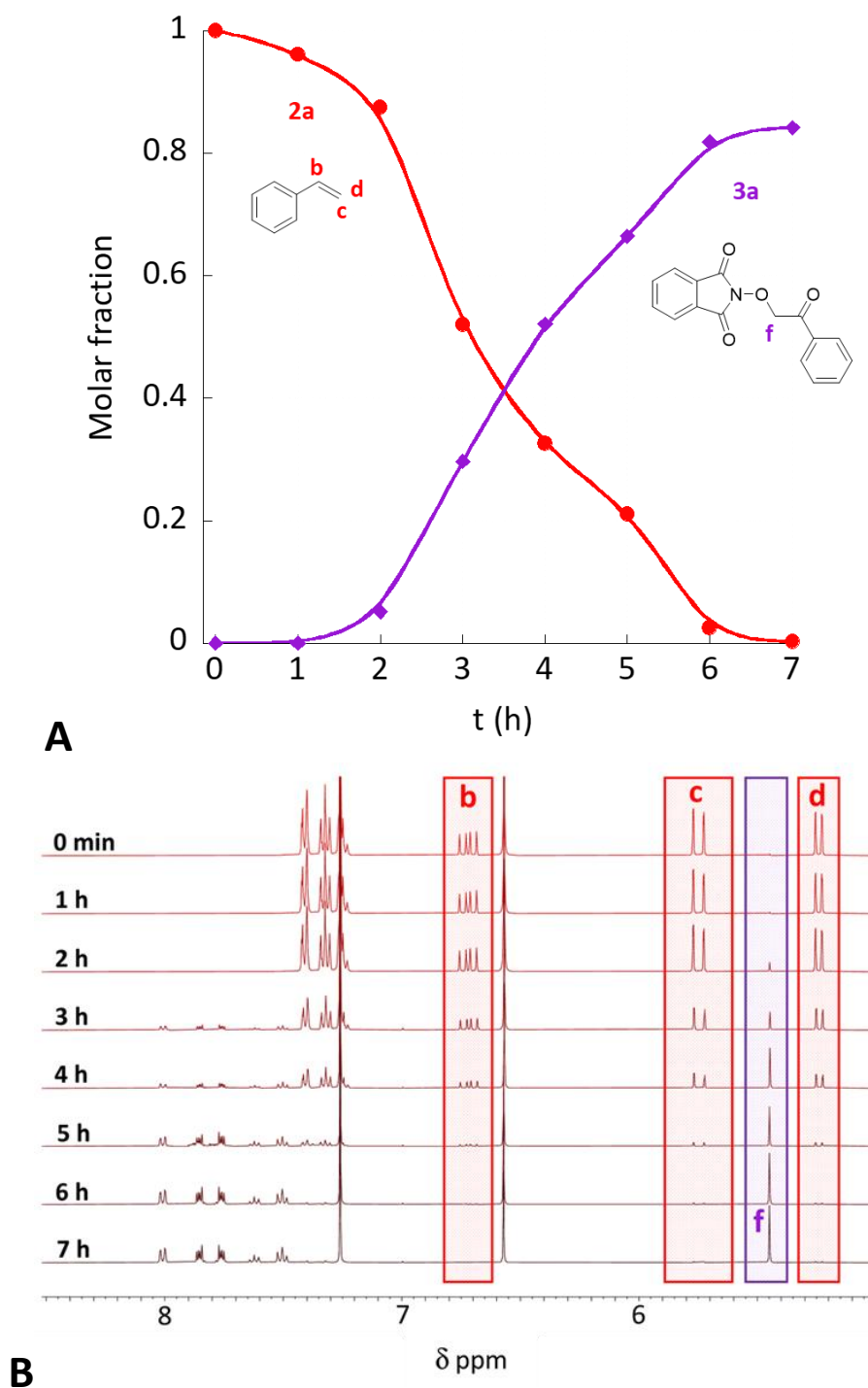
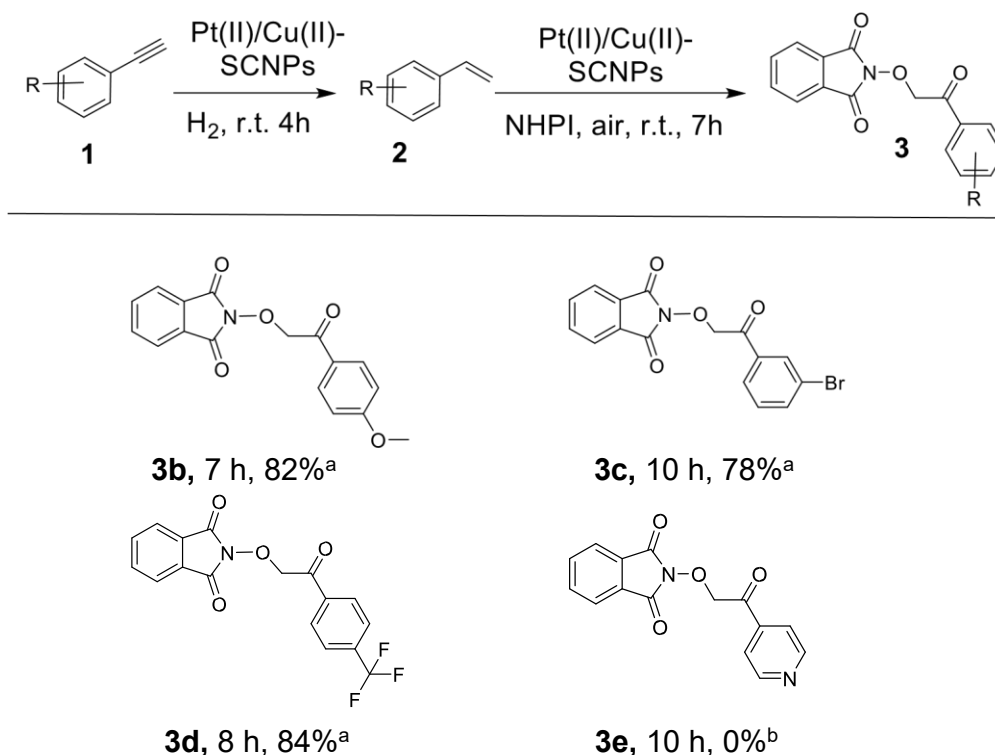


**Figure 79.** (A) Evolution of the amount of intermediate 2a and product 3a (2-(2-oxo-2phenylethoxy)isoindoline-1,3-dione) during the dioxygenation reaction with air and *N*hydroxyphthalimide (NHPI). (B) Reaction kinetics of the dioxygenation of intermediate 2a as followed by <sup>1</sup>H NMR spectroscopy through the disappearance of the vinylic protons of 2a, and the simultaneous appearance of the methylene protons denoted as f of 3a.

Without isolation of 2a, the crude of the semi-hydrogenation reaction containing the bimetallic Pt(II)/Cu(II)-SCNPs was used for the dioxygenation of 2a with air and NHPI at r.t. in the same reaction vessel. Figure 79A illustrates the consumption of 2a and the generation of the  $\beta$ -keto-*N*-alkoxyphthalimide 3a as the target product over reaction time. Also in this case, the kinetics of the dioxygenation reaction in NBP was followed directly by  $^1\text{H}$  NMR spectroscopy through the disappearance of the vinylic protons denoted as b, c and d of 2a (Figure 79B) and the simultaneous appearance of the methylene protons denoted as f in Figure 79B of 3a. After 7 h of reaction time, the conversion of 2a was nearly complete and the yield of 3a was 80%. The turnover number of the Pt(II)/Cu(II)SCNPs in the dioxygenation reaction was TON = 182. This value is 30-fold higher than that corresponding to the classical procedure involving  $\text{Cu}(\text{OAc})_2$  as catalysts.<sup>25</sup>

**Scheme 1.** Substrate scope of the consecutive one-pot alkyne semihydrogenation / alkene dioxygenation reactions catalysed by Pt(II)/Cu(II)-SCNPs in NBP at r.t.



<sup>a</sup>Isolated yield. <sup>b</sup>Dioxygenation of intermediate 2e did not take place.

Finally, we investigated the substrate scope of the consecutive one-pot alkyne semihydrogenation / alkene dioxygenation reactions catalysed by Pt(II)/Cu(II)-SCNPs in NBP (see Scheme 1). Substituted phenylacetylene at the *para*-position with a methoxy group gave the  $\beta$ -keto-*N*-alkoxyphthalimide 3b in 82% isolated yield. The reaction of phenylacetylene bearing a bromine atom at *meta*-position produced the corresponding  $\beta$ -keto-*N*-alkoxyphthalimide 3c in 78% isolated yield. The introduction of a trifluoromethyl substituent in phenylacetylene at the *para*-position afforded the  $\beta$ -keto-*N*-alkoxyphthalimide 3d in 84% isolated yield. In contrast, 4-ethynylpyridine failed to react under our reaction conditions during the dioxygenation reaction.

All products derived from the scope of the reaction were subjected to rigorous Nuclear Magnetic Resonance ( $^1\text{H}$  NMR) spectroscopy analysis. Each product's  $^1\text{H}$  NMR spectrum was meticulously recorded, providing detailed insights into the molecular transformations occurring during the catalytic cycles. The spectra displayed distinct resonances corresponding to the unique proton environments within the  $\beta$ -keto-*N*-alkoxyphthalimides, the targeted reaction products. These  $^1\text{H}$  NMR profiles not only confirmed the successful formation of the desired compounds but also demonstrated the absence of unreacted starting materials or by-products at detectable levels.



5. Consecutive One-Pot Alkyne Semihydrogenation/Alkene Dioxygenation Reactions by Pt(II)/Cu(II) Single-Chain Nanoparticles in Green Solvent

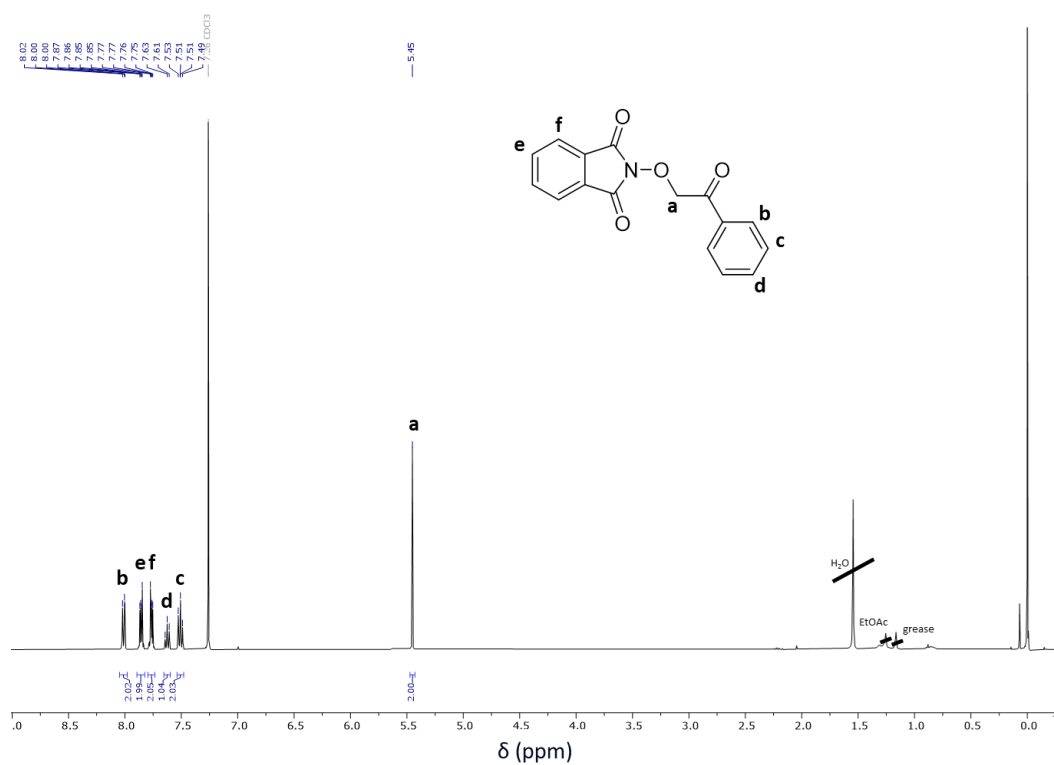


**Figure 82.**  $^1\text{H}$  NMR spectrum of 3a in  $\text{CDCl}_3$ .

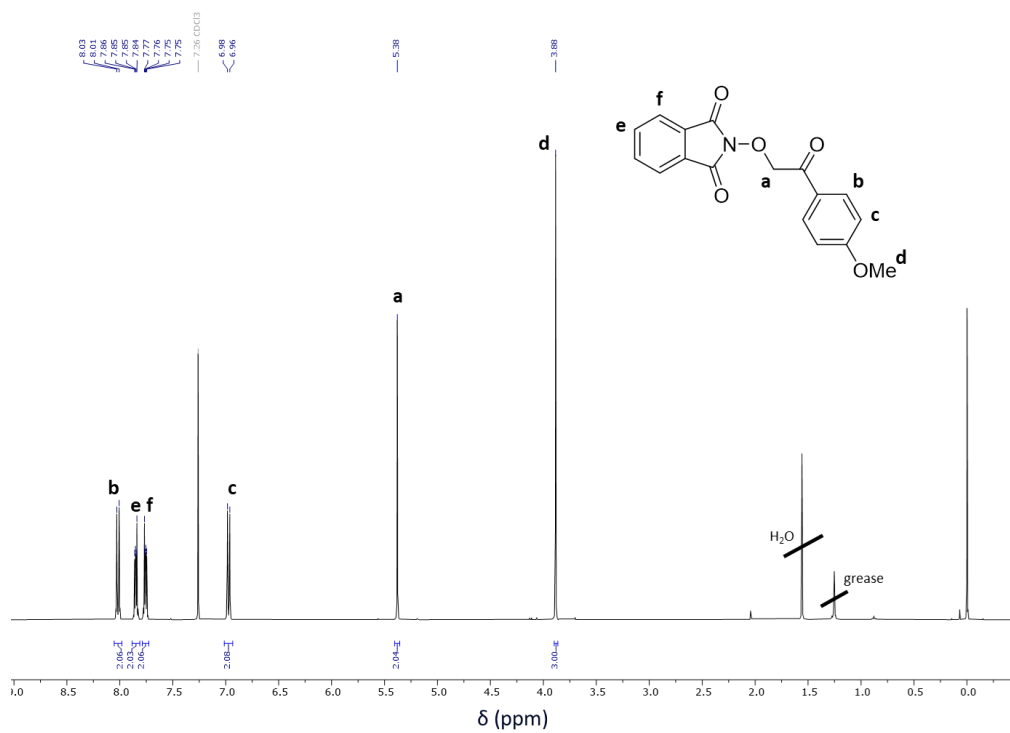


**Figure 83.**  $^1\text{H}$  NMR spectrum of 3b in  $\text{CDCl}_3$ .

5. Consecutive One-Pot Alkyne Semihydrogenation/Alkene Dioxygenation Reactions by Pt(II)/Cu(II) Single-Chain Nanoparticles in Green Solvent

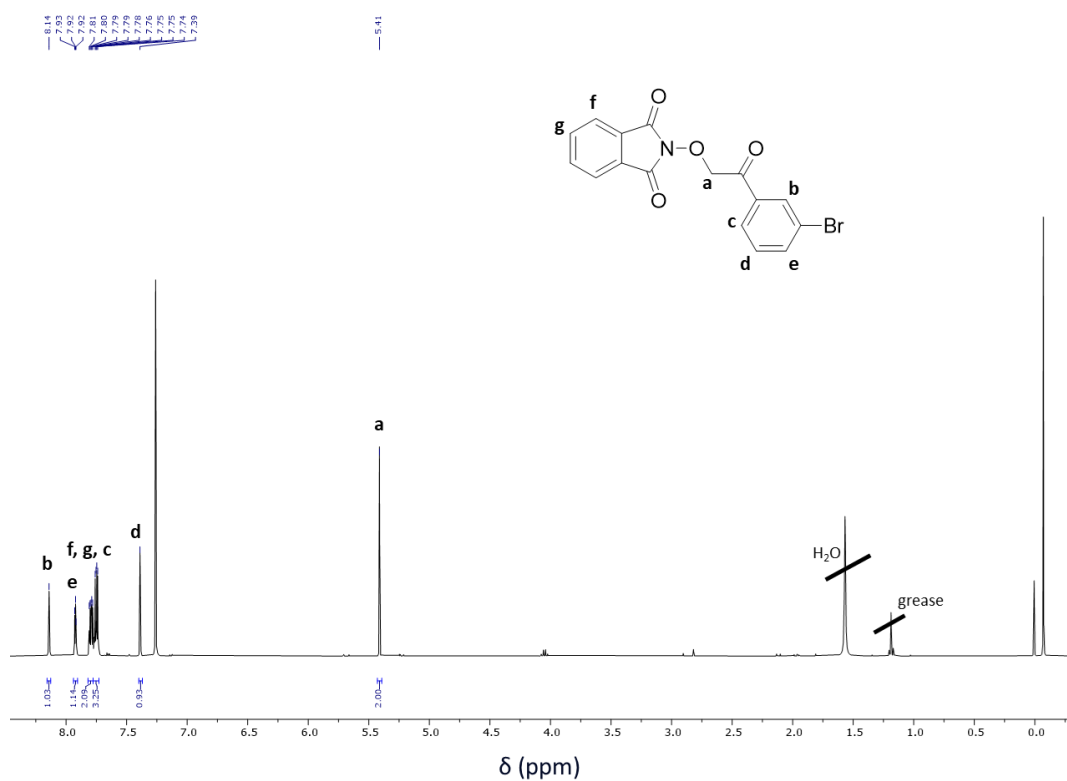


Figure 84. <sup>1</sup>H NMR spectrum of 3c in CDCl<sub>3</sub>.

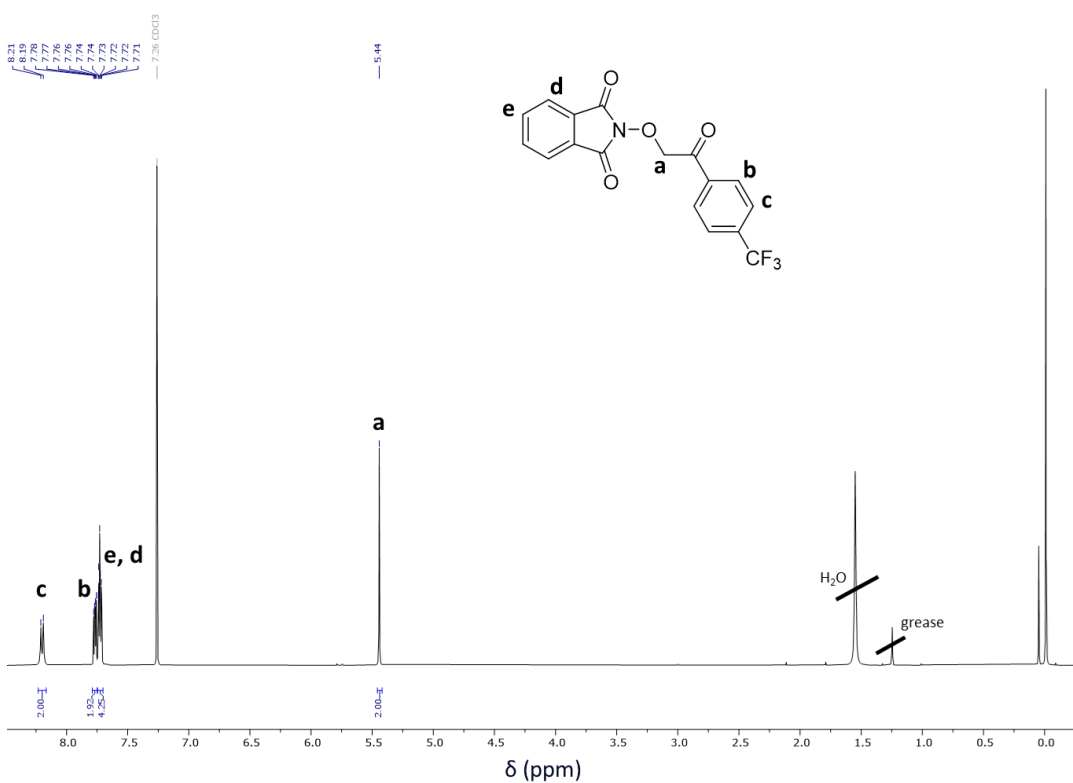


Figure 85. <sup>1</sup>H NMR spectrum of 3d in CDCl<sub>3</sub>.

In the subsequent phase of the experimental procedure, specifically the dioxygenation step, a critical observation was made regarding the role of the catalyst in the continuation of the reaction. After the initial phase of alkyne semihydrogenation, the heterobimetallic Pt(II)/Cu(II) single-chain nanoparticles, serving as the catalyst, were deliberately removed from the reaction mixture to assess their necessity for the reaction's progression.

To achieve this, the catalyst was isolated by inducing precipitation followed by centrifugation, a method effective in separating solid particulates from the liquid substrate. This step was meticulously performed to ensure that the catalyst was completely segregated from the reaction medium. Subsequently, the reaction mixture was allowed to proceed under the previously established conditions (room temperature, ambient air exposure) for an additional three hours.

Remarkably, it was observed that the reaction did not advance beyond its interim stage post-catalyst removal. The yield of the desired product,  $\beta$ -keto-N-alkoxyphthalimide, remained unchanged, clearly indicating that the reaction had ceased upon the removal of the catalyst. This outcome unequivocally demonstrated the indispensable role of the Pt(II)/Cu(II)-SCNPs in driving the dioxygenation process. Without the presence of these catalytic entities, the reaction could not proceed to completion, underscoring their functionality not merely as facilitators for enhancing reaction rates but as essential components for the occurrence of the reaction itself. Thus, this step effectively highlighted the catalyst's vital involvement in the chemical transformation being studied, offering profound insights into the mechanistic pathways of multistep catalytic reactions in green chemistry applications.

5. Consecutive One-Pot Alkyne Semihydrogenation/Alkene Dioxygenation Reactions by Pt(II)/Cu(II) Single-Chain Nanoparticles in Green Solvent

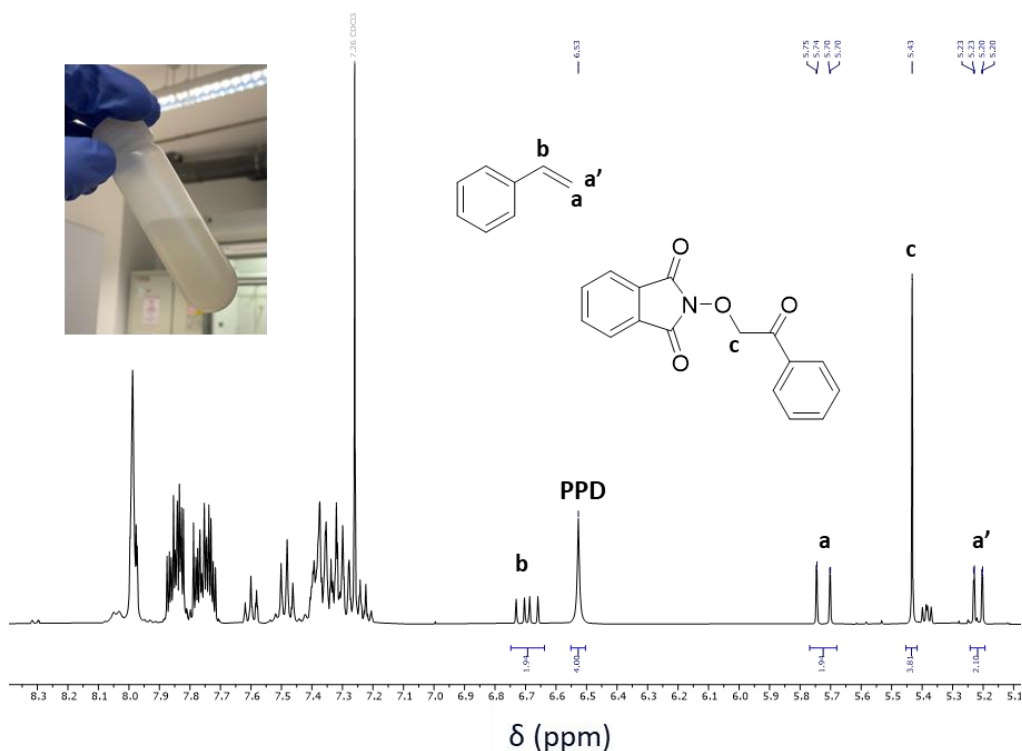


**Figure 86.**  $^1\text{H}$  NMR spectrum of **1a** synthesized with Pt(II)/Cu(II)-SCNPs after 3h of reaction time (yield: 33.6 %). Solvent:  $\text{CDCl}_3$ . Internal standard: PPD.

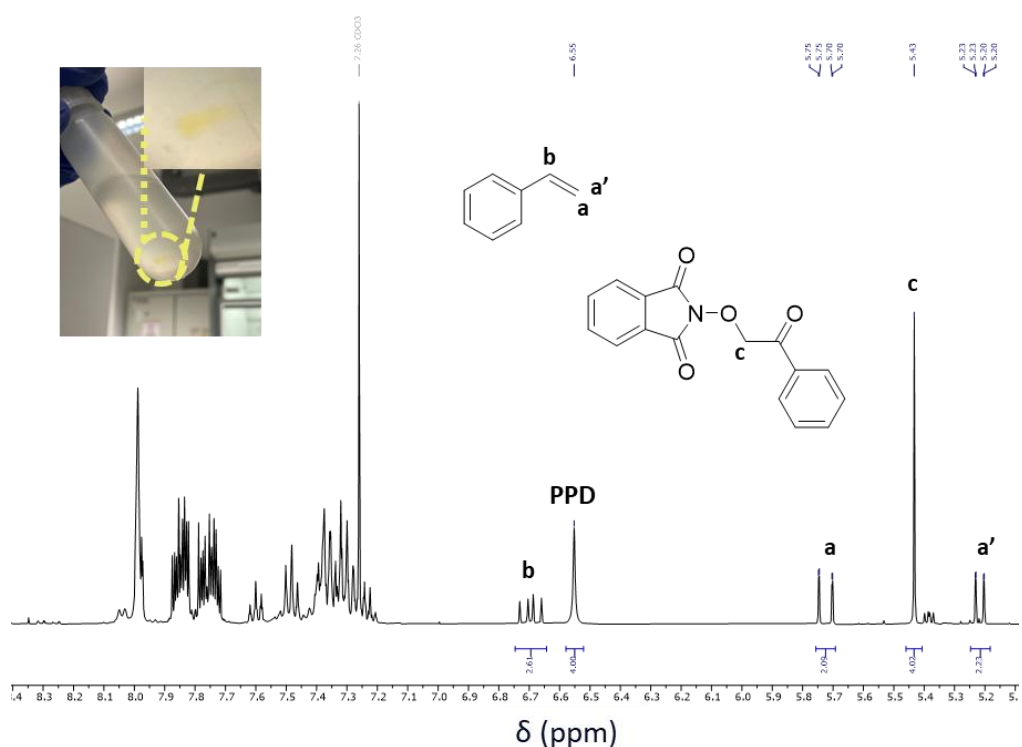


**Figure 87.**  $^1\text{H}$  NMR spectrum of **1a** synthesized with Pt(II)/Cu(II)-SCNPs by removing the catalyst after 3h of reaction time and allowing the reaction to proceed additionally for 4h without Pt(II)/Cu(II)-SCNPs (yield: 35.5 %). Solvent:  $\text{CDCl}_3$ . Internal standard: PPD.

## 5.6. Conclusions

We report bimetallic SCNPs as highly efficient soft nanocatalysts allowing consecutive one-pot (incompatible) reactions to be performed at r.t. in a green solvent. We synthesized a polymeric precursor, P1, containing both  $\alpha$ -diazo- $\beta$ -ketoester and naked  $\beta$ -ketoester functional groups. Pt(II) and Cu(II) ions were sequentially introduced as intra-chain folding elements of P1 chains at high dilution, as revealed by combining IR, SEC and DLS measurements, yielding catalytically active Pt(II)/Cu(II)-SCNPs. This unique heterobimetallic soft nanocatalyst was shown to be highly efficient for consecutive onepot alkyne semihydrogenation / alkene dioxygenation reactions at r.t. in NBP, as a nontoxic alternative solvent to DMF, affording  $\beta$ -keto-*N*-alkoxyphthalimides as intermediates of great utility for the pharmaceutical and agricultural industries. Critically, this work paves the way to multistep chemical reactions in a single reaction vessel with complex multi-metallic SCNPs as advanced nanocatalysts.

## 5.7. References

1. S. Mavila, C. E. Diesendruck, S. Linde, L. Amir, R. Shikler and N. G. Lemcoff, *Angew. Chem. Int. Ed.*, 2013, **52**, 5767.
2. E. Verde-Sesto, A. Arbe, A. J. Moreno, D. Cangialosi, A. Alegría, J. Colmenero and J. A. Pomposo, *Mater. Horiz.*, 2020, **7**, 2292.
3. J. A. Pomposo, *Single-Chain Polymer Nanoparticles: Synthesis, Characterization, Simulations, and Applications*, John Wiley & Sons, 2017.
4. J. A. Pomposo, *Polym. Int.*, 2014, **63**, 589.
5. A. Sanchez-Sanchez, A. Arbe, J. Colmenero and J. A. Pomposo, *ACS Macro Lett.*, 2014, **3**, 439.
6. H. Rothfuss, N. D. Knöfel, P. W. Roesky and C. Barner-Kowollik, *J. Am. Chem. Soc.*, 2018, **140**, 5875.
7. J. Rubio-Cervilla, E. González and J. A. Pomposo, *Nanomaterials*, 2017, **7**, 341.
8. T. Terashima, T. Mes, T. F. A. De Greef, M. A. J. Gillissen, P. Besenius, A. R. A. Palmans and E. W. Meijer, *J. Am. Chem. Soc.*, 2011, **133**, 4742.
9. A. Sanchez-Sanchez, A. Arbe, J. Kohlbrecher, J. Colmenero and J. A. Pomposo, *Macromol. Rapid Commun.*, 2015, **36**, 1592.
10. S. Thanneeru, J. Nganga, A. S. Amin, B. Liu, L. Jin, A. Angeles-Boza and J. He, *ChemCatChem.*, 2017, **9**, 1157.
11. J. Chen, J. Wang, K. Li, Y. Wang, M. Gruebele, A. L. Ferguson and S. C. Zimmerman, *J. Am. Chem. Soc.*, 2019, **141**, 9693.
12. S. Garmendia, S. B. Lawrenson, M. C. Arno, R. K. O'Reilly, D. Taton and A. P. Dove, *Macromol. Rapid Commun.*, 2019, **40**, e1900071.
13. W. Xu, D. Xiang, J. Xu, Y. Ye, D. Qiu and Z. Yang, *Polym. Chem.*, 2021, **12**, 172.
14. W. Wang, J. Wang, S. Li, C. Li, R. Tan and D. Yin, *Green Chem.*, 2020, **22**, 4645.
15. A. Blazquez-Martin, E. Verde-Sesto, A. Arbe and J. A. Pomposo, *Angew. Chem. Int. Ed.*, 2023, **62**, e202313502.

16. K. Mundsinger, A. Izuagbe, B. T. Tuten, P. W. Roesky, and C. Barner-Kowollik, *Angew. Chem. Int. Ed.*, 2024, **63**, e202311734.
17. S. Mavila, I. Rozenberg and N. G. Lemcoff, *Chem. Sci.*, 2014, **5**, 4196.
18. N. D. Knöfel, H. Rothfuss, P. Tzvetkova, B. Kulendran, C. Barner-Kowollik and P. W. Roesky, *Chem. Sci.*, 2020, **11**, 10331.
19. J. L. Bohlen, B. Kulendran, H. Rothfuss, C. Barner-Kowollik and P. W. Roesky, *Polym. Chem.*, 2021, **12**, 4016.
20. S. Gillhuber, J. O. Holloway, H. Frisch, F. Feist, F. Weigend, C. Barner-Kowollik and P. W. Roesky, *Chem. Commun.*, 2023, **59**, 4672.
21. T. Dang-Bao, D. Pla, I. Favier and M. Gómez, *Catalysts*, 2017, **7**, 207.
22. S. Kar, H. Sanderson, K. Roy, E. Benfenati and J. Leszczynski, *Chem. Rev.*, 2022, **122**, 3637.
23. J. Sherwood, F. Albericio and B. G. de la Torre, *ChemSusChem*, 2024, e202301639.
24. J. De-La-Cuesta and J. A. Pomposo, *ACS Omega*, 2018, **3**, 15193.
25. T. K. Claus, J. Zhang, L. Martin, M. Hartlieb, H. Mutlu, S. Perrier, G. Delaittre and C. Barner-Kowollik, *Macromol. Rapid Commun.*, 2017, **38**, 1700264.
26. R. Bag, D. Sar and T. Punniyamurthy, *Org. Lett.*, 2015, **17**, 2010.



## **6. Conclusions**



This thesis encapsulates a multifaceted investigation into the synthesis, characterization, and application of single-chain nanoparticles (SCNPs), focusing on their innovative uses in catalysis and environmental monitoring. The sequential development of three distinct but complementary projects illustrate the versatility and potential of SCNPs in catalysis, advancing green chemistry and enhancing environmental sustainability.

- The development of lanthanide-based SCNPs for detecting copper ions in water aligned with the objective of obtaining a simple, efficient, and selective method for monitoring  $\text{Cu}^{2+}$  levels. These SCNPs change fluorescence emission color under UV light in the presence of high copper concentrations, providing an easy and rapid Pass/Fail detection method without sophisticated instrumentation, thereby addressing a crucial public health issue.
- Incorporating gold nanoclusters (Au-NCs) within SCNPs to enhance catalytic efficiency met the objective of exploring their use as catalytic nanoreactors in aqueous environments. The Au-NCs/SCNPs facilitated nitroaromatic compound reductions in water, adhering to green chemistry principles by minimizing hazardous substances and improving reaction efficiency.
- Synthesizing heterobimetallic Pt(II)/Cu(II) SCNPs for consecutive one-pot reactions in a green solvent addresses the challenges of consecutive chemical processes and reliance on toxic organic solvents. The successful catalysis of alkyne semihydrogenation and alkene dioxygenation in N-butylpyrrolidone (NBP) demonstrated the efficiency and selectivity of these SCNPs, fulfilling the objective of offering sustainable alternatives for complex synthetic applications.

The projects undertaken in this thesis directly align with the initial objectives of developing single-chain nanoparticles (SCNPs) using innovative synthesis methods to address key challenges in environmental monitoring, catalysis, and green chemistry. Thanks to the development and synthesis of new SCNPs for visual detection of copper

ions, catalysis using gold nanoclusters, and heterobimetallic systems for complex reactions in green solvents, this research successfully provides efficient and eco-friendly solutions.

The outcomes of these projects significantly contribute to public health by offering reliable methods for water quality monitoring, and they promote environmental sustainability through the application of advanced nanotechnology and adherence to green chemistry principles. These advancements underscore the potential of SCNPs to revolutionize chemical processes and environmental monitoring, showcasing their versatility and practical viability in addressing contemporary challenges.

## **7. Publications**



This doctoral work has contributed to the following publications:

- Isabel Asenjo-Sanz I.; Claros T.; González E.; Pinacho-Olaciregui, J.; Verde-Sesto, E.; Pomposo, J.A. Significant effect of intra-chain distribution of catalytic sites on catalytic activity in “clickase” single-chain nanoparticles. *Materials Letters*, 304, 130622 (2021).
- Pinacho-Olaciregui, J.; Verde-Sesto, E.; Taton, D.; Pomposo, J.A. Lanthanide Based Single-Chain Nanoparticles as “Visual” Pass/Fail Sensors of Maximum Permissible Concentration of Cu<sup>2+</sup> Ions in Drinking Water. *Macromol. Rapid Commun.*, 2400116 (2024).
- Pinacho-Olaciregui, J.; Verde-Sesto, E.; Taton, D.; Pomposo, J.A. Gold Nanoclusters Synthesized within Single-Chain Nanoparticles as Catalytic Nanoreactors in Water. *Polymers*, 16, 378 (2024).
- Pinacho-Olaciregui, J.; Verde-Sesto, E.; Taton, D.; Pomposo, J.A. Consecutive one-pot alkyne semihydrogenation/alkene dioxygenation reactions by Pt(II)/Cu(II) single-chain nanoparticles in green solvent. *Nanoscale*, 16, 9742-9747 (2024).



## **8. Experimental techniques**



## Size Exclusion Chromatography (SEC)

Size exclusion chromatography (SEC), serves to sort molecules as a function of their size.<sup>1</sup> Originating from the work of Moore at Dow Chemical Company, this method is now widely used in both industrial and academic circles for characterizing polymers.<sup>1</sup> GPC operates on the principle of passing a polymer solution through a column of porous particulates (Figure 85).

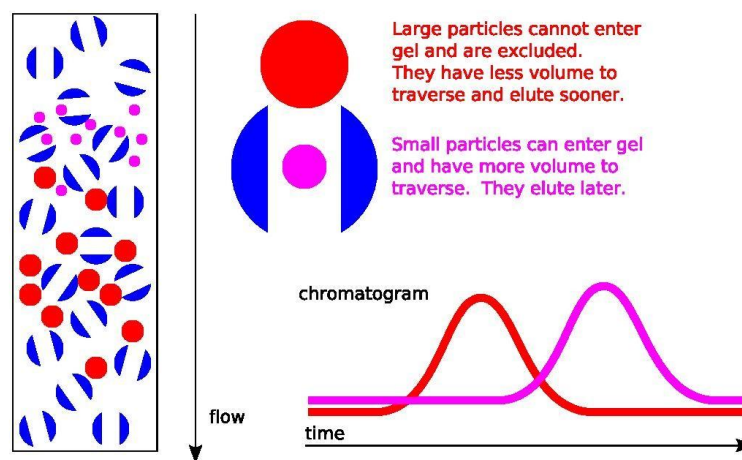


**Figure 88.** Schematic illustration of gel permeation chromatography and how this technique operates.

As a solution of polymers proceeds through this column, macromolecular chains of different sizes will have preferred opportunities for permeating the pores. This will manifest itself as differential elution times. Smaller chains will have more difficulty moving through the column. Their progress will be retarded by significant interactions with the pores. Larger chains will move through the column quite easily. One therefore separates on the basis of the hydrodynamic radius (RH) of the polymers. GPC, thus, is the workhorse for the experimental determination of molecular weight distributions of synthetic polymers. For such analyses, one normally generates a calibration curve using a set of monodisperse polymer standards which have known molecular weights (Mw). The Mw of an unknown sample is then found by interpolating its retention time against this curve. Of critical importance in this method are the concentration sensitive

detectors. Concentration sensitive detectors in GPC include the refractive index (RI) detector and the UV detector. The relationship between the solution's concentration  $c$  and its refractive index  $n$ . The refractive index  $n$  of a solution can be related to that  $n_0$  of the pure solvent and to that  $n_p$  of the analyte by the equation:

$$n \propto n_0 + c(n_p - n_0)$$

Perhaps the most widely used detectors are those based on Ultraviolet (UV) absorptivity, which follow the Beer–Lambert law, and so the absorbance  $A$  of a solution is proportional to its concentration. Unfortunately, these are only applicable to UVactive polymers and therefore are not as universal as Refractive Index (RI) detectors. In contrast to the relative measurements possible with the use of calibration techniques, the introduction of multi-angle light scattering (MALS) detectors has made possible the acquisition of absolute molecular weight (Mw) data. This is because MALS detectors can determinate the molar mass of these polymers without measuring the retention time. This is possible because the angular dispersion of the scattered light is reliant on the dimensions of the analyte, hence providing a direct correlation between the two. It is therefore given by the following equation, where  $I_\theta$  is the intensity of the scattered light at angle  $\theta$ ;  $K$  is an optical constant; and can be read from the y-axis of the detector graph;  $A_2$  is the second virial coefficient, which provides a measure of the polymer's coefficient of expansion in relation to the good solvent;  $R_\theta$  is the Rayleigh ratio for the solvent;  $dn/dc$  is the change in RI (in milliliters per gram) per gram of solute per milliliter for the solution and  $\lambda$  is the wavelength of the light source.

$$I_s \propto M_c (dn/dc)^2$$

Viscometric analysis—which is commonly run in-line with gel permeation chromatography (GPC) setups—presents an avenue to determine the hydrodynamic volume (VH) of polymers by simpler means. The intrinsic viscosity ( $[\eta]$ ) of the solution as expressed in Eq. 2.3 is a quantitative measure of this property, with its linkage to VH—

as suggested by the Einstein–Simha relation—providing a route to derive conformational insight of the polymer.<sup>2</sup> The polymer’s hydrodynamic volume relates to its molar mass (M) and Avogadro’s number ( $N_A$ ), such that the application of the Mark–Houwink–Sakurada equation then arises.

$$V_H = ((M[\eta]) / (2.5 N_A))$$

$$[\eta] = K M^\alpha$$

The parameters K and  $\alpha$  reveal information about the polymer-solvent system, with the former providing a comparison of the size of the solvating polymer with the solvating molecule, and the latter describing the polymer’s structure, where the value is 0 for a solid sphere, 0.5 for a random coil under theta conditions, between 0.5 and 0.8 for a linear polymer in a favorable solvent, and between 1.8 and 2 for a rigid rod.

It was noted that the collapse of the precursor polymer to SCNP can be followed using GPC in a shape-centric manner, as the drop in hydrodynamic volume can be directly quantified.<sup>3</sup> These types of analyses are critical in decoding the complicated mechanisms underpinning nanoparticle formation and distinguishing the roles of polymer composition and solvent interactions.

The GPC experiments were performed at 30°C using an Agilent 1200 system *via* the following configuration: PLgel 5  $\mu$ m Guard and MIXED-C columns, a differential refractive index (RI) detector (Optilab Rex, Wyatt), a multi-angle laser light scattering (MALLS) detector (MiniDawn Treos, Wyatt), and a viscometric (VI) detector (ViscostarII, Wyatt). The data were collected at 671, 475, and 658 nm respectively. The data were analyzed using ASTRA Software (version 6.1, Wyatt) and were collected using tetrahydrofuran (THF) as the eluent at a flow rate of 1 mL/min.

## Dynamic Light Scattering (DLS)

Dynamic light scattering (DLS) (Figure 86) is a technique that allows the size distribution of small particulate suspensions or polymers in solution to be analyzed. In this technique, a sample is dispersed across and a laser beam, and a detector monitors the intensity of the light scattered at a particular angle. The light that is scattered into many different directions interferes, and the interference patterns that are generated will vary with time because the particles source is moving (Brownian motion). This provides a way to observe how kinetically the scatterers are behaving: ultimately, a correlation function is generated that compares the intensity of light at different points in time and thus shows how the particles are moving.

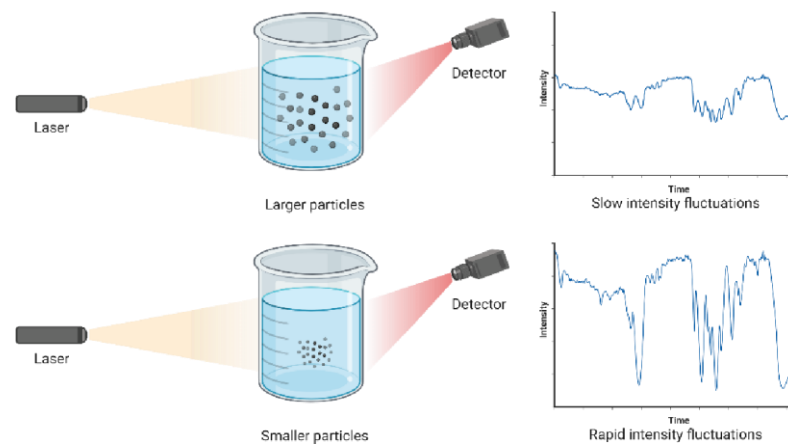


**Figure 89.** Dynamic light scattering (DLS) mechanism and schematic illustration.

The smaller particles will change the intensity of the light more rapidly and hence they will be observed at shorter temporal scales compared to the larger particles, which will change the intensity of light more slowly. It is therefore possible to determine which particle of which size you are seeing in your sample. It is subsequently possible to calculate the particle radius ( $R$ ) from the diffusion coefficient ( $D$ ) for each temporal segment, which is worked out using the Stokes-Einstein equation.<sup>4</sup>

$$R_h = (k_B T) / 6\pi\eta D$$

With the final expression, it is apparent that  $D$  and hence  $R$  is smaller than the same quantities for the stick and slip case: the degrees of freedom evident in a freely joint molecule simply allow it to collide or diffuse on the same time scale. In the enhanced roll regime, the opposite is true, and  $R$  grows with time as per a complex logarithm.

Where  $k_B$  is Boltzmann's constant,  $T$  is the temperature (Kelvin), and  $\eta$  is viscosity, DLS becomes a powerful technique that quantifies the dimensions of single-chain nanoparticles. It will permit the observation of a diminution in the radius of SCNP relative to its precursor entities, thereby shedding some light on the evolution of the size of such nanoparticles.

### Nuclear magnetic resonance (NMR)

In nuclear magnetic resonance (NMR) spectroscopy, an analytical methodology that finds broad use, nuclear excitation within a sample is induced by an external magnetic field, while radiofrequency waves precipitate transitions between the nuclear spin energy levels, or resonance.<sup>5</sup> The latter, dictated by the intramolecular magnetic field that envelops an atom, provides insights into the atomic chemical environment. An external magnetic field modifies the resonant frequency, and such measurements are thus normalized by the aid of a standard reference—usually tetramethylsilane—by which to define the chemical shift, contingent upon the resonance frequencies of the analyte  $\nu$  and reference  $\nu_0$ .

$$\delta = (\nu - \nu_0)/\nu_0$$

$^1\text{H}$  NMR and  $^{13}\text{C}$  NMR spectroscopies are particularly significant in the realm of polymer chemistry, given the prevalence of these nuclei among macromolecular structures and the dispositive value of 1D and 2D spectral analyses in construing a polymer's chemical composition and monitoring the chemical transformations that accrue during the synthesis of single-chain nanoparticles (SCNPs).<sup>6</sup> While such spectroscopy also affords

capabilities for structural and conformational analyses,<sup>7</sup> such applications were not exploited herein; <sup>1</sup>H NMR and <sup>13</sup>C NMR spectra were recorded with the use of a Bruker Avance spectrometer, operating at frequencies of 300, 400, and 500 MHz and equipped with a Z-gradient BBO probe, at ambient temperature, from deuterated solvents.

### **Fourier transform infrared spectroscopy (FTIR)**

Fourier transform infrared spectroscopy (FTIR) is a crucial technique for qualitatively characterizing organics and determining molecular structures. It was used to observe the gain and loss of resonant frequencies corresponding to the creation and dissipation of specific chemical bond networks.<sup>8</sup> This process occurs during the formation of crosslinked network materials following the intrachain folding and collapse process present in the synthesis of single-chain nanoparticles (SCNPs). FTIR spectroscopy offers an advantage over NMR spectroscopy in studying macromolecular structures by acquiring high spectral resolution data across a broad spectral range. In an FTIR spectrometer, it is possible to measure the spectra of a sample concurrently with high spectral resolution over the entire spectral range. This analysis is based on the absorption of electromagnetic radiation (EMR) at resonant frequencies specific to the molecular structure resonance. Consequently, the vibrational frequencies in FTIR spectra can be directly correlated to specific types of chemical bonds. To observe the generation of cross-linked network materials following the intrachain folding and collapse process in SCNP synthesis, FTIR was chosen as an additional diagnostic tool alongside nuclear magnetic resonance (NMR) spectroscopy. The FTIR spectral data were recorded at ambient temperature using 50 scans at a resolution of 4 cm<sup>-1</sup> using a JASCO 3600 FTIR spectrometer (attenuated total reflection (ATR) spectra).

## Ultraviolet–visible spectroscopy (UV-Vis)

Ultraviolet-visible spectroscopy (UV-Vis) is a powerful analytical technique which probes the electronic transitions in materials by shining ultraviolet-visible light, usually in the wavelength range of  $\sim 200\text{--}800\text{ nm}$ .<sup>9</sup> It is especially useful in identifying particular electronic transitions such as  $n\text{--}\pi^*$  and  $\pi\text{--}\pi^*$  in unsaturated systems, and charge transfer transitions in metal-ligand complexes. Despite the preponderance of the use of Nuclear Magnetic Resonance (NMR) and Fourier Transform Infrared (FTIR) spectroscopy to characterize polymers and single-chain nanoparticles (SCNP), UV-Vis spectroscopy is invaluable in studying dramatic chemical transformations such as those induced by chain-transfer agents<sup>10</sup> and the formation of SCNP through metal-ligand interactions.<sup>11</sup> All UV-Vis studies were conducted at ambient temperature with an Agilent 8453A spectroscopy system equipped with a Peltier thermostatic cell holder under the regulation of a T-controller 89090A.



**Figure 90.** Agilent 8453A spectroscopy system.

## Fluorescence spectroscopy

Fluorescence spectroscopy is an analytical technique that is used to tell something about samples based on their intrinsic fluorescent properties. Like ultraviolet-visible (UV-Vis) spectroscopy, it is based on electronic transitions. However, the similarity ends there. In any electronic state, there will be a number of distinct vibrational, upon the absorption of a photon by a fluorescent molecule, an electron is elevated to a higher energy level, causing the molecule to also go to a higher vibrational energy state. Subsequent molecular collisions will cause the molecule to lose enough energy so as to fall down to the lowest vibrational state within the excited electronic level. When the molecule returns from this excited state to its “normal” state (i.e., its ground state), it will emit a photon of a longer wavelength than the one it absorbed.

In fluorescence spectroscopy, as fluorophore solutions are struck with light, the Stokes shift occurs when the excited electrons swiftly tumble to the lowest vibrational level of the excited state. The Stokes shift is the difference between the wavelengths at the maxima of the excitation and emission spectra and prevents excitation light from hitting the detector, thereby bettering precision in measurement. An emission spectrum is obtained by exciting the fluorophore at its optimal absorption wavelength and scanning across all wavelengths, and an excitation spectrum involves traversing through the absorption spectrum and recording emission intensity at a single wavelength, generally at the peak emission intensity. An interesting aspect of some fluorophores is that their emission spectrum is identical to their excitation spectrum, indicating that the vibrational levels of both the ground and excited states are identical. This independence of the emission spectrum from the excitation wavelength is due to rapid internal conversion to the lowest excited state's vibrational level.<sup>12</sup>

Fluorescence spectroscopy illuminates a sample with light from a source, the wavelength of which is isolated by a monochromator, and the light, which has become fluorescence, is observed through a detector at a 90-degree angle to the excitation light, so the two do not interfere.<sup>13</sup>

Fluorescence spectra were collected at room temperature using an Agilent Cary Eclipse spectrometer, with an excitation wavelength at 256 nm.



**Figure 91.** Agilent Cary Eclipse spectrometer

## **Elemental analysis (EA)**

Elemental analysis (EA) is a family of analytical techniques that strives to determine the elemental composition of a sample. The most common form of EA is CHNS analysis, where the content of carbon, hydrogen, nitrogen, and sulfur are quantified. The sample is subjected to combustion which generates carbon dioxide, water, nitrogen oxide, and sulfur dioxide. By measuring the mass of these combustion products, the proportions of the elements are easily recovered. This analytical technique was employed to understand the composition of the samples under investigation and also to validate the validity of the chemical reactions being carried out.

## **Inductively coupled plasma mass spectrometry (ICP-MS)**

Inductively coupled plasma atomic emission spectroscopy (ICP-AES) represents an advanced analytical method for the elemental analysis and quantitation of atomic constituents, typically metal ions, in a solution. The technique utilizes Inductively Coupled Plasma as a means of atom/ion excitation, where they re-radiate light of unique wavelengths for each element. The plasma source starts with a gas, usually argon, that becomes ionized to generate plasma. The interaction of free electrons with an electromagnetic field both increases the number of ions and raises the temperature of the plasma to 6000-10000K. Once the sample is introduced into this extremely highenergy environment, the thermal energy of the plasma begins to break the molecular bonds of the sample, and atoms are released. These atoms, as they are excited to higher electronic states and then relax back to the ground state, emit photons. The wavelength of these photons is indicative of what elements are present. These emissions are then captured and analyzed by a spectrometer to determine elemental composition.<sup>14</sup> The ICP-AES measurements in this paper were performed using an Agilent 7700X spectrometer.

## **UV irradiation**

Ultraviolet (UV) irradiation experiments were conducted using a Penn PhD Photoreactor M2 system (Penn Photon Devices, LLC) as shown in. The setup utilized a mercury-xenon lamp with filter A9616-05, which allowed for transmittance from 300–400 nm, peak at 365 nm, and a transmittance efficiency in the order of 80%. The UV irradiations, with an intensity of 3.5 W/cm<sup>2</sup> and guided through a UV-light guide and focused by a lens was administered.



**Figure 92.** Penn PhD Photoreactor M2 system

## **Transmission electron microscopy (TEM)**

Transmission electron microscopy (TEM) is an advanced form of microscopy in which a beam of electrons is allowed to pass through a thin specimen, forming an image as it does so. This breakthrough in microscopy was first reported by Knoll and Ruska in 1932, with the latter awarded the 1986 Nobel Prize in Physics for his contribution to the field of microscopy. In the TEM method, an electron gun generates electrons, while magnetic lenses focus these electrons into a beam and direct it toward the specimen. Electrons that pass through the sample are captured by a fluorescent screen, producing an image. The contrast visible in a TEM image is due to the material density of the sample; regions of higher atomic density or higher atomic number elements scatter more electrons and therefore fewer are detected, with this ability of the technique to generate image contrast being exploited. The TEM technique features a much higher resolution than is possible with optical microscopy, due to the much smaller De Broglie wavelength of electrons at several orders of magnitude smaller than the wavelength of visible light. This allows visualization down to the atomic level.<sup>15</sup> The TEM analyses presented in this paper were performed with a High-Resolution TECNAI G2 20 TWIN transmission electron microscope. These measurements were collected using a 200 kV accelerating voltage, and under conditions to minimize electron dose to ensure sample integrity.

## References

1. Moore, J. Gel permeation chromatography. I. A new method for molecular weight distribution of high polymers. *Journal of Polymer Science. Part A: General Papers*, **1964**, 2, 835-843.
2. Striegel, A.; Yau, W. W.; Kirkland, J. J.; Bly, D. D. *Modern size-exclusion liquid chromatography: practice of gel permeation and gel filtration chromatography*. John Wiley and Sons, **2009**.
3. Latorre-Sánchez, A.; Alegría, A.; Lo Verso, F.; Moreno, A. J.; Arbe, A.; Colmenero, J.; Pomposo, J. A. A useful methodology for determining the compaction degree of single-chain nanoparticles by conventional SEC. *Particle & Particle Systems Characterization*, **2016**, 33, 373-381.
4. M. Sartor, *Dynamic light scattering to determine the radius of small beads in Brownian motion in a solution*, University of California San Diego 2003, pp. 1-21.
5. Jacobsen, N. E. *NMR spectroscopy explained: simplified theory, applications and examples for organic chemistry and structural biology*. John Wiley and Sons, **2007**.
6. Willenbacher, J.; Altintas, O.; Trouillet, V.; Knofel, N.; Monteiro, M. J.; Roesky, P. W.; Barner-Kowollik. Pd-complex driven formation of single-chain nanoparticles. *Polymer Chemistry*, **2015**, 6, 4358-4365.
7. Tonelli, A. E. Polymer microstructure: the conformational connection to NMR. *Modern Magnetic Resonance*, **2008**, 1, 567-574.
8. P. R. Griffiths, J. A. de Haset, *Fourier Transform Infrared Spectrometry*, John Wiley & Sons, Inc., Hoboken, New Jersey, **2007**.
9. Perkampus, H. H. *UV-VIS spectroscopy and its applications*. Springer Laboratory, **2013**.
10. Boyer, C.; Granville, A.; Davis, T. P.; Bulmus, V. Modification of RAFT-polymers via thiol-ene reactions: a general route to functional polymers and new architectures. *Journal of Polymer Science: Part A: Polymer Chemistry*, **2009**, 47, 3773-3794.
11. Sanchez-Sanchez, A.; Arbe, A.; Colmenero, J.; Pomposo, J. A. Metallo-folded single-chain nanoparticles with catalytic selectivity. *ACS Macro Letters*, **2014**, 3, 439-443.

12. B. Herman, V.E. Centonze Frohlich, J.R. Lakowicz, D.B. Murphy, K.R. Spring, M.W. Davidson, Fluorescence microscopy: basic concepts in fluorescence, Florida State University, **2003**, pp. 2017.
13. A. Sharma, S.G. Schulman, Introduction to fluorescence spectroscopy, Wiley Analytical Science, New York, **1999**.
14. T.J. Manning, W.R. Grow, Inductively coupled plasma-atomic emission spectrometry, The chemical educator, 2 (**1997**) 1-19.
15. D.B. Williams, C.B. Carter, The Transmission Electron Microscope, in: D.B. Williams, C.B. Carter (Eds.) Transmission Electron Microscopy: A Textbook for Materials Science, Springer US, Boston, MA, **1996**, pp. 3-17.



## Agradecimientos/Acknowledgments

First of all, I would like to thank Prof. Juan Colmenero for giving me the opportunity to join the “Polymers and Soft Matter” group in Material Physics Center (CFM/MPC). I would also like to thank the University of the Basque Country (UPV/EHU) and the University of Bordeaux (UB) for granting me the scholarship and giving me the opportunity to complete this Thesis.

I would like to especially thank my thesis supervisors, Prof. José A. Pomposo and Prof. Daniel Taton for their guidance along this long path. Thank you very much for your patience, your constant support and commitment. It has been a work full of new challenges, adversities and frustrations, and I am sure that I would not have been able to carry it out without knowing that you were there to support me.

También quiero mostrar mi agradecimiento a todos los miembros del grupo “Polymers and Soft Matter” del Centro de Física de Materiales por hacerme sentir como en casa durante cuatro años. Ha sido un placer realizar un trabajo tan duro y largo rodeado de vosotros. Muchas gracias especialmente a Isabel, Jon, Amaia, Ester, Bea, Andrea, Eric, Numera, Paula, Dani, Agustin, Baltasar, Pelayo, Ainara y Mikel. Ha sido un placer compartir este capítulo de mi vida con vosotros.

Muchas gracias Davide. No tengo palabras para explicar lo especial que ha sido compartir mi tesis contigo. Nunca olvidaré todas las charlas que hemos tenido, todo lo que he aprendido de ti y todo lo que nos hemos ayudado el uno al otro. Hemos reído y llorado, nos hemos frustrado y enfadado juntos, y gracias a todo eso, siempre tendrás un amigo aquí para todo lo que necesites. Ambos sabemos que mi Tesis no podría haberse desarrollado sin ti, muchas gracias.

Mila esker bidea erraztu didazuen guztiei. Berako lagunak, urte hauetan pixkat desagertu eta oso presente egon ez arren, oso maitatua sentiarazteagatik beti. Aukeratutako familia zaretela esaten da, eta uste dut, ezin izan nuela hobeto aukeratu. Beste hamaika

urterengatik elkarrekin, mila esker Julen, Esna, Javi, Alda, Bittor, Mitxel, Iñigo, Joseba, Errando, Jon, Ruben eta Moreno.

Mila esker Maider, urte hauetan bidailagun izan eta nire gorabehera guztiak ulertu eta aurre egiten laguntzeagatik. Egun onak elkarrekin ospatzea ederra da, baino ezingo dizut hitzez eskertu une zailenetan ere, bion partez indarra atera eta aurrera egiten lagundu izana. Ukitzen duzun dena hobetzen duzu beti. Harro egiten ari zaren bidez, zientzialari aparta izateaz gain, pertsona bikaina zara, eta ez dakizu nola betetzen nauen bidea zure alboan egiteak.

Ama, atta eta Esti. Mila esker zuen zaintzagatik. Urte guzti hauetan nere bertsio onena erakustera motibatzeagatik. Betirako geldituko dira etxeko sukaldean izandako elkarrizketak laborategian zer egiten nuen azaldu nahian, attak boligrafoz marraztu eta ulertzen saiatzen zineten bitartean. Beti egin duzue lan nire ongizatearen alde, eta ez dakizue nola eskertzen dizuedan. Atta barkatu, baina, tesi hau zuretzat da Ama.

Emozionatzen hasi naiz dagoeneko. Ez nuke hau bukatu nahi zuek eskertu gabe, Garazi, Javi, Julen, Andoni, Ane, Txiki, Mattin, Eneko, Elena, Eñaut, Esti eta Sergio.

Seguru izen batzuk ahaztu ditudala, baina hala ere, mila esker hau guztia posible egin duzuen denei, zorretan nago zuekin.

*“Don’t allow your life to be just fine, or okay, or even good. Make it brilliant, spectacular, wild, extraordinary. Be passionate, and fearless, search for your freedom and opportunity. You only have one life. Make it yours.”*